| Title | Angle resolved photoemission studies of the metal adsorbed Si (111) surfaces and transition metal dichalcogenides |
|---|---|
| Author(s) | 奥田, 太一 |
| Citation | 大阪大学, 1997, 博士論文 |
| Version Type | VoR |
| URL | https://doi.org/10.11501/3129134 |
| rights | |
| Note | |

# Angle resolved photoemission studies of metal adsorbed Si(111) surfaces and transition metal dichalcogenides

Taichi OKUDA

*Department of Material Physics,*
*Faculty of Engineering Science,*
*Osaka University*

23rd Jan. 1997

# Abstract

In low dimensional systems such as material's surfaces or layered compounds, many interesting phenomena based on their low dimensionalities appear. On the crystal surface, atomic displacements from the bulk extrapolated position are often observed as called surface reconstruction. They often accompany changes of the surface electronic states having two dimensional character which may differ from the bulk electronic state. Among various material's surfaces, semiconductor surfaces show a full variety of surface reconstructions and have been investigated most intensively because of the industrial importance as well as the academic interests. The layered compound, transition metal dichalcogenide, is another example of the low dimensional system having also a quasi-two dimensional electronic structure because of their weak interaction of van der Waals force along the $c$ axis(surface normal). The interesting phenomenon of these transition metal dichalcogenides is the occurrence of the charge density wave(CDW) caused by their low dimensionality.

Photoelectron spectroscopy is one of the most powerful and suitable methods to investigate the electronic structure of these interesting low dimensional systems. Especially angle resolved photoelectron spectroscopy(ARPES) measurement is the only way to know the band structure of the material directly. In addition, by using a display type analyzer we can easily perform the two dimensional ARPES measurement(the ARPES measurement in full azimuth and polar angles) and obtain the complete electronic structure of the two dimensional systems, namely, the band structure and symmetry of the electronic wave function in the initial state.

In this thesis, I tried to investigate metal adsorbed typical semiconductor surfaces, concentrating on the metal induced reconstructed Si(111) surfaces. As the system, I studied the electronic and geometric structures of the alkali metal induced Si(111)3×1 surfaces by ARPES and core level spectroscopy(CLS). In addition, the Ag induced Si(111)3×1 surface, Au induced Si(111)5×2, $\alpha$- and $\beta$- $\sqrt{3} \times \sqrt{3}$, 6×6 surfaces were also investigated by these photoemission techniques. We obtained the experimental band structures and information of the surface geometric structure of these surfaces and discussed them precisely.

Using the display-type analyzer developed by ourselves I have also performed the 2D-ARPES measurement of the transition metal dichalcogenides, $1T$-$TaS_2$ , $2H$-$TaSe_2$ , $2H$-$NbSe_2$ and obtained the complete electronic structures of these layered compounds. I have also investigated the photon energy dependence of the photoelectron angular distribution(PEAD) patterns of these materials and found some new results on their PEAD patterns. The Fermi surfaces of these layered compounds were directly observed by the display-type analyzer. I also discussed about the Fermi surface nesting which is related strongly with the occurrence of the CDW.

# Contents

# List of Figures

3

# List of Tables

# Chapter 1

# Introduction

## 1.1 Investigation of metal-induced surface reconstructions of Si(111)

The low index Si surfaces such as Si(111) and Si(100) surfaces are one of the most intensively and extensively studied surfaces. Because of the remaining dangling bonds, drastic changes of the surface crystal structure from the bulk structure called "surface reconstruction" occurs on the semiconductor surfaces. Even on the clean surface, very complex surface reconstructions such as famous 7×7 or 2×1 for Si(111) and 2×1 for Si(100) surfaces are observed. When we adsorb some other atoms on these surfaces, more complex surface reconstructions are realized[1]. According to the surface reconstructions, the surface can have different electronic structure from that of bulk. These electronic states are called surface states. Investigation of the geometric and electronic structures of these variously reconstructed surfaces is very much interesting and one of the main subject of the field of the surface science. In consequence of investigating these electronic and geometric structures of the surfaces, we may find new phenomena on the surface or can apply some characteristics of the surfaces, such as surface electron conductivity, to some electronic devices or so, in future. In spite of the great efforts to investigate those surface reconstructions, however, only few reconstructed structures have been solved completely.

One of the purposes of this thesis is to understand the geometric and electronic structures of simple metal(alkali metals(AM), noble metals(Cu, Ag, Au)) induced reconstructions of Si(111) surfaces. These metals have only one $s$ electron in the outer most shell and it is expected that the reaction between adsorbate metals and Si substrate is relatively simple. In spite of the simplicity of the electronic structure of these metals, the induced reconstructions are very complex. By the adsorption of AM on the Si(111) surface, the 3×1, $\sqrt{3} \times \sqrt{3}$, and 4×4 reconstructions have been reported so far[2, 3]. The 3×1 reconstruction also appears when we adsorb Ag atoms on the Si(111) surface at about 600°C , and this surface shows phase transition to 6×1 surface when we cool down the sample below 220°C [5, 4]. On the other hand, Au atoms induce other surface reconstructions on the Si(111) surface such as 5×2(=5×1), $\sqrt{3} \times \sqrt{3}$, and 6×6[6]. In the case of $\sqrt{3} \times \sqrt{3}$ reconstruction induced by Au atoms there are two kinds of $\sqrt{3} \times \sqrt{3}$ reconstructions named $\alpha$-$\sqrt{3} \times \sqrt{3}$ and $\beta$-$\sqrt{3} \times \sqrt{3}$[6]. Ag also induces $\sqrt{3} \times \sqrt{3}$ reconstruction[5, 4] but there are not such two phases and the electronic structure of the surface is considered to differ from that of Au induced $\sqrt{3} \times \sqrt{3}$ surface as indicated by different Scanning Tunneling Microscopy(STM) images [7, 8] or different results of Angle Resolved Photoelectron Spectroscopy(ARPES)[9, 10].

In this thesis, I investigated the surface electronic state including the band structure, bonding character, charge transfer, and tried to deduce the surface structures of 3×1-AM, 3×1-Ag, 5×2-Au, $\alpha$-$\sqrt{3}$×$\sqrt{3}$-Au, $\beta$-$\sqrt{3}$×$\sqrt{3}$-Au, and 6×6-Au surfaces systematically, using several techniques of photoelectron spectroscopy such as ARPES and Core Level Photoelectron Spectroscopy(CLPS).

## 1.2 Investigation of transition-metal dichalcogenides($1T$-TaS$_2$, $2H$-TaSe$_2$ and $2H$-NbSe$_2$) by 2D ARPES measurement

Studies of electronic states of the low dimensional materials are interesting subjects in the material physics. The electronic structures of the layered compounds such as transition metal dichalcogenides(TX$_2$; T:Transition metal, X:chalcogen) have also the quasi-two dimensionality[11]. These layered compounds, TX$_2$, consists of X-T-X sandwiches and each sandwich is bonded weakly by van der Waals force. Because of the weak bonding along the $c$-axis(=surface normal) these materials have a quasi-two dimensional electronic structure. Therefore the band structures of these layered compounds are expected to have two dimensionality and do not depend on the wave vector in the surface normal direction. Thus we can measure the cross section or the constant energy contour of the band of these two dimensional materials directly by the 2D-ARPES measurement. This type of ARPES measurement can be done by conventional electro static spectrometers having small acceptance cone by rotating the sample using a manipulator with stepping motors[12]. However, this type of measurement takes plenty of time. The display type analyzer can solve this problem. The display type analyzers have large acceptance cone and can simultaneously observe the angular distribution patterns of the emitted electrons from sample[13, 14]. By using display type analyzer, one can obtain the photoelectron angular distribution patterns(PEAD) without rotating samples. When we use polarized light such as synchrotron radiation(SR) as the light source of the photoemission, we can easily know the symmetry of the electron wave function of the initial state in addition to the band structure because the sample is fixed in this experiment, whereas the information is lost in the measurement of sample rotating method.

In this thesis I applied these advantages of the display type analyzer and SR light source as well as the two dimensionality of TX$_2$ to the 2D ARPES measurement of $1T$-TaS$_2$, $2H$-TaSe$_2$, and $2H$-NbSe$_2$ and tried to observe the changes of the PEAD patterns. From the results I discuss about the band structure of these TX$_2$'s as well as the symmetry of the electron wave function of the initial state. As for the $1T$-TaS$_2$ I also compare our experimental PEAD patterns with theoretically simulated PEAD patterns. In addition, the difference of the PEAD patterns between $1T$- and $2H$- type crystals are discussed.

According to previous 2D-ARPES studies of Nishimoto$et$ $al.$[15] the PEAD patterns of $1T$-TaS$_2$ is different between the measurement of h$\nu$=21.2eV and 40.8eV. However it is not evident that the difference arises from the resonance photoemission effect or not. To investigate the photon energy dependence of the PEAD patterns more precisely and to ensure whether the difference is due to Ta $5p$-$5d$ resonance photoemission process or not I have also measured the photon energy dependence of the $1T$-TaS$_2$ using several photon energies including the energies of resonance photoemission condition.

Another interesting character of these low dimensional systems, TX$_2$'s, is an appearance

of a charge density wave(CDW)[16]. The CDW is considered to be caused by the Peierls transition[17], metal-insulator transition, which is derived from the low dimensionality of the electronic states. The probability of the occurrence of CDW is considered to be strongly related with the Fermi surface nesting which is strongly related to the shape of Fermi surface. Therefore I tried to observe the shape of the Fermi surface of these $TX_2$'s directly by the display type analyzer and discuss about that briefly at the end of this thesis.

## 1.3   Organization of this thesis

Before stepping into the main subjects, I describe the principle of the photoelectron spectroscopy and the related topics in the next chapter(Chapter2). In Chapter3 explanations about the experimental apparatus used in this work are given. The previous experimental and theoretical studies of clean Si(111) surfaces are given in Chapter4. After that the first subject, "Photoemission studies of the AM and Ag induced Si(111) 3×1 surfaces", are treated in Chapter5. Then I move to the second subject, "Photoemission studies of the Au induced various reconstruction on Si(111) surfaces" in Chapter6. In Chapter7 I discuss about the results of the 2D-ARPES measurements of the transition metal dichalcogenides. Finally, the conclusion remarks are given in Chapter8.

# References

[1] J.M.Maclaren, J.B.Pendry, P.J.Rous, D.K.Saldin, G.A.Somorjai, M.A.Van Hove and D.D.Vvedensky, *Surface Crystallographic Information Service; A Hand book of Surface Structure, D.Reidel Publishing company*, (1988).

[2] H.Daimon and S.Ino, Surf.Sci.**164**, 320 (1985).

[3] S.Mizuno, and A.Ichimiya, Appl.Surf.Sci. **33/34**, 38 (1988).

[4] Y.Gotoh, S.Ino, Thin Solid Films, **109**, 255 (1983).

[5] G.LeLay, V.Yu.Aristov, L.Seehofer, T.Buslaps, R.L.Johnson, M.Gothelid, M.Hammer, U.O.Karlsson, S.A.Flodström, R.Feidenhans'l, M.Nielsen, E.Findeisen, and R.I.G.Uhrberg, Surf.Sci.**307-309**, 280 (1994).

[6] S.Ino, Proc. NATO Advanced Research Workshop on RHEED and reflection electron imaging of surfaces, June 15-19, Netherlands (ed. P.K.Larsen and P.J.Dobson), NATO ASI Series B**188**, 3, Plenum, New York(1988).

[7] A.Ph.Dumas, G.Humbert, P.MAthieu, C.Mathiez, R.Mouttet, F.Roland, F.Salvan, and F.Thibaudau, J.Vac.Sci.Technol.,A**6**, 517 (1988).

[8] R.J.Wilson and S.Chiang, Phys.Rev.Lett.,**58**, 369 (1987), E.J.van Loenen, J.E.Demuth, R.J.Tromp, and R.J.Hamers, Phys.Rev.Lett.,**58**, 373 (1987).

[9] C.J.Karlsson, E.Landemark, L.S.O.Johansson, and R.I.G.Uhrberg, Phys.Rev.B**42** (1990) 9546.

[10] L.S.O.Johansson, E.Landemark, C.J.Karlsson, and R.I.G.Uhrberg, Phys.Rev.Lett.**63**, 2092 (1989).

[11] For example L.F.Mattheiss, Phys.Rev.B, bf 8, 3719 (1973).

[12] For example, P.Aebi, J.Osterwalder, R.Fasel, D.Naumovic, and L.Schlapbach, Surf.Sci.**307-309**, 917 (1994).

[13] H.Daimon, Rev.Sci.Instrum.**59**,545(1988).

[14] D.E.Eastman, J.J.Donelon,N.N.Hien and F.J.Himpsel, Nucl,Instrum. Meth. **172**, 327 (1980).

[15] H.Nishimoto, T.Okuda, T.Nakatani, H.Daimon, T.Matsushita, S.Imada,S.Suga, H.Namba, T.Ohta, y.Kagoshima and T.Miyahara, Solid State Commun. **98**, 671 (1996).

[16] R.Claessen, B.Burandt, H.Carstensen and M.Skibowski,Phys.Rev.B41,8270(1990)

[17] R.E.Peierls, *Quantum Theory of Solids, Clarendon Press, Oxford*, (1955).

# Chapter 2

# Research Methods

## 2.1 Photoelectron spectroscopy(PES)

*Principle of photoemission*

When we inject photons into materials, the photon transfers its energy to an electron. If the excited electrons has enough energy to overcome the threshold energy, which is intrinsic to each materials(called as work-function), they transport to the surface and emit into vacuum. This phenomena is a well known photoemission process and the emitted electrons are called photoelectrons. From energy conservation rule the kinetic energy($E_k$) of the photoelectron is described as

$$E_k = h\nu - \phi - E_B \tag{2.1}$$

and shown by an illustration in Fig. 2.1. Where $h\nu$, $\phi$ and $E_B$ are the energy of incident photon, the work-function of the sample and the binding energy of the initial state of the electron.

Usually the photoemission process is considered by a three step models as follows.
Step 1: Excitation of electrons in a solid by an electromagnetic field of incident photons((1) of Fig. 2.1). Step 2: Propagation of the electron to the surface((2)). Step 3: Transmission of the electron into the continuum level in vacuum((3)). In Fig. 2.3, I presented a schematic view of the processes with the atomic potentials in bulk and surface.

From the energy conservation of eq.(2.1), when we use a plausible electro-static analyzer in vacuum chamber one can observe spectrum illustrated in the figure and can know the initial binding energy of the bounded electrons reference to Fermi energy($E_F$). Besides the "primary" photoelectrons there are other electrons which loses their initial energies by many body effects such as the electron-electron, electron-phonon scattering, excitation of the plasmons, electron-hole pairs *etc.*. The former of the energy lost electrons is the so-called secondary electrons and observed as a smooth background as shown in Fig. 2.1. The latter effects, excitation of the plasmons or electron-hole pairs*etc.*, usually give the satellite structures of the primary peaks. Because of the electron scattering the electron escape depth(=mean free path; $\lambda$) is restricted to about few Åto few tens Åwhereas the photon reaches very deep in sample by the order of about $\sim$1000Å. Therefore the PES measurement is a very surface sensitive technique and very much useful to investigate the surface electronic or geometric structures rather than bulk ones.

The energy dependence of the escape depth does not strongly depend on the materials and described by a famous universal curve as shown in Fig. 2.2.

12
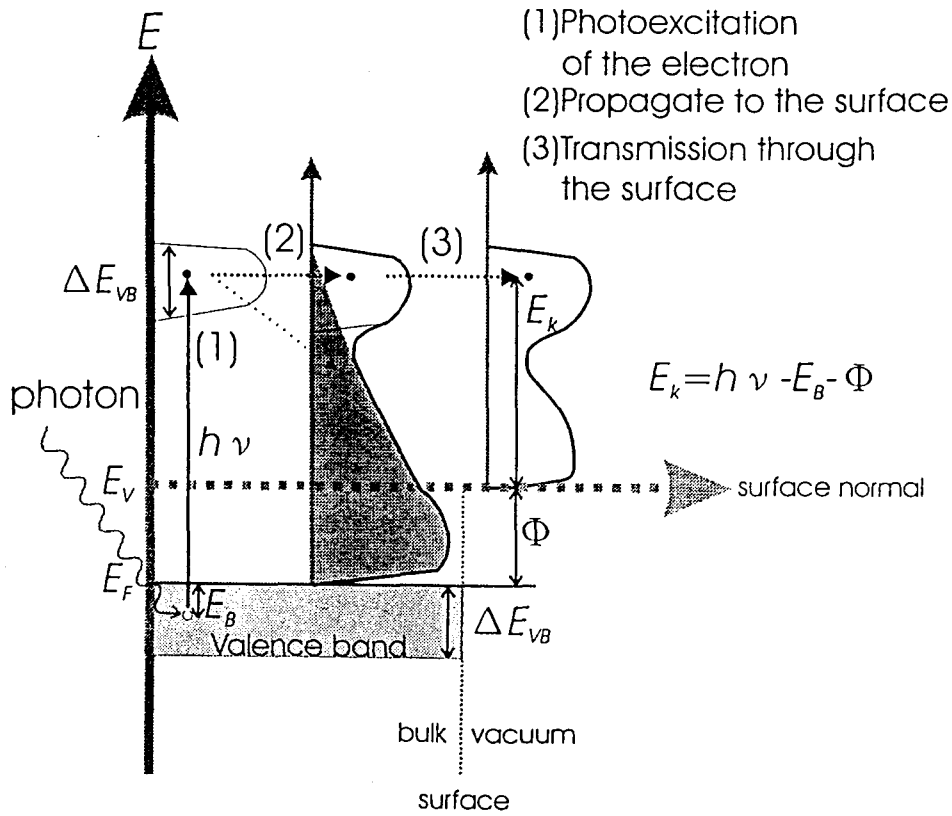
Fig. 2.1: Schematic energy diagram for photoemission from solid and three step model. $E_k$, $h\nu$, $\phi$, and $E_B$ represent the kinetic energy of photoelectron, the photon energy, the work function of the sample, and the binding energy of the initial state of the electron, respectively.
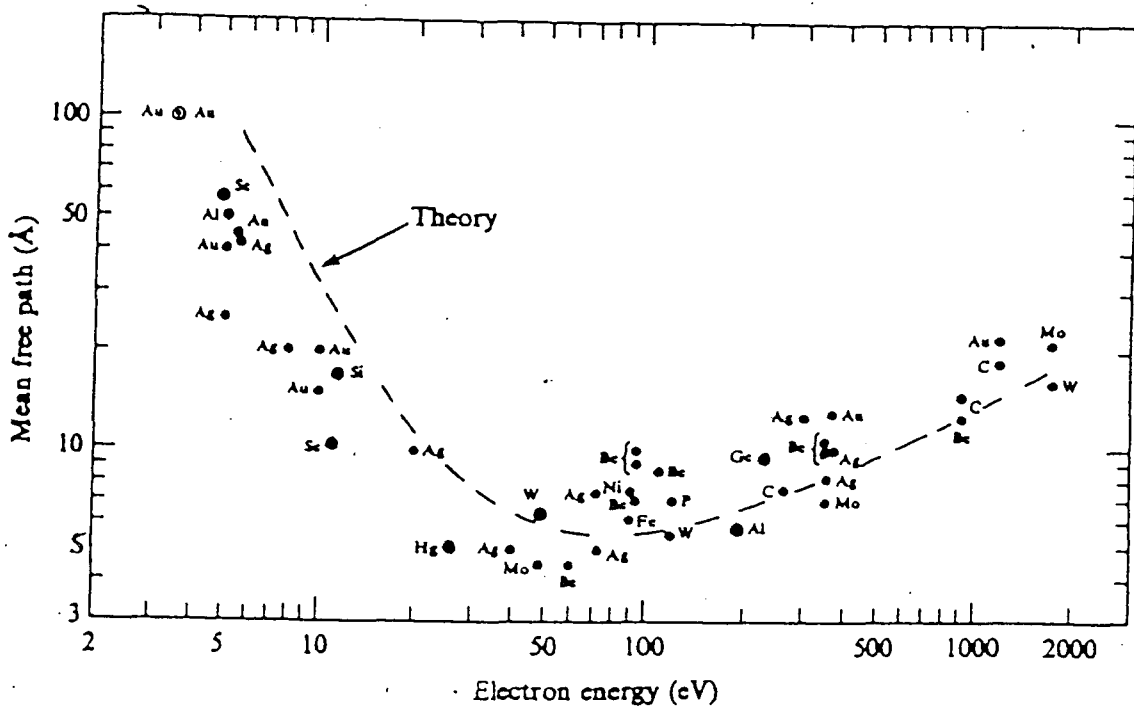


Fig. 2.2: Universal curve of electron escape depth. This characteristic curve is due to the electron-electron or -phonon scattering and excitation of the plasmons etc. This curve does not depend on the materials.

As seen in the figure the escape depth has its minimum at the electron kinetic energy of about from few tens to 100eV. When we use the tunable photon source such as synchrotron radiation(SR) we can easily change the surface sensitivity in the measurement and obtain the information of surface electronic or geometric structures by photoemission.

Typical surface information are the surface states in the bulk band gap or the surface resonant states in the bulk band projection and the surface core level shifts(SCLS) in the core region as schematically shown in Fig. 2.3.
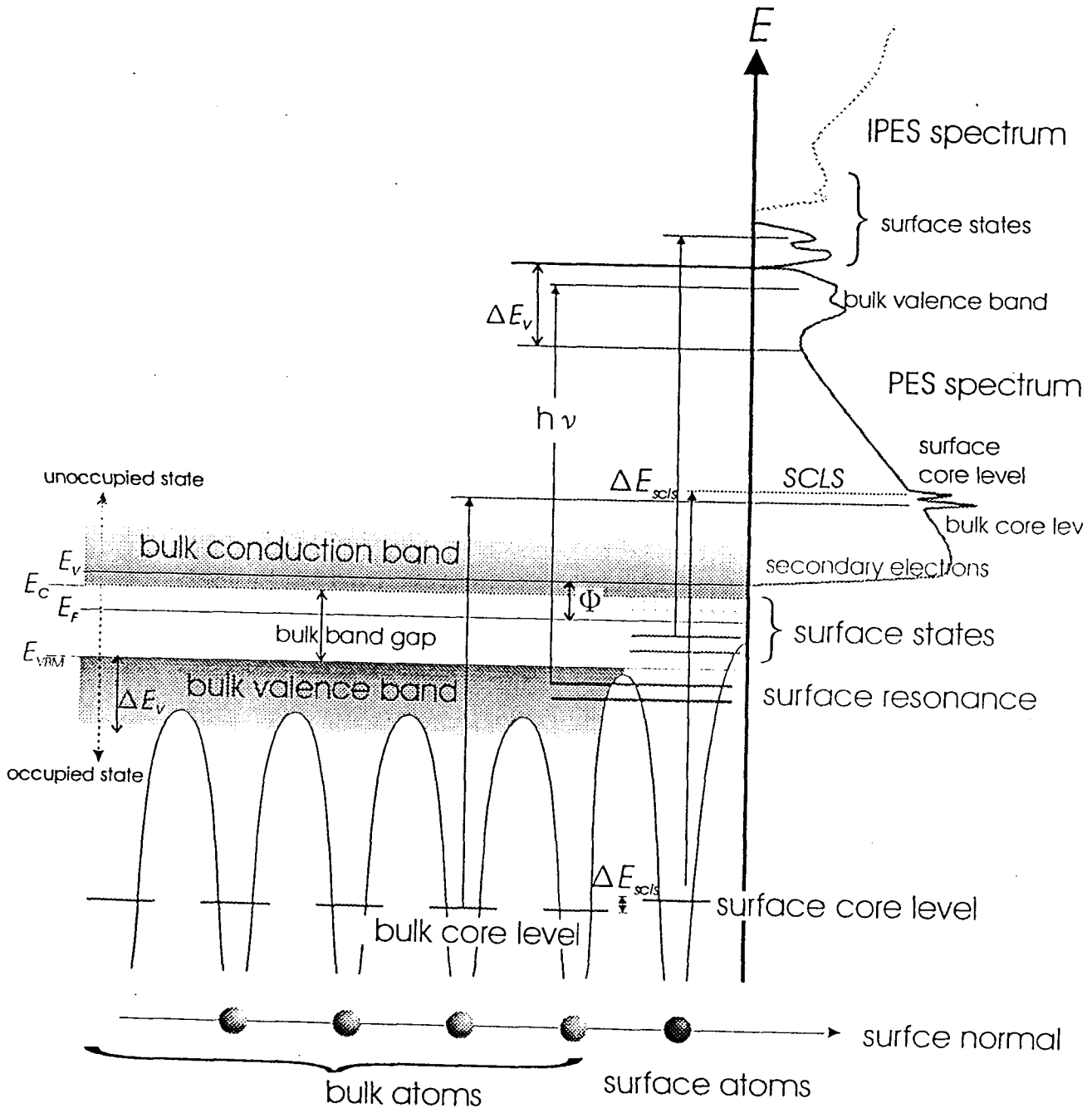


Fig. 2.3: Schematic of the photoelectron spectroscopy of bulk and surfaces.

Because of the two dimensionality of the surface, the surface states(or resonant states) have two dimensional character and usually have almost no dispersion along the surface

14

normal direction. In addition the surface states are generally very sensitive to the contamination or adsorption. Therefore we can distinguish the surface states from bulk band states using these characters. On the other hand because of the different chemical and structural environments of a surface atom from bulk atom, charge redistribution occurs in the surface layer and causes core-level binding energy shifts of the surface atoms from that of the bulk atoms. This binding energy shifts are called surface core level shifts(SCLS). Therefore the SCLS reflects the chemical and structural environments of the surface atoms and we can obtain the information about surface structure or charge redistribution by measuring surface core levels.

## 2.2 Surface Core Level Shift(SCLS)

As mentioned above due to the surface reconstruction or relaxation or adsorption *etc.*, charge redistribution occurs on most of the surfaces. By performing surface sensitive core level photoelectron spectroscopy we can measure the shifted surface core levels due to the charge redistribution as shown in Fig. 2.3. In Fig. 2.4 I show the schematic of the measurement of SCLS. The core levels of surface atoms S1 and S2 shifts higher and lower
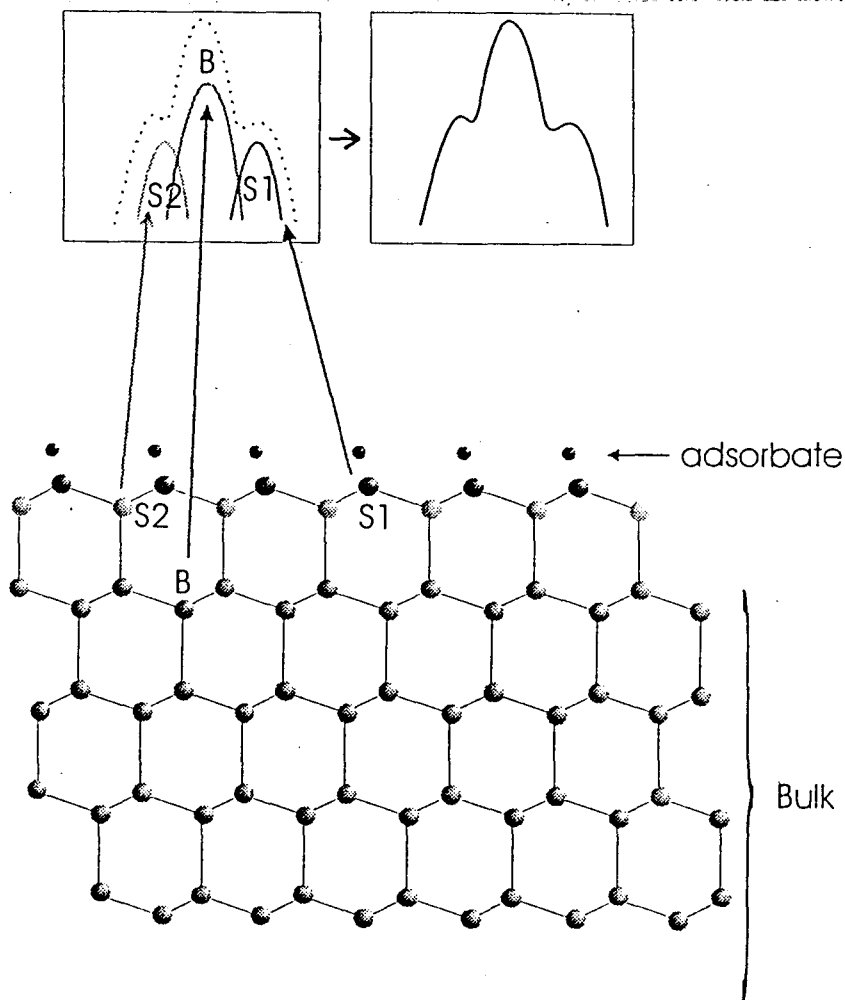


Fig. 2.4: Schematic diagram of the SCLS measurement.

binding energies than the bulk core levels because the surface atoms are charged positively and negatively due to the charge redistribution. A semiquantitative correlation between

15

charge transfer and core level shift has been derived empirically for the Si $2p$ level as follows. The bulk core level shifts for various oxides of silicon with different coordination and charge transfer have been evaluated and the relation $\delta E/\delta q = 2.2\text{eV}/\text{e}^-$ between core-level shift $\delta E$ and charge transfer $\delta q$ has been derived[1].

To deconvolute the mixture of the surface and bulk core levels, a non-linear least-square fitting was used. For the components of curve fitting, I used a well known symmetric Voigt function which is a sum of Lorentzian and Gaussian functions, where Lorentzian represents the life time broadening due to the core hole screening effect and Gaussian represents mainly the instrumental resolution and phonon broadening effects. To estimate the number of the surface atoms in a unit cell contributing to the shifted surface component I used the well known photoelectron layer attenuation model[2]. In this model we assume that each mono-layer attenuates the intensity by an equal degree. Then one can obtain

$$R = \frac{x}{\frac{1}{1-e^{\frac{-d}{\lambda}\cos\theta_{cry}}} - x} \tag{2.2}$$

where $d$ is the spacing between layers, $\lambda$ is the mean free path, $\theta_{cry}$ is the emission angle in the crystal, and $x$ is the fraction of the surface atoms contributing to the surface component in a monolayer. $R$ in the equation is the intensity ratio of the considering surface component($eg.$ $S1$) and defined as

$$R_{S1} = \frac{I_{S1}}{I_{sum} - I_{S1}}. \tag{2.3}$$

Where $I_{S1}$, and $I_{sum}$ represent the observed photoemission intensities of $S1$ and the total of the spectrum. In this thesis I used a mean free path($\lambda$) of 3.9Åfor the Si $2p$ surface sensitive core photoemission($h\nu{\sim}130\text{eV}$), and a spacing between layers($d$) of 1.57Åwhich is the average layer spacing of the Si(111) crystal.In our measurement we took the spectrum at the surface normal direction and the $\theta_{cry}$ was 0. By using this equation I roughly estimated the absolute numbers of the surface Si atoms and discuss about the surface structure of the AM- or noble metal- induced Si(111) surface reconstructions in the following sections.

As mentioned above by deconvoluting the surface and bulk components from the observed core spectrum, which is a mixture of them, we can know (1)the numbers of the kind of surface atoms in different charge distribution, and from their intensities and amount of the shifts we can roughly estimate (2)the absolute numbers of those shifted surface atoms in a unit cell, and (3)the quantities of the charge transfers of each surface component. Therefore the surface-sensitive core-level photoemission study can be a useful tool to investigate the surface geometric structure.

To improve the energy resolution of the SCLS measurement cooling down of the sample is effective because of the reduction of the phonon broadening effect during the transportation of the electrons to the surface. I applied this sample cooling methods to our recent SCLS measurement of Si(111)3×1-Rb and Ag surfaces. Combination of the SCLS measurement and the photoelectron diffraction(PED) method is another useful tool to investigate the surface reconstruction. By measuring a PED pattern of one of the shifted surface core components, we can know the geometric structure around that surface atom. Furthermore if we combine the photoelectron holography method[3] with SCLS measurement we can know the surface structure directly[4] even if the surface consists of the same species of elements. By taking the core level spectra at different photon energies and measure the oscillation of the intensities of the surface core component, we can also know the structural information around the surface atoms in terms of Extended X-ray Absorption Fine Structure(EXAFS)

analysis. The example of these improvement method of SCLS measurement has been reported by several groups[5, 6, 7, 8] on the Si(111)7×7 surface and I will describe about it in detail in the following section. This kind of measurements applying PED to SCLS is useful not only to investigate the surface structure but also to help making general rule of the assignment of shifted surface component in SCLS measurement. To measure such PED effects in the SCLS measurement we have to use the angle resolved photoelectron spectrometer having small acceptance cone or display type analyzer, and inversely when we want to estimate the numbers of the surface atoms from the intensity of the surface component by the aforementioned attenuation model we should use the spectrometer having large acceptance cone to avoid the interference effect.

## 2.3 Angle Resolved Photoelectron Spectroscopy (ARPES)

Of course the aforementioned PED measurement of the core level is powerful application of the ARPES measurement, but the ARPES measurement is the most important as a tool to investigate the band dispersion of the materials and the only way to investigate the band structure experimentally. In the photo-excitation by low energy photons, in which the wave vector of the incident photon $q$ is smaller enough compared to that of the Brillouin zone of the sample, the electron wave vectors before and after the photo-excitation are conserved. Thus the following relations between the electron wave vectors of the initial($K_i$) and the final state($K_f$) are satisfied.

$$\mathbf{K_f} = \mathbf{K_i} + \mathbf{G} + \mathbf{q} \qquad (2.4)$$

$$\mathbf{q} \simeq 0 \qquad (2.5)$$

$$\mathbf{K_f} = \mathbf{K_i} + \mathbf{G} \qquad (2.6)$$

Where $G$ is one of the surface reciprocal lattice vector. When the photoelectron transmits into vacuum from the surface the wave vector perpendicular to the surface($K_{f\perp}$), however, is modified by the potential barrier of so called inner potential($V_0$) as seen in Fig. 2.5. Fortunately the wave vector parallel to the surface($K_{f\parallel}$) is conserved because of the crystal periodicity along the surface. Thus the wave vector parallel to the surface of the transmitted electron, $k_{f\parallel}$ and $K_{i\parallel}$ are related as

$$\mathbf{k_{f\parallel}} = \mathbf{K_{f\parallel}} = \mathbf{K_{i\parallel}} \qquad (2.7)$$

Approximating the final state of the transmitted electron as a plane wave of the free electron, we obtain the wave vector of the initial state parallel to the surface$K_{i\parallel}$ as a function of polar emission angle($\theta_e$) and photoelectron kinetic energy($E_k$) as

$$\mathbf{k_{f\parallel}} = \mathbf{K_{f\parallel}} = \mathbf{K_{i\parallel}} = \frac{\sqrt{2m}}{\hbar}\sqrt{E_k}\sin\theta_e \qquad (2.8)$$

from eq.(2.1)

$$= \frac{\sqrt{2m}}{\hbar}\sqrt{h\nu - \phi - E_B}\sin\theta_e \qquad (2.9)$$

$$= 0.5123\sqrt{h\nu - \phi - E_B(eV)}\sin\theta_e \qquad (2.10)$$

17

normal

$$K_{i\parallel}=K_{i\prime\prime}=k_{i\prime\prime}=k_f\sin\theta$$
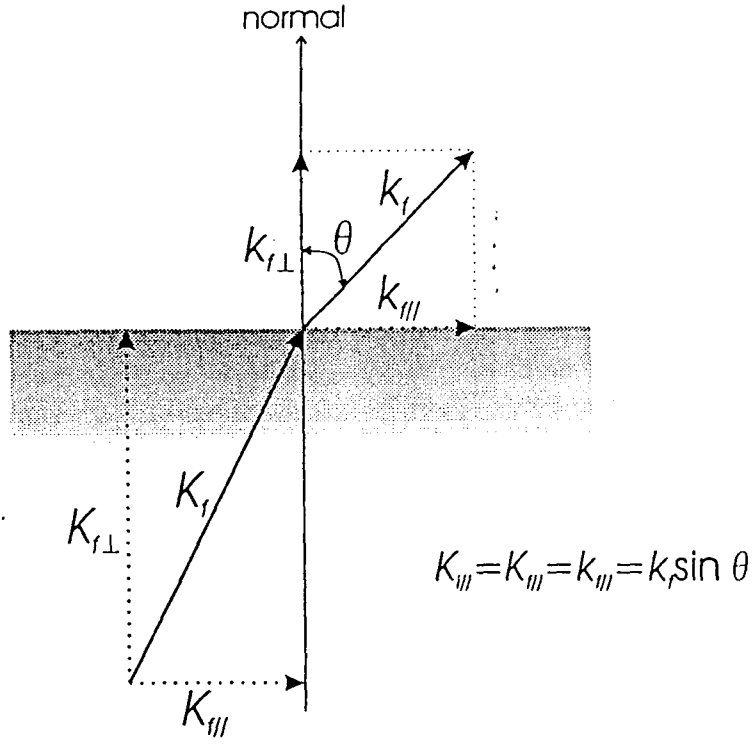
Fig. 2.5: Schematic diagram of the wave vector conservation in photoemission. The wave vector parallel to the surface($K_{f\parallel}$) is conserved in photoemission but that of perpendicular($K_{f\perp}$) is not conserved because of the inner potential.

Therefore we can obtain the relation between $\mathbf{K}_{i\parallel}$ and $E_B$, that is $E_B(\mathbf{K}_{i\parallel})$ by measuring the $E_k$ and polar angle $\theta_e$. The schematic diagram of the ARPES measurement is shown in Fig. 2.6.

Though $\mathbf{K}_{i\perp}$ does not conserve because of the $V_0$, if we count for the energy conservation including the inner potential $V_0$ we can also obtain the relation between $\mathbf{K}_{i\perp}$ and $E_B$ as

$$\mathbf{K}_{i\perp}=\frac{\sqrt{2m}}{\hbar}\sqrt{(h\nu-\phi-E_B)\cos^2\theta_e+V_0} \qquad (2.11)$$

$$=0.5123\sqrt{(h\nu-\phi-E_B(eV))\cos^2\theta_e+V_0} \qquad (2.12)$$

Therefore when we fix the analyzer at surface normal direction eq.(2.9) and eq.(2.11) are

$$\mathbf{K}_{i\parallel}=0 \qquad (2.13)$$

$$\mathbf{K}_{i\perp}=\frac{\sqrt{2m}}{\hbar}\sqrt{(h\nu-\phi-E_B)+V_0} \qquad (2.14)$$

and by scanning the photon energy, $h\nu$, we can also know the dispersion along the surface normal. The unknown $V_0$ can be estimated by changing the value of $V_0$ so that the obtained dispersions have symmetry around $\bar{\Gamma}$ point. By measuring the energy dispersion along the surface normal direction we can obtain a useful evidence to discriminate the surface states from the bulk states based on the characteristic of the surface state having only small(or no) dispersion along the surface normal direction. By using this ARPES technique we have measured the electronic structure of Si(111)3×1-Na, 5×2-Au, $\alpha$-$\sqrt{3}$×$\sqrt{3}$-Au, $\beta$-$\sqrt{3}$×$\sqrt{3}$-Au and 6×6-Au surfaces. In addition we have also performed 2 dimensional ARPES(2D-ARPES) on the transition metal dichalcogenides using display type analyzer.

Using a polarized photon such as synchrotron radiation, we can know about not only the band dispersion but also the symmetry of the surface states. It is based on the well
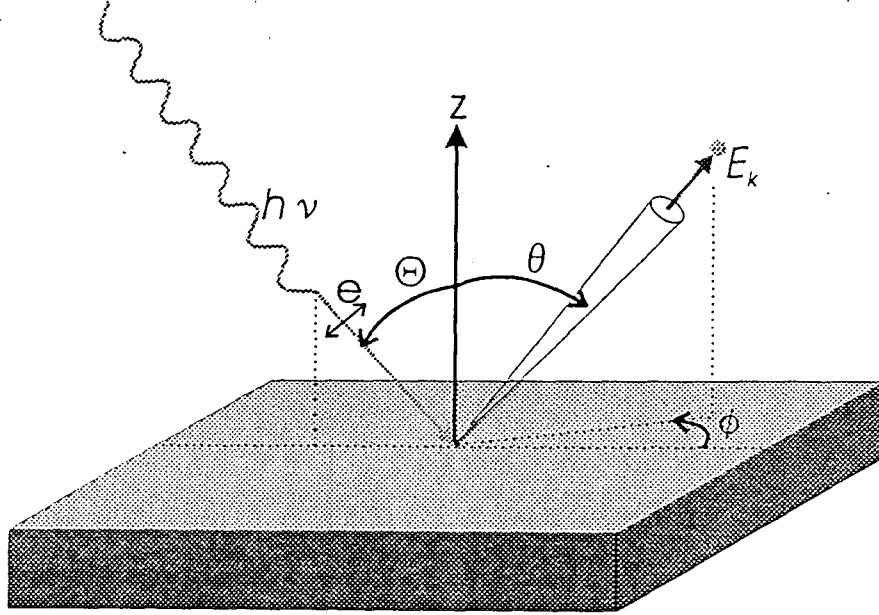
Fig. 2.6: Diagram of ARPES measurement.

known symmetry selection rule of a dipole transition, where the transition probability is proportional to $\langle f|\mathbf{A} \cdot \mathbf{p}|i\rangle$, where $|i\rangle$ and $|f\rangle$ are the initial and final state wave functions, respectively, $\mathbf{A}$ the vector potential of the incident photon and $\mathbf{p}$ the momentum operator. Since only the final state of even symmetry can be observed and $\mathbf{p}$ is conserved in the mirror reflection operation, a specific symmetry of the initial state can be selected by the symmetry of $\mathbf{A}$: if $\mathbf{A}$ is even for a given mirror plane only even symmetry of initial state is excited and vice versa.

In order to determine the initial state symmetries, two different measurement geometries, denoted as $A_\parallel$ and $A_\perp$ can be used[9](see Fig. 2.7). In the $A_\parallel$ geometry, the photoelectron emission always lies in the plane defined by the surface normal $(\hat{n})$ of the sample and the incident light whose polar angle($\Theta$) from surface normal. $\Theta$ is fixed at about $45°$ in all measurements in this thesis. Since the linear polarization vector($\hat{e}$) of incident synchrotron radiation is always in the horizontal plane which is the same as the plane of emission in this geometry, only the electronic states of even symmetry are detected for a scan in the mirror plane. In this thesis we done all the ARPES measurement for the metal adsorbed Si(111) surfaces in this geometry.

On the other hand, in the $A_\perp$ geometry the emission is kept in the plane which contains $\hat{n}$ and is perpendicular to the plane defined for $A_\parallel$ geometry. If $\Theta$ is zero in this geometry, $\hat{e}$ is always perpendicular to the plane of emission, thus only the odd symmetry states can be excited. By using this symmetry dependence of the photoemission we can determine the symmetries of each surface state. In our 2D-ARPES measurement the both $A_\parallel$ and $A_\perp$ geometries can be performed simultaneously and we discuss about the symmetry of the wave function of the initial state electrons of transition metal dichalcogenides.

19
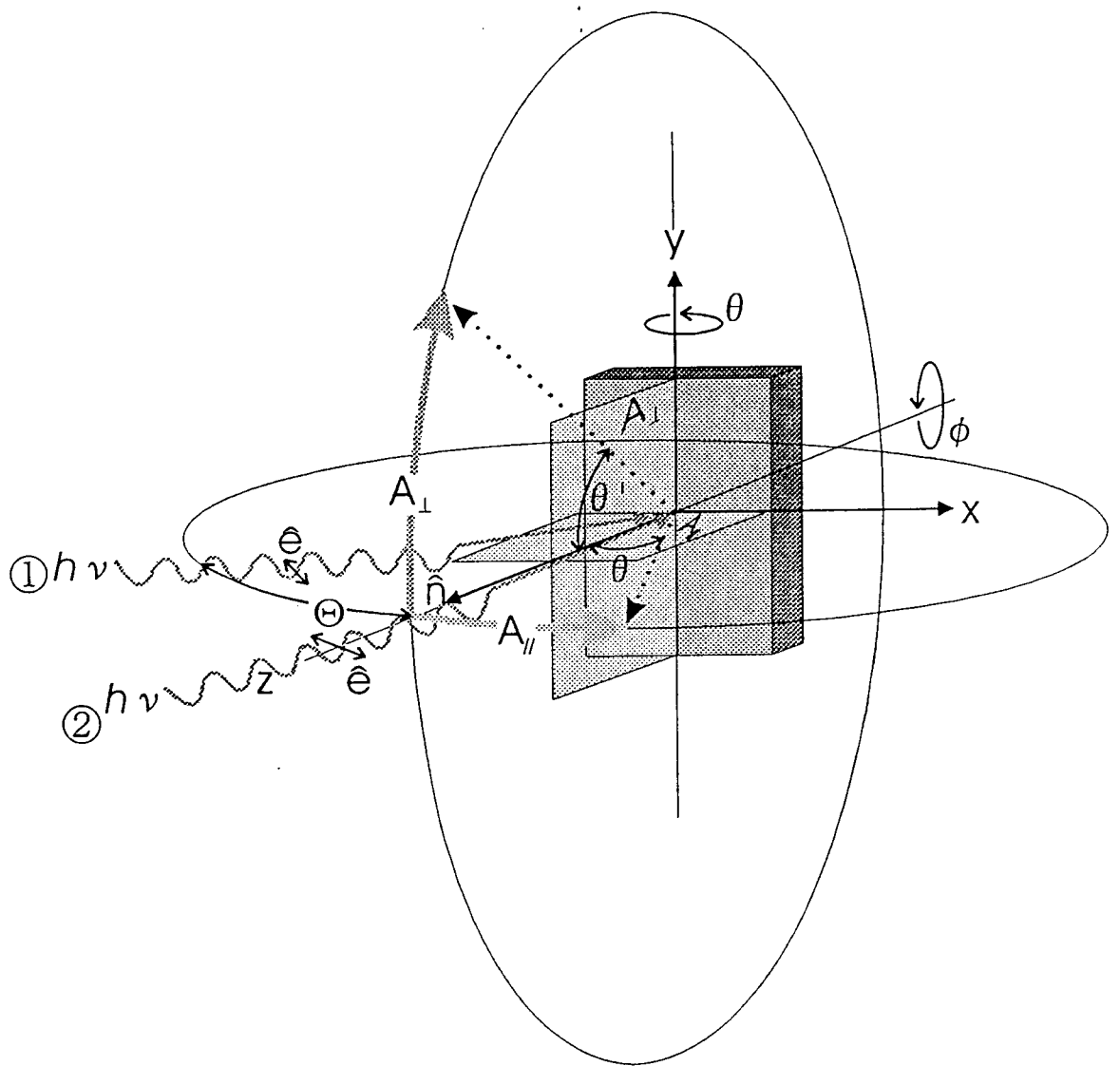
Fig. 2.7: Schematic diagram of the ARPES measurement geometries with polarized light.

## 2.4 Resonance Photoemission Spectroscopy(RPES)

Resonance photoelectron spectroscopy(RPES) is another powerful technique of the photoemission to investigate certain valence band features. "Resonance" photoemission means, that one excites photoemission with photons of an energy $h\nu$ very close to the absorption threshold of a core level. As mentioned already in this thesis we performed the 2D-ARPES of the transition dichalcogenides and also measure the 2D angular distribution patterns of them in the photon energy range of resonance photoemission, that is Ta $5p$-$5d$ resonance photoemission condition in $1T$-$TaS_2$ and $2H$-$TaSe_2$ . The schematic of the process of Ta $5p$-$5d$ resonance photoemission is shown in Fig. 2.8 As seen in the figure in this case the direct
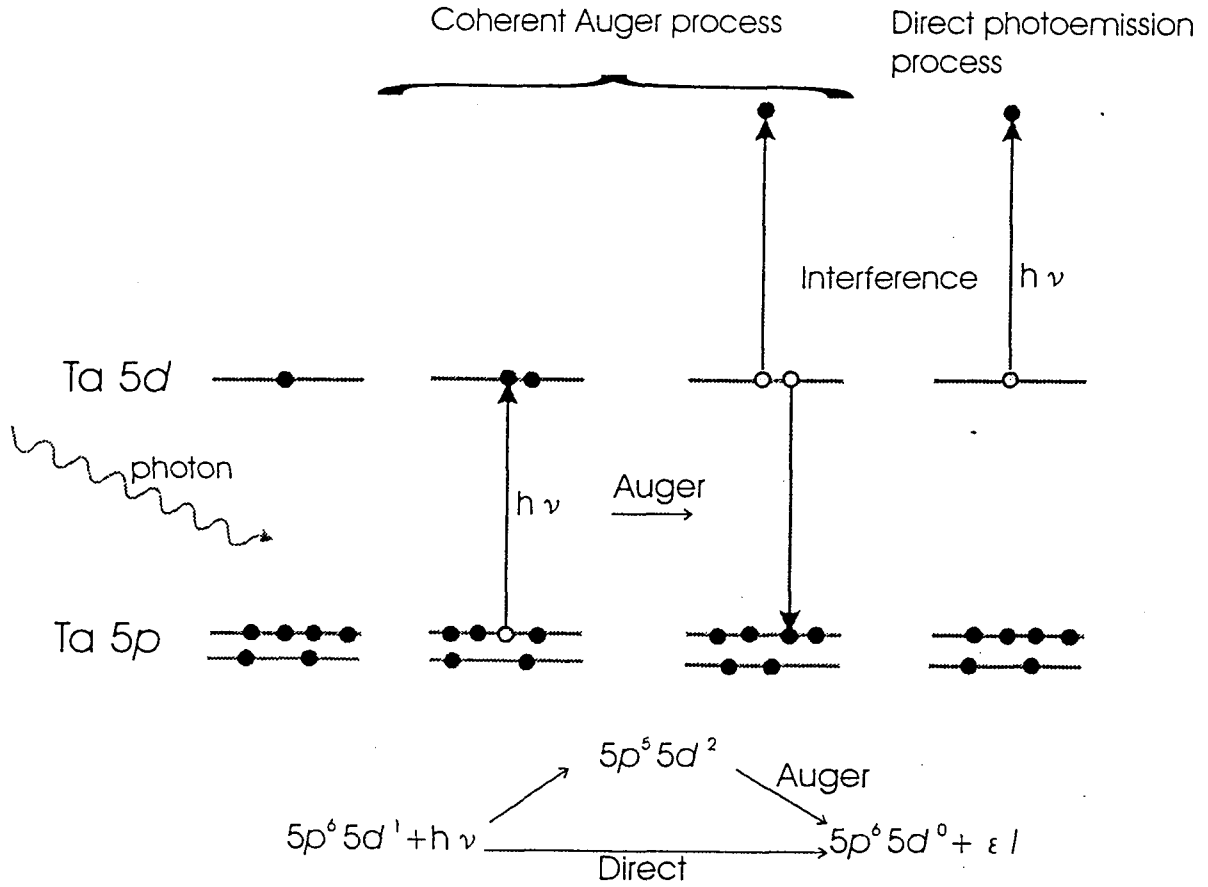


Fig. 2.8: Schematic diagram of the process of Ta $5p$-$5d$ resonance photoemission

photoemission process of Ta $5d$ valence band can interfere with Ta $5p5d5d$ Auger process that are excited by a Super Koster Kronig process. The photon energy dependence of the intensity $I(h\nu)$ for the feature in the valence band where the direct photoemission process and the Auger emission overlap is given by the so-called Fano line shape

$$I(h\nu) \simeq \frac{(\epsilon + q)^2}{\epsilon^2 + 1} \tag{2.15}$$

$$\epsilon = \frac{h\nu - h\nu_j}{\Delta(h\nu_j)/2} \tag{2.16}$$

where $h\nu_j$ is a photon energy equal to the binding energy of a core level, $q$ is a parameter for the particular process and $\Delta(h\nu_j)$ is the width(FWHM) of that core level. The coherent interference between the direct photoemission process and the Auger process is only possible exactly within the energy range of $\Delta(h\nu_j)$ around the resonance; only then the excitation from the core level of $5p$ into the empty valence level of $5d$ is possible. At higher photon energies only the nonresonant("normal") Auger electrons are observed and at lower photon energies only the direct photoemission process is available.

# References

[1] F.J.Grunthaner, P.J.Grunthaner, R.P.Vasquez, B.F.Lewis, J.Maserjian, and A.Madhukar, Phys.Rev.Lett.**43**, 1683 (1979).

[2] For example, C.J.Karlsson, E.Landemark, L.S.O.Johansson, U.O.Karlsson, and R.I.G.Uhrberg, Phys. Rev. B**41**, 1521 (1990).

[3] J.J.Barton, Phys.Rev.Lett. **61**,1356 (1988).

[4] M.T.Sieger, J.M.Roesler, D.-S.Lin, T.Miller, and T.-C.Chiang, Phys.Rev.Lett.,**73**, 3117 (1994).

[5] G.LeLay, M.Göthelid, T.M.Grehk, M.Björkquist, and U.O.Karlsson, and V.Yu.Aristov, Phys.Rev.B**50**, 14277 (1994).

[6] J.J.Paggel, W.Theis, and K.Horn, Phys.Rev.B**50**, 18686 (1994).

[7] C.J.Karlsson, E.Landemark, Y.-C.Chao, and R.I.G.Uhrberg, Phys.Rev.B,**50**, 5767 (1994).

[8] J.A.Carlisle, M.T.Sieger, T.Miller, T.-C.Chiang, Phys.Rev.Lett. **71**, 2955 (1993).

[9] For example, C.J.Karlsson, E.Landemark, L.S.O.Johansson, and R.I.G.Uhrberg, Phys.Rev.B**42** (1990) 9546.

# Chapter 3

# Apparatus

## 3.1 Beamline BL-18A of Photon Factory

ARPES and SCLS measurements of the metal/semiconductor surfaces except for the ARPES measurement of Au/Si(111) have performed at beamline BL-18A[1] of Photon Factory(PF) in National Laboratory for High energy Physics(KEK). This beamline has been constructed by staff of Institute for Solid State Physics(ISSP) to be dedicated to the photoemission experiments of surfaces and interfaces with high energy and angle resolutions. The schematic view of the optics of this beamline is illustrated in Fig. 3.1. The Synchrotron Radiation(SR) from the bending magnet are monochromatized by a constant deviation angle grazing incidence monochromator and aligned and focused into $2mrad$ of horizontal divergence by five mirrors and delivered into the analyzer chamber.

The photon energy available here(BL-18A) is 15 to 150eV by using four different spherical gratings and energy resolution is 50meV at the Fermi edge of Au at h$\nu$=15eV. As shown in Fig.3.2, in this analyzer chamber two commercial electron static spectrometers are equipped. One of them is VG-ADES 500($\phi$100) for angle resolved measurement on the two axis goniometer to rotate the analyzer with acceptance cone of $\pm0.5°$ . For the angle integrated measurement VG-CLAM-II with larger acceptance cone($\pm8.0°$ ) is available and we used this spectrometer to record the core spectra for SCLS measurement. Besides these spectrometers, LEED optics, manipulator with five axis goniometer, conventional X-ray source, He resonance lamp are available. To deposit metals on to the Si samples we attached metal evaporators and quartz oscillator film thickness monitor at adequate ports. To cool down the sample temperature we also used the He cryostat. The base pressure of the chamber was $2.0\times10^{-11}$ Torr.

## 3.2 Beamline BL-4 of SOR-RING

For the 2D-ARPES studies of the transition metal dichalcogenides we used the beamline of BL-4[2] at SOR-RING[3]. This storage ring is the oldest ring in Japan for synchrotron light source constructed in Tanashi, Tokyo by the staff of ISSP in 1976 and will be shut down in this March(1997). The SR generated by this 500MeV storage ring using a bending magnet transports into the analyzer chamber through the Plane Grating Monochromator(PGM) which is illustrated in Fig. 3.3. This monochromator is equipped with three Plane Mirrors(PM1 to 3) and two Focusing Mirrors(FM1 and 2) and plane grating(G) (2400 lines/mm). Changing the combinations of the PM and FM the monochromator covers the

# Constant deviation angle grazing incidence monochromator of BL-18A, KEK, PF



$M_0$: circular cylindrical mirror

$M_1$: plane mirror $\theta_1=86°$

$M_2$: illiptical cylindrical mirror $\theta_2=86°$

$M_i$: intercept mirror $\theta_i=86.75°$

$M_3$: toroidal mirror $\theta_3=87°$

G: spherical Grating (G1,G2,G3,G4)

D: Diaphragm

$S_i,S_e$:incident and exit Slits
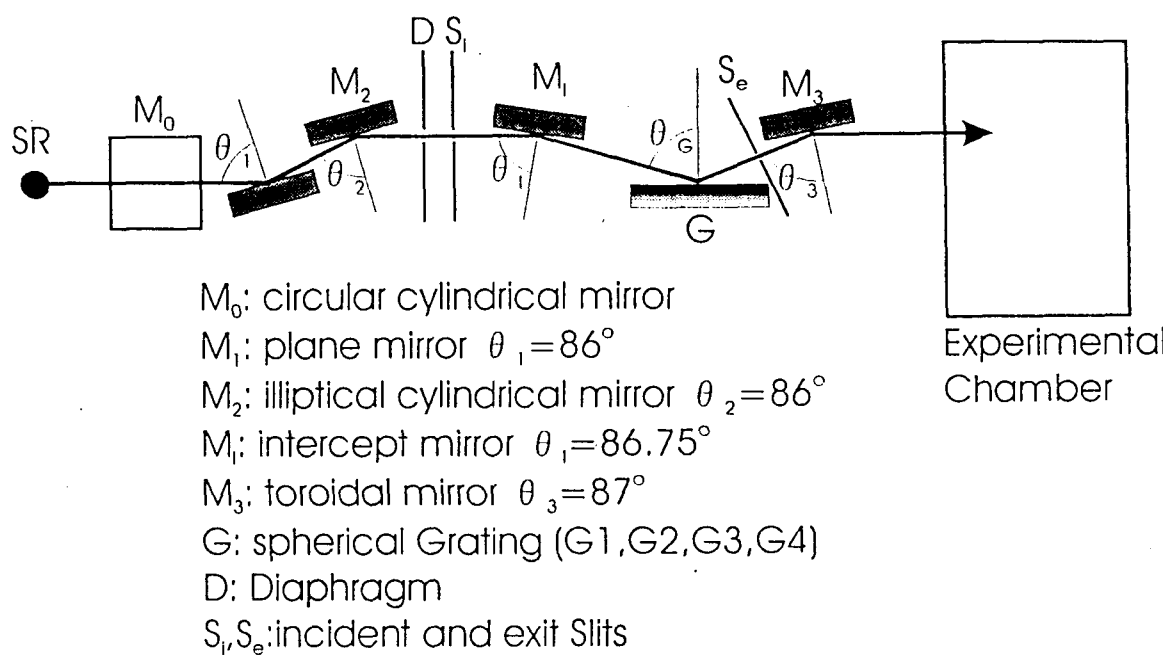
Fig. 3.1: Schematic diagram of the beamline BL18A of Photon Factory.
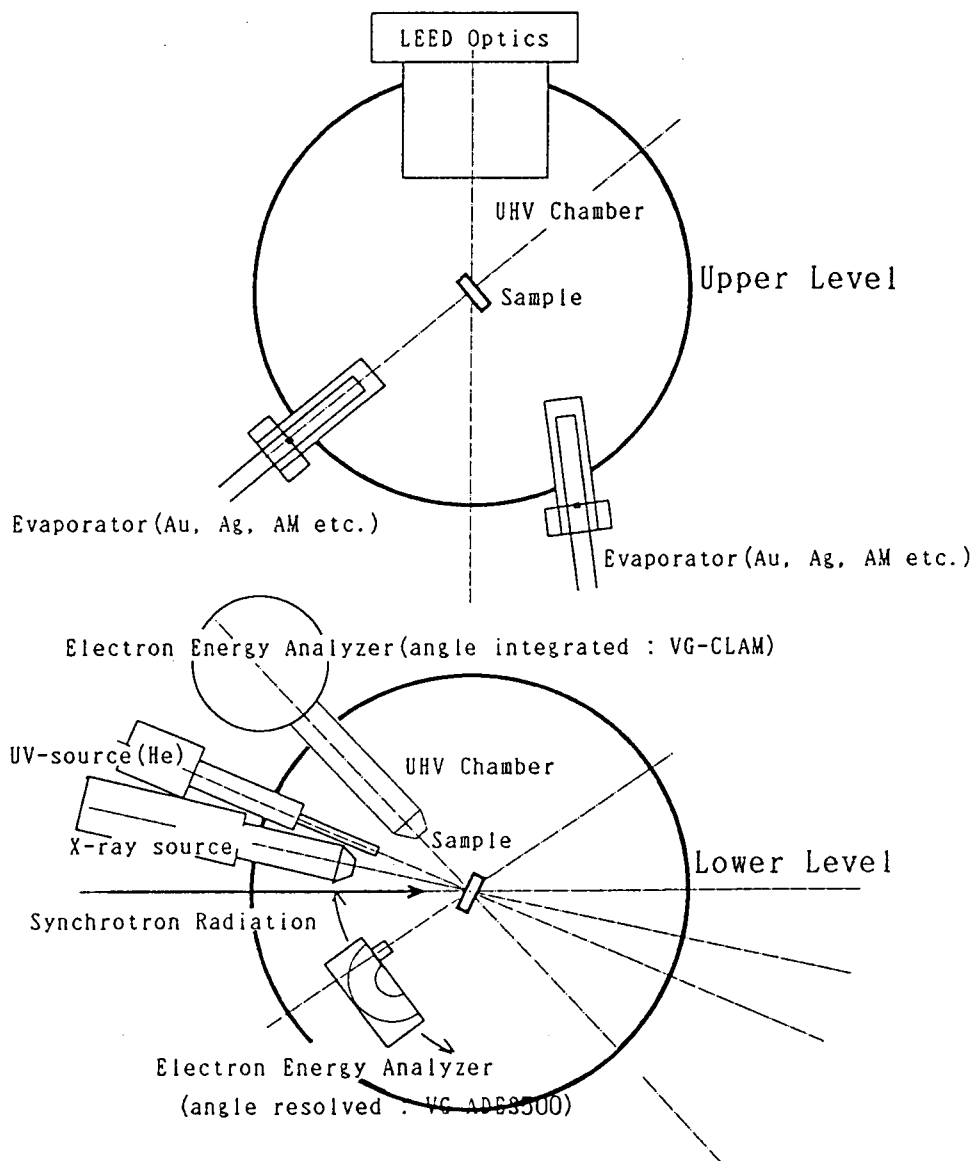
Fig. 3.2: Equipment of the analyzer chamber of BL18A

photon energy of 20eV to 200eV. We used photon energies of 30eV to 60eV for the measurement of the photon energy dependence of the photoelectron angular distribution pattern of transition metal dichalcogenides and over all energy resolution of the measurement was 250meV to 400meV.

## Constnat deviation angle
## grazing incidence monochromator of BL-4



SR:Synchrotron Radiation
D:entrance Diaphram
PM:Plane Mirror
FM:Focussing Mirror
S:exit Slit
fm:focusing mirrors
s:sample
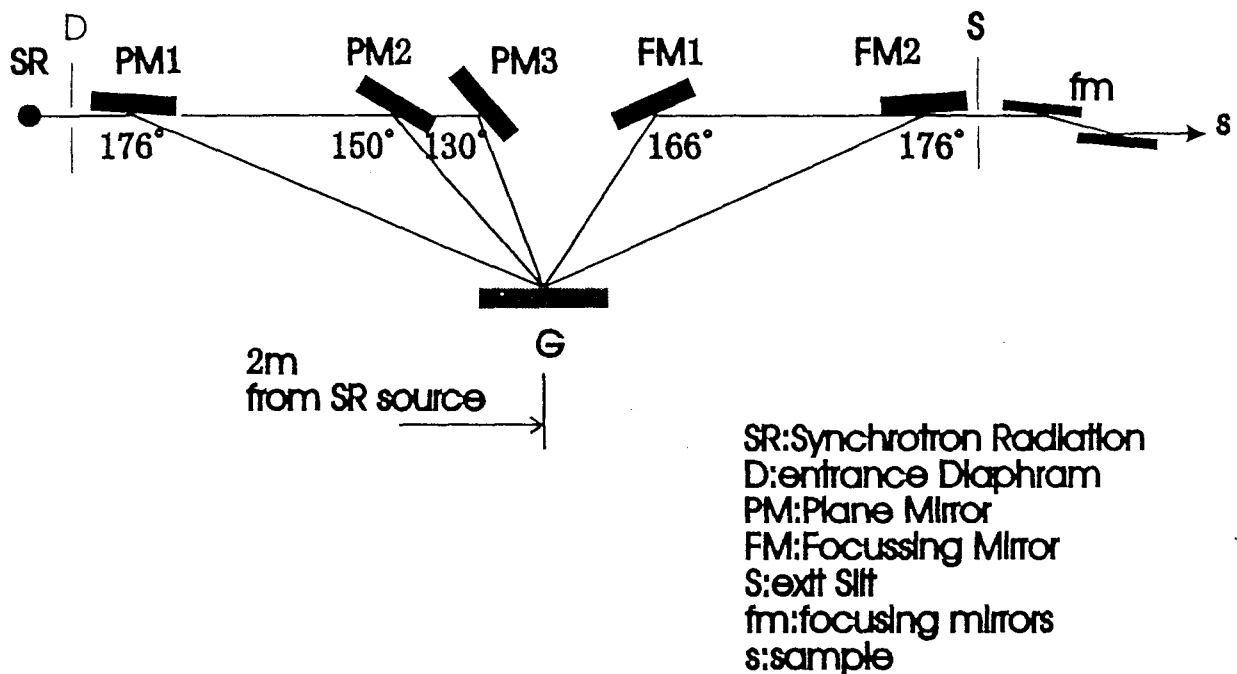
Fig. 3.3: Optics of the beamline BL-4 of SOR-RING.

The measurements of the 2D-ARPES were done at the main chamber which connected to the monochromator chamber. Figure 3.4 is the schematic view of the main chamber and the diagram of the measurement. In this chamber the two dimensional display type hemispherical mirror analyzer which is developed and improved by ourselves[4] and the manipulator(VG) with five axes goniometer are equipped. As mentioned in following section, by using this analyzer we can measure the two dimensional angular distribution patterns of the emitted photoelectrons which are displayed on the phosphorous screen. The patterns are observed from the out side of the chamber by commercial CCD camera(XE77, SONY) via a view port. And the observed images are collected tentatively in the image-freezer(C-tec) and stored in the personal computer(9801 , NEC) as shown in the measurement diagram. In the display type analyzer the small electron gun are also equipped and LEED and Auger measurements are also available. The measured samples were cleaved at the preparation chamber and transferred into the main chamber. Au deposition for the measurement of the energy resolution was done in the main chamber. The quartz oscillator to estimate the film thickness of the Au was also equipped. The base pressure of the main and preparation chambers are $1.5 \times 10^{-10}$ and $1.0 \times 10^{-9}$ Torr, respectively.
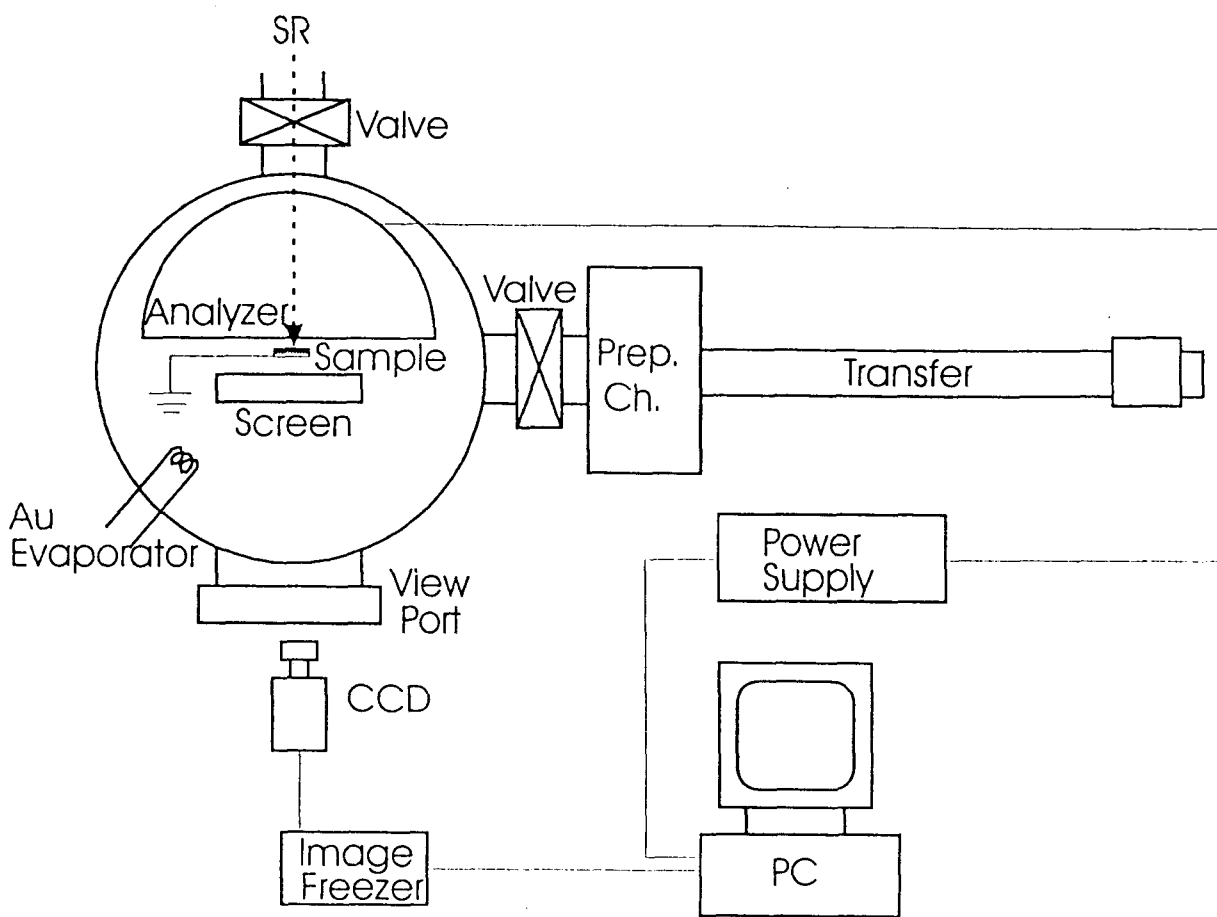
Fig. 3.4: Schematic view of the analyzer chamber of the BL-4. The diagram of the measurement is also shown.

## 3.3 Two-dimensional display-type hemispherical mirror analyzer

2D ARPES measurement was performed using two dimensional hemispherical mirror analyzer(illustrated in Fig. 3.5) which is constructed by ourselves[4].
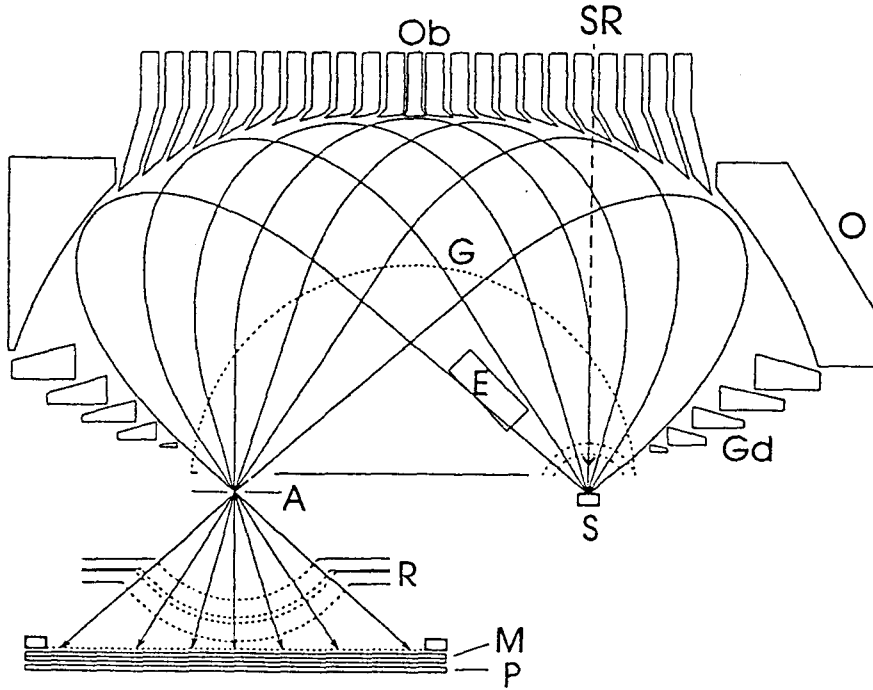


Fig. 3.5: Cross-sectional view of two dimensional hemispherical mirror analyzer applied to 2D ARPES measurement of transition dichalcogenide.

This analyzer basically consists of hemispherical outer sphere(O) and inner grid(G) which is as half of radius as the outer sphere(O). The photon is injected from the hole at the back of the analyzer and excited photoelectrons are transmitted from sample(S). In the space between outer electrodes(O) & (Ob) and inner grid(G), the hemispherical equipotential electric field is realized. In this space the charged particles moves according to the central force which is caused by this hemispherical equipotential electric field. Therefore the emitted photoelectron moves straight until the edge of the inner grid(G) but repulsed by these outer electrodes and moves the elliptical orbit and after the repulsion the electron is focused on the other side of the sample, small hole named aperture(A). The transmission angle from surface normal and the injection angle at the aperture is the same[4] and the electron distribution pattern can be detected on the phosphorous screen(P) after amplified by Micro-Channel-Plate(MCP;M in the figure). The electrons having higher and lower kinetic energy than the pass energy are excluded away by the objective ring(Ob) and retarding grid(R), respectively. Our used analyzer can detect the photoelectron angular distribution of $\pm 60°$ from sample normal without distortion and energy resolution of the analyzer is better than 1/100 of the pass energy. By using aforementioned small electron gun(E) we can observe the LEED pattern on the phosphorous screen and also perform the Auger electron spectroscopy.

Although the energy resolution is little bit worth than conventional photoelectron spectrometer at present, this display type analyzer has a lot of advantages as follows. Since we can measure the photoelectron distribution at almost the full of azimuthal and polar angles of photoelectron at the same time by this analyzer we can measure the electronic structure of the surface completely that is to say not only the complete band structure but also the symmetry of the electron orbital of the initial state. This observation of the electron orbital symmetry of initial state is only available with using display type analyzer and not available by the 2D-ARPES measurement with the sample rotating method[5] as already mentioned in section1.2. In addition display type analyzer can detect electrons at a large range of the reciprocal space at the same time that it is suitable to observe the band structure with small dispersion such as large electron-electron correlation materials which have small dispersion because of the relatively localized electrons. By the property that the analyzer can display the undistorted PEAD patterns we can also use this analyzer to observe the shape of Fermi surface directly [1]. Observing the change of the Fermi surface between phase transition such as the transition of CDW or surface reconstruction like a $\beta$-$\sqrt{3} \times \sqrt{3}$-Au to 6×6-Au surfaces is very important and interesting subject. Though there is another famous way to obtain the Fermi surface structure called de Haas-van Alphen(dHvA) effect, however, the dHvA method is very complex to analyze the data and requires very pure material stoichiometrically. Contrast to the dHvAp method 2D ARPES can measure the Fermi surface of any materials directly. As mentioned already display type analyzer is also useful to PED and holography measurement. To obtain reliable data for holography the many holograms in different photoelectron kinetic energies are required[7] and the rapidity of measurement by the display type analyzer is suitable to this kind of measurement. The measurement rapidity is of course very effective to prevent the sample to be contaminated by residual gases. In addition to these previously developed application methods, the display type analyzer has many possibility to find new physical phenomena and some new finding have been reported recently such as photoemission circular dichroism in non magnetic and non chiral materials[8]. As one of such new finding making good use of this display type analyzer, the last half of this thesis I report the new results of unusual photoelectron distribution of the transition metal dichalcogenides in the resonance photoemission process.

## 3.4  Cleavage technique of the layered compounds

The cleavage of the layered compounds such as $1T$-$TaS_2$, $2H$-$TaSe_2$, $2H$-$NbSe_2$ can be achieved very easily by so called scotch tape method. At first we attached the layered compounds on the Cu plate by some special bond[9] which has the electricity conductance and the out gas is very small in vacuum. After that a strip of the commercial scotch tape was attached on the sample as shown in Fig. 3.6.

At the one side of the scotch tape, a small ring of Cu wire was attached and the sample was set into the preparation chamber. After the pumping out the preparation chamber at ultra high vacuum(UHV) we hanged up the Cu wire by a bauble stick and stripped away the scotch tape carefully. As doing this we could obtain a very clean and flat surface with mirror reflection. This cleaving method is so simple and easy and can apply to the cleavage of any layered compounds whose layer is bonded weakly by van der Waals force.

---

[1]This feature of undistortion of the patterns our display type analyzer have an advantage over another display type analyzer which has been developed by Eastman et al.[6].
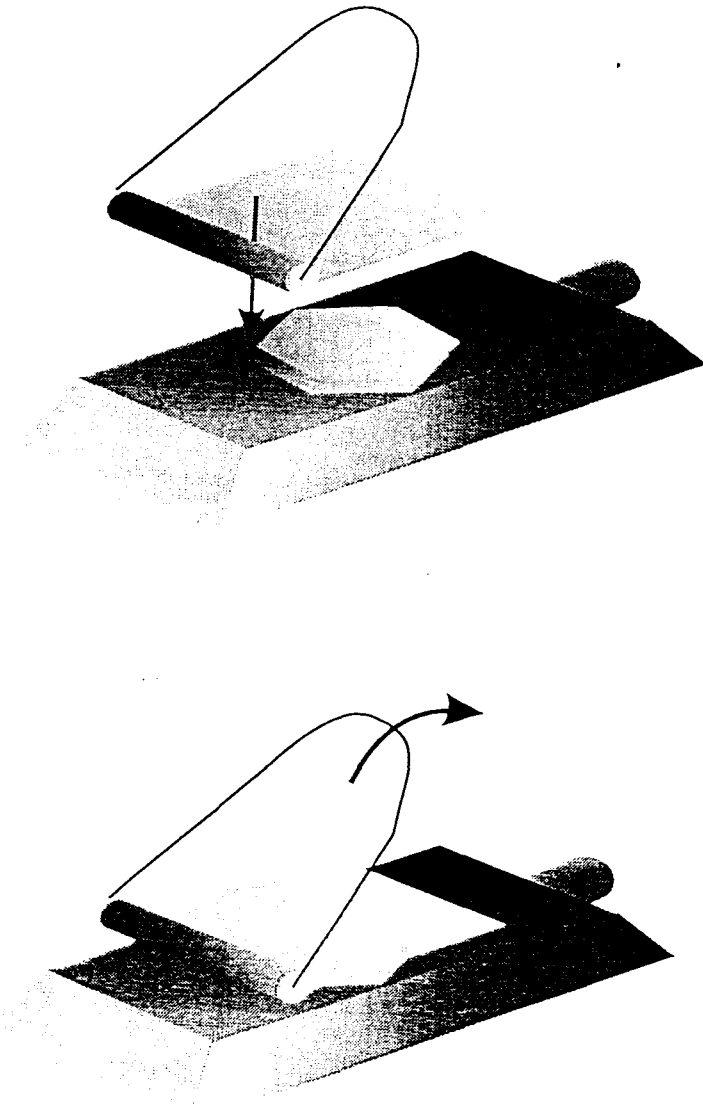
Fig. 3.6: Schematic view of the way of cleaving sample using scotch tape.

# References

[1] S.Suzuki, T.Kashiwakura, A.Kakizaki, T.Kinoshita, A.Harasawa, J.Fujii, S.Suga, M.Fujisawa, H.Kato, S.Sato, and T.Ishii, *Activity Report 1989, Synchrotron Radiation Laboratory, Institute for Solid State Physics, The University of Tokyo*, p.60 (1990).

[2] *Activity Report 1994, Synchrotron Radiation Laboratory, Institute for Solid State Physics, The University of Tokyo*, p.12 (1995).

[3] *Activity Report 1994, Synchrotron Radiation Laboratory, Institute for Solid State Physics, The University of Tokyo*, p.4 (1995).

[4] H.Daimon, Rev.Sci.Instrum.59,545(1988).

[5] For Example, P.Aebi, J.Osterwalder, P.Schwaller, L.Shlapbach, M.Shinoda, T.Mochiku, and K.Kadowaki, Phys.Rev.Lett., 2757 (1994).

[6] D.E.Eastman, J.J.Donelon,N.N.Hien and F.J.Himpsel, Nucl,Instrum. Meth. **172**, 327 (1980).

[7] For example, B.L.Petersen, L.J.Terminello, J.J.Barton, and D.A.Shirley, Chem.Phys.Lett. **220**, 46 (1994).

[8] H.Daimon, T.Nakatani, S.Imada, S.Suga, Y.Kagoshima, and T.Miyahara, Rev.Sci.Instrum, **66**, 1510 (1995).

[9] For example the Muromac bond which is the products of MUROMACHI KAGAKU Co.,Ltd.

# Chapter 4

# Electronic and geometric structures of Si(111) clean surfaces

Before describing our result of the studies on the metal induced reconstructions on Si(111) surfaces, it is worthwhile to summarize the electronic and geometric structures of clean Si(111) surfaces. Two kinds of reconstructions for have been found on the Si(111) clean surfaces so far, e.g. 7×7 and 2×1. They have been examined very much intensively, and their electronic and geometric structures have almost solved by pioneers of surface science.

## 4.1　Si(111)7×7

Si(111)7×7 surface appears when the clean Si(111) surface is annealed at above 300°C . The geometric structure of the surface had been investigated for more than 20 years, and now is considered to be dimer, adatom, stacking fault(DAS) structure as shown in Fig. 4.1. This structure consists of 12 adatoms(A), 6 rest atoms(R), 1 corner hole atom(C), 18 dimers(D) with stacking fault(S) in the 7×7 unit cell . By this reconstruction the numbers of the dangling bonds are reduced to 19(adatom+rest atom+ corner hole atom) from 49 of ideal surface. The theoretical band calculation of the model[1] revealed that the binding energy level of the adatoms is higher than that of the rest atoms. Because of the higher binding energy of the adatoms, electrons of adatoms transfer to the rest atoms and the surface state band of the adatoms becomes half filled and the 7×7 surface has metallic electronic state. This results of the higher binding energy of the rest atoms than adatoms are strongly supported by the STM images of Fig. 4.2 in which the filled image of higher sample bias(b)($-0.8$eV) and that of lower sample bias(a)($-0.35$eV) correspond to the positions of the rest atoms and adatoms, respectively[2]. The bright spots of (c) at sample bias of $-1.7$eV, are considered to be the back bonds state of the adatoms. Photoelectron spectroscopy had, of course, helped to understanding the electronic structures of this 7×7 surface. Figure 4.3 shows the ARPES spectrum at surface normal of the 7×7 surface. Two surface states labeled $S_1$ and $S_2$ are observed and they correspond to the adatom states which is half filled and indicate the metallic state, and rest atom state which has higher binding energy than adatom state as mentioned. Another surface state $S_3$ which is assigned as the backbond state of the adatoms also locates at $E_B \sim 1.8$eV but merged into the strong bulk state in the normal spectrum. The experimental band structure of the surface(Fig. 4.4) shows the relatively flat dispersions of the $S_1$, $S_2$, and $S_3$ states and the $S_1$ state indicates the sign of the metallic surface state at every wave number.
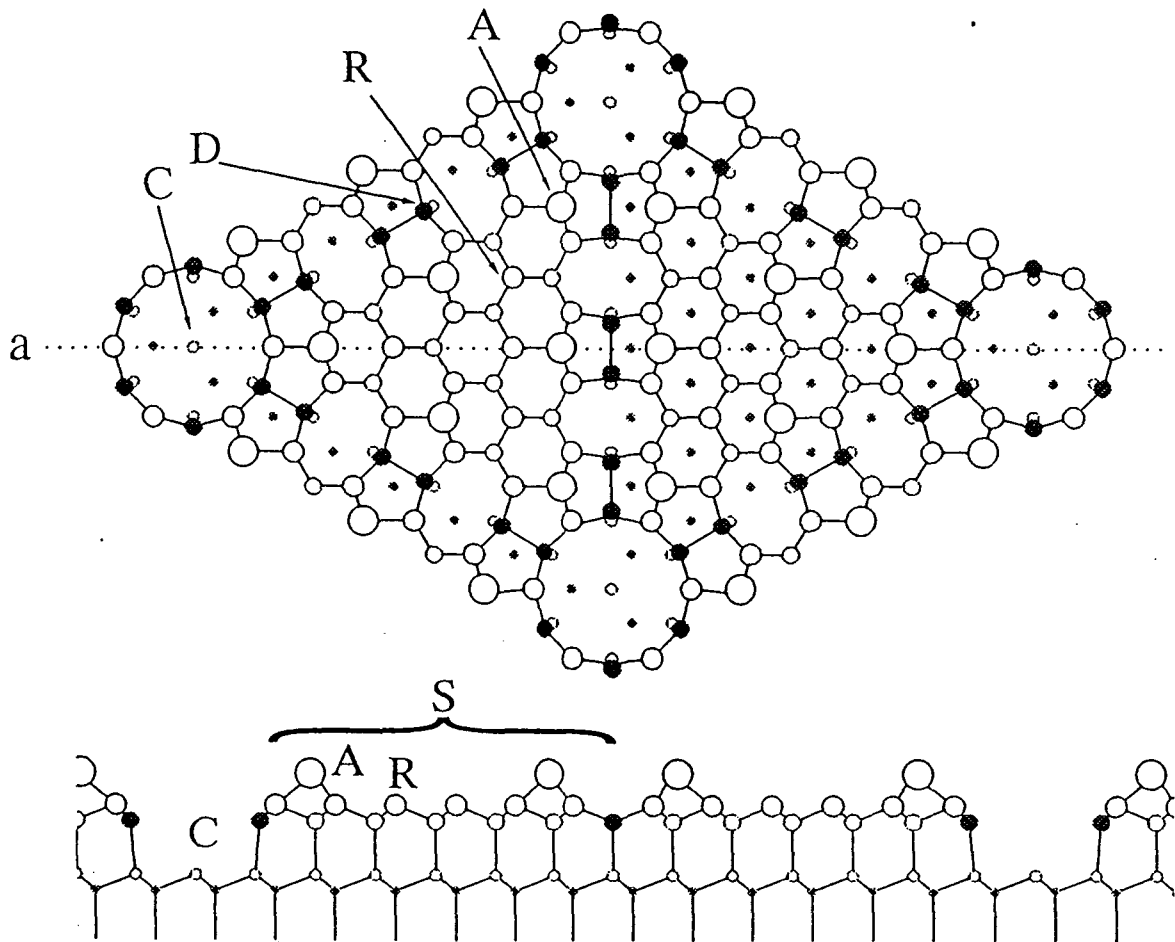
Fig. 4.1: Geometric structure of Si(111)7×7 surface. This structure is called DAS model, which consists of 12 adatoms(A), 6 rest atoms(R), 1 corner hole atom(C), 18 dimers(D) with stacking fault(S) in the 7×7 unit cell

(a)

(b)

(c)
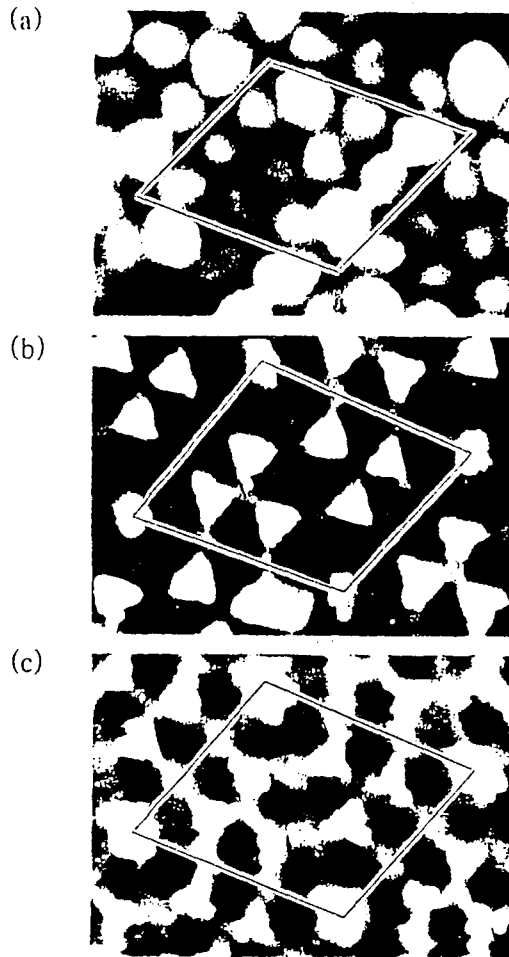
Fig. 4.2: STM images of Si(111)7×7 surface obtained by the Current-Imaging-Tunneling-Spectroscopy mode from ref.[2]. These images correspond to the electronic state of (a)$E_B$=0.35eV(adatom state), (b)0.8eV(rest atom state), and 1.7eV(back bond state of adatoms).
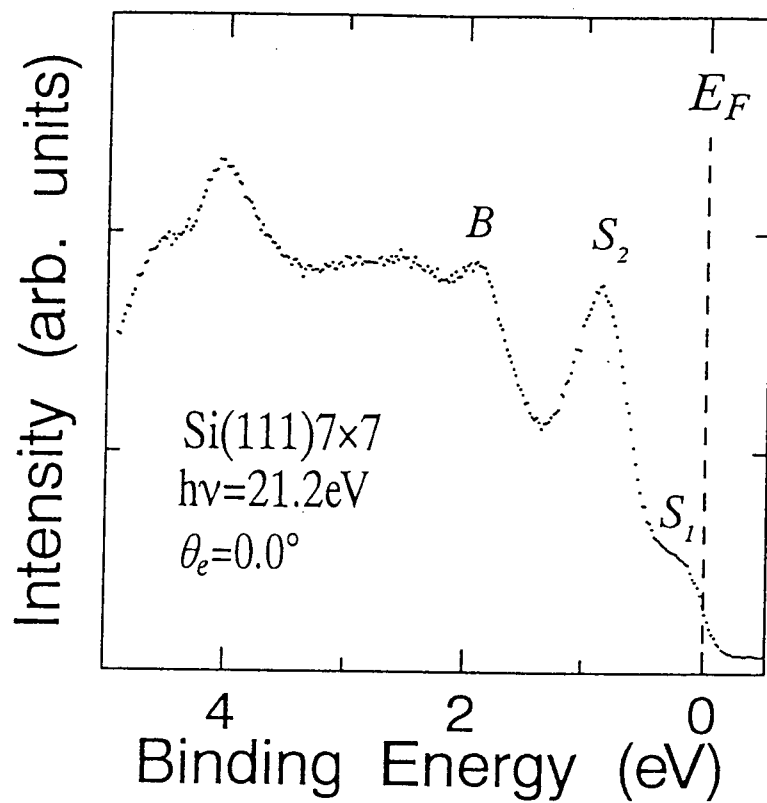
Fig. 4.3: ARPES spectrum of the Si(111)7×7 surface at normal direction which are measured by ourselves. Adatom surface state($S_1$) and rest atom surface state($S_2$) are observed.
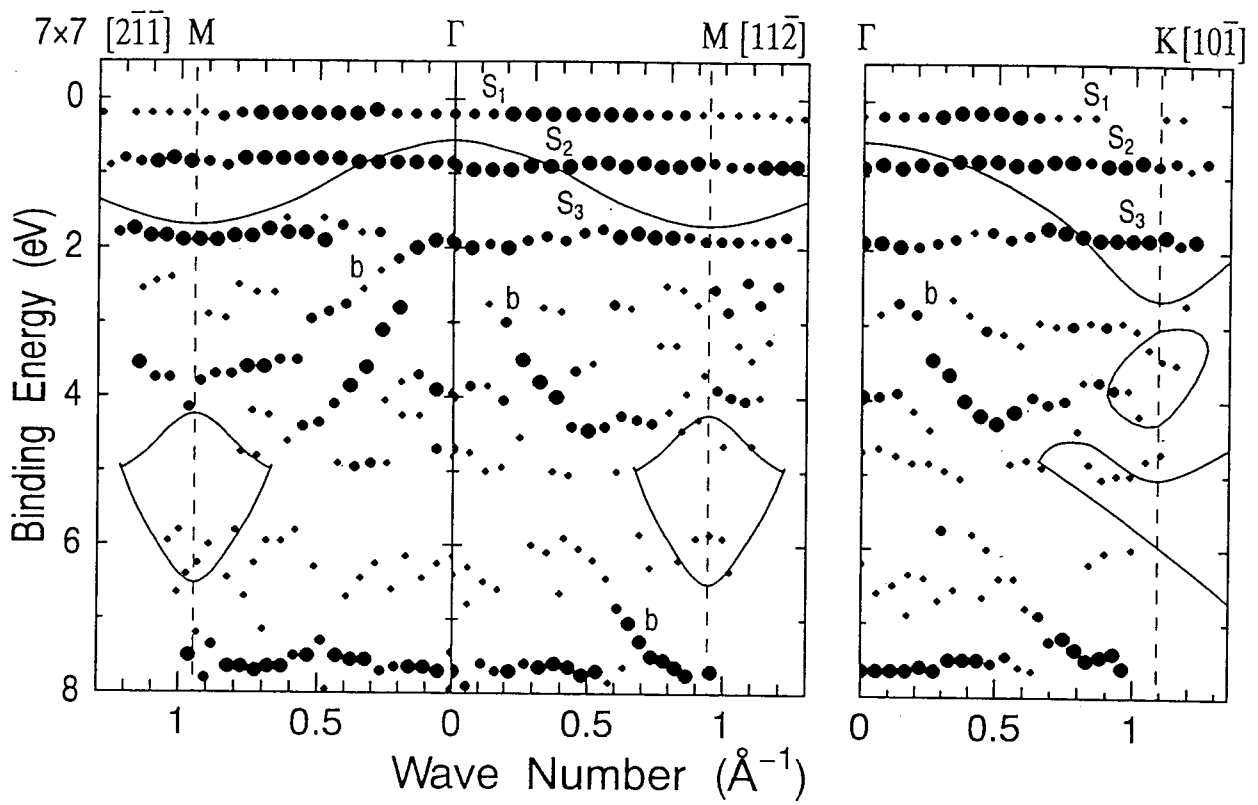
Fig. 4.4: Band map of Si(111)7×7 surface measured by ourselves.

Comparing to the ARPES results, the results of SCLS measurement of the surface has been controversial problem. As seen in the previous results(Fig. 4.5) the surface sensitive Si $2p$ spectrum of the surface has a small bump at lower binding energy than main peak. This spectrum had been fitted by curve fitting into two surface($S1$, $S2$) and one bulk(B) Si $2p$ components as shown in the figure.

## Si $2p$ core spectrum of Si(111)7×7
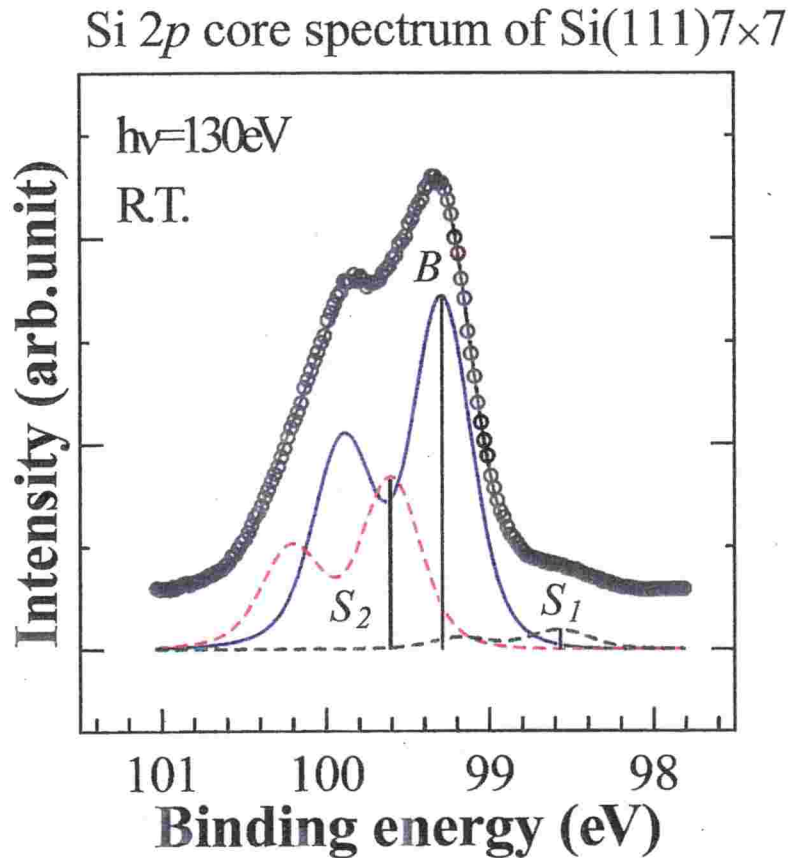


Fig. 4.5: Surface sensitive Si $2p$ core spectrum of the 7×7 surface measured at $h\nu$=130eV by ourselves. The spectrum is decomvoluted into two surface($S1$ and $S2$) and one bulk($B$) components by curve fitting

Miller, Hisieh and Chiang[3] assigned the $S1$ and $S2$ component as adatoms and other surface atoms from the peculiarity of the adatom state. On the other hand, Karlsson $et$ $al.$[4] assigned that the $S1$ is rest atom which shift from the bulk Si $2p$ position because of the charge transfer from adatoms referring to aforementioned theoretical calculation[1]. They considered the $S2$ consists of the adatoms and pedestal atoms of adatoms from the intensity ratio of the $S2$ to $S1$ referring to the number of the adatoms+pedestal atoms and rest atoms. Recently Carlisle $et$ $al.$[5] have performed the Si $2p$ core spectrum measurement by photons of many excited energies using SR and observed the oscillation of the intensity of these surface components($S1$ and $S2$). Then they applied the Extended X-ray Absorption Fine Structure(EXAFS) analysis to the oscillation of the surface core components and concluded that the $S1$ and $S2$ are arisen from adatoms and rest atoms, respectively. This analysis had seemed to terminate the controversial problem of the assignment of these surface component. Very much recently, however, several groups[6, 7, 8] have reported the high energy resolution Si $2p$ core spectra of 7×7 surface by cooling down the sample to about 100K to reduce

the phonon broadening effect. The another shoulders are observed in their surface sensitive spectrum as shown in Fig. 4.6, and they deconvoluted the core spectrum into one bulk and four surface components. The intensities of these surface components are proportional to
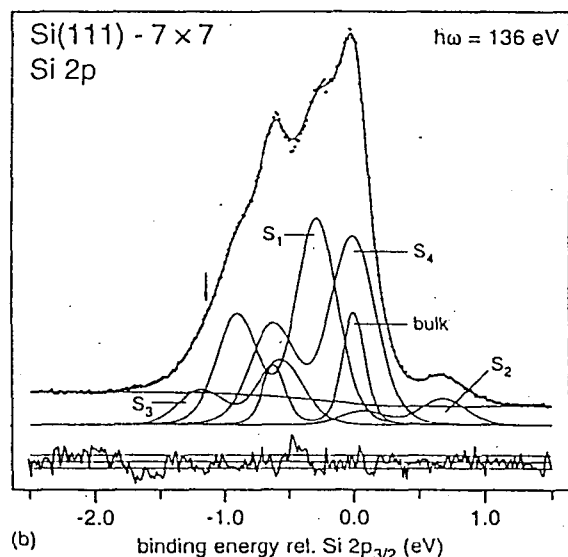


Fig. 4.6: Surface sensitive Si $2p$ core spectrum with high energy resolution obtained by cooling down the sample about 100K from ref.[6]. New shoulders which were not seen in Fig. 4.5 are observed.

the number of the surface atoms such as adatom, rest atom, dimer atom, and pedestal atoms. The $S1$ has been assigned as the rest atoms by these high resolution measurement. At present the assignment of these studies are considered to be more reasonable and the assignment based on the EXAFS analysis are considered to be questionable since the analysis was assumed only two surface component in the spectrum.

## 4.2  Si(111)2×1

The other surface structure of the clean Si(111) surface has 2×1 periodicity and appears when we cleave Si crystal along the Si(111) surface in vacuum. The electronic and geometric structures of this surface were also investigated intensively, and almost have been solved. The surface structural model was proposed by Haneman[9] at first considering two kinds of surface Si atoms which are located upper and lower site from the ideal surface position in the 2×1 unit cell. By moving these two surface atoms upward and downward, the bonding angle of the lower surface Si atoms become flatter than that of ideal surface($sp^3$ configuration) and the bonding character becomes $sp^2$ like character as shown in Fig. 4.7. On the other hand

the bonding angle of upper surface Si atoms become steeper than ideal one and bonding character becomes $p^3$ like state. As seen in Fig. 4.7 the binding energy of the dangling bond at $sp^2$ state is lower than that at $p^3$ states, that the electron of the atoms at $sp^2$ state transfers to the atoms at $p^3$ state. This model can explain the SCLS results[10] in which
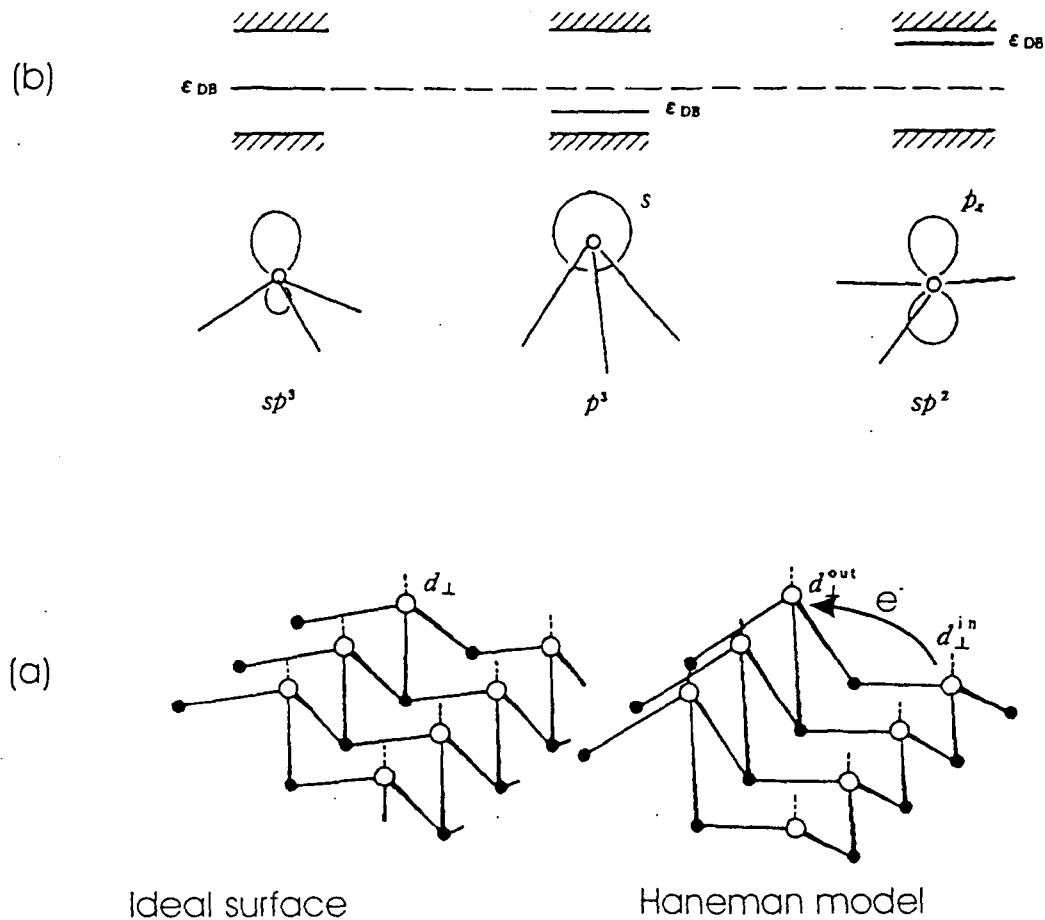


Fig. 4.7: (a) Ideal surface and Haneman model of the Si(111)2×1 surface. (b) Schematic diagram of the binding energy of dangling bonds for different bonding angles are also presented.

the two differently charged surface components shifted to lower and higher binding energies compared to the bulk component(Fig. 4.8).

However, the band dispersion derived from the Haneman model could not explain the upward dispersion with dispersion width of about 0.5eV measured by ARPES measurement[11]. To understand the experimental band structure Pandey[12] have proposed the new model for the 2×1 surface which consistent of 5 and 7 membered rings as shown in Fig. 4.9. The two dangling bonds of 7-membered ring form the $\pi$-bonded chains along [10$\bar{1}$] direction. In Fig. 4.10 calculated band structure based on the $\pi$-bonded chain structure[13] and experimental dispersion[11] of the Si(111)2×1 surface are presented. The agreement between the calculated results and experimental ones are fairly good and the structure of the 2×1 clean Si surface is now considered to be the Pandey's model. When the atoms making the $\pi$-bonded chain structure become asymmetry, total energy of the surface is more stable because of the same reason of the Haneman model. Thus one of the Si atoms making $\pi$-bonded chain, projected upward and are charged negatively and the other Si atoms dented downward and are
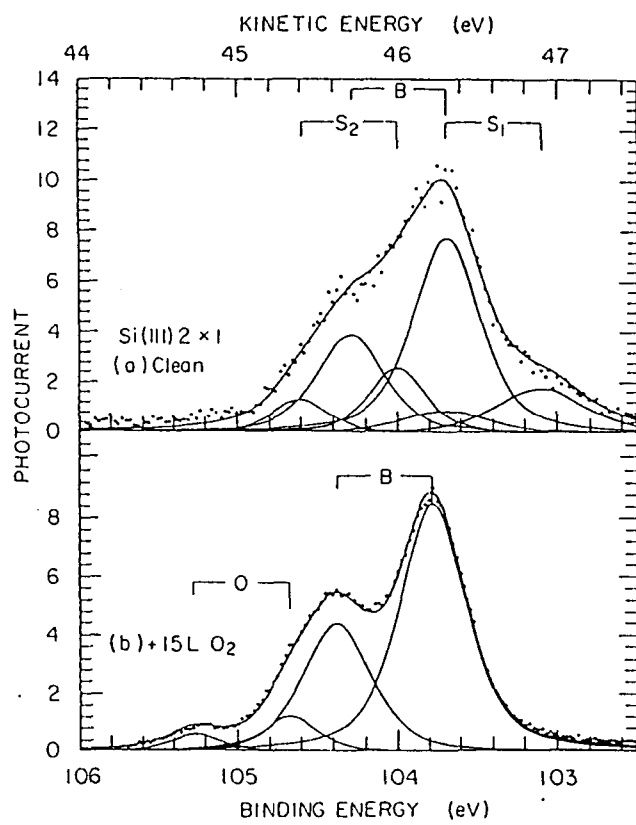
Fig. 4.8: Surface sensitive spectrum of Si $2p$ core of the Si(111)2×1 surface from ref.[10]
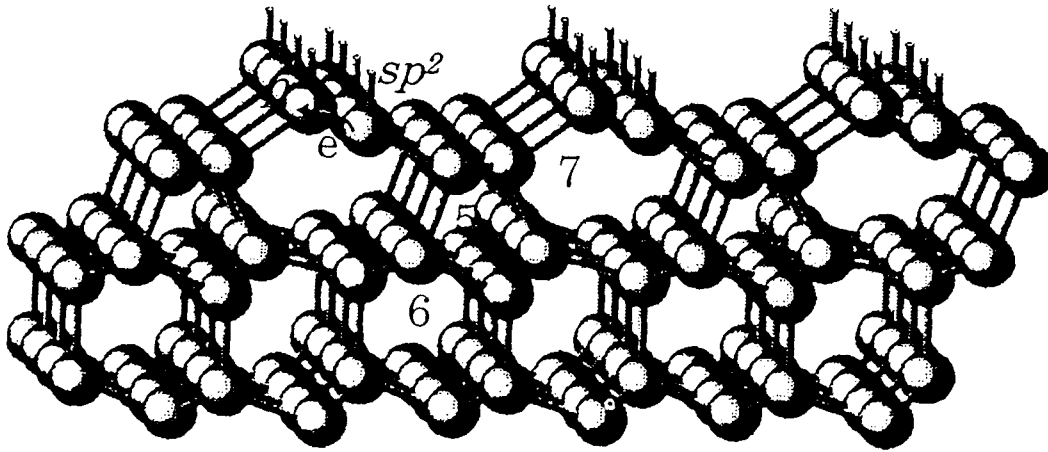
Fig. 4.9: Pandey model of the Si(111)2×1 surface. The dangling bonds of 7-memebered ring form π-bonded chains along [10$\bar{1}$] direction.



Fig. 4.10: Dispersion of the surface state of Si(111)2×1 observed by ARPES measurement from ref.[11]. The results of the band calculation for the Pandey model[13] are also incorporated.

charged positively. The SCLS results of Si(111)2×1 surface can be understood by this charge redistribution. This is one of the good example indicating that comparing ARPES measurement and calculation is very important to investigate the surface structures as well as the electronic structures. Inversely this indicate that the assignment of the surface component on the SCLS measurement is accompanying the some difficulties.

# References

[1] J.E.Northrup,Phys.Rev.Lett.,**57**,154,(1986).

[2] R.J.Hammers, R.M.Tromp, and J.E.Demuth, Phys.Rev.Lett., **56**, 1972 (1986).

[3] T.Miller, T.C.Hisieh, and T.-C.Chiang, Phys. Rev. **B33**, 6983 (1986).

[4] C.J.Karlsson, E.Landemark, L.S.O.Johansson, U.O.Karlsson, and R.I.G.Uhrberg, Phys. Rev. **B41**, 1521 (1990).

[5] J.A.Carlisle, M.T.Sieger, T.Miller, T.-C.Chiang, Phys.Rev.Lett. **71**, 2955 (1993).

[6] G.LeLay, M.Göthelid, T.M.Grehk, M.Björkquist, and U.O.Karlsson, and V.Yu.Aristov, Phys.Rev.**B50**, 14277 (1994).

[7] C.J.Karlsson, E.Landemark, Y.-C.Chao, and R.I.G.Uhrberg, Phys.Rev.B,**50**, 5767 (1994).

[8] J.J.Paggel, W.Theis, and K.Horn, Phys.Rev.**B50**, 18686 (1994).

[9] Haneman, Phys.Rev.**121** 1093 (1961).

[10] S.Brennan, J.Stohr, R.jaeger and J.E.Rowe, Phys.Rev.Lett.**45**, 1414 (1980).

[11] R.I.G.Uhrberg, G.V.Hansson, J.M.Nicholls, S.A.Flodstrom, Phys.Rev.Lett.**48**, 1032 (1982).

[12] K.C.Pandey, Phys.Rev.Lett.**47**, 1913 (1981).

[13] J.E.Northrup, M.S.Hybertsen, and S.G.Louie, Phys.Rev.Lett.**66**, 500 (1991).

# Chapter 5

# Photoemission studies of Alkali-metal- and Ag-induced Si(111)3×1 surfaces: Si(111)3×1-Na, Si(111)3×1-Rb, Si(111)3×1-Ag

## 5.1  Introduction

As mentioned already in the previous chapter, the alkali metal/semiconductor interfaces have been the subject of intense interest from both fundamental and application points of view. The large work-function reduction is one of the major issues of these systems and applied to making a good electron source. On the other hand, these adsorbate systems are expected to promote fundamental understanding of general metal/semiconductor interfaces, because only one $s$ valence electron of the alkali atom is expected to take part in the bonding to the semiconductor substrate. Noble metals such as Cu, Ag, and Au have also only one $s$ electron in their most outer shell and can be another candidate of adsorbate which help understanding the bonding properties of metal/semiconductor interfaces as discussed following sections. In spite of the simplicity of these alkali metal or noble metal/semiconductor systems, however, many issues are still controversial.

Among these systems, alkali metal or Ag induced Si(111)3×1 reconstructed surfaces have been studied intensively in these days to understand their electronic and geometric structures. The alkali metal induced Si(111)3×1 reconstructed surfaces were first found by means of the reflected high energy electron diffraction(RHEED) measurement for most of the alkali metal adsorbates (Li, Na, K, Rb, and Cs)[1]. For the Ag/Si(111) system a similar 3×1 reconstruction has also been observed when we adsorb the Ag on annealing Si(111) surface[2] at adequate temperature. As shown in Fig. 5.1 this Ag induced 3×1 surface changed into 6×1 surface at $T_c$=220°C reversibly. However the local structures of them are considered to be almost the same and I use the expression of "3×1-Ag" as the 6×1-Ag surface in this thesis. In spite of similar electronic state of gold to silver, however, gold does not induce the 3×1 reconstruction.

Until now many experimental suggestions for the geometric and electronic structures of the 3×1 surface have been reported and a lot of structural models for the 3×1 reconstruction have been proposed. Any consensus of the surface structure, however, has not been achieved
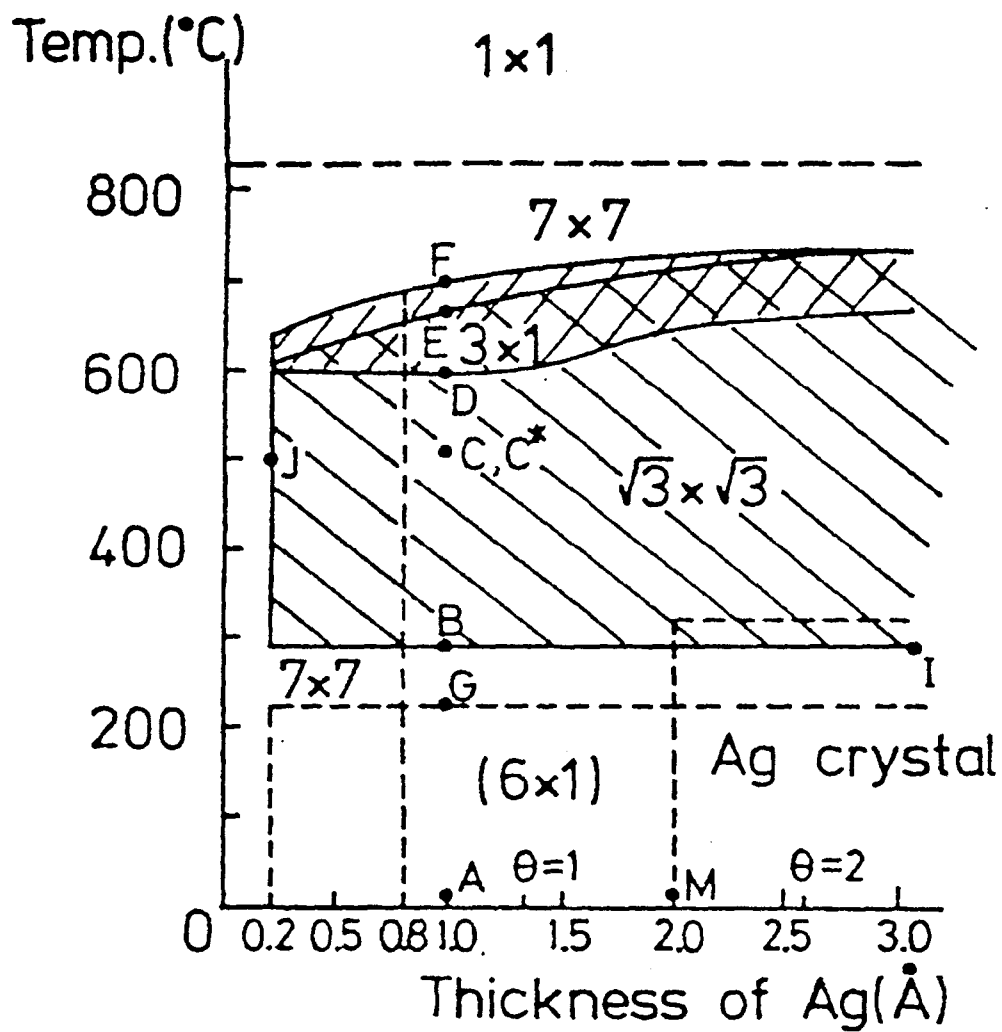
Fig. 5.1: Phase diagram of the Ag/Si(111) system from Ref.[1]

yet.

The scanning tunneling microscopic (STM) images of the filled states of the Si(111)3×1-Na[3], -K[4], -Li[5], and -Ag[5] surfaces show a similar bright zig-zag chains consisted of two atoms in every three atomic lines lying along the [10$\bar{1}$] direction. Fan and Ignatiev[6] suggested that these surfaces were essentially identical from the low energy electron diffraction (LEED) $I - V$ curves of the 3×1-Li, Na and Ag surfaces. In addition the similarity of the $I - V$ curve in different adsorbates which have different cross sections implies that the reconstruction is realized by the rearrangement of Si substrate. There is another experimental suggestion that the 3×1-AM surface is inactive against oxidation compared with the 7×7 clean surface [7] by their Auger electron spectroscopy(AES) measurement contrary to the general tendency of AM making adsorbed surface active.

As for the coverage of the 3×1 surface, it was considered to be 2/3ML from the RHEED-Total Reflection Angle X-ray Spectroscopy(TRAXS)[1] and STM images[3] at first. According to Tikhov et al.[7], however, only the coverage of 1/10 of saturate coverage of Na/Si(111) was required to make 3×1 surface. Fan and Ignative[6] also suggested from their AES measurement that only small amount of AM as a contamination level(0.01ML) can realize the 3×1 surface. As will be discussed next section of my thesis, our X-ray photoelectron spectroscopy (XPS) data[8, 9], however, led to the conclusion that the saturation coverage of the 3×1-Na was 1/3ML. Recently, some experimental results which support the 1/3ML coverage of 3×1-AM and Ag have been reported by several groups[10, 11, 12, 13].

Regarding to the electronic structure, there were not so many studies so far. The scanning tunneling spectroscopic(STS) current-voltage ($I - V$) curve measurement[3] indicated that the Si(111)3×1-Na surface was semiconducting with an energy gap of about 0.7~1.0eV. According to the Electron Energy Loss Spectroscopic(EELS) measurement[7] on the 3×1-Na new loss peaks at 11.9 and 3.7eV were appeared but reasonable assignment of the peak had not been done. As for the electronic structure of Si(111)3×1-Ag, there is no studies at present as far as I know.

To obtain the further information of the crystal structure and the bonding character of these surfaces I have performed the surface sensitive Si $2p$ core photoelectron spectroscopy for the Si(111)3×1-Na, Rb, and Ag surfaces and discussed about their surface core level shifts (SCLS) as well as the difference between these surfaces. In addition I describe about the results of our ARPES measurement of the 3×1-Na[14] and discuss about the electronic structure of the surface precisely comparing to the recently reported several theoretical band calculations[15, 16, 17].

## 5.2  Experimental

All of the present experiments were performed at the Institute for Solid State Physics(ISSP) beam line BL-18A of Photon Factory of National Laboratory for High Energy Physics. Both sample preparation and measurements were carried out in an ultra-high-vacuum (UHV) chamber with the base pressure of $2×10^{-11}$Torr. Silicon wafers (P doped, n-type, $\rho$=2.4-4.0$\Omega$cm) were cleaned by repeated resistive-heating up to ~ 1250°C for five seconds in the UHV chamber. The cleanliness of the sample was checked by the clear 7×7 LEED pattern and the lack of O $1s$ and C $1s$ components in the XPS spectra. The 3×1 reconstructed surfaces were realized by Na or Rb deposition onto the clean Si(111)7×7 surface at the substrate temperature of about 500°C . Alkali metals(Na and Rb) were evaporated from thoroughly out-gassed chromate dispensers (SAES Getters) under a pressure of less than

$5 \times 10^{-10}$Torr. The distance between the AM dispenser and the Si wafer was about 3cm. To obtain a high quality(=homogeneous) 3×1-AM surface, we stopped the AM exposure and the Si heating at the same time. If the heating(exposure) continued further after the stop of the exposure(heating), the obtained 3×1 surface will accompany less(more) AM than the saturation coverage of the perfect 3×1 surface. The quality of the reconstructed surface was ascertained by the bright 3×1 LEED spots without any other spots. In accord with the three-fold symmetry of the Si(111) substrate, the LEED patterns indicated the existence of three equivalent 3×1 domains rotated by 120° from each other in the azimuthal angle. To evaluate the coverage of this surface we have checked the ratio of the intensities of the Na $1s$ core photoemission and the Si $LVV$ Auger peaks in the XPS spectra. We also checked the work function change of the 3×1-Na surface. The work function change was estimated by the secondary electron cut off energy of the PES spectra. The position of the Fermi energy was estimated by ARPES spectra of the Ta sheet which was used to attach the Si wafer onto the sample holder. The precise photon energy of the synchrotron radiation was obtained by measuring the difference of the two kinetic energies corresponding to the Fermi level excited by the first and the second order photons.

The Si $2p$ core spectra were measured with the angle integrated spectrometer (VG-CLAMII) in order to reduce the photoelectron diffraction effect. In the core level spectroscopy of the Si(111)3×1-Na, the surface sensitive measurements were done at the photon energy of $h\nu$=130eV where the kinetic energy of the Si $2p$ is about 27eV and mean free path of the Si $2p$ photoelectrons is very short ($\sim$4Å) and the spectra well reveal the contribution of the surface Si $2p$ emission as discussed in the chapter2 section2.1. For the bulk sensitive measurements we used $h\nu$=110eV at which the mean free path is estimated to be $\sim$ 20Å. The overall energy resolution(full width of half maximum:FWHM of the Si $2p$ core) of the surface sensitive measurement of the 3×1-Na was $\sim$ 0.28eV.

In the measurement of the Si(111)3×1-Rb and -Ag surfaces we used the He cryostat to cool down the sample temperature referring to the recent high energy resolution measurement in which the sample temperature are cooled down to reduce the phonon broadening effect and achieved high resolution measurement of Si $2p$ core spectrum. After making the 3×1 surfaces the samples are cooled down to about 75K by using He cryostat immediately. In this measurement of the 3×1-Rb and Ag, I used the photon energy of $h\nu$=133eV, 125eV, 115eV to change the surface sensitivity for the precise analysis of the core spectra. The photon incidence angle and the photoelectron detection angle for the core level measurements were 45° and 0° from the surface normal direction. To increase the photoelectron intensity from surface contribution we also use the configuration of the photoelectron detection angle of 60° from surface normal for the measurement of Si(111)3×1-Ag surface.

For the ARPES measurement we used several photon energies (18.0, 21.2, 23.0, and 51.0eV) in order to reliably determine the surface state. The analyzer was horizontally rotated for the ARPES measurement. The photon incidence angle was basically 45° from the surface normal. We changed the incidence angle from 45° to 35° , only when we measured the spectra for the $\theta_e$ beyond 40° in order to prevent the reflected synchrotron radiation(SR) beam from entering directly to the analyzer. The SR is linearly polarized in the horizontal plane and the incident light was $p$ polarized. The configuration of the ARPES measurement is illustrated in Fig. 5.2. The accurate surface normal direction was estimated from the symmetry of the observed dispersion around the $\bar{\Gamma}$ point. The overall instrumental angular and energy resolutions of the ARPES measurement were about ±0.5° and 150meV at $h\nu$=18.0eV.
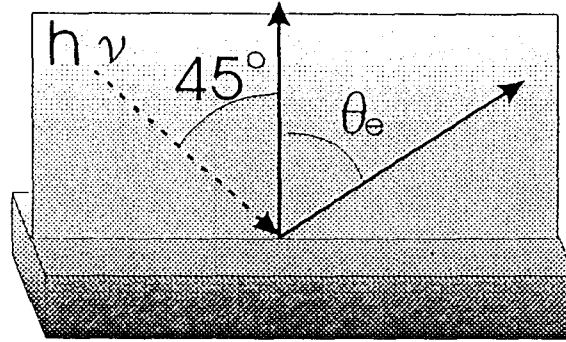
Fig. 5.2: Schematic diagram of the ARPES measurement configuration

## 5.3 Results

### 5.3.1 Coverage and work-function change of 3×1-Na

To investigate the AM coverage on the Si(111)3×1 surface I have performed XPS of the Si(111)3×1-Na and Si(111)$\delta$7×7-Na surfaces (Na deposited Si(111)7×7 surface at room temperature). The filled squares and circles in Fig. 5.3 show the results of Na1$s$/Si$LVV$ AES peak intensity ratio in the XPS spectra and the work-function for the Si(111) surface, exposed to the evaporated Na at room temperature (i.e. $\delta$7×7-Na case). The abscissa is the integrated exposure time of Na onto the clean Si(111)7×7 surface. The Na/Si peak intensity ratio increases monotonously and almost saturates at about 1.1 ~ 1.3 after 10 minutes. For the 3×1-Na surface, this ratio is ~ 0.34±0.08 as indicated by an open square. (Its horizontal position has no particular meaning.) Hence, if we consider the saturation coverage of Na in the $\delta$7×7-Na structure as about 1ML[1, 18], it is immediately concluded that the saturation coverage of the 3×1-Na surface is close to 1/3ML. Recently, some experimental results which support the 1/3ML coverage have been reported by several groups using several experimental techniques[10, 11, 12, 13] and the coverage of the 3×1-AM has been considered to be 1/3ML at present.

Seeing the work-function change of the Na/Si(111)7×7 surface, the work-function decreases monotonously until about 6 minutes, where the minimum value is 2.18eV, and then it increases again and saturates at ~ 2.46eV after 10 min. The value of the work function of the 3×1-Na surface(3.95±0.16eV) is indicated by an open circle for comparison purpose. The small change of the work-function ($\Delta\phi_s$ ~0.6eV; from 4.6eV on the clean surface to 3.95eV on the 3×1-Na surface) in this study differs from that reported by Jeon et al.($\Delta\phi_s$=1.6eV)[3]. We consider that the disagreement between our result and that of the STM[3] study is due to the low annealing temperature (360°C) of them which may be accompanied by more adsorption of Na and more reduction of the value of the work function than that at the saturation coverage at 500°C. According to our measurement of the Auger electron spectra, the amount of the adsorbed alkali metal of the 3×1 surface at 360°C was more than the saturation coverage. The $\Delta\phi_s$ presently observed for the 3×1-Na surface (0.6eV) is even smaller than the value corresponding to the 1/3ML exposure in the initial stage of the $\delta$7×7-Na surface (~2.0eV at 3.3min). This means that the electric dipole moment induced by each Na atom on the 3×1-Na surface is smaller than that on the $\delta$7×7-Na surface.

49
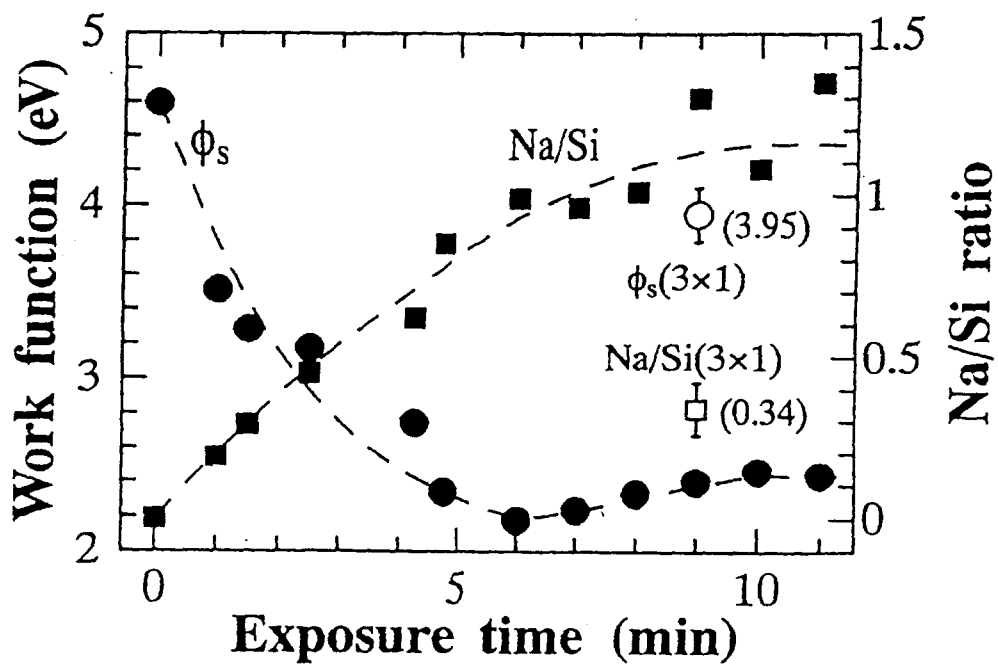
Fig. 5.3: Changes of the work function(filled circles) and the Na $1s$/Si $LVV$ XPS ratio(filled squares) against the integrated exposure time (under the same condition) of Na onto the clean Si(111) surface at room temperature. The work function and the Na/Si ratio of the 3×1-Na surface are also shown by on open circle and a square for comparison (with no particular meaning for their horizontal positions).

## 5.3.2 SCLS of Si(111)3×1-Na

In Fig. 5.4 are summarized the results of the surface sensitive photoelectron spectroscopy of (a)clean 7×7, (b)3×1-Na and (c)$\delta$7×7-Na surfaces. Each spectrum is normalized at the highest peak. The dots are experimental data points corrected for the secondary-electron-background. The experimental spectra were fitted by means of a nonlinear least-squares method with considering spin-orbit doublet components convoluted by Gaussian (experimental energy resolution) and Lorentzian (life-time broadening) functions. We determined the widths of the Gaussian and the Lorentzian as common parameters for all spectra in the fitting procedure. On the other hand the branching ratios were allowed to vary among these spectra considering the final state effect. All spectra can be well fitted with three doublet components. The parameters used here are tabulated in Table 5.1. The blue solid and

Table 5.1: Table5.1 Fitting parameters used for the line-shape analysis and the values of the bulk core level shifts(from the bulk component of the 7×7 clean surface) and the surface core level shifts(from the corresponding bulk component of each spectrum) as well as the intensity ratio of the surface components compared with the bulk component. A positive value of the shift represents a shift to larger binding energies. The estimated number of surface atoms in the 1×1 unit cell($\theta_s$) is also given.

|  |  | (a) 7×7 | (b) 3×1-Na | (c) $\delta$7×7-Na |
|---|---|---|---|---|
| Spin-orbit splitting | (eV) | 0.608 | 0.608 | 0.608 |
| Branching ratio $(2p_{1/2}/2p_{3/2})$ |  | 0.600 | 0.586 | 0.541 |
| Lorentzian width | (eV) | 0.18 | 0.18 | 0.18 |
| Gaussian width | (eV) | 0.28 | 0.28 | 0.28 |
| Bulk component$(B)$ |  |  |  |  |
|    Bulk core level shift | (eV) | — | −0.131 | 0.007 |
| Surface component$(S1)$ |  |  |  |  |
|    Core level shift | (eV) | −0.716 | −0.437 | −0.341 |
|    Intensity ratio |  | 0.055 | 0.425 | 0.332 |
| Surface component$(S2)$ |  |  |  |  |
|    Core level shift | (eV) | 0.314 | 0.267 | 0.197 |
|    Intensity ratio |  | 0.488 | 0.446 | 0.318 |

broken curves(red and green) in Fig. 5.4 represent the bulk (labeled $B$) and surface (labeled $S1$, $S2$) components, respectively. The doublets labeled $S$ are interpreted as the surface contribution because of their intensity reduction in the bulk sensitive spectra (at $h\nu$=110eV, Fig. 5.5). Each solid curve which is the sum of the surface and bulk contributions, reproduces the experimental spectrum very well.

The shape of the spectrum of the 7×7 clean surface (Fig. 5.4(a)) is very similar to the results of other groups [19, 20]. As mentioned already, according to recent high energy resolution spectrum of the 7×7 surface[21, 22, 23] the $S2$ peak include some different kinds of the surface component such as the adatoms and pedestal atoms of adatoms but in our spectrum in finite energy resolution we decomvolute it only one surface component as $S2$. Thus I consider that the $S1$ is the contribution from the rest atoms (6 atoms) and the $S2$ is that from the adatoms (12 atoms) as well as the atoms which are bonding with adatoms (36 atoms) in the DAS model. The intensity ratios and the surface shifts in Table 1 support this interpretation.
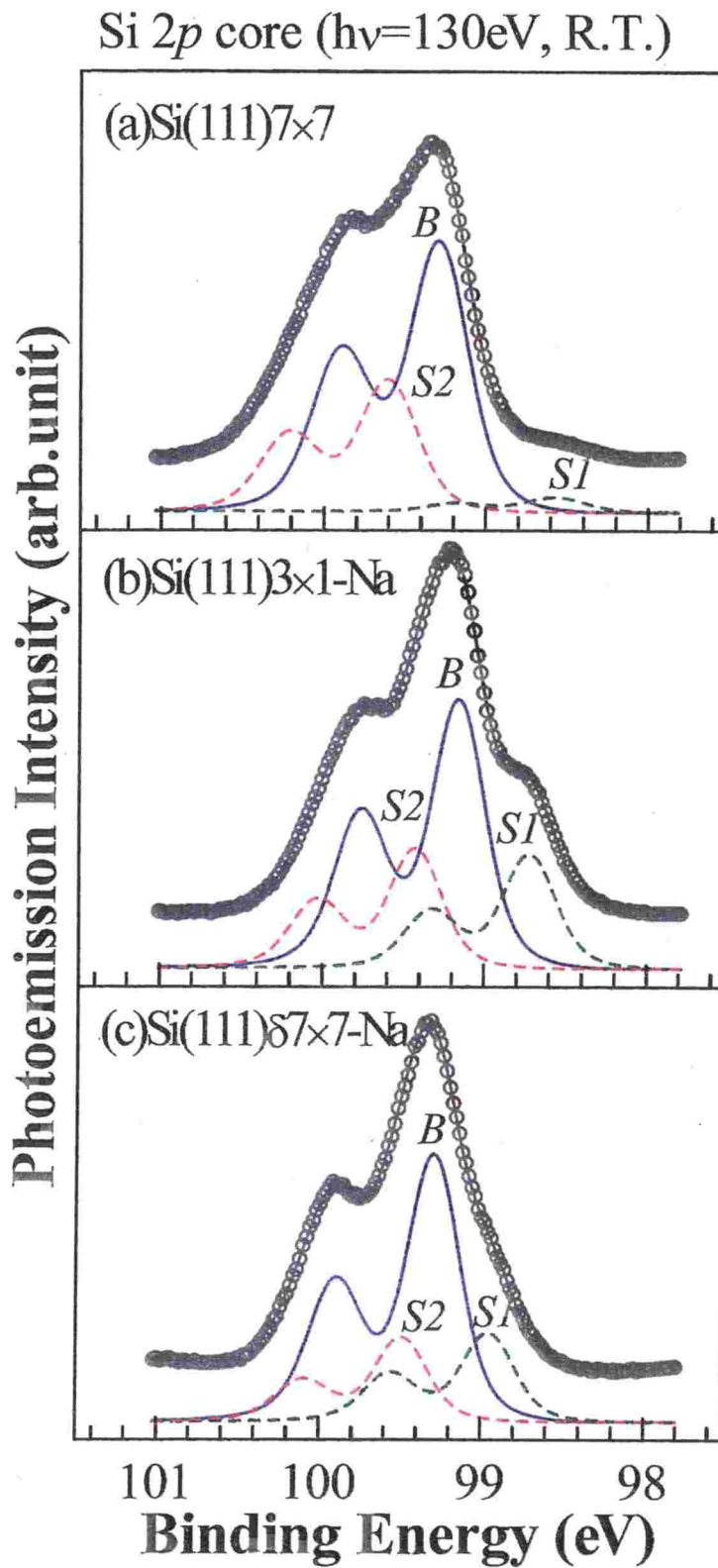
Fig. 5.4: Surface sensitive Si $2p$ core level spectra of (a)Si(111)7×7, (b)Si(111)3×1-Na and (c)Si(111)$\delta$7×7-Na surfaces. Every spectrum can be fitted with one bulk($B$) and two surface components($S1$ and $S2$).
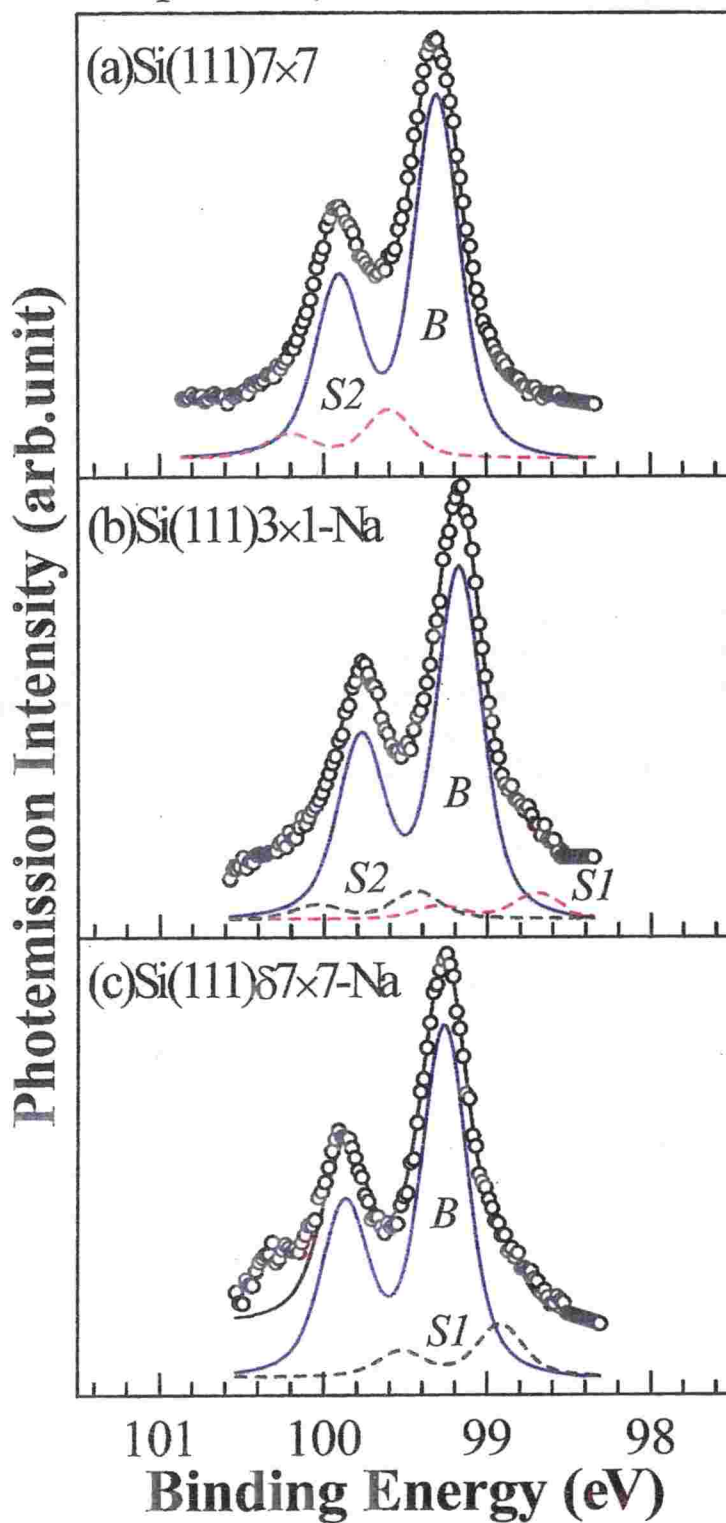
Fig. 5.5: Bulk sensitive Si 2*p* core level spectra of (a)Si(111)7×7, (b)Si(111)3×1-Na and (c)Si(111)δ7×7-Na surfaces.

With regard to the energy position of the bulk Si $2p$ core component, we notice that it is shifted appreciably toward smaller binding energies (by $-0.13$eV) for the $3\times1$-Na surface, but it is hardly shifted for the $\delta7\times7$-Na surface. Namely the valence band maximum of this n-type sample further bends by $0.13$eV toward the Fermi level on the $3\times1$-Na surface in contrast with the $\delta7\times7$-Na surface.

As for the surface components the intensity ratio between the $S2$ and the $S1$ components becomes almost comparable in both the $3\times1$-Na and $\delta7\times7$-Na surfaces. We also notice that the intensity of the $S2$ component of the $7\times7$ clean surface which is ascribed to the adatoms has been much reduced on the $\delta7\times7$-Na surface. According to the UPS study of the $7\times7$ surface adsorbed with Li and K [24],the adatom dangling bond state likely disappears at the saturation coverage. For the Cs adsorbed surface, the adatom dangling bond is terminated by the Cs atom at the first stage of the adsorption [25]. On this analogy we think that the tendency of the reduction of the $S2$ component on the $\delta7\times7$-Na surface may be due to the Na adsorption on the adatom dangling bonds.

One notices that the total $S1$ and $S2$ peak intensity $(S1+S2)$ of (b) is appreciably larger than that of (c). This fact suggests that the number of surface Si atoms with electronic characters different from those of the bulk Si atoms, is more on the $3\times1$-Na surface than on the $\delta7\times7$-Na surface. The number of the surface Si atoms in a $1\times1$ unit cell $(\theta_s)$ for each surface is estimated from the intensity ratios of the surface components by well know attenuation model as mentioned in section2.2 and given in Table 5.1. For this estimation we used the values of the average spacing between the Si layers as $1.57$Å($\frac{1}{2}$ of the distance between the 1st layer and the 3rd layer of the ideal Si(111) surface) and the mean free path of $3.9$Å for the surface sensitive measurement.

For example, $\theta_s$ in the $7\times7$ clean surface is experimentally evaluated as $1.06$. If we assume the number of surface Si atoms of the $7\times7$ surface as 54 (adatoms + pedestal atoms + rest atoms $= 12 + 36 + 6 = 54$) in the $7\times7$ unit cell(49 atoms), the $\theta_s$ should be $\frac{54}{49}$. This theoretical value ($\frac{54}{49}\simeq1.10$) is in good agreement with the experimental value ($1.06$). From the $\theta_s$ values we estimate that the number of surface atoms is about 4 ($4.23 = 1.41 \times 3$) for the $3\times1$ surface in the $3\times1$ surface unit cell, and about 58 ($58.3 = 1.19 \times 49$) for the $\delta7\times7$ surface in the $7\times7$ unit cell.

With respect to the electronic characters of these surface Si atoms, the values of the surface core level shifts (SCS) of both $S1$ and $S2$ components of (b) have larger absolute values than those of (c). This result indicates that the amount of charge transfer from the Na atoms to the surface Si atoms or between different kind of surface Si atoms is larger for the $3\times1$-Na surface (b) than for the $\delta7\times7$-Na surface(c).

## 5.3.3 SCLS of Si(111)3×1-Rb and -Ag with high energy resolution

*High energy resolution core level spectroscopy*

Referring to the recent high energy resolution core spectroscopy measurement of the Si(111)$7\times7$ surface by cooling down the sample at about 100K, I have attempted to apply the high energy resolution method to the measurement of the $3\times1$-Rb and Ag surfaces. I have cooled down the sample about 75K after making the $3\times1$-Rb and Ag samples and shut the slit of SR light as possible as I can to improve the energy resolution of the light.

Figure 5.6 shows the results of the high resolution surface sensitive photoelectron spectroscopy of the Si 2p core for clean Si(111)$7\times7$ surface recorded by $h\nu=133$eV. Seeing the
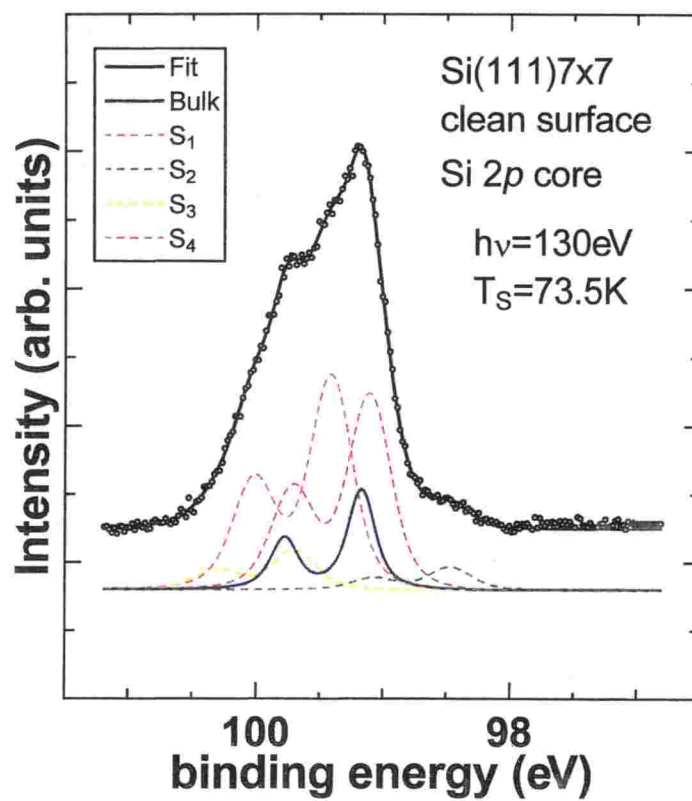
Fig. 5.6: Si 2$p$ core spectrum of the Si(111)7×7 in high energy resolution mode recorded by $h\nu$=133eV at $T_S$=75K.

spectrum we can find some new shoulders (indicated by arrows) which could not be detected by previous room temperature measurement of 7×7 surface(Fig. 4.5) because of the reduction of the phonon broadening effect and indicating the achievement of the high resolution measurement. I fitted this spectrum by curve fitting procedure. The experimental data points(dots) are fairly reproduced by the fitted curve(solid curve) in each spectrum. I needed four surface(broken curves) and one bulk(blue solid curve) components to fit the 7×7 surface spectrum. These values of shifts are consistent with those of previous studies[22, 23, 21] and the intensities are close to the results of Paggel$et$ $al.$[22]. The fitting parameters is represented in Table5.2 and very similar to those estimated by Paggel $et$ $al.$[22], but little bit different from those by Karlsson $et$ $al.$[23] or LeLay$et$ $al.$[21].

Table 5.2: Fitting parameter of the high energy resolution spectrum of Si $2p$ core of Si(111)7×7 surface

| | | |
|---|---|---|
| Spin-orbit splitting | (eV) | 0.608 |
| Branching ratio($2p_{1/2}/2p_{3/2}$) | | 0.500 |
| Lorentzian width | (eV) | 0.180 |
| Gaussian width($B$) | (eV) | 0.137 |
| Gaussian width($S$) | (eV) | 0.293 |
| Surface component($S_1$) | | |
| Core level shift | (eV) | 0.240 |
| Intensity ratio($S_1/B$) | | 2.980 |
| Surface component($S_2$) | | |
| Core level shift | (eV) | −0.702 |
| Intensity ratio($S_2/B$) | | 0.313 |
| Surface component($S_3$) | | |
| Core level shift | (eV) | 0.527 |
| Intensity ratio($S_3/B$) | | 0.561 |
| Surface component($S_4$) | | |
| Core level shift | (eV) | −0.064 |
| Intensity ratio($S_4/B$) | | 2.735 |

### Si $2p$ core spectra of Si(111)3×1-Rb and -Ag

Figures5.7 and 5.8 show the Si $2p$ core spectra of the Si(111)3×1-Rb and -Ag taken at some different photon energies($h\nu$=115, 125, and 133eV) and T$_S$=75K. Though we can fit the spectra of the 3×1-Na by two surface and one bulk components, however, we need three surface and one bulk components to best fit the spectrum of the Si(111)3×1-Rb as shown in the Fig. 5.7. Therefore there are at least three kinds of surface Si atoms on the 3×1-Rb surface. The directions of the shifts of two surface components, $S1$ and $S2$, are negative and positive consistent with the case of the 3×1-Na surface. The amount of shift of the $S3$ is very little(−0.105eV) and the same component may merge into the bulk component in the spectrum of 3×1-Na surface. From the intensity ratio of the $S1$, $S2$, $S3$ and $B$ we estimated the number of surface atoms. In the Table5.3 I presented the fitting parameters and estimated numbers of surface Si atoms. As presented in the table $S1$, $S2$, and $S3$ correspond to 1.56, 1.33, and 2 surface Si atoms in the unit cell. The valence band bending of this 3×1-Rb surface compared to the Si(111)7×7 surface is estimated from the bulk core level shift as 0.06eV toward the $E_F$ and more smaller than that of the 3×1-Na surface(0.131).

On the other hand we need two surface components and one bulk component to fit the Si(111)3×1-Ag surface without inconsistency between different spectra in different surface
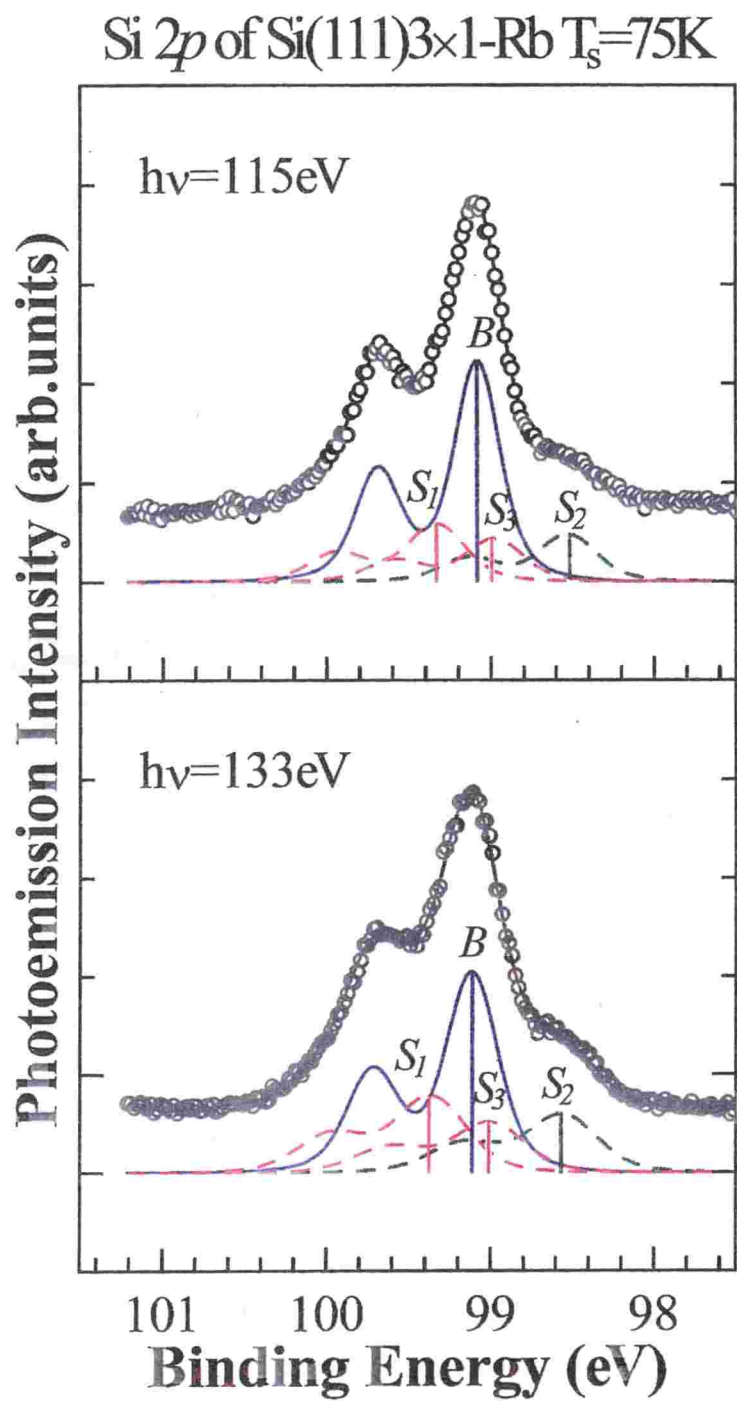
Fig. 5.7: Si 2$p$ core spectra of the Si(111)3×1-Rb surface recorded by $h\nu$=115 and 133eV at $T_S$=75K.

sensitivity as shown in Fig. 5.8. The fitting parameters are also tabulated in Table5.3.
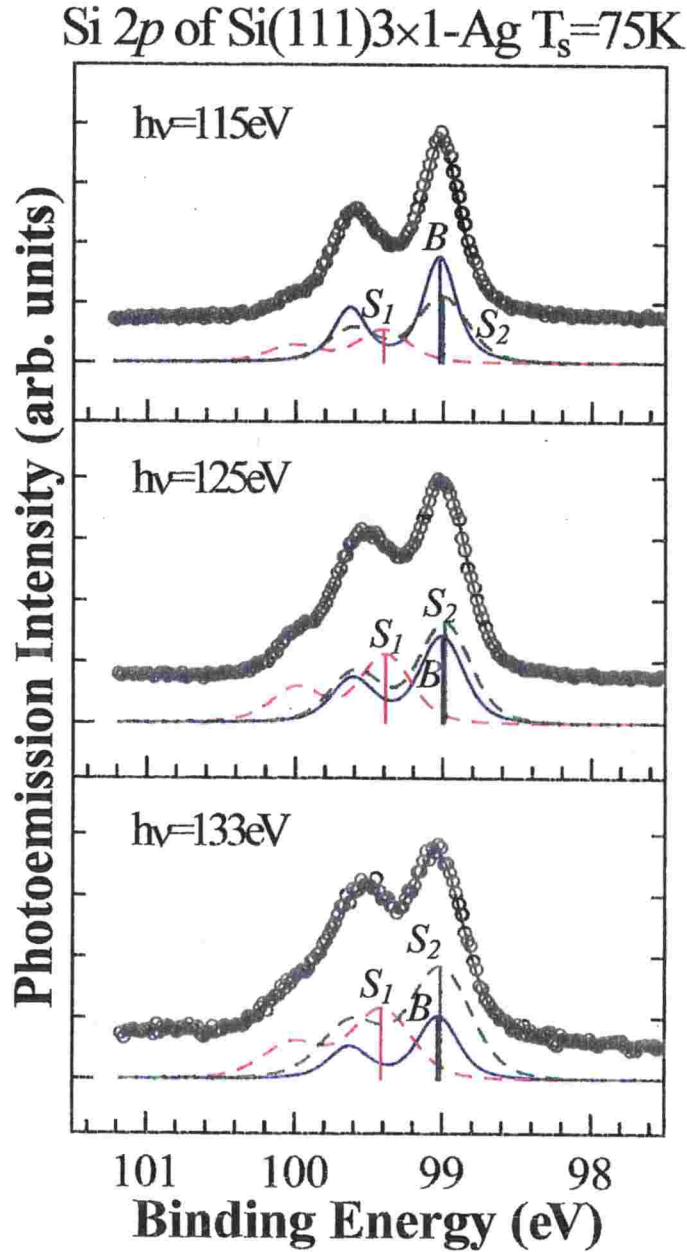


Fig. 5.8: Si $2p$ core spectra of the Si(111)3×1-Ag surface recorded by $h\nu$=115, 125, and 133eV at $T_S$=75K.

As seen in the Fig. 5.8 and Table5.3 the position of $S1$ component is very close to the bulk position compared to the AM induced 3×1 surface and the intensity of the $S1$ is very much larger than $S2$ component. The intensity of the $S1$ is larger than the bulk component in the surface sensitive($h\nu$=133eV) spectrum. The estimated numbers of the surface atoms on this surface is about 4.2 and 2.8 in the surface unit cell as shown in Table5.3. On this 3×1 surface the band bending toward $E_F$ is 0.107eV and smaller than that of 3×1-Na(0.131) but larger than 3×1-Rb(0.06).

*Rb4p and Ag 4d core spectroscopy*    In addition to the Si $2p$ core spectroscopy we also measured the Rb $4p$ core and Ag $4d$ core spectra. Figure 5.9 shows the results of the core measurement of these adsorbates. To obtain the pure information of the adsorbate in the case of the 3×1-Rb surface we annealed the Si(111)3×1 surface little bit and make the mixed

Table 5.3: Fitting parameters of the Si(111)3×1-Rb and 3×1-Ag surfaces

|  |  | (a) 3×1-Rb | (b) 3×1-Ag |
|---|---|---|---|
| Spin-orbit splitting | (eV) | 0.605 | 0.605 |
| Branching ratio($2p_{1/2}/2p_{3/2}$) |  | 0.500 | 0.500 |
| Lorentzian width | (eV) | 0.180 | 0.180 |
| Gaussian width($B$) | (eV) | 0.269 | 0.213 |
| Gaussian width($S_1, S_2$) | (eV) | 0.407 | 0.382 |
| Bulk core level shift | (eV) | −0.06 | −0.107 |
| Surface component($S_1$) |  |  |  |
|   Core level shift | (eV) | −0.249 | −0.016 |
|   Intensity ratio($S_1/B$) |  | 0.37 | 2.47 |
|   Number of atoms in unit cell |  | 1.56 | 4.2 |
| Surface component($S_2$) |  |  |  |
|   Core level shift | (eV) | 0.445 | 0.381 |
|   Intensity ratio($S_2/B$) |  | 0.49 | 1.55 |
|   Number of atoms in unit cell |  | 2.0 | 2.8 |
| Surface component($S_3$) |  |  |  |
|   Core level shift | (eV) | −0.105 | — |
|   Intensity ratio($S_3/B$) |  | 0.32 | — |
|   Number of atoms in unit cell |  | 1.33 | — |

surface of the 3×1-Rb and 7×7 clean surfaces. By doing that the observed photoelectron of Rb restricted to only from the 3×1 surface. As seen in the figure each spectrum contain no shifted peak and could be fitted with only one component of the doublet. These results indicate that the bonding site of Rb and Ag on the 3×1 surface is only one kind and are consistent with the coverage of 1/3ML.

## 5.3.4 ARPES of Si(111)3×1-Na

*normal emission*

Figure 5.10 shows the ARPES spectra for the surface normal direction of the Si(111)7×7 clean surface and the Si(111)3×1-Na surface measured at $h\nu$=21.2eV.

The broken vertical line indicates the Fermi level position. As mentioned before, in the spectrum of the 7×7 surface, the adatom dangling bond state("$S_1^{7\times7}$"), which is crossing the Fermi level, and the rest atom dangling bond state("$S_2^{7\times7}$",binding energy($E_B$)$\simeq$ 0.9eV) are clearly seen. The adatom back bond state of the 7×7 surface ($E_B\simeq$ 1.7eV) cannot be clearly recognized due to the strong intensity of the bulk state("$B$") for the normal emission. Other peaks at $E_B$= 4.05, 2.99, and 2.53eV and the shoulder at $E_B$=4.61eV are also observable in the 7×7 spectrum(marked by wedges).

In the spectrum of the 3×1-Na surface, the"$S_1^{7\times7}$" and "$S_2^{7\times7}$" states disappeared and other peaks or shoulders labeled "$a$", "$b$", "$c$", "$d$", and "$e$" appeared at $E_B$=1.34, 1.66, 2.98, 3.90, and 4.26eV, respectively. In this spectrum of the 3×1-Na we can no longer see the sign of the metallic character like the "$S_1^{7\times7}$" state. Among these peaks and shoulders of the 3×1-Na surface, the peak "$b$" is thought to be a bulk state which is of the same origin
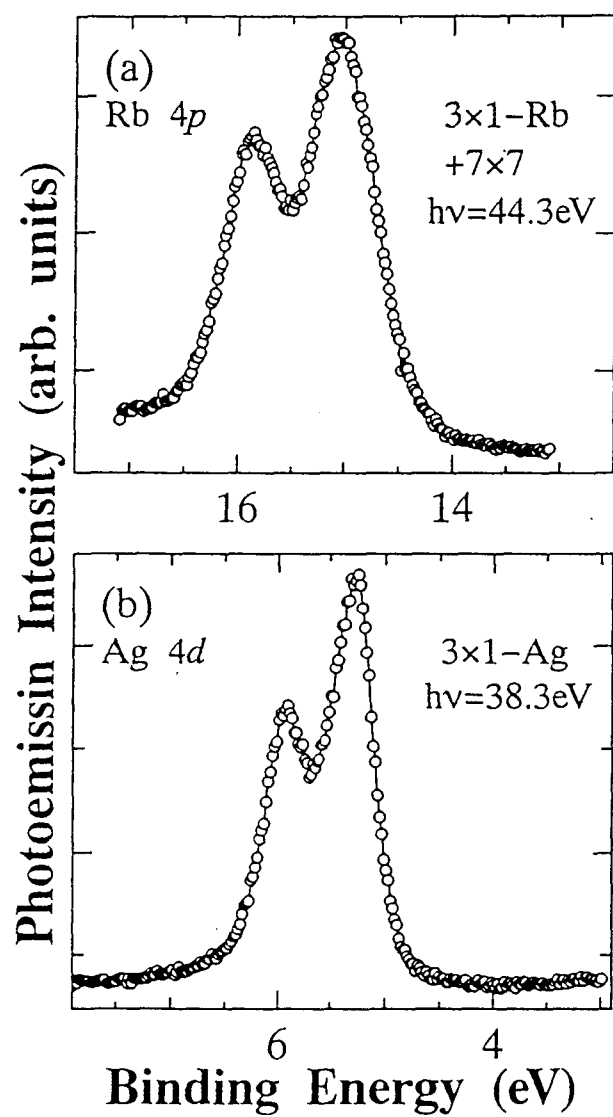
Fig. 5.9: Rb 4$p$ and Ag 4$d$ core spectra of Si(111)3×1-Rb and -Ag surfaces
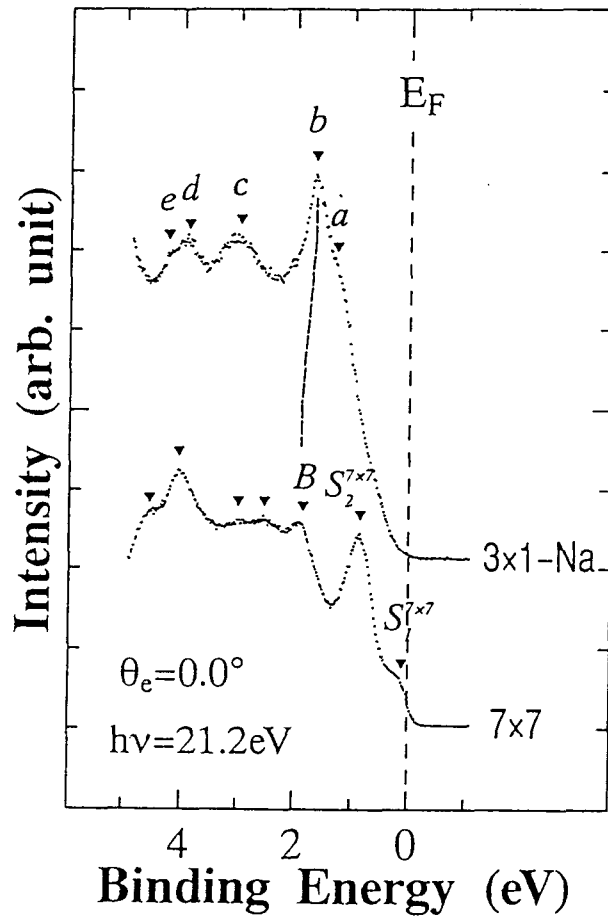
Fig. 5.10: ARPES spectra of Si(111)3×1-Na at surface normal direction recorded at
$h\nu$=21.2eV

as the peak "$B$" of the 7×7 spectrum, because the states "b" and "B" have similar large dispersions(it will be shown later in Fig. 5.13 and Fig. 5.14). The shift of the peak from $E_B$=1.85eV(peak "$B$") of the 7×7 surface to $E_B$=1.66eV(peak "$b$") of the 3×1-Na surface in the normal emission is thought to be due to band bending. The amount of the shift (−0.19eV=1.66−1.85eV) is comparable with the band bending(−0.13eV) estimated by the Si $2p$ core measurement.

*Surface Brillouin zone*

Figure 5.11 shows the surface Brillouin zone(SBZ) of the 3×1 surface (thick broken lines) as well as those of the 1×1(solid lines) and the 2×1 surface(dotted lines).
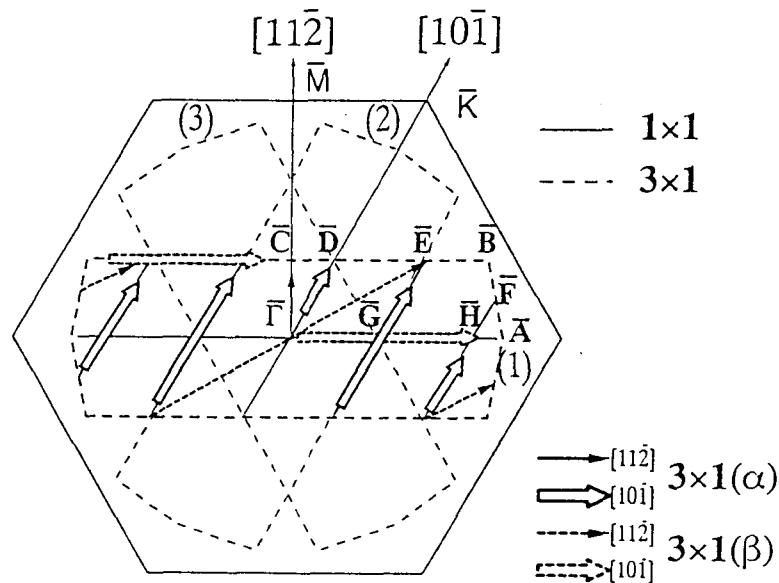


Fig. 5.11: (a)Surface Brillouin zones(SBZ's) of the 3×1 surface as well as that of the 1×1 surfaces.

We performed the ARPES measurement along the [11$\bar{2}$] and [10$\bar{1}$] directions which correspond to $\bar{\Gamma}$ −$\bar{M}$ and $\bar{\Gamma}$ −$\bar{K}$ directions of the 1×1 symmetry, respectively. $\bar{\Gamma}$ is common to the 1×1, 2×1 and 3×1 SBZ's and the symbols $\bar{M}$ and $\bar{K}$ indicate the symmetry points of the 1×1 SBZ. The symbols $\bar{A}$ , $\bar{B}$ , $\bar{C}$ , $\bar{D}$ , $\bar{E}$ , $\bar{F}$ , $\bar{G}$ and $\bar{H}$ are the symmetry points of the 3×1 SBZ, which is shown by thick broken lines, labeled(1), named tentatively. The symbols $\bar{J}$ , $\bar{J}'$ , and $\bar{K}'$ are the symmetry points for the 2×1 SBZ. Because the present sample has three equivalent 3×1 domains, we have to consider other two equivalent SBZ's(thin broken lines, labeled (2) and (3) in Fig.1). Consequently, each dispersion measured along the [11$\bar{2}$] or the [10$\bar{1}$] directions is the mixture of those arises from two kinds of domains. That is the measurement along the [11$\bar{2}$] direction corresponds to the $\bar{\Gamma}$ −$\bar{C}$ −$\bar{\Gamma}$ −$\bar{C}$ ...symmetry line as well as the $\bar{\Gamma}$ −$\bar{E}$ −$\bar{F}$ −$\bar{E}$ −$\bar{\Gamma}$ ... symmetry line of the 3×1 SBZ. In the same way, the measurement along the [10$\bar{1}$] direction corresponds to the $\bar{\Gamma}$ −$\bar{D}$ −$\bar{G}$ −$\bar{E}$ −$\bar{H}$ −$\bar{F}$ −$\bar{H}$ −$\bar{E}$ ... symmetry line and the $\bar{\Gamma}$ −$\bar{G}$ −$\bar{H}$ −$\bar{A}$ (=$\bar{B}$ )−$\bar{E}$ −$\bar{D}$ −$\bar{C}$ −$\bar{D}$ −$\bar{E}$ ... line at the same time. We defined the dispersions obtained in the measurement along [11$\bar{2}$] and [10$\bar{1}$] directions in the SBZ(1) domain, which are along $\bar{\Gamma}$ -$\bar{C}$ -$\bar{\Gamma}$ -$\bar{C}$ ... and $\bar{\Gamma}$ -$\bar{D}$ -$\bar{G}$ -$\bar{E}$ -$\bar{H}$ -$\bar{F}$ ... directions(indicated

by solid arrows), respectively as the 3×1α dispersions. As the same way we defined the 3×1β dispersions as the dispersions along [11$\bar{2}$] and [10$\bar{1}$] directions for SBZ(2), which reduced to those along $\bar{\Gamma}$ -$\bar{E}$ -$\bar{F}$ -$\bar{E}$ ... and $\bar{\Gamma}$ -$\bar{G}$ -$\bar{H}$ -$\bar{A}$ (=$\bar{B}$ )-$\bar{E}$ -$\bar{D}$ -$\bar{C}$ directions for the SBZ(1) domain as shown by broken arrows in Fig. 5.11. By this definition the measured dispersions along [11$\bar{2}$] and [10$\bar{1}$] directions arisen from SBZ(3) domain correspond to that of 3×1β and 3×1α dispersions, respectively, as shown in Fig. 5.11.

*Angle resolved photoemission spectra*

Figure 5.12 show the typical angle resolved spectra for [11$\bar{2}$] and [10$\bar{1}$] directions measured at $h\nu$=18.0eV. In the figures, the vertical bars show the states assigned to the surface states
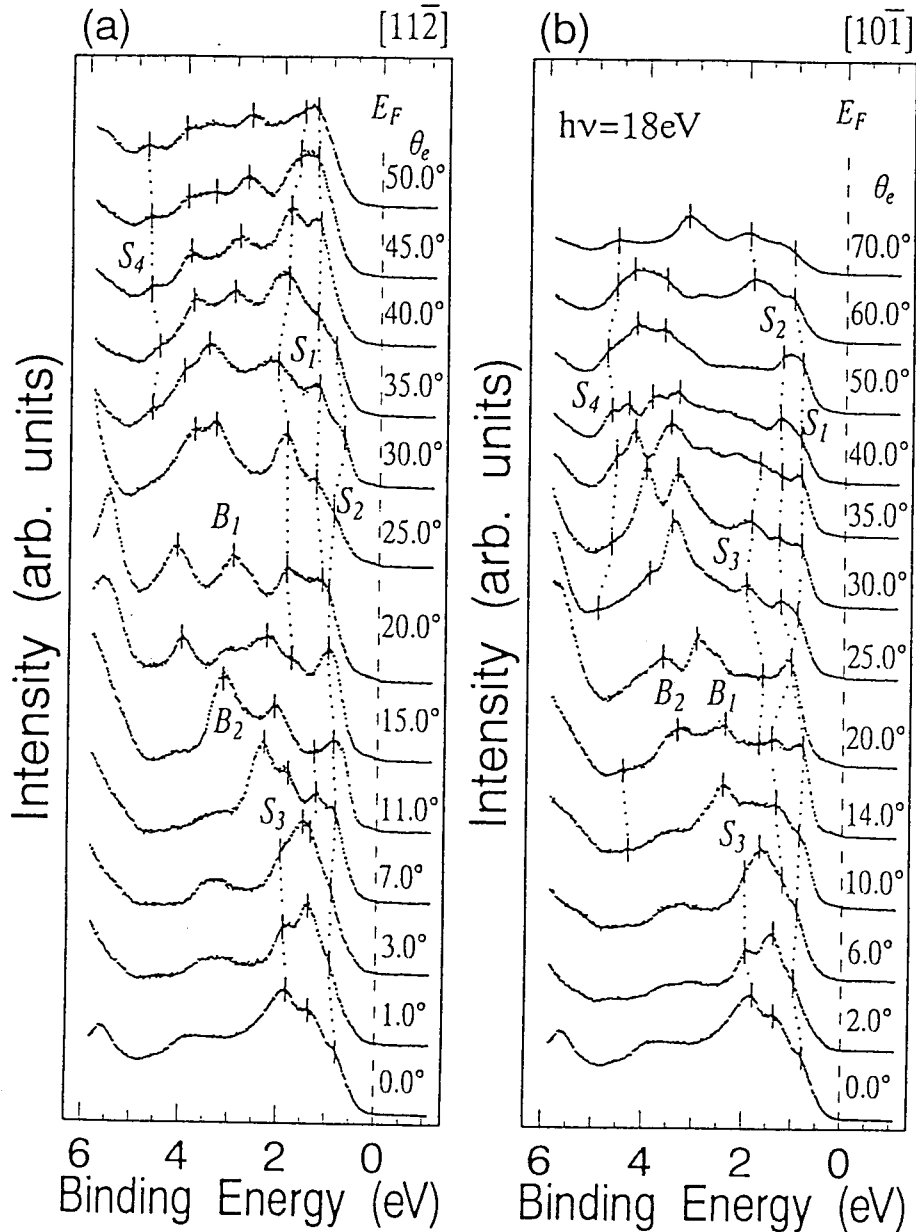
Fig. 5.12: ARPES spectra of the Si(111)3×1-Na of (a)for [11$\bar{2}$] and (b) for [10$\bar{1}$] directions recorded at $h\nu$=18.0eV.

of the 3×1-Na surface as well as other prominent peaks which are thought to be bulk like

bands of the substrate. The precise energies of these peaks and shoulders were determined by taking the minimum positions of the second energy derivative spectra[8]. These spectra show that there is no appreciable density of states(DOS) at the Fermi level(broken vertical lines). Other spectra taken at $h\nu=21.2$, 23.0 or 51.0eV neither showed any signal of DOS at the Fermi level. Therefore the 3×1-Na surface is not metallic as the 7×7 surface but semiconducting. This semiconducting character of the 3×1-Na surface is consistent with the results of the STS $I - V$ curve measurement[3] for the 3×1-Na surface and our ARPES measurement for the 3×1-K surface[8].

### Band maps

Figures 5.13 and 5.14 show the band maps of the 3×1-Na surface for $h\nu=18.0$eV and 21.2eV obtained from the ARPES spectra. The left- and right-hand sides of the figures show the dispersions along the [11$\bar{2}$] and [10$\bar{1}$] directions.
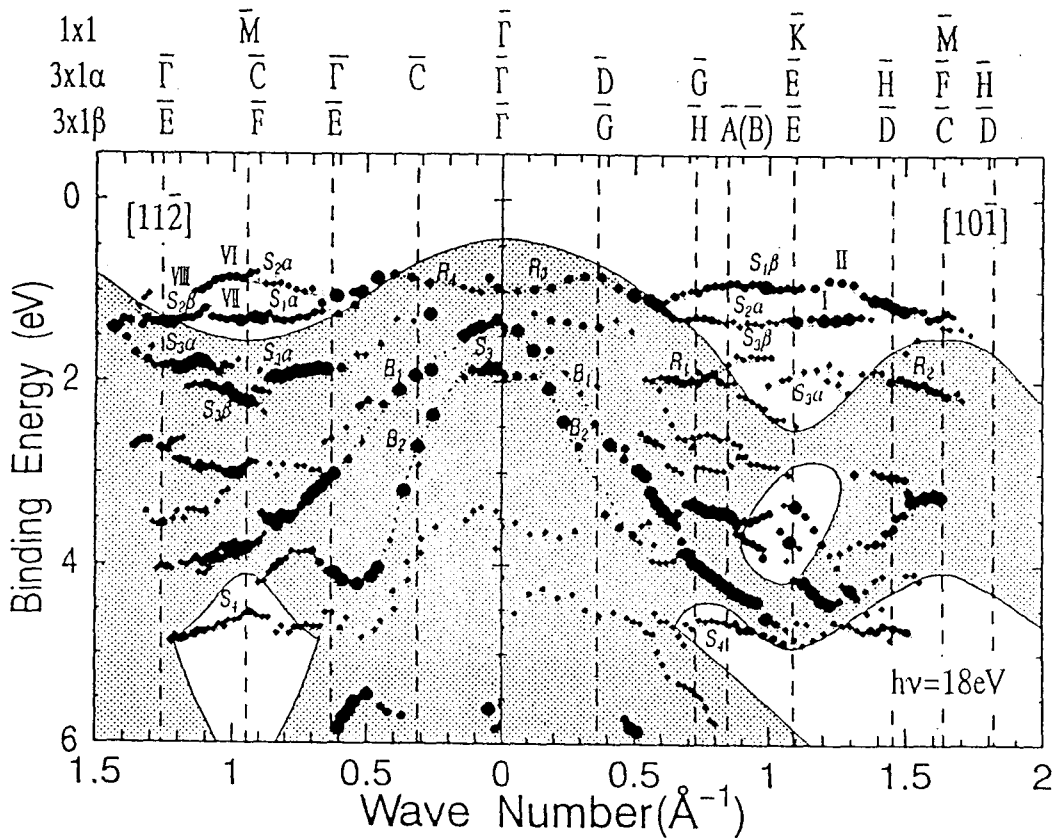


Fig. 5.13: Band map of the Si(111)3×1-Na surface for $h\nu=18.0$eV. The positions and the intensity of the peaks and shoulders are shown by filled circles changing their sizes by three grades. The left- and right-hand sides of the figure show the dispersions along the [11$\bar{2}$] and [10$\bar{1}$] directions.

We do not present the band maps for $h\nu=23.0$eV and $h\nu=51.0$eV because of the scarcity of the measured data points. We have also presented the band maps of the 7×7 surface for $h\nu=21.2$eV in Fig. 4.4 in the section4.1 for comparison. The ordinates show the binding energy relative to the Fermi level. The bottom and the top abscissa correspond to the wave
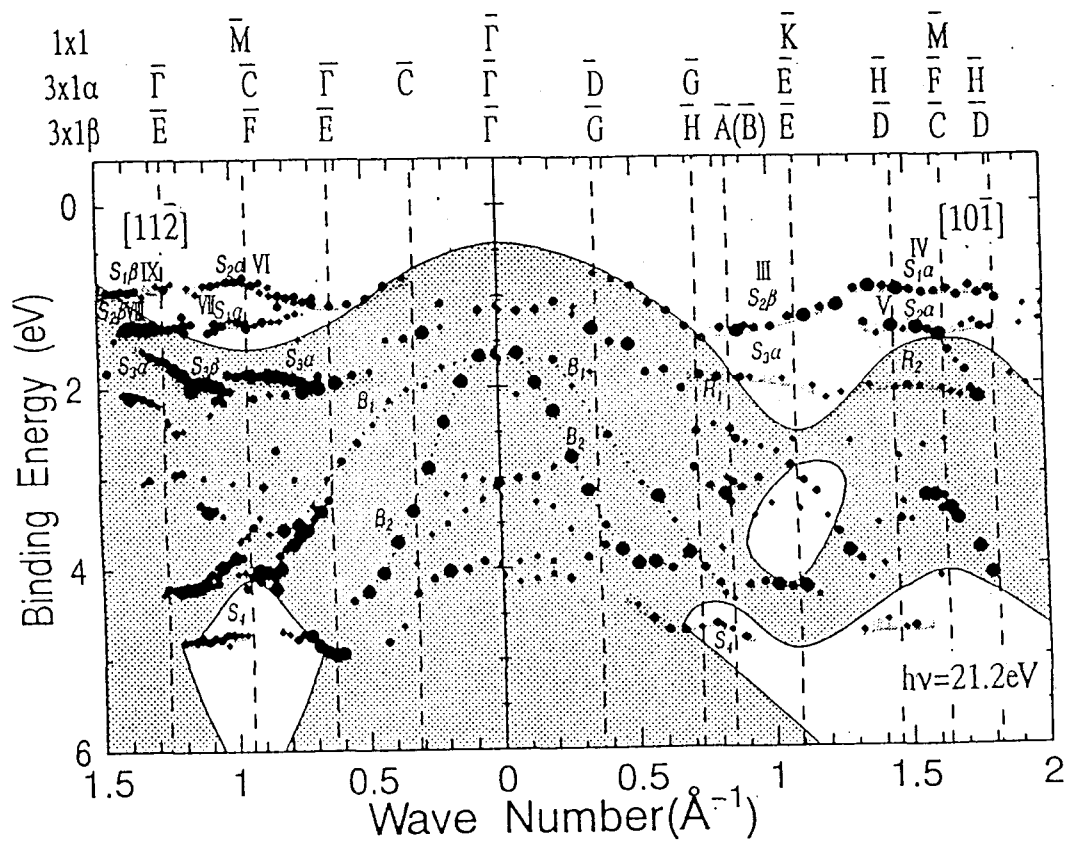
Fig. 5.14: Band map of the Si(111)3×1-Na surface for $h\nu$=21.2eV. Other parameters and rotations are the same as in Fig. 5.13.

number and the position of the symmetry point. Along with the 1×1 symmetry points, the aforementioned two sets of the 3×1 symmetry points (3×1($\alpha$) and 3×1($\beta$)) are presented.

In these figures, the data positions are represented by filled circles. The size of the circles in three grades represents the intensity of the peaks or shoulders in the ARPES spectra. The shaded area corresponds to the bulk band projection taken from ref.[26]. The energy position of the valence band maximum(VBM) from the Fermi level($E_F$), $E_B$(VBM), was estimated from the relation, $E_F - E_B$(VBM) $= E_F - E_B$(Si2$p_{3/2}$)$-98.74$eV, which was proposed by Himpsel et al. for the Si(111) surface[27]. We can know the binding energies of the Si $2p_{3/2}$ core level of the 3×1-Na surface as 99.16eV, and of the 7×7 surface as 99.29eV, from our measured core level spectra. Therefore the energy difference between the Fermi level and the VBM is $E_F - E_B$(VBM)$=99.16-98.74=0.42$eV for the 3×1-Na surface and $99.29-98.74=0.55$eV for the 7×7 surface.

*Assignment of surface states*

According to Figures 5.13 and 5.14 we can easily find several surface states which exist in the band gap of the bulk band projection. Since there are three 3×1 domains on this sample we have to be careful to count the number of the surface states and to determine the directions of the observed dispersions. Otherwise we may regard the same surface state which appears in the different directions as different surface states. Fortunately the symmetry point of $\bar{E}$ in the direction of [10$\bar{1}$] has the same wave number in both 3×1($\alpha$) and ($\beta$) directions as seen in the top of Figs5.13 and 5.14. Therefore we can easily know the number of surface states by counting the number of states in the band gap at the $\bar{E}$ point. At the $\bar{E}$ point of Fig. 5.13[10$\bar{1}$] we can discriminate several surface states which are at $E_B$~0.8eV(later named $S_{1\beta}$), 1.3eV($S_{2\alpha}$), and 1.7eV($S_{3\alpha}$), in the bulk band gap. In the region of $E_B$ >4eV with $k_{\parallel}$ between ~0.8 and 1.5 Å$^{-1}$, we can also see another surface state($S_4$) in the bulk band pocket. These surface states are considered to be different surface states and named $S_1$, $S_2$, $S_3$, and $S_4$. In Fig. 5.14[10$\bar{1}$] we can also see some surface states at $E_B$≃1.3 and 1.6eV near the $\bar{E}$ point. There is another surface state in the $E_B$ region larger than 4eV at $k_{\parallel}$=~0.8, and 1.4 Å$^{-1}$. These surface states are thought to correspond to the $S_2$, $S_3$, and $S_4$ states considering their binding energies comparing with those of Fig. 5.13. Comparing the dispersions of these states in Figs5.13 and 5.14 with those of the 7×7 surface(Fig. 4.4), it is easily recognized that these surface states are characteristic to the 3×1 surface. In Fig. 5.14[10$\bar{1}$], however, the $S_1$ state is not observable at the $\bar{E}$ point. In addition, it is worth noting that the shape of the dispersion curve of the $S_2$ state in Fig. 5.13[10$\bar{1}$] is different from that in Fig. 5.14[10$\bar{1}$]. This result suggests that the observed directions of the dispersions are different from each other. These difference between different photon energy measurements may be the final state effect.

There are also some states which are considered to be resonant states, in the bulk band projection. The states labeled $R_1$ and $R_2$ which continue to the $S_3$ state, and $R_3$ continuing to the $S_2$ state are considered to be resonant states of these surface state.

The energy levels of the $S_1$, $S_2$, and $S_4$ states hardly shift(less than the margin of the energy resolution ~0.15eV) in the measurements at different photon energies, indicating that these states are real surface states. The surface state marked $S_3$ is somewhat unclear at the $\bar{E}$ point in Fig. 5.13[10$\bar{1}$] and one can not confirm that its $E_B$ does not change with the photon energy. However the resonant states $R_1$ and $R_2$ of $S_3$ states do not shift appreciably with photon energies and we think the $S_3$ state is a real surface state. The fair agreement between the transition positions from the prominent $R_1$ and $R_2$ states to the more weak and broad $S_3$ state and the bulk band projection edges shown in Fig. 5.13 also implies that the $R_1$ and $R_2$ states are surface resonant states. This agreement also means that the estimated

$E_B$(VBM) is appropriate.

In Fig. 5.13[11$\bar{2}$] and Fig. 5.14[11$\bar{2}$] we can see some surface states in the bulk band gap. These states are considered to be the $S_1$, $S_2$, and $S_4$ states from their energy levels. In addition, there are some prominent states around $E_B$=2eV inside the bulk band projection. We regard these states as well as the state at $E_B$=1.8eV around $k_{\parallel}$=0 Å$^{-1}$ in Fig. 5.13 having flat dispersions as the resonant states of the $S_3$ state judging from their energy positions and absents of the states in 7×7 surface as seen in Fig. 4.4.

Besides these surface states, several bands with bulk character are also seen in both Fig. 5.13 and Fig. 5.14. Among those bulk bands we labeled clear ones as $B_1$ and $B_2$. These structures correspond to "$b$" of Fig. 5.10. These states have large dispersions as clearly seen in Fig. 5.12. In a strong contrast to the case of the surface states, similar bands are seen for the 7×7 surface in Fig. 4.4, which converge to "$B$" in Fig. 5.10(The $B_1$ and $B_2$ states look degenerated at the $\bar{\Gamma}$ point). In addition, the $B_1$ and $B_2$ states have considerable energy shifts for different $h\nu$ due to the dispersions along the surface normal. The amount of the shift near the $\bar{\Gamma}$ point was less than 0.27eV for the measurements at $h\nu$=18.0, 21.2, 23.0, and 51.0eV. The energy difference was the largest between $h\nu$=21.2eV and 51.0eV. The dispersion or the energy shift of the $B_1$ and $B_2$ states, for example, obscures the $S_3$ resonant state near the $\bar{\Gamma}$ point in Fig. 5.14 due to the mutual overlap. Thus confirmed surface states, resonant states and prominent bulk states are labeled as $S_1$, $S_2$, $S_3$, $S_4$, $B_1$, and $B_2$ in Fig. 5.12, in which the surface states and the resonant states were traced with dotted lines.

Besides these states we can also see several states in the small bulk band pockets near the $\bar{E}$ point around $E_B$~3.5eV in Fig. 5.13[10$\bar{1}$] and Fig. 5.14[10$\bar{1}$], which may also be surface states. Their binding energy shifts of about 0.35eV for different $h\nu$ are, however, a little bit too large for surface state and we will no more discuss about these states.

*Extraction of the surface states along 3×1 SBZ*

From these dispersion data of Fig. 5.13 and Fig. 5.14 we can confirm that this surface is semiconducting and has at least four surface states even though the data are mixtures of three different 3×1 domains. In order to compare them with the theoretically calculated band dispersions, however, we have to ascertain the true directions of the observed dispersions in the 3×1 SBZ.

In our assignment we classified the bands of $S_1$ and $S_2$ into nine individual parts and labeled 'I' ~ 'IX' in Fig. 5.13 and Fig. 5.14. From Fig. 5.13 we can know that the states having 3×1 periodicity in the [11$\bar{2}$] direction('VI') is the $S_2$ state along 3×1$\alpha$ direction, since the state continues to the $S_2$ state of the [10$\bar{1}$] direction('I'). Thus we could obtain the $E_B$s of the $S_2$ state at $\bar{\Gamma}$, $\bar{C}$ and $\bar{E}$ points. If the $S_2\alpha$ state labeled 'I' in the Fig. 5.13 was along the 3×1$\beta$ direction, the $E_B$ of the state at $\bar{G}$ ($\beta$) point is lower than that at $\bar{E}$ point. The dispersion feature of $S_2$ state labeled 'III' in Fig. 5.14 is different from that of 'I' in Fig. 5.13. Then the $S_2$ of 'III' should be along the 3×1$\alpha$ direction. In this case, however, the $E_B$ of the state 'III' at $\bar{G}$ ($\alpha$) point is higher than that at $\bar{E}$ point in Fig. 5.14. This inconsistency was caused by the misassumption that the $S_2$ state labeled 'I' is along the 3×1$\beta$ direction. Therefore the $S_2$ states of 'I' and 'III' must be along the 3×1$\alpha$ and $\beta$ directions, respectively. From the assignment we could know the $E_B$ of the $S_2$ at almost all the symmetry points. After the assignment we considered all the combinations of the sorts and directions of the remaining surface states and compared the energy levels of them at major symmetry points . Then we determined the true energy levels of each surface state at each symmetry point without any inconsistency.

Consequently, the directions of the observed dispersions were determined as indicated in the Fig. 5.13 and Fig. 5.14 by $S_1\alpha$, $S_1\beta$ ...etc. and we could know the $E_B$ of the $S_1$, $S_2$ and $S_3$ states at most of the major symmetry points. We did not determine the binding energy of the $S_4$ state at any symmetry points due to the limited data points.

Figure 5.15 is a summary of the extracted dispersions of the $S_1$, $S_2$, and $S_3$ states along the boundary of the 3×1 SBZ. The filled circles, filled triangles and asterisks in Fig. 5.15 are the data points of $h\nu$=18.0eV[10$\bar{1}$], 21.2eV[10$\bar{1}$], and 51.0eV[10$\bar{1}$], respectively. The empty
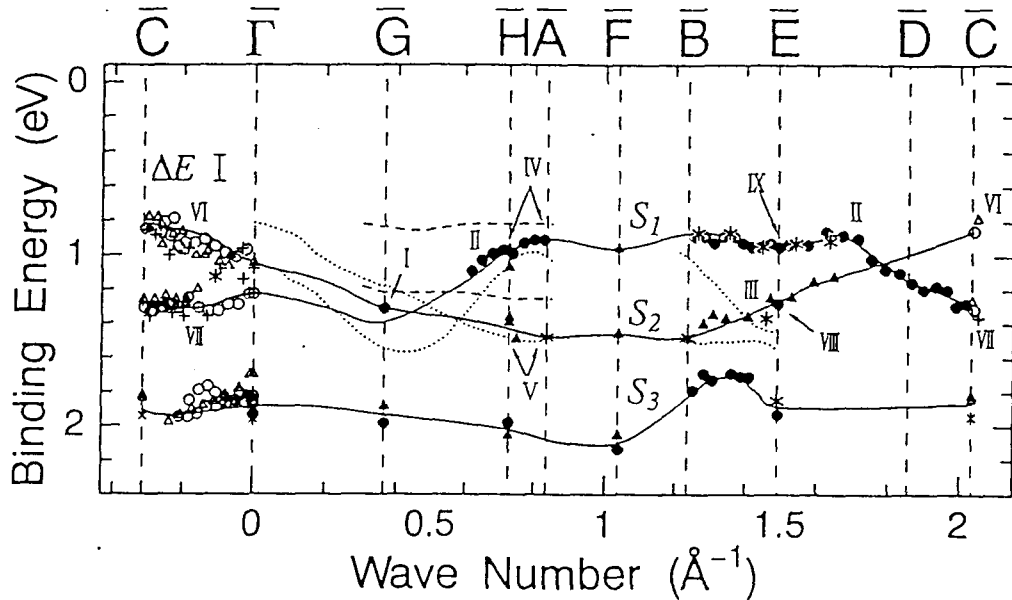


Fig. 5.15: Summary of the extracted dispersions of the surface states of Si(111)3×1-Na surface along 3×1 SBZ. The filled circles, filled triangles and asterisks are the data points of $h\nu$=18.0eV[10$\bar{1}$], 21.2eV[10$\bar{1}$], and 51.0eV[10$\bar{1}$], respectively. The empty circles, empty triangles and crosses indicate the data of $h\nu$=18.0eV[11$\bar{2}$], 21.2eV[11$\bar{2}$], and 23.0eV[11$\bar{2}$].

circles, empty triangles and crosses indicate the data of $h\nu$=18.0eV[11$\bar{2}$], 21.2eV[11$\bar{2}$], and 23.0eV[11$\bar{2}$](The measurement was done only along the [11$\bar{2}$] direction for $h\nu$=23.0eV and only along the [10$\bar{1}$] direction for $h\nu$=51.0eV). For $S_1$ and $S_2$ states, we also labeled 'I'~'IX' which corresponds to each part of the dispersion of Fig. 5.13 and Fig. 5.14. We can notice that the data points of both the $S_1$ and $S_2$ states from different $h\nu$ measurements are in fair agreement. As for the $S_3$ state, however, the energy positions for different $h\nu$'s are relatively scattered compared with those of the $S_1$ or $S_2$ state. The scatter of the data points may be due to the wide adoption of the observed states even in the bulk band-projection region of the [11$\bar{2}$] direction as the surface resonant states of $S_3$, and we cannot remove a possibility that some of the data plotted in Fig. 5.15 as the $S_3$ states are not from true $S_3$ states.

*Band widths of the surface states*

From Fig. 5.15 we can estimate the possible band widths($W$) of these surface states as $W(S_1)\geq$0.50eV, $W(S_2)\geq$0.71eV, $W(S_3)\geq$0.44eV and $W(S_4)\geq$0.30eV, respectively although some ambiguities still remain about the observed dispersions in the cases of the $S_3$ state.

# 5.4 Discussion

## 5.4.1 Assignment of the surface states $S_1$ and $S_2$ of ARPES

Seeing the dispersion feature of the $S_1$ state in Fig. 5.15, the $S_1$ has a characteristic upward dispersion from $\bar{\Gamma}$ to $\bar{H}$ point(corresponding to $\bar{\Gamma}$ to $\bar{J}$ direction of the 2×1 SBZ; see Fig. 5.11) reminiscent the famous dispersion of the $\pi$-bonded chain state[28] of the Si(111)2×1 surface as mentioned in section4.2. This characteristic surface states has been also observed on the 3×1-K surface[8]. The band width between $\bar{\Gamma}$ and $\bar{A}$ points of 0.47eV is also almost the same as to that of the $\pi$-bonded chain of the Si(111)2×1 surface which are estimated as the 0.58eV[29] or 0.47eV[28]. From these results we propose the existence of the $\pi$-bonded chain structure on the 3×1-Na surface. According to the experimental [30, 31] and theoretical[32] studies for the alkali metal adsorbed Si(111)2×1 cleaved surface, the $\pi$-bonded chain is unstable against Na adsorption whereas it is stable with K adsorption. We think that the configuration difference between the alkali metal adsorbed 2×1 and 3×1 surfaces may explain the difference of the stability of the $\pi$-bonded chain between these two surfaces.

In contrast to the $S_1$ state, the $S_2$ state has a downward dispersion by the amount of ~0.45eV from $\bar{\Gamma}$ to $\bar{A}$ point(corresponding to the direction of $\bar{\Gamma}$ $-\bar{K}$ of the 1×1 SBZ). The energy range of this state is around 1.0eV~1.5eV below $E_F$. According to the theoretical calculations[33, 34, 35] and ARPES measurement[36] for the Si(111)1×1-Na surface with 1ML of Na coverage, the Si 3$p$ state bonding with the Na atom has a similar downward dispersion along $\bar{\Gamma}$ $-\bar{K}$ direction of the 1×1 SBZ with the band width of ~0.5eV[34]. From the similarities of the energy levels and the dispersion feature of the $S_2$ state to those of the Na-Si bonding state of the Si(111)1×1-Na surface, we assign the $S_2$ state to the Si 3$p$-Na 3$s$ bonding state.

## 5.4.2 Model of the Si(111)3×1 surface

From the results of the coverage estimation, SCLS and ARPES measurements the model of the Si(111)3×1 requires following terms.

From the coverage and work function estimation, The coverage is 1/3ML. The dipole moment of the surface is small.

From the SCLS measurement, The surface has at least two kinds of surface Si atoms positively and negatively charged. The surface should explain the intensity of the surface components.

From the ARPES measurement, The model has $\pi$-bonded chain structure and Si-Na bonding state. The surface electronic state is semiconducting. The surface has at least four surface states.

From the other experiments such as STM, AES, LEED, and so on, The surface explain the STM images. The surface is passive against oxidation(=has small amount of dangling bonds). The reconstruction of the substrate Si has been occurred.

Considering these terms we proposed three types of structural models for the Si(111)3×1 surface having $\pi$-bonded chain structure with 1/3ML coverage. The model of Fig. 5.16(a) has a ring consisting of 5 Si atoms on the ideal surface as seen in the side view of (a). So we named this the 5-membered model. In the same way we named the models of (b) and (c) the 5-6-7 model and 5-7 model, respectively. The dangling bonds are represented by the ovals in the figures and those associated with the A and B atoms are omitted in the top views for simplicity. The filled circles stand for the AM atoms. The thick solid lines show the unit cell

[10̄1] [11̄2]

π-bonded chain



(a)

π-bonded chain



(b)

π-bonded chain



(c)

Top view                     Side view
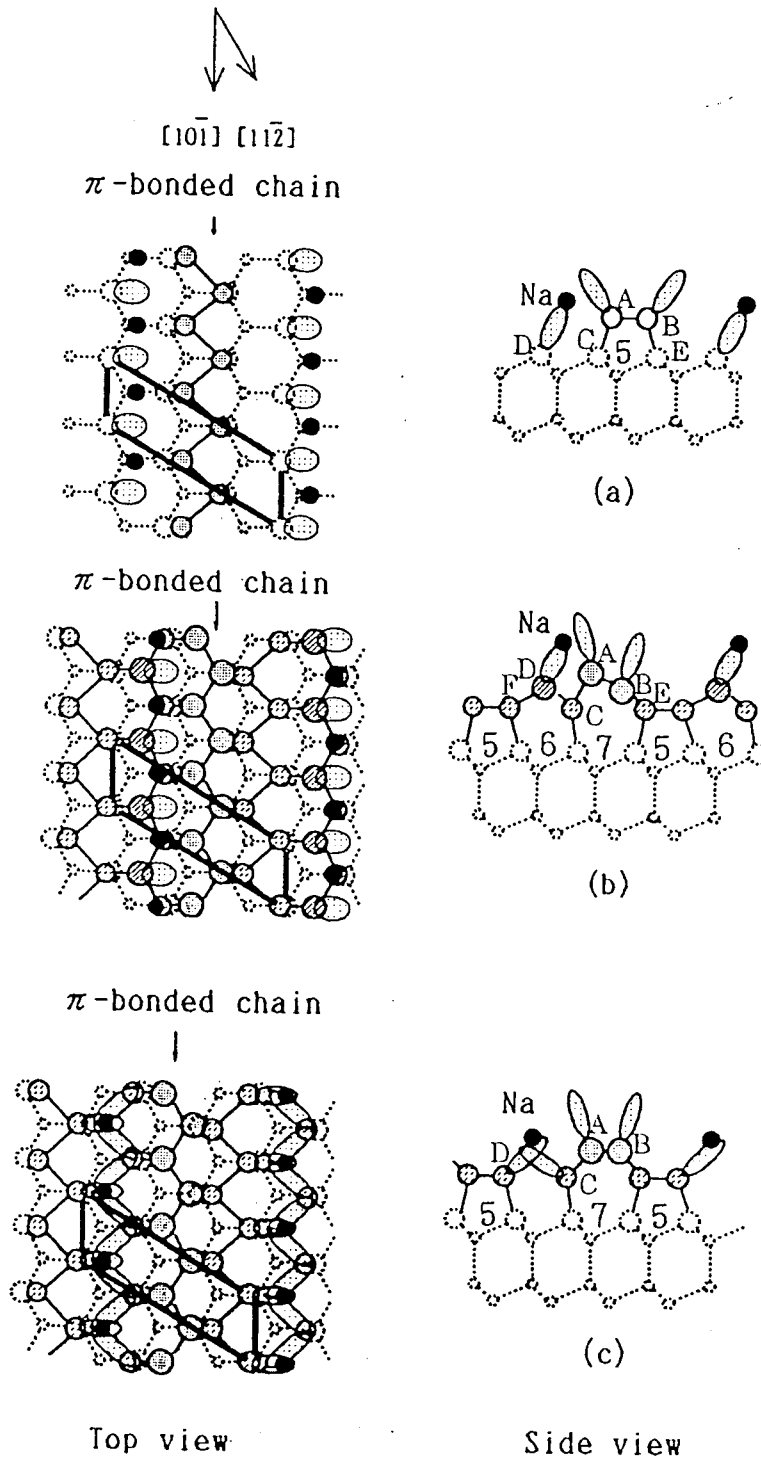
Fig. 5.16: Models of the Si(111)3×1 surface proposed from our ARPES and SCLS results. (a)5-membered ring model, (b)5-6-7 model, (c)5-7 model.

70

of the 3×1-Na surface. Therefore the coverage of Na in these models is 1/3ML. The location of the Na is tentatively assumed to be at the $T_4$ site in both (a) and (b). In (c) we assume that the Na atoms sit on the site where the dangling bonds gather up so as to terminate them. As seen in the figure the atoms **A** and **B** of these models make the π-bonded chains as the Pandey's model for the Si(111)2×1 surface[28].

### 5.4.3 Assignment of the surface components of the SCLS

In these models we can also explain the results of SCLS. As mentioned in section4.2, the surface atoms making π-bonded chain become asymmetry because the asymmetry structure is stable than symmetry π-bonded chain and the charge transfer between these surface atoms occurs. Thus the model is consistent with the SCLS data if we consider the $S1$ and $S2$ components which shift lower and higher binding energies from the bulk component $B$, are the surface atoms making π-bonded chains projected upward and bumped downward, respectively(correspond to **A** and **B** atom in Fig. 5.16(b)). Figure5.17 is the summary of the values of SCLS of Si(111)2×1 clean surface and those of the 3×1-AM and 3×1-Ag surfaces. The energy difference between $S1$ and $S2$ of the Si(111)2×1(0.89eV)[37] is almost comparable to that of the Si(111)3×1-Na(0.70eV) and Rb(0.80eV) surfaces.
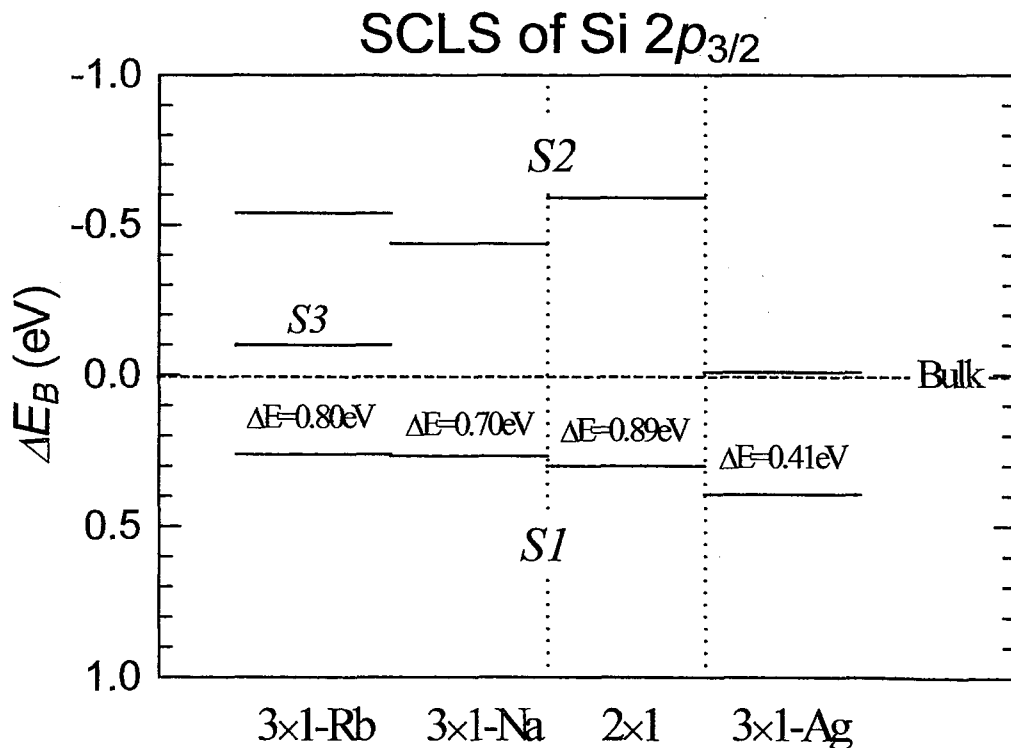


Fig. 5.17: Summary of the SCLS of Si(111)2×1, 3×1-AM and 3×1-Ag surfaces.

The estimated numbers of the surface components, however, was about $S1$:$S2$=2:2 for both 3×1-Na and Rb in the unit cell and seems to conflict to the aforementioned assignment. Seeing the model atoms **D** which is bonding with AM should be negatively charged because of the charge transfer from AM. Therefore we consider that the $S1$ state shifting lower $E_B$ include the **D** atoms too. If one of the other surface atoms such as **C**, **E** and **F** charged

71

positively and shift higher binding energy as same as that of **B** atom the number of the surface atoms can be 2:2 on the 3×1 surface.

Remaining problem is the existence of the $S3$ state on the 3×1-Rb. The shift of this $S3$ state is very small and almost the same energy level to the bulk energy level. **C**, or **E** or **F** atoms can be the candidate of the atom which contribute to the $S3$ component because these atoms are considered to be more bulk like comparing to **A**, **B**, and **D** atoms. Therefore we think the $S3$ component may correspond to one of these atoms. The absence of the $S3$ state on the 3×1-Na surface may be due to the overlapping of the $S3$ state with the $B$ component.

The estimated numbers of the surface Si atoms on 3×1-Ag surface of $S1:S2$=4.2:2.8, however, seems not to be consistent with the models. However, even if we measure the core level spectrum by angle integrated analyzer some ambiguities of the measured intensity because of the PED effect must remain and the 16% of larger number of surface atoms derived from $S2$ state may be not so considerable. And we consider that the shift of the $S1$ and $S3$ components on the 3×1-Ag surface is very close and merged into each other. If we consider like this, $S1$ component of the 3×1-Ag surface is corresponding to the surface atoms of **B,C,D** and **F**. The another remaining problem is the inconsistency of the energy difference between $S1$ and $S2$ of the Si(111)3×1-Ag(about 0.41eV) and those of 3×1-AM and 2×1 surfaces. If the surface structure of the 3×1-Ag is the almost the same structure of the 3×1-AM as suggested by the LEED $I - V$ curve[6] and STM[3, 5] measurements this results may indicate that the charge transfer of asymmetric $\pi$-bonded chain structure should be small on the 3×1-Ag surface and suggested that the asymmetry is restrained by the Ag atoms.

On the basis of the models, the Na atoms terminate the remaining dangling bonds of the atoms labeled **D**(and **C** in the model (c)) on the 3×1-AM surface, and the semiconducting electronic property of this surface can also be interpreted within one electron approximation. The absence of the dangling bond is also consistent with the inactivity against oxidation[7] of the 3×1-AM surface. In addition, the result of the small dipole moment on the 3×1-Na surface can be consistently explained by these models especially by model (a) and (c). As seen in the side view of these models, the distance between the AM layer and the top Si layer is very short, and the electric dipole moment perpendicular to the surface is very small. In the case of the $\delta$7×7-Na surface, however, the dipole moment should be much larger, because the Na adsorption site is thought to be the ontop site of the first layer Si atom, which means the distance between the Na layer and the top Si layer is long and the electric dipole moment perpendicular to the surface must be larger than that of the 3×1-Na surface. The small dipole moment may suggest that the bonding angle of AM is tilted on the surfaces.

At a first glance, our new models seem to conflict with the results of STM measurement[3, 5]. But STM images do not always show the atomic images. If we consider that the zigzag image of the filled state in the STM [3] corresponds to the combination of the electronic state of the $\pi$-bonded chains of Si and Si atoms influenced by AM or Ag atoms, it will not be inconsistent with our results.

## 5.4.4   Comparison of our ARPES results with recent theoretical works

Comparing to experimental works theoretical studies of these 3×1 surface has been relatively behind. Recently three different theoretical works, however, have been reported. Fortunately, these theoretical studies[15, 16, 17] support our proposed models basically and

further more helping to decide which model is the most plausible one. Here we compare these theoretical results with our ARPES data and discuss about the most plausible model for the 3×1-AM surface at present.

Jeong and Kang calculated the equilibrium structure and energy bands for the Si(111)3×1-Na surface at two different coverages, 1/3ML and 2/3ML, using a pseudopotential density-functional total-energy method[15]. They considered the simple Na-overlayer model on the relaxed bulk-terminated surface proposed by Jeon et al., and they proposed that the largely corrugated bulk-terminated surface with 1/3ML of Na on the $T_4$ site as the equilibrium structure. According to their calculation, two occupied and two unoccupied surface states exist on the surface. These states originate from the three Si dangling bonds(two occupied and one unoccupied states) and one Na $3s$ orbital(unoccupied state). We incorporated their dispersions(dashed curves) with our extracted dispersions(solid curves and marks) of the $S_1$ and $S_2$ states in Fig. 5.15. We reproduce their results taking the reference point at the VBM. As seen in the figure, the two calculated occupied surface bands have very flat dispersions with small dispersion width in contrast to the relatively large upward and downward dispersions of the experimentally derived $S_1$ and $S_2$ states. The difference in dispersion features between our results and Jeong and Kang's calculation indicates that the simple Na-overlayer model on the relaxed bulk terminated surface does not satisfactorily explain the 3×1-Na surface.

On the other hand, Erwin has performed the first-principle total energy calculations for several models with several alkali-metal-atom adsorbates[16] and determined the most stable model and equilibrium structure. The surface models employed for his calculation are 1)the extended Pandey chain model[16](=5-6-7 model[9]), 2)the Seiwatz chain model[38](= 5membered model[8][9][12]), 3)the simple missing top layer model[5], 4)the bulk-terminated surface model[3] and 5)the substitutional models of the extended Pandey model(=5-7model[9]) and Seiwatz model in which the alkali metal atom substitutes for the surface silicon atom in the six-membered ring. According to his calculation, the bulk-terminated surface model is not the most stable one, being in agreement with our aforementioned discussion, but the extended Pandey chain model(= the 5-6-7 model) is the most stable one.

According to the Erwin's calculation, the $\pi$-bonded chain becomes asymmetric, because the charge of the A atoms transfers to the B atoms due to the alkali metal adsorption. This is consistent with our assignment of the SCLS results. Further more his calculated STM images of the 5-6-7 model is also consistent with that of observed STM images having bright zig-zag chains. From his calculation, this surface is expected to have two occupied surface states in the bulk band gap; one of which is arising from the Si atoms in the $\pi$-bonded chain and the other from the Si atom bonding with the alkali metal in the six fold ring . We have also plotted these two surface bands(dotted curves) in Fig. 5.15. Comparing the results of the Jeong and Kang's calculation, Erwin's dispersions and our experimental results are in fair agreement. The upward and downward dispersion features of the $S_1$ and $S_2$ states are qualitatively reproduced by his calculation. These two states of his calculation are crossing at about the middle of $\bar{G}$ and $\bar{H}$ point as shown in the figure. According to our assignment of the surface states the energy of $S_1$ at $\bar{C}$ and at $\bar{\Gamma}$ is lower than that of $S_2$ state and they are reversed at $\bar{H}$ point as shown in Fig. 5.15. Hence the $S_1$ and $S_2$ cross each other between $\bar{\Gamma}$ and $\bar{H}$ points, which is consistent with Erwin's result though it is not evident that the crossing point is at the mid point of $\bar{\Gamma}$ and $\bar{H}$ points or not. The higher $E_B$ of $S_1$ than $S_2$ state at $\bar{C}$ point is also supported from their down ward and upward dispersions from $\bar{E}$ to $\bar{C}$ point. This dispersion feature also accompanies another crossing point between $\bar{E}$ and $\bar{C}$ .

Comparing the data quantitatively, the dispersion width of the calculation, 0.6eV, for

the $\pi$-bonded chain state is a little bit larger than that of the $S_1$ state($\sim$0.47eV). The calculated band width for the $S_2$ state between $\bar{\Gamma}$ and $\bar{A}$ (0.69eV) is also a little bit larger than that of the $S_2$ state(0.40eV). In addition the minimum energy gap of the 3×1-Na surface estimated from the smallest $E_B$ of the $S_1$ state at $\bar{A}$ point is 0.91eV, which is larger than the calculated band gap of 0.42 eV. This calculated value is also smaller than the STS $I - V$ curve measurement($E_g = 0.7\sim1.0$eV)[3]. If we consider the usual tendency of the underestimation of the gap in the LDA calculation, however, the discrepancy may not be so serious. One of the most serious discrepancies is that the observed dispersion of the $S_1$ state is relatively flat from $\bar{B}$ point to $\bar{E}$ point in contrast to the clear downward dispersion of the calculation. His result suggests that the energy difference between the two occupied surface states is very small at $\bar{E}$ point($\sim$0.05eV) in contrast to our result ($\sim$0.5eV). Notice that $\bar{E}$ point is the special point where there are no ambiguities of the observed direction and the discrepancy is not due to the miss assignment of the observed direction of the $S_1$ state.

Very recently Jeong and Kang[17] reported another calculation for the 3×1-AM surfaces using the same method to the previous calculation[15]. They also calculated the dispersions for the 5-membered ring model and 5-6-7 model along the whole 3×1 SBZ. Strangely, the results of them are different from those of Erwin's calculation. They concluded that the most stable model is the 5-membered ring model.

In Fig. 5.18 their dispersions of 5membered and 5-6-7 models are plotted by dashed and dotted curves with our experimental results. Their result shows that there are two surface states for both the 5-membered ring and 5-6-7 models. As seeing the figure the two surface



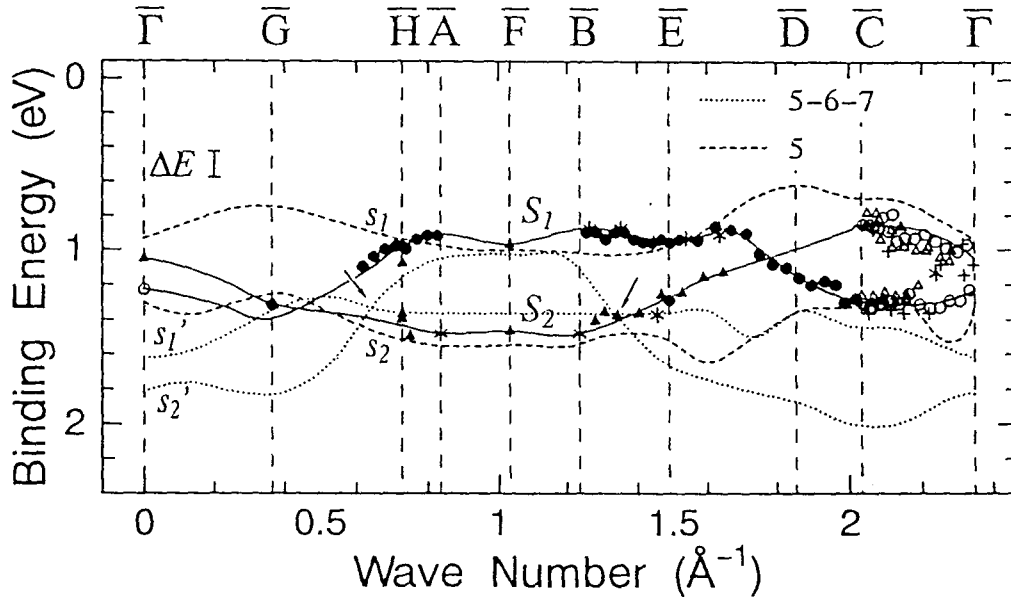Fig. 5.18: Calculated dispersions for 5-memebered ring and 5-6-7 models by Jeong and Kang[17] compared to our experimental dispersions.

bands of 5-membered ring(dashed curves) are roughly parallel in each other and the band width of these surface bands are 0.40eV and 0.30eV, respectively. Contrarily, the bands of the 5-6-7 model(dotted lines) cross each other at the mid of $\bar{G}$ and $\bar{H}$ (almost the same position

to the crossing point of Erwin's calculation), and B and E points. The most conspicuous discrepancy between their result and the Erwin's one is the higher binding energies of their calculated bands at $\bar{\Gamma}$ point. Because of the high $E_B$'s, the band width of the surface band which is corresponding to $S_1$ state is estimated as 0.97eV and the discrepancy between the calculation and our experiment becomes large and the discrepancy led the authors to conclude that the 5-membered ring model is more suitable to explain the experimental results[17]. The double crossing feature of their calculation for the 5-6-7 model, however, is qualitatively consistent with our experimental results, and the parallel feature of that for the 5-membered ring model is different from the experimental results. From these results we believe that the 5-6-7 model(=extended $\pi$-bonded chain model) is more plausible than the 5-membered ring although the discrepancy between Erwin's calculation and Jeong and Kang's one is not evident.

### 5.4.5 Assignment of the surface states $S_3$ and $S_4$ of ARPES

Although there are no predictions or information about the $S_3$ and $S_4$ states by calculations, we think that these states are the $\sigma$ bond states of the surface Si atoms. There are many $\sigma$ bond states of the surface Si atoms(the thick bonds in Fig. 5.16) which are in different conditions from that in the bulk. Among them, the bonds between A−B, B−E, A−C and E−F atoms of 5-6-7 model are considered to be in different conditions from that of the normal bulk bonds. We think that the $S_3$ and $S_4$ states may correspond to these $\sigma$ bond states. The litter of the data positions of the $S_3$ state may be due to the mixture of the some $\sigma$ bond states.

## 5.5 Summary

To investigate the surface crystal and electronic structures of the Si(111)3×1-Na, Rb, and Ag surfaces we have performed surface sensitive Si $2p$ core level photoelectron spectroscopy, angle resolved photoelectron spectroscopy(ARPES) and determined the surface core level shifts(SCLS) of these surfaces and surface state band dispersion of the Si(111)3×1-Na surface experimentally. As a result I have found the saturation coverage of the 3×1-Na as 1/3ML. The SCLS results show the existence of at least two kinds of surface Si atoms charged positively and negatively on these surfaces. The ARPES results indicate that there are at least four occupied surface states on the Si(111)3×1-Na surface, and the surface is the semiconducting. One of the surface states, $S_1$ have the characteristic dispersion being similar to that of the $\pi$-bonded chain structure of the Si(111)2×1 surface. From these results I proposed three types of surface structural models. I have also compared the experimental dispersions with the theoretical ones which are recently reported by Jeong and Kang[15, 17], and by Erwin[16]. By comparing them I can exclude the overlayer model on the bulk terminated surface for the 3×1 surface from the discrepancy between our results and the calculation[15]. The calculated dispersions[16, 17] for our previously proposed 5-6-7 model show a qualitative agreement with the experimental dispersions suggesting that the 5-6-7 model is most plausible for the 3×1-AM surface among the so far proposed models. The quantitative discrepancy between the calculations and our experimental results may require the modification of the model or other new model with $\pi$-bonded chain structure. Some discrepancy between AM induced 3×1 surface and Ag induced one are observed in the SCLS measurement suggesting the different surface structure or some modified structure of the 3×1-Ag surface compared with that of the 3×1-AM.

# References

[1] H.Daimon and S.Ino, Surf. Sci.**164**, 320 (1985).

[2] G.LeLay, V.Yu.Aristov, L.Seehofer, T.Buslaps, R.L.Johnson, M.Gothelid, M.Hammer, U.O.Karlsson, S.A.Flodström, R.Feidenhans'l, M.Nielsen, E.Findeisen, and R.I.G.Uhrberg, Surf.Sci.**307-309**, 280 (1994).

[3] D.Jeon, T.Hashizume, T.Sakurai, and R.F.Willis, Phys.Rev.Lett.**69**, 1419 (1992).

[4] T.Hashizume, K.Motai, Y.Hasegawa, I.Sumita, H.Tanaka, S.Amano, S.Hyodo, and T.Sakurai, J.Vac.Sci.Technol.**B9**, 745 (1991).

[5] K.J.Wan, X.F.Lin, and J.Nogami, Phys.Rev.**B46**, 13635 (1992).

[6] W.C.Fan, and A.Ignatiev, Phys.Rev.B,**41**3592 (1990).

[7] M.Tikhov, L.Surnev, and M.Kiskinova, Phys.Rev.**B44**, 3222(1991).

[8] K.Sakamoto, T.Okuda, H.Nishimoto, H.Daimon, S.Suga, T.Kinoshita, and A.Kakizaki, Phys.Rev.**B50**, 1725 (1994).

[9] T.Okuda, H.Shigeoka, H.Daimon, S.Suga, T.Kinoshita, and A.Kakizaki, Surf.Sci.**321**, 105 (1994).

[10] T.Hashizume, M.Kayama, D.Jeon, M.Aono, and T.Sakurai, Jpn.J.Appl.Phys.**32**, L1263 (1993).

[11] J.J.Paggel, H.Haak, W.Theis, and K.Horn, J.Vac.Sci.Technol.**B11**, 1439 (1993).

[12] H.H.Weitering, N.J.DiNardo, R.Perez-Sandoz, J.Chen, and E.J.Mele, Phys.Rev.**B49**, 16837, (1994).

[13] T.Fukuda, Phys.Rev.**B50**,1969(1994).

[14] T.Okuda, K.Sakamoto, H.Nishimoto, H.Daimon, S.Suga, T.Kinoshita, and A.Kakizaki, Phys.Rev.B to be appeared.

[15] S.Jeong, and M.H.Kang, Phys.Rev.**B51**, 17635 (1995).

[16] S.C.Erwin, Phys. Rev. Lett.**75**, 1973 (1995).

[17] S.Jeong, and M.H.Kang, Phys.Rev.**B54**,8196,(1996).

[18] R.Avci, O.B.Dabbousi, and M.S.Jazzar, in *Proceedings of the 17th ICPS Conference*, edited by J.D.Chadi and W.A.Harrison (Springer, New York, 1985), p105.

[19] T.Miller, T.C.Hisieh, and T.-C.Chiang, Phys. Rev. B33, 6983 (1986).

[20] C.J.Karlsson, E.Landemark, L.S.O.Johansson, U.O.Karlsson, and R.I.G.Uhrberg, Phys. Rev. B41, 1521 (1990).

[21] G.LeLay, M.Göthelid, T.M.Grehk, M.Björkquist, and U.O.Karlsson, and V.Yu.Aristov, Phys.Rev.B50, 14277 (1994).

[22] J.J.Paggel, W.Theis, and K.Horn, Phys.Rev.B50, 18686 (1994).

[23] C.J.Karlsson, E.Landemark, Y.-C.Chao, and R.I.G.Uhrberg, Phys.Rev.B,50, 5767 (1994).

[24] Y.Tezuka, H.Daimon, and S.Ino, Jpn. J. Appl. Phys.,29, 1773 (1990).

[25] K.O.Magnusson, S.Wiklund, R.dudde, and B.Reihl, Phys.Rev.B44, 5657(1991).

[26] K.C.Pandey,Phys.Rev.B 14,1557(1976).

[27] F.J.Himpsel,G.Hollinger, and R.A.Pollak,Phys.Rev.B, 28,7014(1983).

[28] K.C.Pandey, Phys.Rev.Lett.47, 1913 (1981).

[29] J.E.Northrup, and M.L.Cohen, Phys.Rev.Lett.49, 1349 (1982).

[30] B.Reihl and K.O.Magnusson,Phys.Rev.B,42,11839 (1990).

[31] B.Reihl,S.L.Sorensen,R.Dudde,and K.O.Magnusson,Phys.Rev.B,46,1838(1992).

[32] I.Moullet,Wanda Andreoni, and Michele Parrinello, Phys.Rev.B46, 1842(1992).

[33] S.Ossicini, C.Arcangeli, and O.Bisi, Phys.Rev.B42, 7671 (1990).

[34] J.E.Northrup, J.Vac.Sci.Technol.A4, 1404 (1986).

[35] I.Moullet, W.Andreoni, and Michele Parrinello, Surf.Sci.269/270, 1000 (1992).

[36] B.Reihl, and K.O.Magnusson, Phys.Rev.B42,11839(1990).

[37] S.Brennan, J.Stohr, R.jaeger and J.E.Rowe, Phys.Rev.Lett.45, 1414 (1980).

[38] R.Seiwatz, Surf.Sci.2, 473 (1964).

# Chapter 6

# Photoemission studies of Au induced various reconstructions on Si(111) surface: Si(111)5×2-Au, Si(111)$\alpha$-$\sqrt{3}$×$\sqrt{3}$-Au, Si(111)$\beta$-$\sqrt{3}$×$\sqrt{3}$-Au, Si(111)6×6-Au

## 6.1 Introduction

Gold adsorbed Si(111) surface shows a full variety of surface reconstructions. As shown in the Fig. 6.1 depending on the Au coverage and the temperature of Si substrate, Si(111)5×2(5×1)-Au(abbreviated as 5×2-Au hereafter), $\alpha$-$\sqrt{3}$×$\sqrt{3}$-Au, $\beta$-$\sqrt{3}$×$\sqrt{3}$-Au(abbreviated as $\alpha$- and $\beta$-$\sqrt{3}$-Au hereafter), and 6×6-Au reconstructions have been found by means of RHEED studies[1]. Among these reconstructed surfaces the $\sqrt{3}$ × $\sqrt{3}$-Au structure has been studied most intensively. One of the interests about this surface is its difference from the Si(111)$\sqrt{3}$×$\sqrt{3}$-Ag surface[2] despite the electronic resemblance between Ag and Au atoms. As mentioned already in section1.1, the scanning tunneling microscope(STM) images of the $\sqrt{3}$ × $\sqrt{3}$-Au[3], for example, reveal a single bright spot in each $\sqrt{3}$×$\sqrt{3}$ unit cell in contrast with the two spots seen in the Ag-induced $\sqrt{3}$ × $\sqrt{3}$ surface[4]. This difference in the STM image suggests the difference in surface electronic structure between the $\sqrt{3}$-Au and that of the $\sqrt{3}$-Ag surfaces. Karlsson *et al.* also suggested the electronic structural difference between these two surfaces by their ARPES results[5, 6].

For the atomic structures of the $\sqrt{3}$×$\sqrt{3}$-Ag surface, the honeycomb chained trimer(HCT) model[7] with 1ML Ag coverage has been strongly supported both experimentally[8] and theoretically[9] recently. On the contrary, there is no consensus about the atomic structure of the $\sqrt{3}$-Au surface at present. Even the exact coverage of gold on this surface is still controversial. There are several coverage estimations such as 2/3ML[1], 0.77ML[10], 0.8ML[5] 0.8ML-0.95ML[11], and 1ML[12, 13], and numerous models have been proposed so far. Recent total energy calculation[14] suggests that the conjugate-HCT(CHCT) model is the most stable among the previously proposed models with 1ML Au coverage, and some experiments have also supported this model[15, 16, 17].

In addition, it is known that there are two different phases for the $\sqrt{3}$-Au surface called as $\alpha$- and $\beta$-$\sqrt{3}$-Au, respectively[1]. The $\alpha$- and $\beta$-$\sqrt{3}$-Au phases are the low and high coverage phases. We showed the photographs of the LEED patterns of the (A)5×2-Au, (B)$\alpha$- and
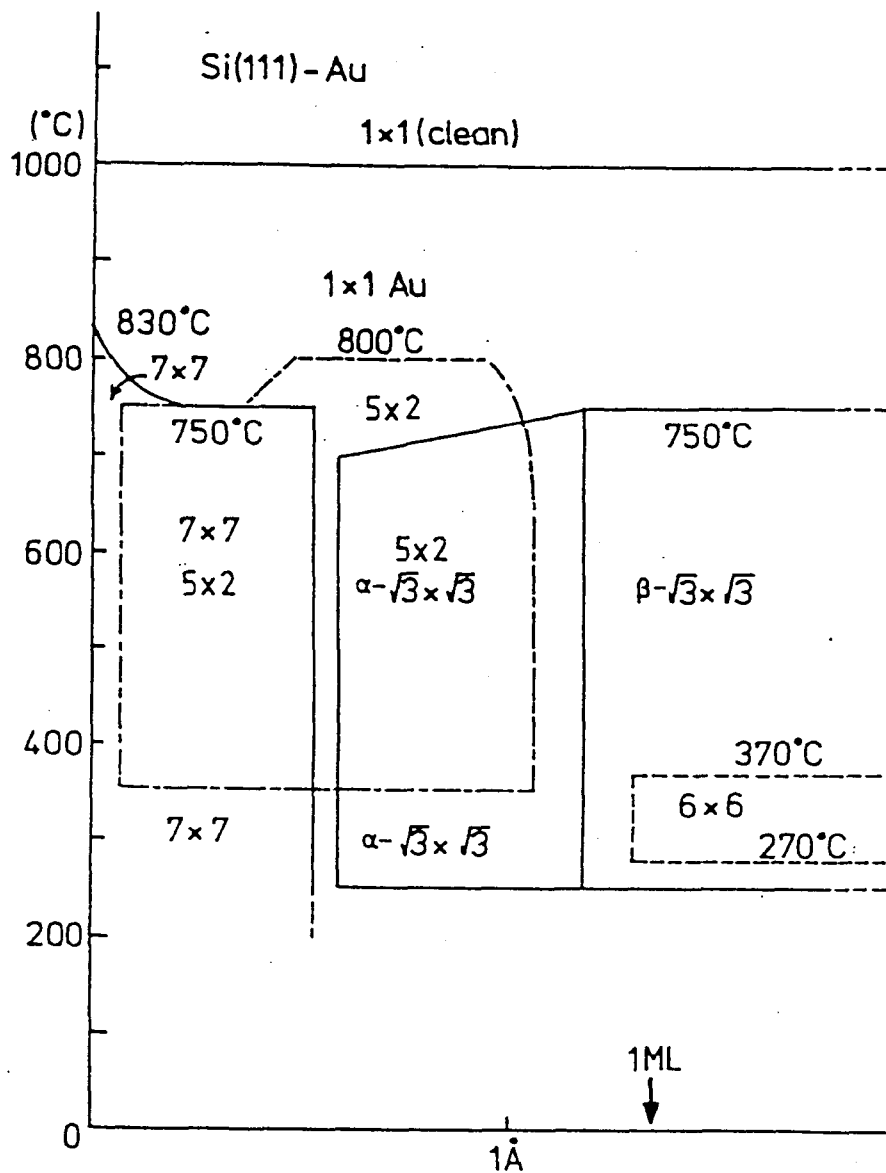
Fig. 6.1: Phase diagram of the Au/Si(111) surface from ref.[1]

(C)$\beta$-$\sqrt{3}$-Au, and (D)6×6-Au surfaces in Fig. 6.2. The LEED pattern of $\alpha$-$\sqrt{3}$-Au shows
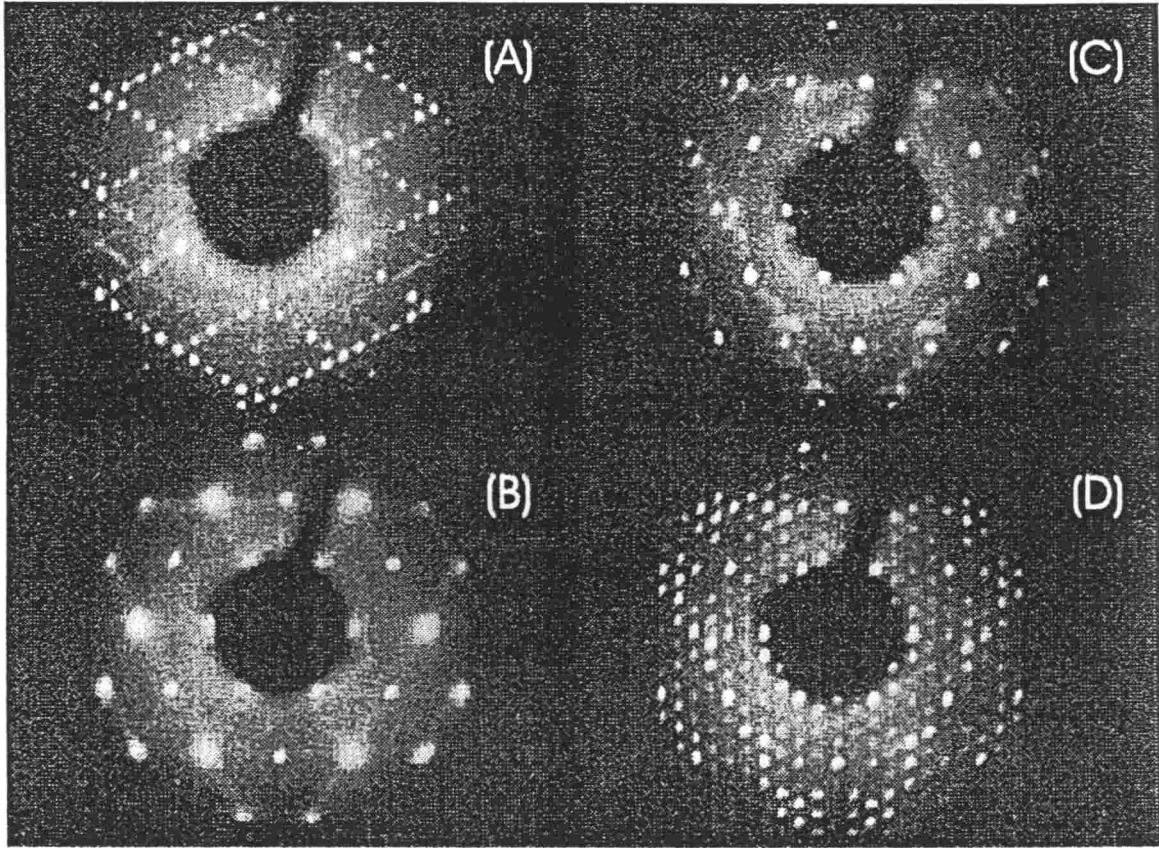


Fig. 6.2: LEED patterns of the (A)5×2-Au, (B)$\alpha$-$\sqrt{3}$-Au and (C)$\beta$-$\sqrt{3}$-Au, and (D)6×6-Au surfaces.

diffuse $1/\sqrt{3}$ spots, in contrast to the sharp $1/\sqrt{3}$ spots of the $\beta$-$\sqrt{3}$-Au surface accompanied by the ring-like streaks. In most of the previous studies, however, the difference between the $\alpha$- and $\beta$-$\sqrt{3}$-Au had been ignored and the intermediate phase between $\alpha$- and $\beta$-$\sqrt{3}$-Au was called merely the $\sqrt{3} \times \sqrt{3}$-Au structure. This is one of the reason why the study of $\sqrt{3}$-Au surface is having a hard going.

Another interest of the $\sqrt{3} \times \sqrt{3}$-Au surface is the phase transition to the 6×6 surface with increasing Au coverage from $\alpha$-$\sqrt{3}$-Au or with holding the temperature at around 400°C from $\beta$-$\sqrt{3}$-Au(see Fig. 6.1). From the LEED measurement, Higashiyama et al.[12] suggested that the $\sqrt{3}$-Au is the precursor of the 6×6-Au surface. The STM study[11] suggests a strong relation between the density of domain walls on the $\sqrt{3} \times \sqrt{3}$ surface and the formation of the 6×6 reconstruction. The in-plane X-ray diffraction study[18] also implies that the domain walls may contribute to the formation of the 6×6 surface. On the other hand, from the impact-collision ion-scattering spectroscopy (ICISS) measurement Huang et al.[10] proposed the mixed structure of the 70% of honeycomb and 30% of centered honeycomb for the $\sqrt{3}$-Au structure and the 25% of former and 75% of latter for the 6×6-Au structure.

As for the 5×2-Au surface, there is not so much information compared with the $\sqrt{3} \times \sqrt{3}$-Au surface. Although the coverage of this surface is considered to be about 0.4ML−0.5ML[19, 20, 21], some researchers suggested higher coverages[2, 10, 11]. The STM images[20, 22, 23, 24] of the filled state of the 5×2-Au surface show the bright spots forming a "Y" shaped unit

and this unit is slightly skewed. Besides these "Y" units, some other large bright spots called "protrusions"[23] have also been observed on this surface. Some STM study, however, reported that the sample prepared at low temperature(under 500°C ) shows no protrusion[25]. Although a few structural models have been proposed for this surface[21, 22, 26, 27], there are no consensus about the surface structure at present.

Comparing to above mentioned large number of structural analysises[10]-[27] few studies of surface electronic structure of these Au induced Si(111) reconstructed surfaces are available[28, 29, 5, 30]. The electronic structure of the $\sqrt{3}\times\sqrt{3}$-Au surface have been investigated by angle resolved photoelectron spectroscopy(ARPES)[5, 29] and angle resolved inverse photoemission spectroscopy(ARIPES)[30] so far. Houzay $et\ al.$ performed ARPES study along $\bar{\Gamma}$-$\bar{K}'$-$\bar{M}'$ of the $\sqrt{3}\times\sqrt{3}$ surface Brillouin zone(SBZ)(See Fig. 6.3) and found the dispersive two surface states having the $s$ character. On the other hand three surface states along the $\bar{\Gamma}$-$\bar{M}'$ and two surface states along $\bar{\Gamma}$-$\bar{K}'$-$\bar{M}'$ are observed by Karlsson $et\ al.$. By the ARIPES study the prominent unoccupied states at binding energy($E_B$) of $-2.0$eV were observed on the surface. Their observed surface is considered to be the near structure to $\alpha$-$\sqrt{3}$ surface judging from the condition of their surface preparation. These studies, however, did not distinguish the $\alpha$- and $\beta$-$\sqrt{3}$ surfaces. Collins $et\ al.$[31] reported the one dimensional metallic surface states on the single domain 5×2 surface by means of ARPES measurement. For the 6×6 surface there have been no studies of ARPES measurement as far as we know but aforementioned ARIPES study suggest the metallic character of the surface.[30]

In order to understand the atomic and electronic structures of these complex surfaces we have performed surface sensitive Si $2p$ core photoelectron spectroscopy for these reconstructed surfaces and determined the SCLS, which give us hints to their surface reconstructions and their bonding properties. In addition I report the results of ARPES measurements for all of the Au induced Si(111) reconstructions. I determined the surface states dispersions of each surface experimentally and discuss about the properties of electronic structures of these surfaces systematically. In these experiments I also distinguished the $\alpha$- and $\beta$-$\sqrt{3}$-Au surfaces and discuss about the electronic and geometric structural differences of these two surfaces.

## 6.2    Experimental

The measurements of the Si $2p$ core level spectroscopy were carried out at the beamline BL-18A of the Photon Factory(PF) in the National Laboratory for High Energy Physics. An n-type Si(111) single crystal wafer(P doped 2.4-4.0$\Omega$cm) was cleaned by direct current heating up to 1250 °C under a base pressure of $2.0\times10^{-11}$Torr. The sample cleanliness was checked by LEED and XPS. Au was evaporated onto the surface from a thoroughly out gassed tungsten spiral filament under a pressure of less than $3\times10^{-9}$Torr. The amount of the deposited gold and the deposition rate are monitored by quartz oscillator. After Au deposition, the sample was annealed at adequate temperatures to make reconstructed surfaces. The condition of the sample preparation, amount of the deposited gold and the annealing temperature of each reconstruction are tabulated in Table 6.1.

Since the quarts oscillator was located at not the same distance from the Au evaporator to the sample, these values of the deposited gold mean only the relative coverages. Consequently we have obtained clear LEED patterns of the 5×2, $\alpha$-$\sqrt{3}$, $\beta$-$\sqrt{3}$, and 6×6-Au surfaces as shown in Fig. 6.2. When we make a new sample we heated the previous sample up to 1250°C by direct current heating so as to remove the gold from the substrate.

Table 6.1: Conditions, amount of deposited gold and annealing temperature, of the preparation of the samples. The value of the deposited gold means only the relative coverage of Au. The absolute coverage of each surface which is derived from the relative coverage and the coverage of the 5×2-Au suggested by the studies so far is also shown. The values in the parentheses are the coverages when we consider the "protrusions" of the 5×2-Au as gold atoms

| | 5×2-Au | $\alpha$-$\sqrt{3}\times\sqrt{3}$-Au | $\beta$-$\sqrt{3}\times\sqrt{3}$-Au | 6×6-Au |
|---|---|---|---|---|
| Annealing | 750°C×10sec | 800°C×10sec | 600°C×5sec | 800°C×5sec+300°C×2sec |
| Coverage of Au | 0.7Å | 1.6Å | 2.1Å | 2.1Å |
| Absolute coverage(ML) | 0.40 (0.45) | 0.91 (1.03) | 1.20 (1.35) | 1.20 (1.35) |
| | 0.50 (0.55) | 1.14 (1.26) | 1.50 (1.65) | 1.50 (1.65) |
| | 0.70 (0.75) | 1.60 (1.71) | 2.10 (2.25) | 2.10 (2.25) |

As same as that of the Si(111)3×1-AM or Ag surface, the photon incident angle was 45° from the surface normal and the Si $2p$ core spectra were measured at the sample normal direction with an angle integrated photoelectron spectrometer(VG-CLAMII) For the surface(bulk) sensitive measurement of the Si $2p$ core photoelectron spectroscopy we selected the photon energy of h$\nu$=130eV(h$\nu$=110eV). In this condition the photoelectron mean free path is expected to be about 4Å(20Å) for the surface (bulk) sensitive measurement. The Fermi level position was determined from the spectrum of Ta sheet of the sample holder.

On the other hand the ARPES measurements were performed at the laboratory. The n-type Si(111) wafer(P doped 4×20×0.3 mm$^3$ 50$\Omega$cm) was cleaned by direct current heating up to 1200°C under the base pressure of less than 1×10$^{-10}$ Torr. The sample cleanliness were checked by RHEED and XPS. Au was deposited onto clean Si(111) surface which was kept about 500°C . Insitu observed RHEED pattern was changed gradually from 7×7 to $\beta$-$\sqrt{3}\times\sqrt{3}$ pattern via 5×2, and $\alpha$-$\sqrt{3}\times\sqrt{3}$ patterns as increasing the amount of Au. When changing the RHEED pattern to the entire reconstructed pattern from the mixture of the previous and newly appeared patterns we stopped deposition and after that we annealed the sample at 700°C ×2sec for the case of 5×2 and $\alpha$-$\sqrt{3}$ surfaces. When we annealed the $\beta$-$\sqrt{3}$ surface at about 300°C the pattern changed to clear 6×6 pattern gradually.

The ARPES measurements of these reconstructed surfaces were made using $\phi$150 hemispherical analyzer VG ADES 400 system with He lamp. The partial pressure of the He was less than 1×10$^{-9}$ Torr. The photon incident angle was 45° from the sample normal and the photoelectron was detected along [10$\bar{1}$], [11$\bar{2}$] and [2$\bar{1}\bar{1}$] directions. The relationship between measured directions and 1×1 SBZ as well as the $\sqrt{3}\times\sqrt{3}$ SBZ are indicated in Fig. 6.3. The energy resolution was estimated as 140meV for the pass energy of 10eV from the Fermi level cut off of the Ag powder.

# 6.3 Results and Discussion

## 6.3.1 SCLS of Au induced Si(111)5×2, $\alpha$-$\sqrt{3}$, $\beta$-$\sqrt{3}$, 6×6 surfaces

*Curve fitting*

Figure 6.4 shows the surface sensitive spectra (h$\nu$=130eV) of the Si $2p$ core levels and the results of the curve fitting, for (a)the Si(111)7×7 clean surface, (b)the Si(111)5×2-Au,
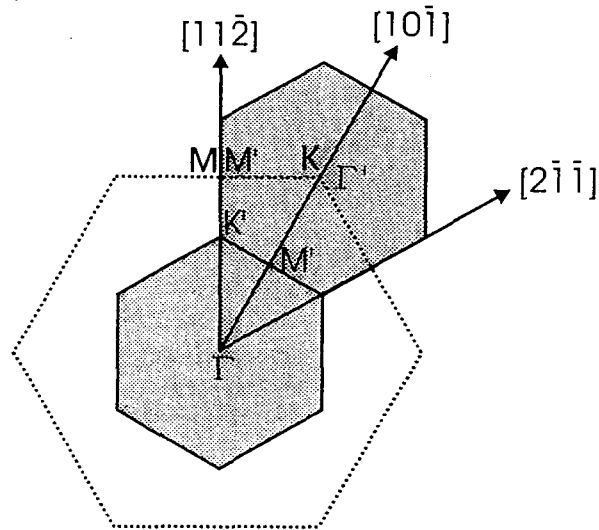
Fig. 6.3: SBZ of the $\sqrt{3} \times \sqrt{3}$ surface as well as that of the 1×1 surface. The observed directions are also indicated by arrows.

(c)the $\alpha$-$\sqrt{3}$-Au, (d)the $\beta$-$\sqrt{3}$-Au, and (e)the 6×6-Au surfaces in the order of Au coverage, although the coverage of the $\beta$-$\sqrt{3}$-Au and 6×6-Au are the same. The abscissae and ordinates represent the binding energies($E_B$) of the core levels and the photoemission intensities, respectively. The empty circles are the experimental data points corrected for the secondary-electron background.

Seeing the row spectra the spectral shapes of $\alpha$-$\sqrt{3}$ and $\beta$-$\sqrt{3}$ surfaces are different each other suggesting the different surface structure from each other and indicating the necessity of distinguishing these two surfaces. On the contrary the spectra of $\beta$-$\sqrt{3}$ and 6×6 surfaces are very similar and suggesting that the local structures of these surfaces are very similar in each other. At first glance the spectrum of the 5×2 surface is also similar that of the $\beta$-$\sqrt{3}$ and 6×6 surfaces, however, seeing the following fitting results the surface is evidently different from the other surfaces.

In order to analyze these data quantitatively we fitted the experimental data by means of aforementioned(see section2.2) nonlinear least-squares method with considering spin-orbit doublet components convoluted by Voigt function(=Gaussian+Lorentzian functions). All spectra were fitted with one bulk component(blue solid curves, marked $B$) and two surface components(red and green broken curves, marked $S1$ and $S2$) as seen in Fig. 6.4. In the figures, the vertical bars indicate the locations and relative heights of the Si $2p_{3/2}$ components. Each solid curve behind the experimental data points, which is the sum of the surface and bulk contributions, well reproduces the experimental spectrum. The used parameters and fitted results are summarized in Table6.2.

Since we take the spectra in R.T. that we cannot see the extra shoulder which we can observe in the high resolution measurement(see section5.3) because of the finite energy resolution of the experiment. Thus we deconvoluted the spectrum of the 7×7 surface into two surface and one bulk components as same as the previous studies. Consequently the Gaussian width for the fitting of 7×7 surface becomes little bit larger than those of the other

Au/Si(111)

Si 2$p$ core spectra

h$\nu$=130eV, R.T.

Fig. 6.4: Si 2$p$ core spectra and the results of the curve fitting, for (a)Si(111)7×7 clean surface, (b)Si(111)5×2-Au, (c)$\alpha$-$\sqrt{3}$-Au, (d)$\beta$-$\sqrt{3}$-Au, and (e)6×6-Au surfaces
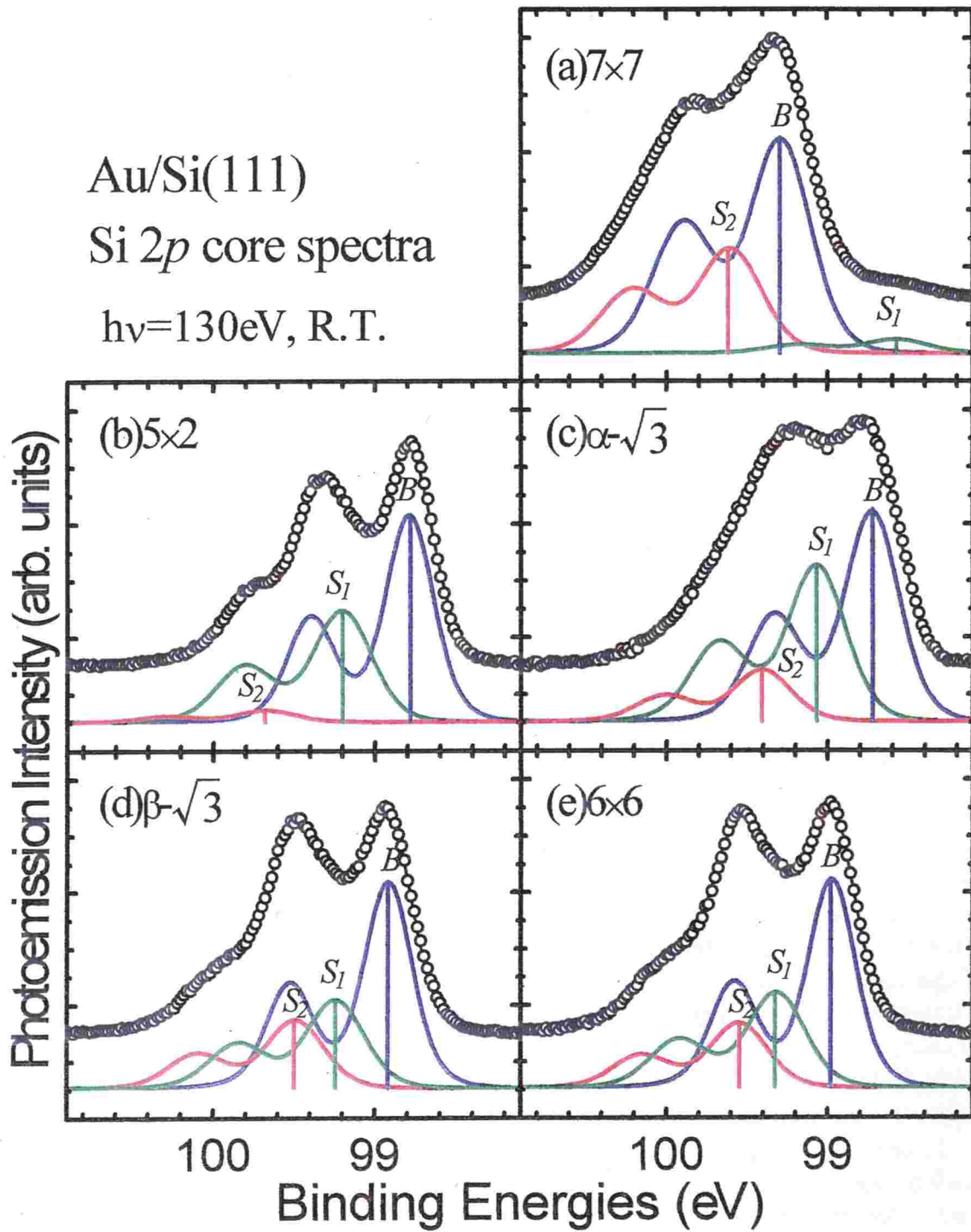
Table 6.2: Fitting parameters and results of the SCLS for (a)7×7, (b)5×2-Au, (c)$\alpha$-$\sqrt{3}$×$\sqrt{3}$-Au (d)$\beta$-$\sqrt{3}$ × $\sqrt{3}$-Au and (e)6×6-Au surfaces.

| | | (a) 7×7 | (b) 5×2-Au | (c) $\alpha$-$\sqrt{3}$-Au | (d) $\beta$-$\sqrt{3}$-Au | (e) 6×6-Au |
|---|---|---|---|---|---|---|
| Spin-orbit splitting | (eV) | 0.608 | 0.608 | 0.608 | 0.608 | 0.608 |
| Branching ratio($2p_{1/2}/2p_{3/2}$) | | 0.600 | 0.500 | 0.500 | 0.500 | 0.500 |
| Lorentzian width | (eV) | 0.13 | 0.13 | 0.13 | 0.13 | 0.13 |
| Gaussian width($B$) | (eV) | 0.37 | 0.27 | 0.32 | 0.27 | 0.27 |
| Gaussian width($S_1, S_2$) | (eV) | 0.39 | 0.35 | 0.35 | 0.35 | 0.35 |
| Bulk component($B$) | | | | | | |
| Bulk core level shift | (eV) | — | −0.500 | −0.565 | −0.372 | −0.316 |
| Surface component($S_1$) | | | | | | |
| Core level shift | (eV) | 0.314 | 0.411 | 0.342 | 0.324 | 0.342 |
| Intensity ratio($S_1/B$) | | 0.488 | 0.635 | 0.787 | 0.504 | 0.539 |
| Surface component($S_2$) | | | | | | |
| Core level shift | (eV) | −0.716 | 0.883 | 0.682 | 0.573 | 0.576 |
| Intensity ratio($S_2/B$) | | 0.055 | 0.067 | 0.259 | 0.391 | 0.366 |

surfaces.

*Electronic structure*

Figure 6.5 shows a summary of the core level binding energies of the Si $2p_{3/2}$ of bulk(squares, $B$) and surface components(triangles for $S1$ and inverse triangles for $S2$), as well as those of the Au $4f_{7/2}$ lines(circles) which are measured at the same time. The $E_B$ of the metal Au $4f_{7/2}$[32] was also given for comparison(double circle). The abscissae at the left and right hands are the binding energies for Si $2p_{3/2}$ and for Au $4f_{7/2}$, respectively. First we focus on the bulk core level binding energy shifts(BCLS) of the reconstructed surfaces from that of the clean 7×7 surface. Seeing the figure we notice that all the bulk peaks($B$) of the reconstructed surfaces shift to lower binding energies compared to that of the clean 7×7 surface. Especially the shifts of −0.50eV for the 5×2-Au and −0.57eV $\alpha$-$\sqrt{3}$-Au are remarkable. These results indicate that the large band bending of the valence band toward the Fermi level has occurred on these surfaces. Since the binding energy of the valence band maximum(VBM) on the 7×7 surface was estimated to be about 0.63eV[33], the VBM's of these surfaces are very close to the Fermi level and the $p$-type inversion layer may be created. The results of the surface conductivity change under depositing gold on the 5×2, $\alpha$- and $\beta$-$\sqrt{3}$, and 6×6-Au[34] indicated that the surface conductivity of all reconstructed surfaces decreased at the first stage of the Au deposition and then their conductivity increased again(see Fig. 6.6). Hasegawa and Ino[34] explained this change of conductivity on the basis of the existence of the inversion layer on these surfaces. Our obtained values of the band bending of the 6×6-Au($\sim$ −0.37eV) and $\beta\sqrt{3}$-Au($\sim$ −0.32eV) surfaces, however, seems to be a little bit small to create the $p$-type inversion layer on these surfaces. In addition the amount of the conductivity change of each surface does not proportional to the amounts of their band bendings. Hence it seems that the interpretation of the conductivity change needs more investigation in future.

These tendencies of the BCLS shifting lower $E_B$'s seem to be reasonable considering the stronger electronegativity of Au(2.4 as the Pauling's index) compared to that of Si(1.8). On
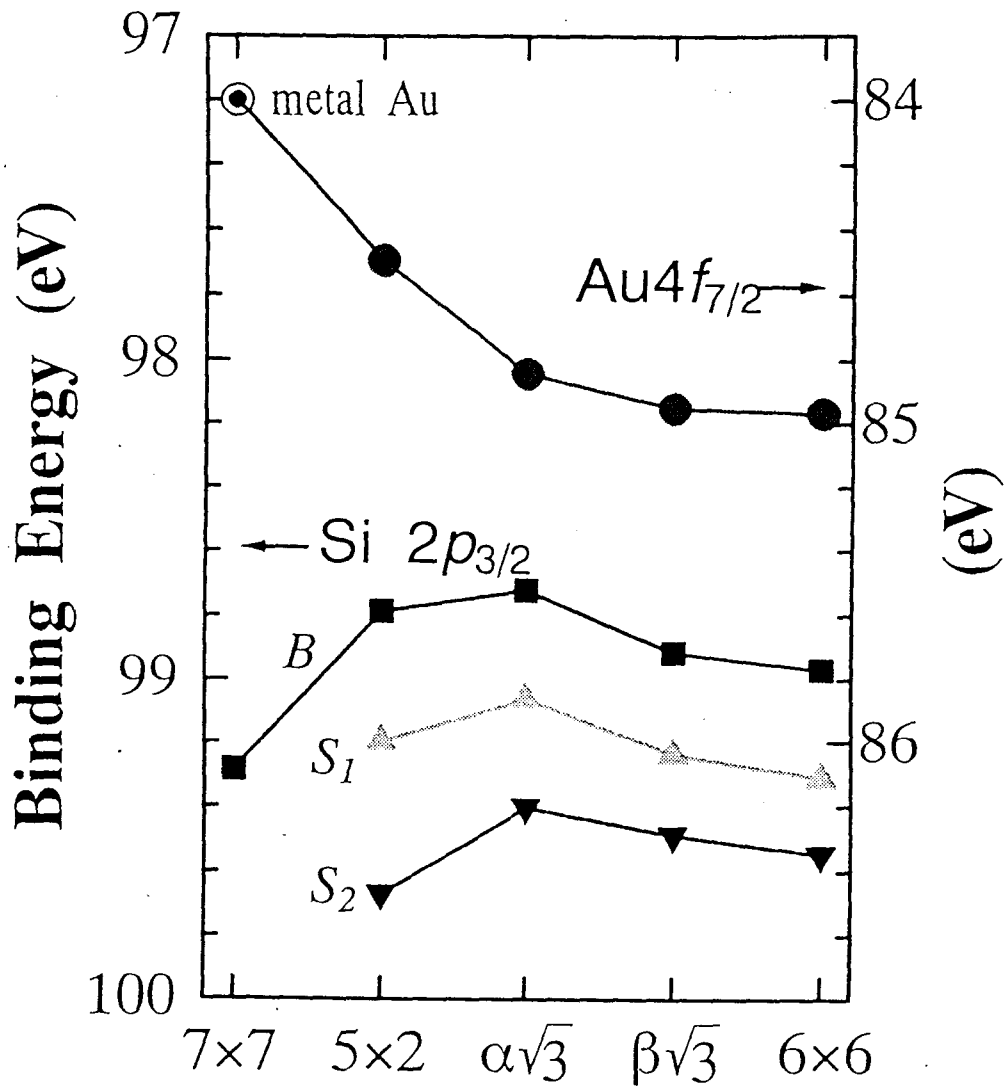
Fig. 6.5: Summary of the core level binding energies of the Si $2p_{3/2}$ and Au $4f_{7/2}$ of each reconstructed surface. The vertical axis at the left- and right-hand sides are the binding energies for Si $2p_{3/2}$ and for Au $4f_{7/2}$, respectively.
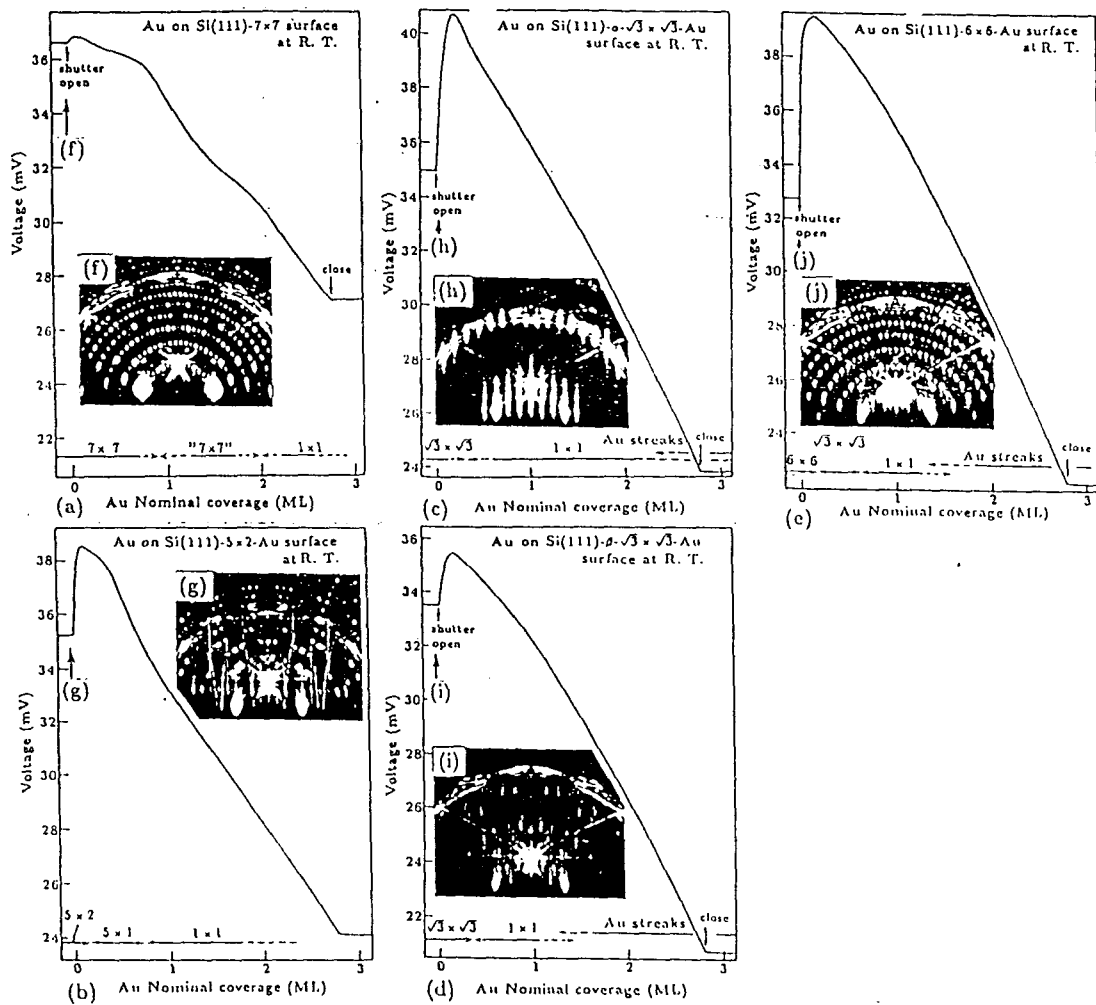
Fig. 6.6: Surface-conductivity changes under depositing gold on Au induced Si(111) reconstructed surfaces from ref.[34]

the reconstructed surfaces, the Fermi level pinning due to the metallic surface state of the 7×7 can vanish since the dangling bonds can bond to Au atoms, and the Fermi level position may easily change. Because of the strong electronegativity of Au, the electrons of the surface region of substrate transfer to Au layer and the valence band of this n-type Si should bend toward the Fermi level. Therefore the VBM will rise toward the Fermi level and the core level of the bulk Si will be pulled up at the region close to the surface.

The smaller amount of the BCLS's on the $\beta$-$\sqrt{3}$ and 6×6-Au surfaces than those on the $\alpha$-$\sqrt{3}$ or the 5×2-Au may seem to be strange. Considering the larger amount of Au on the former surfaces than the latter ones, the BCLS's of the $\beta$-$\sqrt{3}$ and the 6×6-Au surface should be larger than those of the $\alpha$-$\sqrt{3}$ or the 5×2-Au surface. This behavior, however, is similar to the work-function change with respect to alkali atom coverage, which is well explained by the idea of dipole-dipole interaction[35]. Because of the higher densities of Au atoms on the $\beta$-$\sqrt{3}$ and 6×6-Au surfaces the coulomb repulsion forces between electrons of neighboring Au atoms becomes larger on these surfaces than those on the 5×2 or $\alpha$-$\sqrt{3}$-Au surfaces and the charge of Au may retransfer to Si substrate. The energy position of the VBM, however, is strongly affected by the positions of the surface states, especially when the surface state pins the Fermi level. According to the ARPES studies which are discussed in following section(6.3.2) on the $\beta$-$\sqrt{3}$-Au and 6×6-Au surfaces there are metallic surface state and the state may pin the Fermi level positions of these surfaces.

As for the SCLS, each surface component for the reconstructed surfaces shifts to higher binding energies than its bulk component as seen in Fig. 6.4 and Fig. 6.5. These shifts are also natural considering the stronger electronegativity of Au atoms than that of Si as in the case of the BCLS. If the surface components are originated from the surface Si atoms connecting with Au atoms, the valence electrons of Si atoms transfer to the Au atoms because of the stronger electronegativity of Au. Hence the binding energies of the $S1$ and $S2$ become higher than that of the bulk component($B$) since the surface Si atoms have positive charge. This picture of the SCLS's are understood more clearly by comparing the SCLS results of Au/Si reconstructed surfaces with those of aforementioned other surfaces adsorbed by AM or Ag. Figure 6.7 is the summary of the surface core level binding energy shifts from the bulk peaks($\Delta E_B$) of the each surface components($S1$, $S2$ (and $S3$ for 3×1-Rb surface)) of reconstructed surfaces. The abscissa represents the value of the Pauling's electronegativity. As seen in the figure the $\Delta E_B$ of each surface lines almost downward indicating the trend of positively charged Si on the AM adsorbed Si surface and negatively charged Si on the Au adsorbed Si surfaces. The surface adsorbed by Ag shows the small value of $\Delta E_B$ and is consistent with the almost the same electronegativity between Ag(1.9) and Si(1.8). Thus we can roughly understand the tendency of the SCLS by the difference of the electronegativity of between each atoms.

Regarding the shift of the Au $4f$ state, simple consideration of the charge transfer from Si atoms to the Au atoms makes us expect that the binding energies of the Au $4f_{7/2}$ shift to lower binding energies than that of pure Au. Seeing Fig. 6.5, however, the Au $4f_{7/2}$ of reconstructed surfaces shifts to higher binding energies than that of the metal Au. Similar results of the shifts to higher binding energies of the Au $4f_{7/2}$ level reacting with Si atoms has been reported by several groups[36, 37]. Figure 6.8 illustrated the explanation of this abnormal shift of the Au $4f$ electrons which are proposed by Lu, Sham and Norton[36]. Firstly, due to their stronger electronegativity, gold receives electrons from Si valence electron and put them into $6s$ orbital. On the other hand, to bond with Si atom an $s$-$d$ hybridization is formed and gold atom loses its $5d$ electrons. Since the coulomb interaction $F^0(4f,\text{cond})$ between the Au $4f$ and the $6s$ conduction electrons is much smaller than $F^0(4f,5d)$ between

88
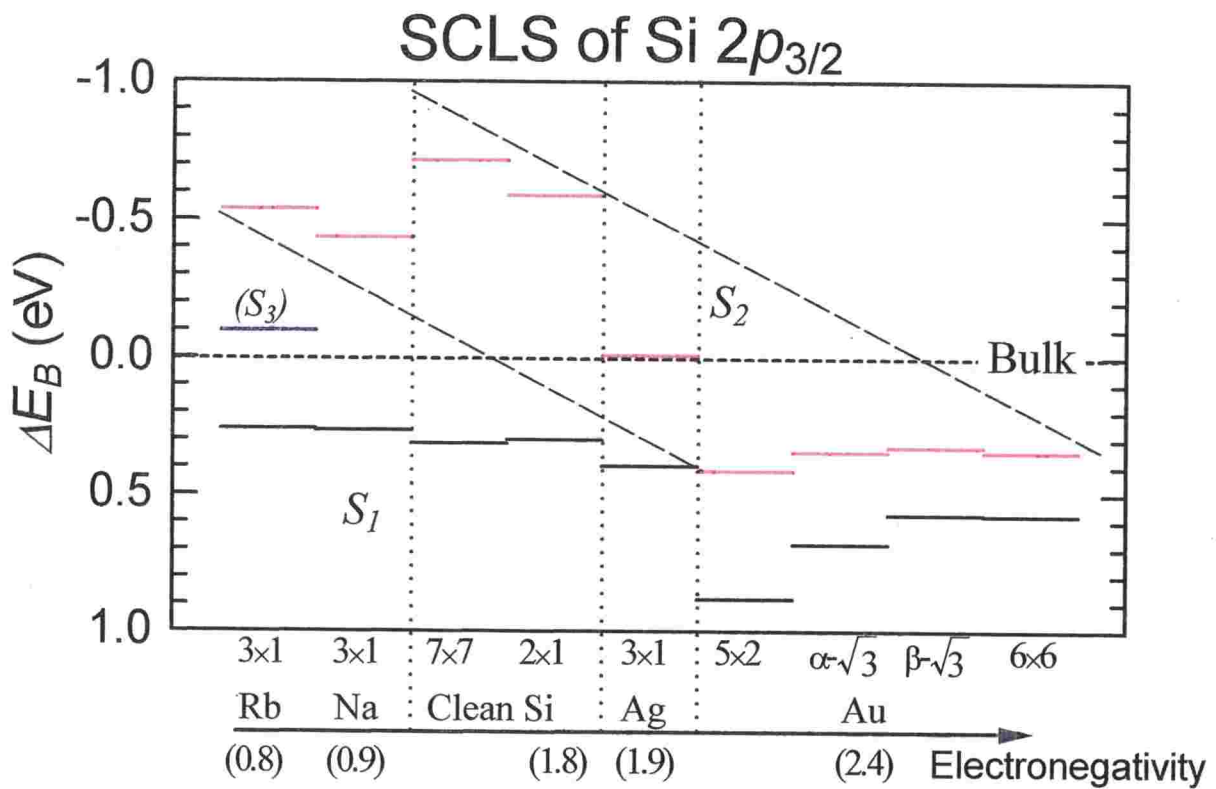
Fig. 6.7: Summary of the surface-core-level binding-energy shifts from the bulk peaks($\Delta E_B$) of each surface components($S1$, $S2$ (and $S3$ for 3×1-Rb surface)) of reconstructed surfaces. The abscissa very roughly corresponds to the value of the Pauling's electronegativity.(the numbers in the parentheses)

the $4f$ and localized $5d$ electrons by about 3eV, the core level of the $4f$ electron consequently shift to higher binding energies in spite of net electron increase on Au. Recent total energy
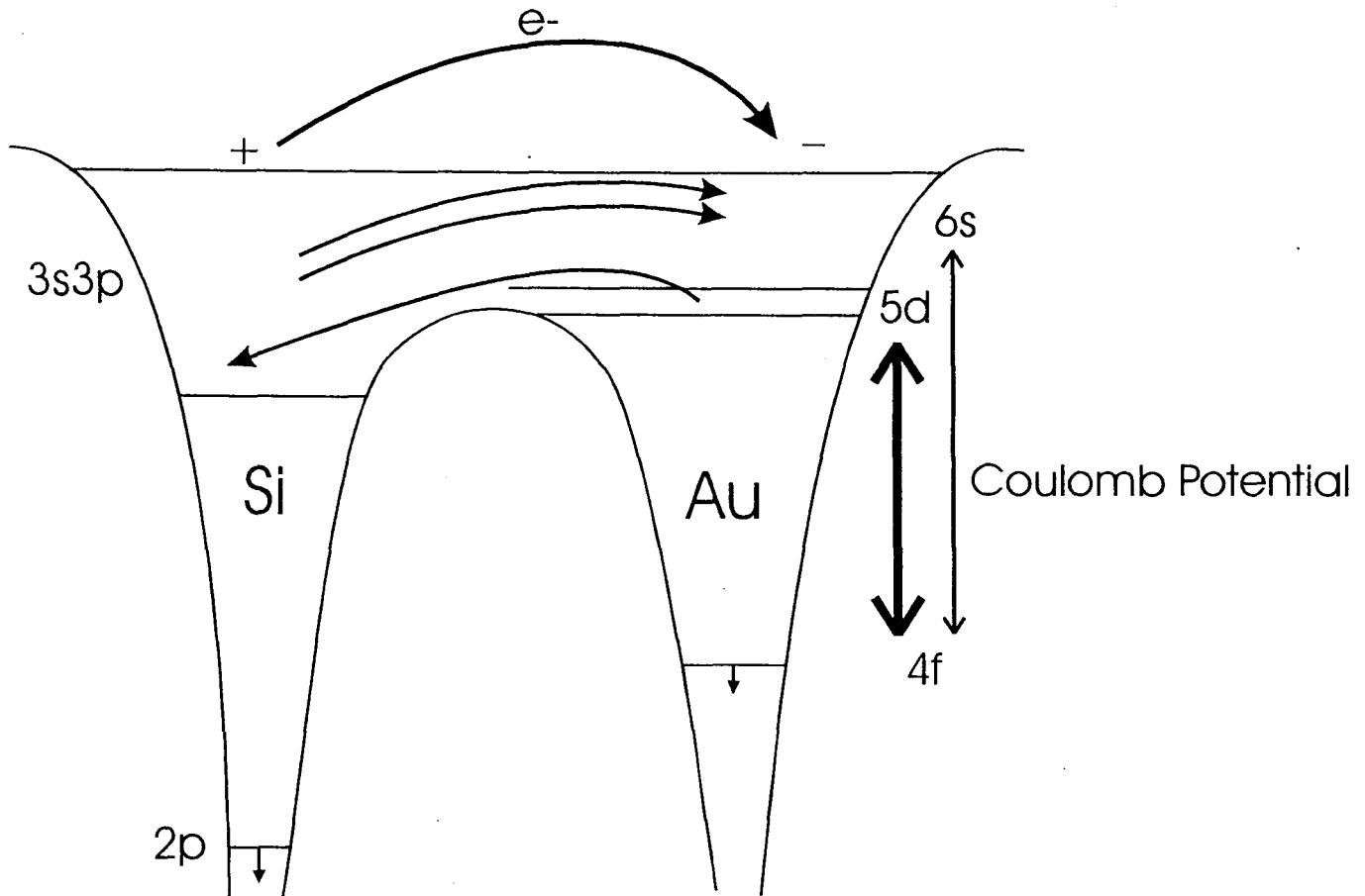


Fig. 6.8: Schematic diagram of the electron redistribution at Au/Si interface explained by Lu, Shum and Norton[36]

cluster calculation[38] and the surface sensitive X-ray diffraction study[39] of the $\sqrt{3}$-Au system, however, suggested a charge transfer from gold to silicon atoms and this problem may require further investigation in future.

*Geometric structure*

As mentioned already, the characteristic Si $2p$ core spectrum of each surface reconstruction is the convolution of some SCLS peaks originating from atoms in different atomic environment.

Using the layer attenuation model as I mentioned in section 2.2, we roughly estimated the number of the surface Si atoms contributing to the surface components from the fitting results of these Au/Si(111) surfaces. The estimated values of the surface components (numbers of the atoms in each unit cell of the reconstructed surfaces) are summarized in Table 6.3.

As seen in the table, the numbers of the surface Si atoms on each reconstruction in each unit cell is about 11.3 and 1.2 for 5×2-Au, 3.5 and 1.1 for $\alpha$-$\sqrt{3}$-Au, 2.4 and 1.9 for $\beta$-$\sqrt{3}$-Au and 30.6 and 20.9 for 6×6-Au surfaces.

Table 6.3: Numbers of surface Si atoms in each unit cell estimated by the *layer attenuation model* The numbers in parentheses for (e) are the amount of the surface Si atoms in a $\sqrt{3} \times \sqrt{3}$ unit cell.

| | | (a) 7×7 | (b) 5×2-Au | (c) $\alpha$-$\sqrt{3}$-Au | (d) $\beta$-$\sqrt{3}$-Au | (e) 6×6-Au |
|---|---|---|---|---|---|---|
| Number of surface atoms | | | | | | |
| Total of Surface atoms($S_1 + S_2$) | (ML) | 1.06 | 1.25 | 1.54 | 1.42 | 1.43 |
| | (atoms/unit cell) | 52.0 | 12.5 | 4.6 | 4.3 | 51.5(4.3) |
| $S_1$ component | (ML) | 0.95 | 1.13 | 1.16 | 0.80 | 0.85 |
| | (atoms/unit cell) | 46.6 | 11.3 | 3.5 | 2.4 | 30.6(2.6) |
| $S_2$ component | (ML) | 0.11 | 0.12 | 0.38 | 0.62 | 0.58 |
| | (atoms/unit cell) | 5.4 | 1.2 | 1.1 | 1.9 | 20.9(1.7) |

— *5×2-Au surface*

In Fig. 6.9 I show some models of the 5×2 surface so far proposed by several groups[20, 21, 22]. The crosses, small empty circles, and large empty circles represent the 4th, 2nd and 1st layer Si atoms of the ideal Si(111) surface. The filled circles represent the positions of the gold atoms and large shaded ones are so called "protrusions"(labeled P). Parallelograms are the unit cells of the 5×2 surfaces. These models are based on the idea of simple adsorption of Au onto the ideal Si(111) surface. The models (A1) and (A2) were proposed by reflection high energy electron diffraction (RHEED) study of the Si(111)5×2-Au surface and the surface changed by Li adsorption[21]. From the positions of the bright spots of the filled state STM image the models (B)[20] and (C1)[22] were proposed. In the model (C1) there are also some small shaded circles which represent the positions of the additional faint spots of the STM image. It has not been clarified that these additional spots are due to Au atoms or Si atoms yet. We also show the model (C2)[22] as the variation of (C1) changing the relative position to the substrate, which corresponds to the case that the first double layer of Si atoms are removed when the 5×2 surface is formed. As seen in Fig. 6.9, the Au coverage of the model (A1),(A2) and (B) is 0.4ML and that of (C) is 0.5ML when we neglect the protrusions and small shaded circles of (C). When we consider the small shaded circles of (C) as Au atoms, the coverage should be 0.7ML. According to the STM study[20] each protrusion is separated by $(4+2n)a$ along the $[1\bar{1}0]$ direction(where $a$ and $n$ are the lattice constant and an integer). Therefore if the protrusions are Au atoms, the coverages of (A1),(A2),(B) and (C) are less than 0.45ML and 0.55ML(or 0.75ML for the case that the small shaded circles are Au atoms) respectively.

In the bottom of Table6.1 we presented the estimated coverages of the other reconstructed surfaces which are derived from the ratio of the deposited values and the gold coverages of the 5×2-Au surface estimated above. The coverages counting the protrusions as gold are also indicated in the parentheses. When we consider the $\alpha$-$\sqrt{3}$-Au is covered by the well ordered $\sqrt{3}$ structure, the coverage should be the integer multiple of 1/3ML. Hence, the coverages of 1.60 and 1.71ML for the $\alpha$-$\sqrt{3}$-Au, which are derived from the coverages of 0.7 and 0.75ML for the 5×2-Au seems to be unreasonable. The coverages of 1.14 and 1.26ML which are derived from the 0.50 and 0.55ML for the 5×2-Au, are also a little bit too large. It seems that the coverage of 0.4(0.45)ML for the 5×2 surface leads to the reasonable coverages of about 0.91(1.03)ML for the $\alpha$-$\sqrt{3}$-Au surface. In this case, the coverage of the 1.20(1.35)ML for the $\beta$-$\sqrt{3}$-Au, and 6×6-Au surfaces is almost the same as many other
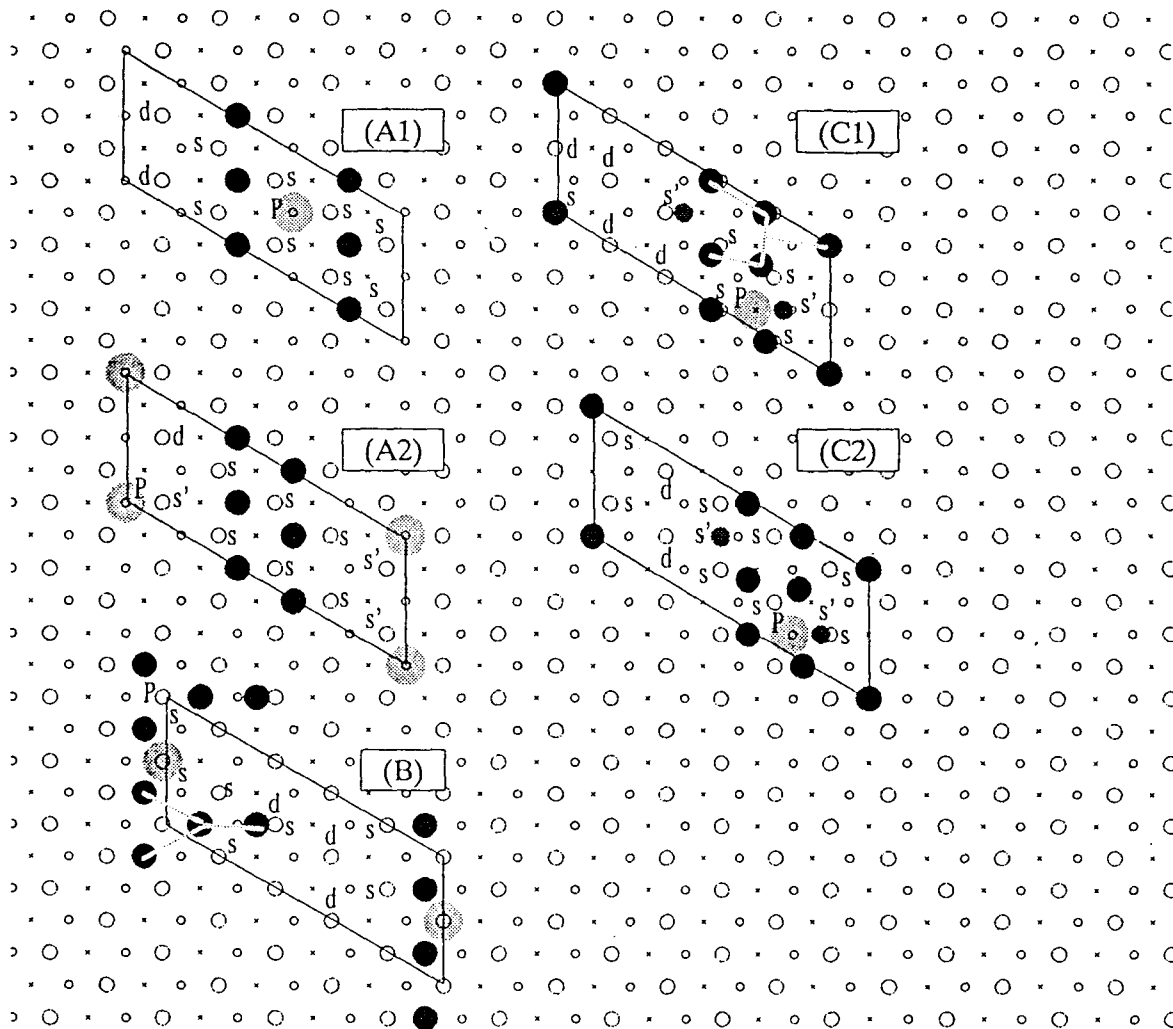
Fig. 6.9: Representative models of the Si(111)5×2-Au surface. The crosses, small empty circles, and large empty circles represent the 4th, 2nd and 1st layer Si atoms of the ideal Si(111) surface. The filled circles represent the positions of the gold atoms and large shaded ones are so called "protrusions"(labeled P). Parallelograms are the unit cells of the 5×2 surface.

92

experimental results(1.0ML[11],1.1ML[10],1.4ML[12, 40] and 1.5ML[13]). Therefore we think that the coverages of the 5×2, $\alpha$-$\sqrt{3}$, and $\beta$-$\sqrt{3}$ and 6×6 are 0.4~0.45ML, 0.9~1ML, and 1.2~1.35ML respectively, and the small shaded circles of the model(C) are not gold atoms.

Our SCLS results imply the existence of at least two kinds of surface Si atoms influenced by Au atoms on the 5×2-Au surface. As can be seen in Fig. 6.4(b) one of the surface components, $S2$, has very small intensity relative to that of $S1$. The SCLS from the bulk core level of $S2$ is larger than that of $S1$. Thus on this surface there are large amount of surface atoms which are influenced by Au atoms corresponding to the $S1$ component and a small amount of surface atoms which are more strongly influenced by Au atoms corresponding to $S2$ component. Considering the small amount of gold and large number of surface atoms corresponding to $S1$ the Au on the 5×2 surface should be sitting at the site where one Au atoms can influence as many Si atoms as possible like a $T_4$ or $H_3$ site. From the quantitative analysis the numbers of these two kinds of surface Si atoms are estimated as about 11 and 1 in the 5×2 unit cell. Supposing simply that only the surface Si atoms bound to the adsorbed Au atoms are influenced by Au, only the atoms labeled "s" are the Si atoms which contribute to the $S1$ or $S2$ component. The numbers of "s" atoms are 8,6,7,5 and 8 for the model (A1),(A2),(B),(C1) and (C2), respectively. The numbers for (A1) or (C2) are comparable to the estimated number of surface Si atoms of $S1$ component. Assuming the small shaded circles("s'") of (C1) and (C2) are surface Si atoms contributing to the surface component, the numbers of surface Si atoms of (C1) and (C2) are 7 and 10. In this case the number of (C2) is much closer to the experimental results of 11. The small intensity ratio of the $S2$ component($S2/S1$=1/11) can be explained by adopting the idea that the $S2$ component is originating from the surface Si atoms under the Au protrusions or from the Si protrusions themselves. We can easily notice, however, that among the "s" atoms, there are some groups of atoms in different conditions. In the model (A2), for example, the first group of "s" atoms neighbors to only one Au atom and the second group neighbors to two Au atoms and the third group is surrounded by three Au atoms. The SCLS of these different conditioned groups would be different each other. Besides the "s" atoms, the core levels of the Si atoms labeled "d" (with dangling bonds) and labeled "s'" also would shift differently. Very recently other surface structure for the 5×2 was proposed[27] by high resolution electron microscopy and heavy-atom holography study. Figure6.10 is the schematic view of the model. As seen in the figure the number of the surface Si atoms surrounding Au atoms may be about 10(checked by arrows) and if we consider the $S2$ is silicon adatom from the peculiarity the small intensity of the $S2$ is also consistent. However, the surface structure is more complex than previous ones and also would have many kinds of SCLS corresponding to different surface Si atoms. Although the finite energy resolution of the present SCLS measurement may hide the subtle shifts of many surface components, our SCLS results cannot be explained completely by these previously proposed models. The more high-resolution experiment or some theoretical suggestion is required.

## — $\sqrt{3} \times \sqrt{3}$-Au and 6×6-Au surfaces

As mentioned already the SCLS of $S1$ and $S2$ components of $\alpha$- and $\beta$-$\sqrt{3}$-Au surfaces are different from each other especially for the $S2$ component. Contrarily, the SCLS of the $\beta$-$\sqrt{3}$-Au is almost the same as that of the 6×6-Au. Thus the atomic structure of the $\beta$-$\sqrt{3}$-Au is considered to be very similar to that of the 6×6-Au, but different from that of the $\alpha$-$\sqrt{3}$-Au, and we need to distinguish these two $\sqrt{3}$ structures as different structures.

Plenty of models have been proposed so far for the $\sqrt{3}$-Au surface. We show some

a

b

● Gold
◔ Silicon Between Gold (MTL Like Sites)
◑ First Layer Silicon
○ Second Layer Silicon
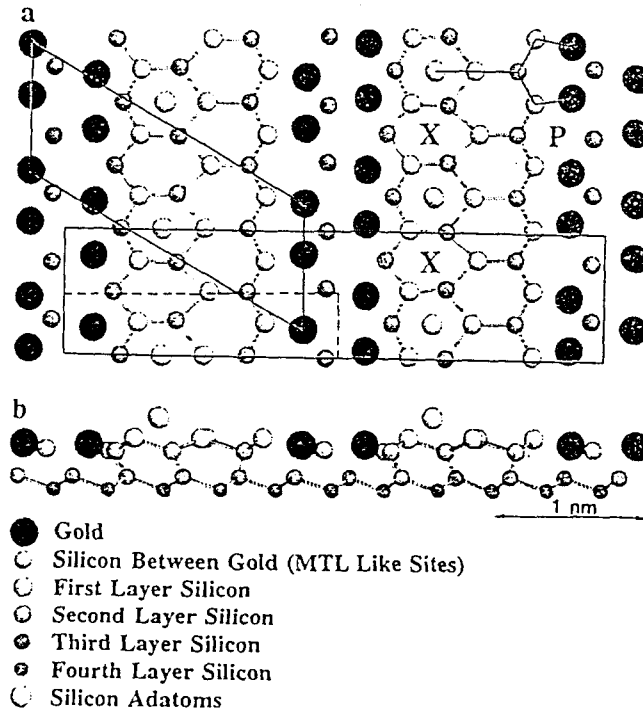◉ Third Layer Silicon
◐ Fourth Layer Silicon
◌ Silicon Adatoms

Fig. 6.10: Surface structure model of the 5×2-Au proposed by Marks and Plass[27]

representative models in Fig. 6.11. Each mark has the same meaning as that in Fig. 6.9. The double circles are the additional surface Si atoms above the 1st Si layer. The parallelograms are the unit cells of the $\sqrt{3} \times \sqrt{3}$ surface. These models are (A)Honeycomb[10], (A')Centered honeycomb[10], (B)Modified Triplet Coplanar(MTC)[13], (C)Milk stool[41], (D)Trimer[18], (E)Honeycomb Chained Trimer(HCT)[7] and (F)conjugate HCT(CHCT-1) model[14]. Among these models only the model (A) has a 2/3ML of Au coverage and the others have a 1ML coverage.

At first we consider the case that the $\alpha$-$\sqrt{3}$-Au surface is homogeneous. That is the size of domain size of the surface is very large and the influence of the domain wall region can be ignored. Assuming the homogeneous surface structure for the $\alpha$-$\sqrt{3}$-Au surface, two surface components of Fig. 6.4(b) correspond to the two different surface Si atoms in a $\sqrt{3} \times \sqrt{3}$ unit cell. The numbers of Si atoms corresponding to each component are estimated as about 3 and 1 for $S1$ and $S2$, respectively, as shown in Table 6.3. The models (A),(A'),(C) and (D), are considered to have two kinds of the surface Si atoms; one of which is connecting with Au atoms and the other is connecting with those Si atoms and both the number of these atoms are three. The model(B) is also considered to have two kinds of surface Si atoms; one of which is connecting with Au atom and the other has a dangling bond. The numbers of these two types of surface Si atoms are, however, not 3 and 1 but 3 and 2 in the unit cell. Therefore, it seems that these models cannot explain the SCLS results successfully.

The HCT type model ((E) and (F)) is the most widely supported model for the $\sqrt{3} \times \sqrt{3}$ surface, recently. The HCT-1 model(E) is considered to be the correct model of the $\sqrt{3} \times \sqrt{3}$-Ag surface now a days[7]. On the other hand, the CHCT-1 structure is suggested that the most stable structure among the so far proposed $\sqrt{3} \times \sqrt{3}$-Au surface with 1ML coverage
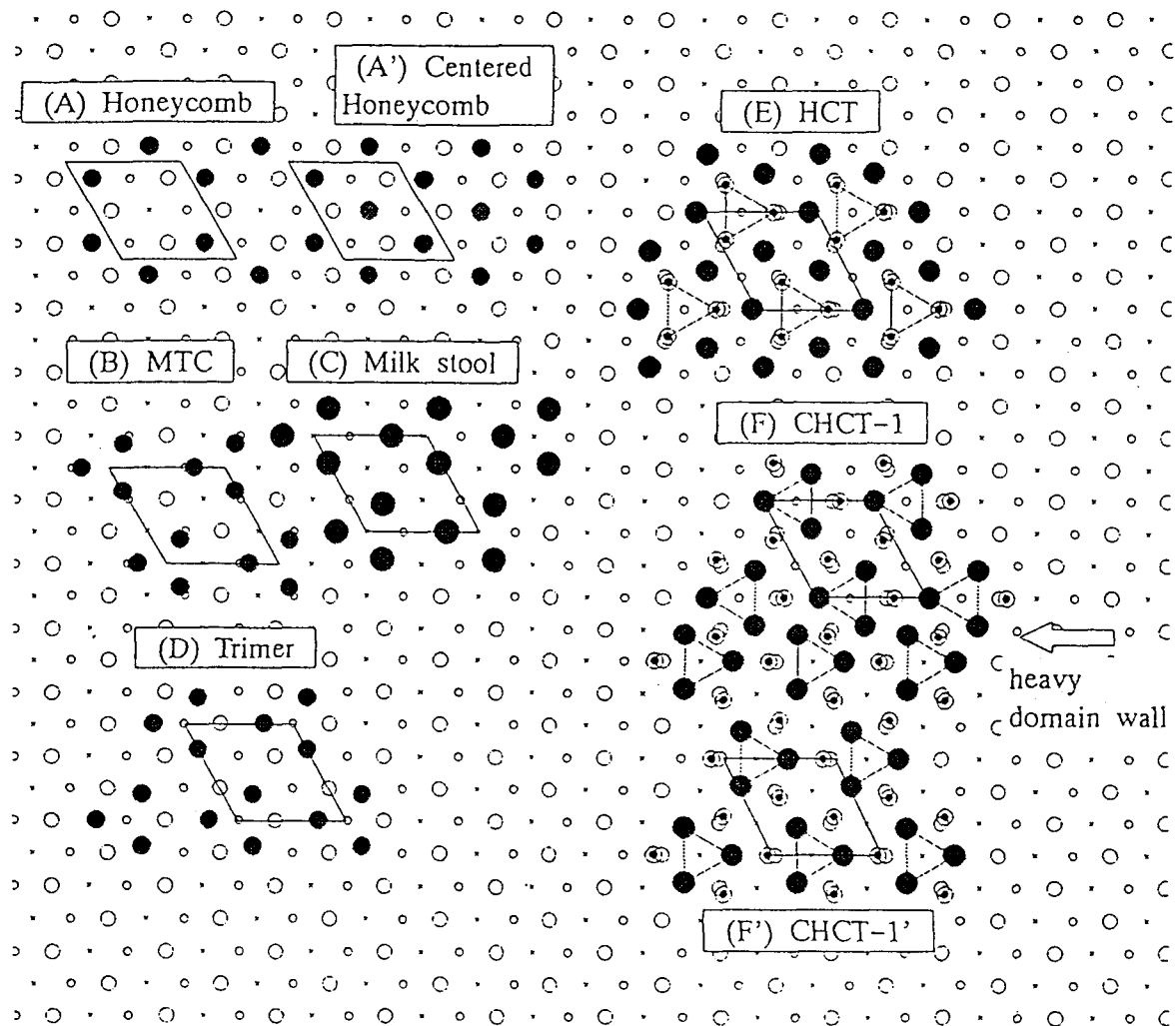
94

Fig. 6.11: Representative models of the Si(111)$\sqrt{3} \times \sqrt{3}$-Au surface. Each mark has the same meaning as that in Fig. 6.9. The double circles are the additional surface Si atoms above the 1st Si layer. Parallelograms are the unit cells of the $\sqrt{3} \times \sqrt{3}$ surfaces.

by theoretical calculations[14]. These two structures are very similar, and from only the SCLS measurement we cannot discuss about the difference between them. These models have also two kinds of surface Si atoms. One is the 1st layer surface Si atoms(double circles) connecting with Au atoms and the other is the 2nd layer Si atoms connecting with the 1st layer surface Si atoms. In these cases, the ratio of the $S1$ to $S2$ would be 3:3 and inconsistent with the experimental results of 3:1.

According to the SCLS measurement of the $\sqrt{3} \times \sqrt{3}$-Ag surface[42] there are three surface components; two with higher binding energies and one with lower binding energy than bulk component. Herman $et\ al.$ assigned that the lower binding energy component as the domain boundary Si and the highest binding energy component as the 2nd layer Si atoms and the other component as the 1st layer Si connecting with Ag of the HCT-1 model. Neglecting the domain boundary state of the $\sqrt{3}$-Ag surface, the directions of the SCLS and intensity feature of the two components of the $\sqrt{3}$-Ag are qualitatively consistent with our results of $\sqrt{3}$-Au. They explained the smaller intensity of the 2nd layer Si by the attenuation effect of the photoemission intensity. In the HCT type models, the difference of the height between 1st and 2nd layer Si are relatively larger than those of (A),(A'),(B),(C) and (D), and we may have to consider the attenuation effect of the 2nd layered surface Si atoms. Assuming that the $S2$ is the attenuated component and considering the attenuation effect, the amount of atoms corresponding to $S2$ was adjusted as 0.66ML(=1.98 atoms in the unit cell) by using the mean-free-path of 3.9Åand the distance between 1st and 2nd layer of 2.16Åfor the CHCT-1 model. Even if we consider the attenuation effect, however, the $S1 : S2$ is 3:2 and it seems that the SCLS results are not completely explained by these models. The larger SCLS of $S2$ than $S1$ is also strange because charge transfer of $S1$ should be larger than $S2$ if we consider the $S1$ as the 1st layer surface Si atoms connecting with Au directly.

Another idea of the surface structure of the $\sqrt{3} \times \sqrt{3}$-Au surface is the mixed structure of the different structural units. Huang $et\ al.$ proposed a model of the mixture of the (A) honeycomb and (A')centered honeycomb models named "mixed honeycomb model" for the $\sqrt{3} \times \sqrt{3}$-Au surface from their ICISS measurement[10]. The intensity ratio of $S1:S2 \simeq 3:1$ is roughly consistent with the ratio of the mixed honeycomb model which consists of 70% of honeycomb and 30% of centered honeycomb structures[10] when we consider the $S1$ and $S2$ are due to the surface Si atoms of the honeycomb and the centered honeycomb structure. The our results of intensity ratio(0.85:0.58) of $S1$ and $S2$ for the 6×6 surface, however, is not consistent with their idea of mixed honeycomb model(1:3) for the 6×6 structure[10]. Hence when we consider the homogeneous surface structure neglecting the domain wall effect we cannot explain the SCLS results of $\alpha$-$\sqrt{3}$-Au surface completely by any so far proposed models.

Another possible interpretation of the $\sqrt{3} \times \sqrt{3}$ surface with two surface components is that one component originates from the Si atoms forming domain walls(assuming to be $S2$) and the other is those in the domain(assuming to be $S1$). According to the STM measurement[11] on the $\sqrt{3}$-Au surface there are not a little domain walls. In this case the surface components inside the uniform domain($S1$) are only one and we cannot deny the so far proposed models, (A)~(F), assuming the surface contribution is only from the top most Si layer. Considering on the basis of this interpretation, the energy difference of the $S2$ between $\alpha$- and $\beta$-$\sqrt{3}$-Au may suggest the difference of domain wall structures between these two surfaces and we cannot conclude that the structures inside the each domain($S1$) are different. Almost the same energy shifts of $S1$ of each surfaces is also consistent with the interpretation. Nogami $et\ al.$ observed by STM[11] that the phase transition from the $\sqrt{3} \times \sqrt{3}$ to 6×6 surface occurs by ordering the domain walls with increasing the coverage of

Au. The increase of the relative intensity of the $S2$ comparing to $S1$ on the $\beta$-$\sqrt{3}$ and 6×6 surfaces from the $\alpha$-$\sqrt{3}$ surface is consistent with the STM observation. The slight change of the intensity ratio between $\beta$-$\sqrt{3}$-Au and 6×6-Au may indicate the change of the ratio of the domain walls because of the ordering of the domain walls. Recently, Falta et al.[40] studied the domain wall structure of the $\sqrt{3} \times \sqrt{3}$ surface by their STM and X-ray standing wave(XSW) measurements. They explained the domain wall structure by considering two types of the CHCT-1 model. One has normal Au trimer sitting on the $H_3$ site and the other has that sitting on $T_4$ site as shown in (F')CHCT-1' in Fig. 6.11. According to the total energy calculation[14] the energy difference between CHCT-1 and CHCT-1' type surfaces is so small that the co-existence of these two types of the trimers is not strange. Since the distance between Au(filled circles) and the topmost Si atoms(double circles) and their configuration in the (F) and (F') models are almost the same as seen in Fig. 6.11, the SCLSs of both surfaces are considered to be very similar. At the domain wall the density of the Au atom is higher than that inside the walls as seen in the figure, and the SCLS of the Si atom at the wall will be larger than those inside the wall. The concentration of Au at the domain wall(heavy domain wall) has been suggested by the STM observation[40] and the estimated coverage of exceeding 1ML is reasonable because the coverage of the heavy domain wall is 3/2ML.

## 6.3.2 ARPES of Si(111)5×2(5×1), $\alpha$-$\sqrt{3}$, and $\beta$-$\sqrt{3}$ and 6×6-Au surfaces

Figures 6.12(a) to 6.15(d) show the typical ARPES spectra of the 5×2, $\alpha$-$\sqrt{3}$, $\beta$-$\sqrt{3}$ and 6×6 surfaces.

The most prominent peaks and shoulders in every spectrum at $E_B$ of 4eV~8eV are Au $5d$ states and we labeled them as **A, B, C, C', C", D** and **D'**. The $E_B$'s of **A** and **C** states at $\bar{\Gamma}$ are about 4.2 and 6.2, 4.35 and 6.8, 4.3 and 7.1, and 4.3 and 7.1eV for 5×2 , $\alpha$-$\sqrt{3}$ , $\beta$-$\sqrt{3}$ , and 6×6 surfaces. These values for $\alpha$-$\sqrt{3}$ surface is comparable to Houzay's measurement(4.5 and 6.9eV)[29] though the energies are shifted from our data, but little bit different from Karlsson's one(4.8 and 6.8eV)[5]. Our data and Collin's data(4.2 and 6.0eV)[31] for 5×2 surface is also in good agreement. In the region of lower $E_B$'s than 4eV there are some other peaks which are thought to be the Au $6s$ and Si $3s3p$ bonding states and labeled as **E, V, S, S', S"** and **s**.

To easily understand the dispersion features we made band maps from the spectra and represented in Figs. 6.16to 6.19. We determined the peak and shoulders position precisely by referring the second derivative spectrum of each spectrum. The positions which we determined are ticked in Fig.2. In this procedure making band maps we used the values of 5.1, 5.0, 4.9 and 4.9eV as the work-functions of 5×2 , $\alpha$-$\sqrt{3}$ , $\beta$-$\sqrt{3}$ , and 6×6 surfaces which were estimated from the cut off energy of secondly electrons.

The filled circles represent the data point and their sizes in three grade indicate the intensities of peaks and shoulders. We indicated the edges of the bulk band projection[43] by solid curves.

The valence band maximum(VBM) of the projection of each reconstructed surfaces were shifted by −0.50, −0.57, −0.37, and −0.32eV for 5×2, $\alpha$-$\sqrt{3}$, $\beta$-$\sqrt{3}$, 6×6 from the VBM of 7×7 surface referring to the values of the aforementioned bulk core level shifts.

Seeing these band maps or spectra the **A** states have relatively small dispersions, 0.2, 0.25, 0.3, and 0.45 for 5×2 , $\alpha$-$\sqrt{3}$ , $\beta$-$\sqrt{3}$ , and 6×6 surfaces and are considered to be the non-bonding Au $5d$ state. This state seems to accompany relatively weak states labeled **B**
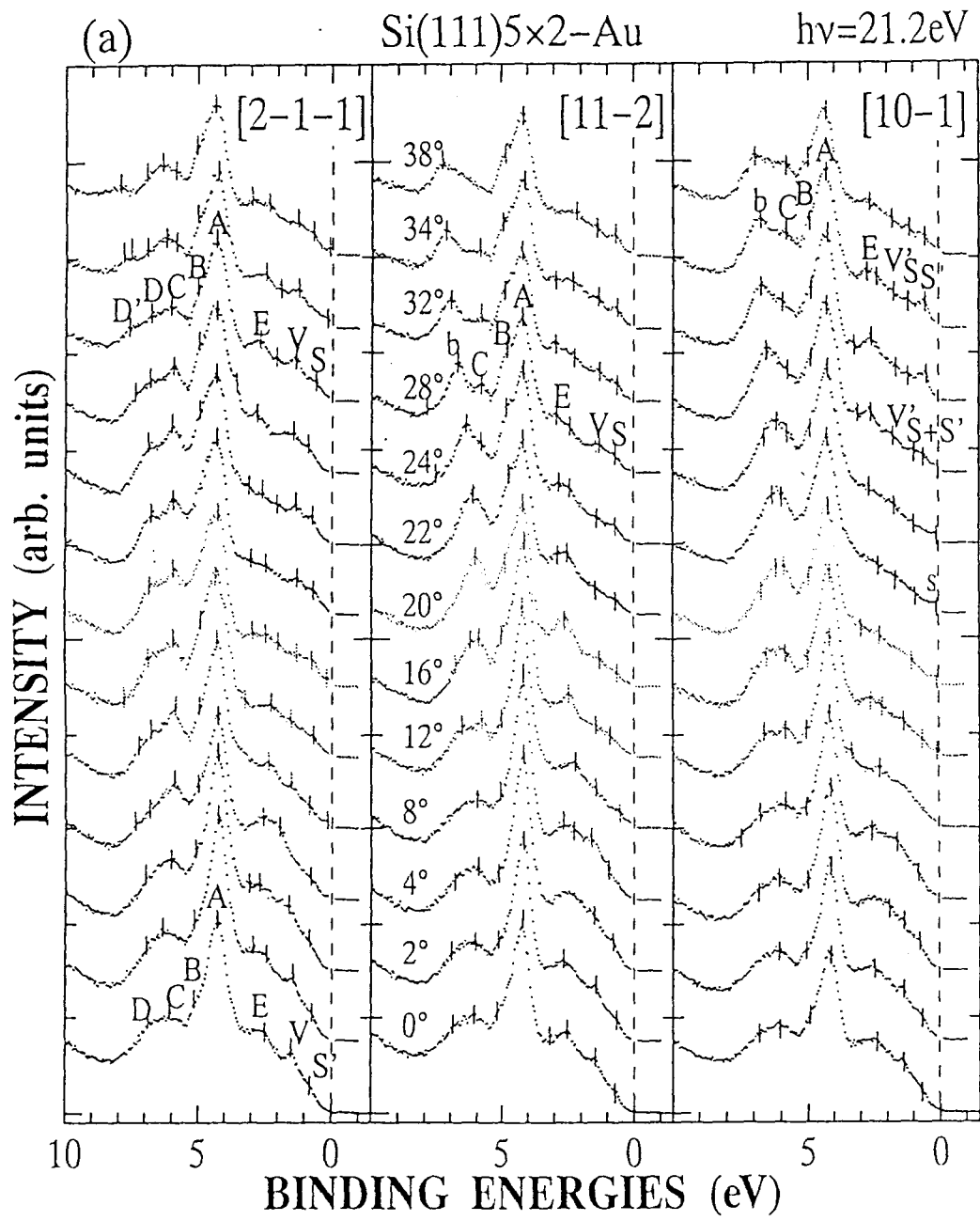
Fig. 6.12: Typical ARPES spectra of the Si(111)5×2 surface

(b)　　　　Si(111)α–√3×√3–Au　　　hν=21.2eV
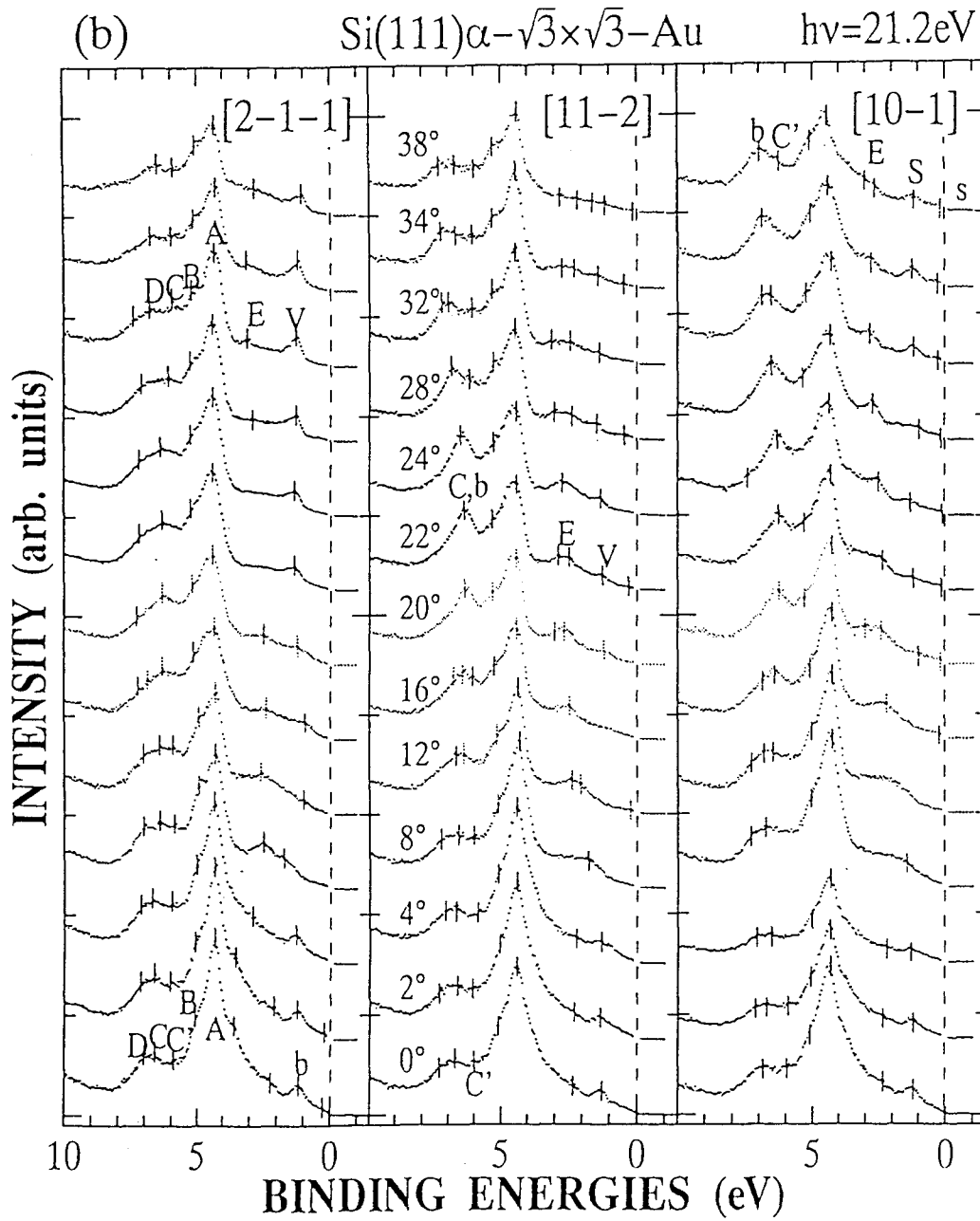


Fig. 6.13: Typical ARPES spectra of the Si(111)α-√3-Au surface

Fig. 6.14: Typical ARPES spectra of the Si(111)$\beta$-$\sqrt{3}$-Au surface
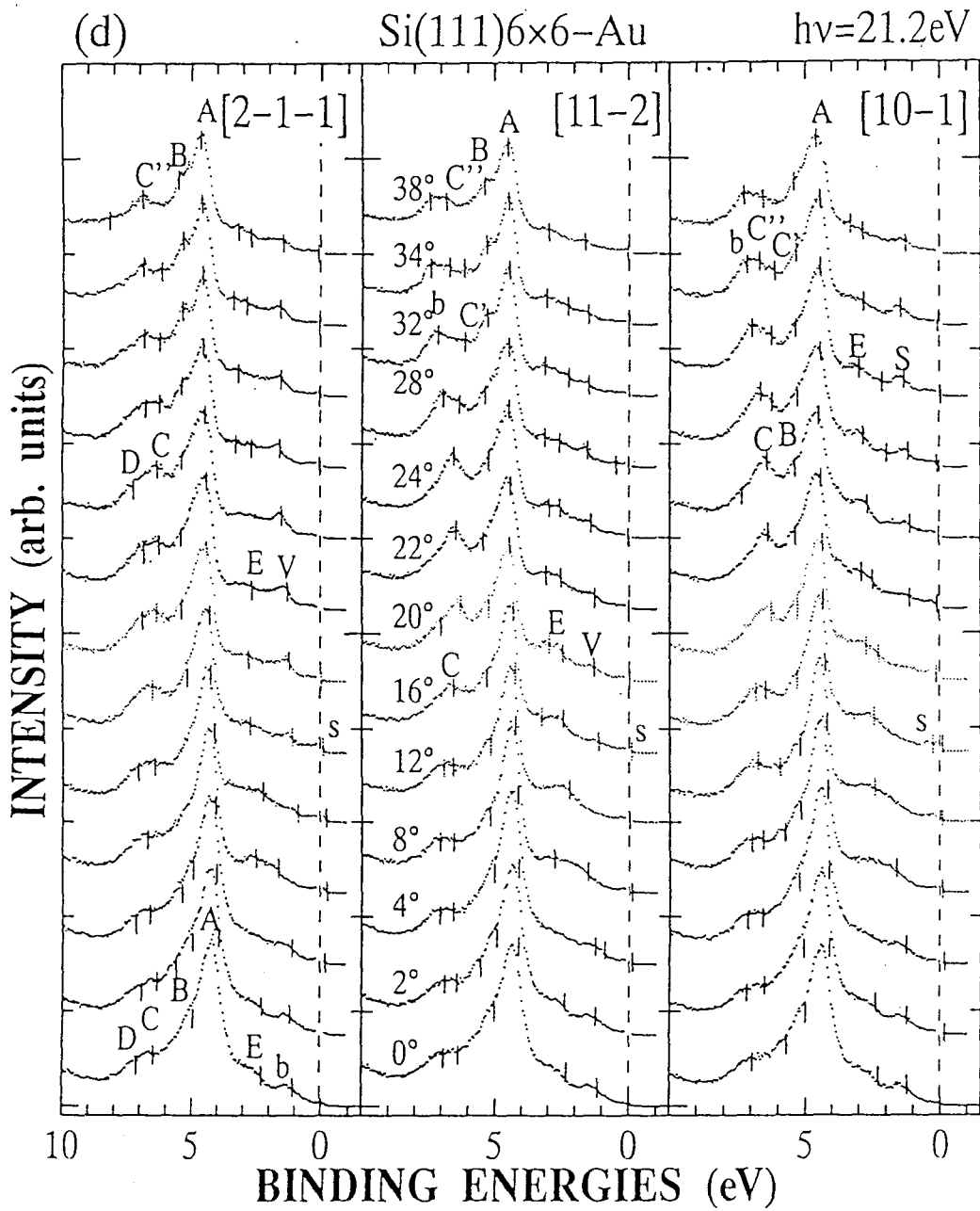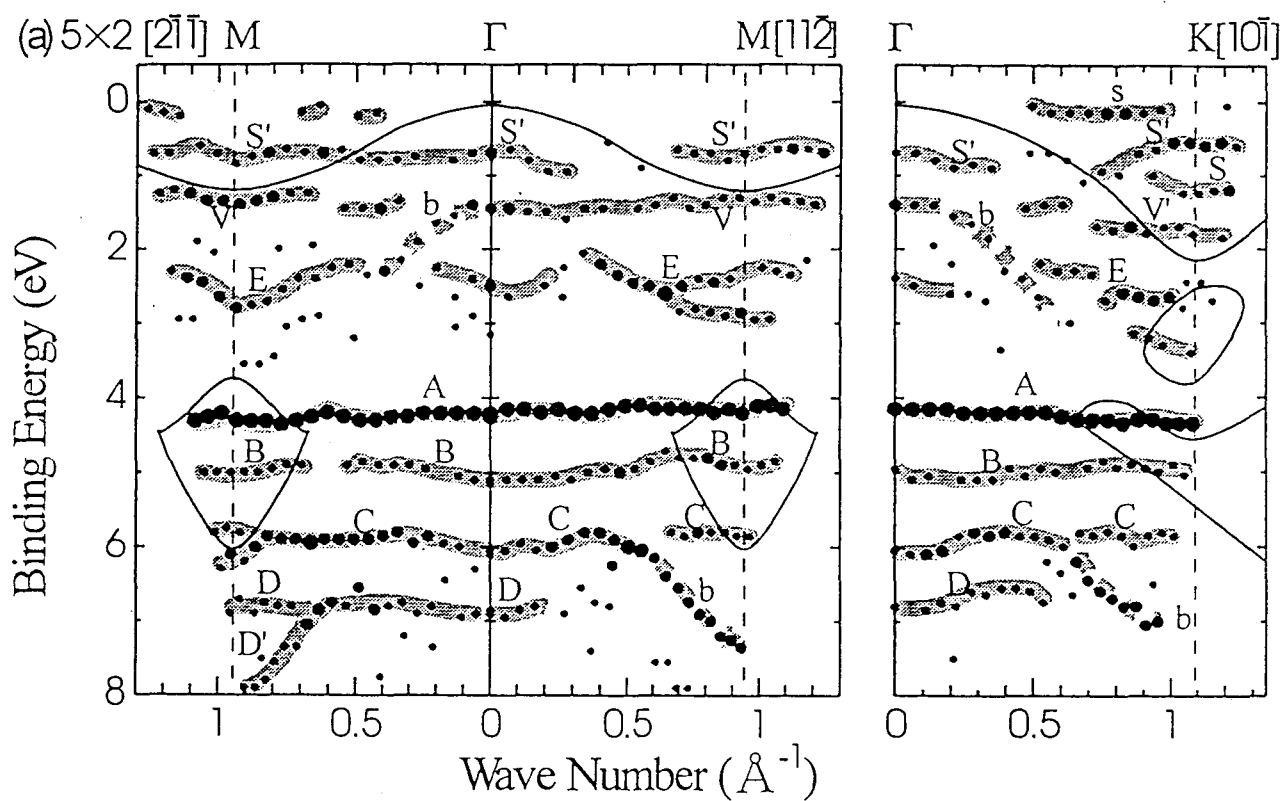
Fig. 6.15: Typical ARPES spectra of the Si(111)6×6-Au surface

Fig. 6.16: The band map of the Si(111)5×2-Au surface measured at hν=21.2eV

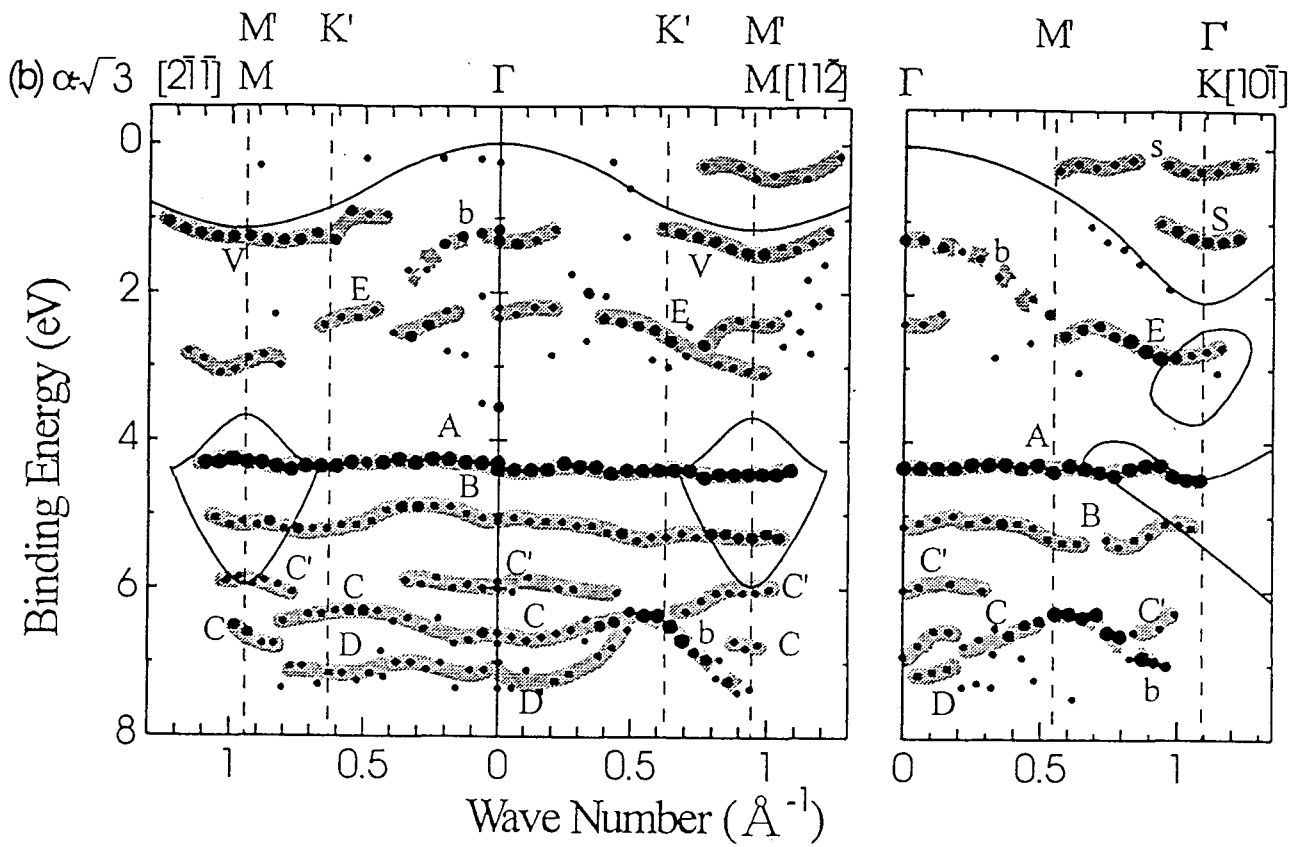Fig. 6.17: The band map of the $\alpha$-$\sqrt{3}$ surface measured at h$\nu$=21.2eV
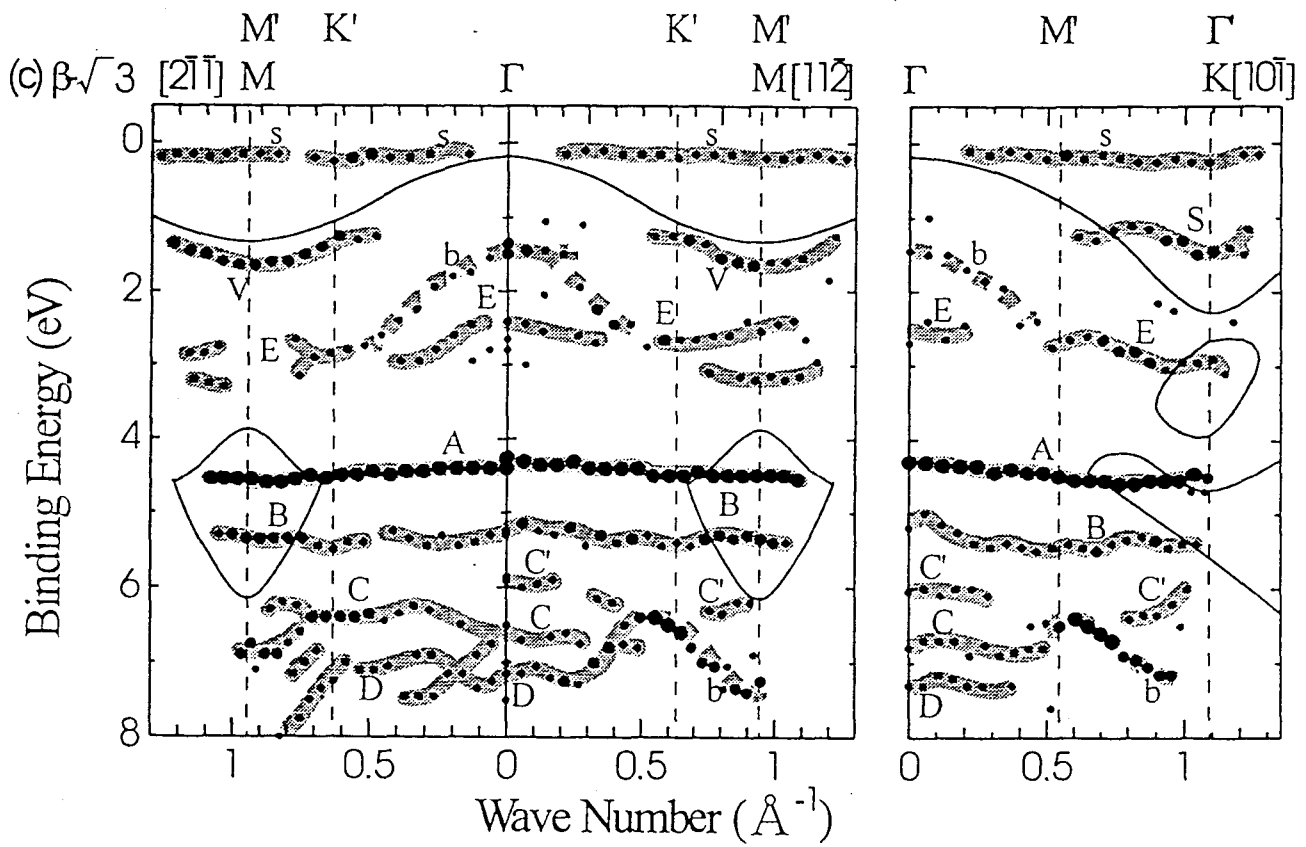
Fig. 6.18: The band map of the $\beta$-$\sqrt{3}$-Au surface measured at $h\nu$=21.2eV
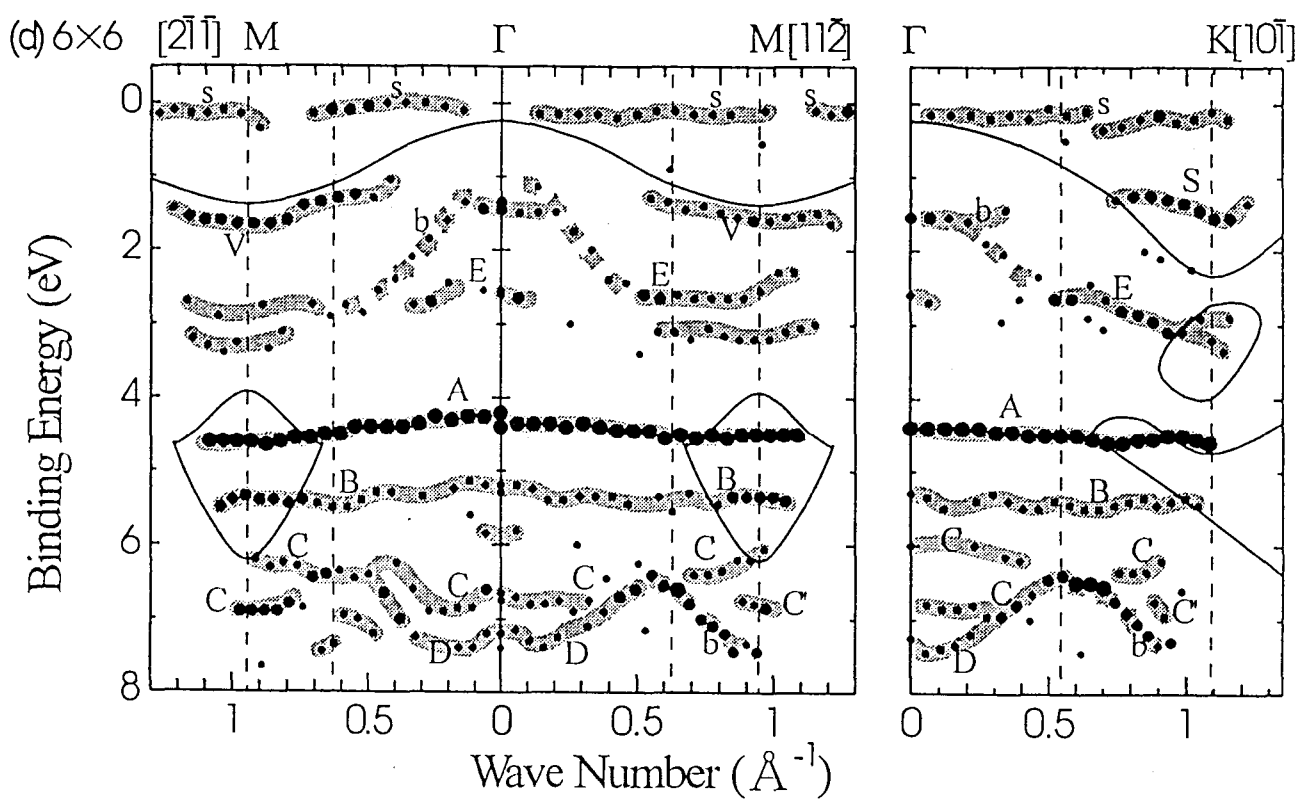
Fig. 6.19: The band map of the Si(111)6×6-Au surface measured at hν=21.2eV

in each surface. The states are observed as the shoulders of the peak $A$ in the Fig. 6.12 to 6.15. The states $B$ are almost parallel to the states $A$ suggesting that the $B$ and $A$ are the same states split into two states by the spin-orbit interaction. The energy difference between $A$ and $B$ of about 0.6~1.0eV is also comparable to the energy of the spin-orbit splitting of Au $5d$ states(about 0.7eV) expected by theoretical and experimental studies of bulk Au crystal[44].

The states $C$ and $D$ are also prominent and easily observed in Fig. 6.12 to 6.15 of every surface. Some faint state labeled $C'$ is also observed in $\alpha$-$\sqrt{3}$ , $\beta$-$\sqrt{3}$ , and 6×6 surfaces. On the contrary to $A$ and $B$, the states labeled $C$, $C'$ and $D$ have relatively large and complicated dispersions and also accompany $C''$ or $D'$ states especially in $\alpha$- and $\beta$-$\sqrt{3}$ and 6×6 surfaces suggesting that the states are composed of bonding $5d$ electrons. The bonding energies(the energy differences of $A$ and $C$ states) are about 2.0, 2.4, 2.8, and 2.8eV for the 5×2, $\alpha$-$\sqrt{3}$, $\beta$-$\sqrt{3}$ and 6×6 surfaces at $\bar{\Gamma}$ point. The existence of the $5d$ electrons making bonding state is consistent with the SCLS results in which $5d$ electrons are implied to hybridized with Si $3s3p$ electrons. By summing up all of the spectra of each reconstructed surfaces and compared the intensity ratio between peaks $A+B$ and $C+D$ we can know very roughly how many of $5d$ electrons of each surface participates in the bonding state although DOS of some bulk states(will be mentioned, and labeled b) may be included in the intensity of $C+D$. As the results the ratios between peaks $A+B$ and $C+D$ are estimated as about 6:4, 6.5:3.5, 7:3 and 7:3 for 5×2 , $\alpha$-$\sqrt{3}$ , $\beta$-$\sqrt{3}$ , and 6×6 surface, respectively. The numbers of the bands around $C$ state of $\alpha$-$\sqrt{3}$ , $\beta$-$\sqrt{3}$ and 6×6 of three($C$, $C'$ and $D$) is consistent the estimated number of the bonded $5d$ electrons on these surfaces. Seeing the dispersion feature around $C$ states of the $\alpha$- and $\beta$-$\sqrt{3} \times \sqrt{3}$ and 6×6 surfaces these dispersions have a turning points or degenerate points at the high symmetry point of $\sqrt{3} \times \sqrt{3}$ SBZ which are indicated by dashed lines(labeled K', M', and $\Gamma$' in the figures of $\sqrt{3}$ surfaces). Especially the states around K' points of [$2\bar{1}\bar{1}$] and [$11\bar{2}$] directions of $\alpha$-$\sqrt{3}$ are remarkable. The similar dispersion feature of 6×6 surface to that of $\beta$-$\sqrt{3}$ surface implying that the 6×6 surface has also a $\sqrt{3} \times \sqrt{3}$ periodicity in the local structure. This similarity of the $\beta$-$\sqrt{3}$ and 6×6 are consistent with the similar SCLS of the Si $2p$ of these surfaces. The prominent parts, labeled b, continues to $C$ states however, may be the bulk state of the substrate or the resonant states because there are similar states on the 7×7 surface(see Fig. 4.4). Other dispersions labeled b in more lower $E_B$ are also the bulk states judged from the same examination.

Now I focus on the several surface states in the energy range between $E_F$ and $E_B$ ~4eV. Although the dispersion curvature of the states labeled $V$ is similar to the edge of VBM and may not be surface states the deviation from the VBM especially in the 5×2 surface and the absence of the state in the 7×7 surface suggests the possibility that $V$ is the real surface state. Karlsson et al.[5] also found these states $V$ on the $\sqrt{3} \times \sqrt{3}$ surface(their measured sample is considered to be near structure to the $\alpha$-$\sqrt{3}$ phase from their LEED pattern and conditions to prepare the sample) and assigned them as surface states by their independence from the photon energy. In the bulk band projection there are another state labeled $E$ in every surface and from the comparison to the band map of 7×7 surface this state is also considered to be the surface state. The dispersion feature of this state is similar between each reconstruction, but that of the 5×2 surface is little bit differ from other surfaces.

In the bulk band gap in the [$10\bar{1}$] direction the surface states($S$) are shown on every surface. The energy level of these states in different surface is almost the same from the VBM position. These $S$ and $V$ states of the $\alpha$-$\sqrt{3}$ corresponds to the $S_3$ and $S_3'$ states observed by Karlsson et al. although our results shift about 0.28eV higher $E_B$ than theirs. This difference may be due to the different band bending between these two experiments

106

because of the different amounts of doping. The dispersion curvature of our observed S state is also little bit different from that of their $S_3$ state. The $S_2$ and $S_2$' states which are observed Karlsson *et al.*, however, were not observed in our measurement. Comparing to the results for $\sqrt{3}$-Au of Houzay *et al.* which were measured along the $\bar{\Gamma}$ -$\bar{K}'$ -$\bar{M}'$ direction their observed two surface states are fairly agreement with V and E state, respectively.

On the 5×2 surfaces another surface state S' is also observed and they are also shown in the $[11\bar{2}],[2\bar{1}\bar{1}]$ directions and around $\bar{\Gamma}$ in the bulk band projection. In addition V' state which is considered to be the same state of the V judging from the energy level is also observed in 5×2 surface.

On every surface there are faint states(s) lying under the Fermi level and the states are implying the metallic character of these surfaces. Considering the very small Density of states(DOS) of these states in their spectra especially on the $\alpha$-$\sqrt{3}$ surface comparing to the metallic state of the 7×7 surface or the states of other surfaces, however, the states may be the defect states. Karlsson *et al.*[5] also observed the dispersionless state lying under the Fermi level and concluded the states are domain wall states. According to the ARPES study of the single domain surface by Collins *et al.*[31], the 5×2 surface is one dimensional metal along the $[1\bar{1}0]$ direction. Thus our results of metallic character along $[10\bar{1}]$ and non-metallic character along $[11\bar{2}]$ for the three domain 5×2 surface is consistent with their results although the DOS of the metallic state is very much small. The existence of the s states at whole angles in $\beta$-$\sqrt{3}$ and 6×6 surface strongly implies the metallic character of these surfaces.

As shown in previous discussion the surface states dispersions of the 5×2 surface is different from those of other reconstructed surfaces suggesting the different bonding structure of the 5×2 surface comparing to other reconstructions. And the relatively complicated surface states on the 5×2 surface is suggesting the complicated surface structure. This results is conflicting to the SCLS results of only two surface components on the surface and the Si $2p$ core spectrum of the 5×2 surface may include many surface components close to each other. The dispersion feature of the $\alpha$-$\sqrt{3}$ , $\beta$-$\sqrt{3}$ , and 6×6 is similar in each other. The most remarkable difference between $\alpha$-$\sqrt{3}$ and $\beta$-$\sqrt{3}$ is the metallic states, s appeared in whole direction of the $\beta$-$\sqrt{3}$ surface. This result is consistent with the interpretation that the surface structures of the $\alpha$-$\sqrt{3}$ , $\beta$-$\sqrt{3}$ and 6×6 are almost the same structure having $\sqrt{3} \times \sqrt{3}$ periodicity in the domain and the difference between these surfaces are the domain wall structures as discussed in the subsection 6.3.1

For the accurate assignment of these surface states, however, theoretical band calculations are eagerly expected.

# 6.4 Summary

We have performed the Si $2p$ core level spectroscopy and ARPES measurement for the Si(111)5×2, $\alpha$-$\sqrt{3}$, $\beta$-$\sqrt{3}$ and 6×6-Au surfaces and determined their BCLS, SCLS and surface band structure. From the BCLS of these surfaces large band bendings of VBM toward the Fermi level were observed, especially on the 5×2 and $\alpha$-$\sqrt{3}$-Au surfaces. We could fit every Si $2p$ spectrum by one bulk and two surface components which shift to higher binding energies from their bulk peak positions because of the charge transfer from Si to Au atoms. The results of the SCLS indicated that the surface structures of the $\alpha$- and $\beta$-$\sqrt{3}$-Au are different from each other and suggest the necessity of the discrimination between $\alpha$- and $\beta$-$\sqrt{3}$-Au surfaces when we study the $\sqrt{3} \times \sqrt{3}$-Au surface. On the other hand the similar SCLS results

of the $\beta$-$\sqrt{3}$ and 6×6 structures indicate that the local structures of them are almost the same. This structural similarity is supported by the similar surface band structures on these surfaces observed by ARPES measurement.

So far proposed models of 5×2-Au and $\sqrt{3} \times \sqrt{3}$-Au surface can not successfully explain their SCLS results when we consider the uniform surfaces without domain walls. Assuming that one of the surface component of the $\sqrt{3} \times \sqrt{3}$ surface is the contribution of the Si atoms at the domain walls, our SCLS results is consistent with the picture that the ordering domain wall cause the phase transition from the $\alpha$-$\sqrt{3} \times \sqrt{3}$ to 6×6 surface via $\beta$-$\sqrt{3} \times \sqrt{3}$ surface

On every surface the evident of the existence of non-bonding and bonding Au $5d$ electrons were observed both in ARPES and SCLS measurement. On the $\beta$-$\sqrt{3}$ and 6×6 surface the DOS at the Fermi level was observed at almost whole wave number indicating the metallic character of these surfaces. The main difference between $\alpha$-$\sqrt{3}$ and $\beta$-$\sqrt{3}$ is this clear metallic surface states of the $\beta$-$\sqrt{3}$ compared to the very faint states of $\alpha$-$\sqrt{3}$ . Another surface dispersion of these two $\sqrt{3}$ surfaces are almost the same and the surface structure of these surfaces in domain walls may be the same structure. Among these surfaces 5×2 surface has relatively different and complex surface dispersions from those of the other surfaces indicating the different bonding character between Si and Au atoms on the surface. This complex surface dispersion suggests the complex surface structure of 5×2 but conflict to the SCLS results in which only two surface components exist. This discrepancy may be due to the finite energy resolution of the SCLS measurement and in the spectrum more surface components may be included.

# References

[1] S.Ino, Proc. NATO Advanced Research Workshop on RHEED and reflection electron imaging of surfaces, June 15-19, Netherlands (ed. P.K.Larsen and P.J.Dobson), NATO ASI Series B188, 3, Plenum, New York(1988).

[2] G.LeLay, V.Yu.Aristov, L.Seehofer, T.Buslaps, R.L.Johnson, M.Gothelid, M.Hammer, U.O.Karlsson, S.A.Flodström, R.Feidenhans'l, M.Nielsen, E.Findeisen, and R.I.G.Uhrberg, Surf.Sci.**307-309**, 280 (1994).

[3] A.Ph.Dumas, G.Humbert, P.MAthieu, C.Mathiez, R.Mouttet, F.Roland, F.Salvan, and F.Thibaudau, J.Vac.Sci.Technol.,A**6**, 517 (1988).

[4] R.J.Wilson and S.Chiang, Phys.Rev.Lett.,**58**, 369 (1987), E.J.van Loenen, J.E.Demuth, R.J.Tromp, and R.J.Hamers, Phys.Rev.Lett.,**58**, 373 (1987).

[5] C.J.Karlsson, E.Landemark, L.S.O.Johansson, and R.I.G.Uhrberg, Phys.Rev.B**42** (1990) 9546.

[6] L.S.O.Johansson, E.Landemark, C.J.Karlsson, and R.I.G.Uhrberg, Phys.Rev.Lett.**63**, 2092 (1989).

[7] T.Takahashi, S.Nakatani, N.Okamoto, T.Ishikawa and S.Kikuta, Jpn.J.Appl.Phys.**27**, L753 (1988).

[8] M.Katayama, R.S.Williams, M.Kato, E.Nomura, and M. Aono, Phys.Rev.Lett.**66**, 2762 (1991), H.Over, H.Huang, S.Y.Tong, W.C.Fan and A.Ignatiiev, Phys.Rev.B**48**, 15353 (1993).

[9] Y.G.Ding, C.T.Chan, and K.M.Ho, Phys.Rev.Lett.**67**, 1454 (1991), S.Watanabe, M.Aono, and M.Tsukada, Phys.Rev.B **44**, 8330 (1991).

[10] J.H.Huang and R.S.Williams, Phys.Rev.B**38**, 4022 (1988).

[11] J.Nogami, A.A.Baski, and C.F.Quate, Phys.Rev.Lett.**65**, 1611 (1990).

[12] K.Higashiyama, S.Kono, and T.Sagawa, Jpn.J.Appl.Phys.,**25**, L117 (1986).

[13] K.Oura, M.Katayama, F.Shoju, and T.Hanawa, Phys.Rev.Lett.**55**, 1486 (1985).

[14] Y.G.Ding, C.T.Chan, and K.M.Ho, Surf.Sci.Lett.**275**, L691 (1992).

[15] Y.Kuwahara, S.Nakatani, M.Takahashi, M.Aono, and T.Takahashi, Surf.Sci.**310** 226 (1994).

[16] P.B.Howes, C.Norris, M.S.Finney, E.Vlieg and R.G.van Silfhout, Phys.Rev.B44, 1454 (1991).

[17] J.Quinn, F.Jona, and P.M.Marcus, Phys.Rev.B46, 7288 (1992

[18] D.Dornisch, W.Moritz, H.Schulz, R.Feidenhans'l, M.Nielsen, F.Grey, and R.L.Johnson, Phys.Rev.B44, 11221 (1991).

[19] L.E.Berman, B.W.Batterman and J.M.Blakely, Phys.Rev.B38, 5397 (1988), J.H.Huang and R.S.Williams, Surf.Sci.204 445 (1988).

[20] A.A.Baski, J.Nogami, and C.F.Quate, Phys.Rev.B42, 10247 (1990).

[21] H.Daimon, C.Chung, S.Ino and Y.Watanabe, Surf.Sci.162, 634 (1990).

[22] J.D.O'Mahony, C.H.Patterson, J.F.McGilp, F.M.Leibsle, P.Weightman and C.F.J.Flipse, Surf.Sci.Lett.277, L57 (1992).

[23] Y.Tanishiro, K.Yagi, and K.Takayanagi, Surf.Sci. 234, 37 (1990).

[24] T.Hasegawa, K.Takata, S.Hosaka, and S.Hosoki, J.Vac.Sci.Technol.A8, 241 (1990).

[25] T.Hasegawa, and S.Hosaka, Jpn.J.Appl.Phys.,31, 1492, (1992).

[26] E.Bauer, Surf.Sci.Lett.250, L379 (1991).

[27] L.D.Marks and R.Plass, Phys.Rev.Lett. 75, 2172 (1995).

[28] S.Kono, Y.Enta, T.Abukawa, N.Nakamura, K.Anno, and S.Suzuki, Phys. Scri.T 31, 96 (1990).

[29] F.Houzay, G.M.Guichar, A.Cros, F.Salvan, R.Pinchaux, and J.Derrien, J.Phys.C 15, 7065 (1982).

[30] J.M.Nicholls, F.Salvan, and B.Reihl, Phys.Rev.B 34, 2945 (1986).

[31] I.R.Collins, J.T.Moran, P.T.Andrews, R.Cosso, J.D.O'Mahony, J.F.McGilp, and G.Margaritondo, Surf.Sci. 325, 45 (1995).

[32] K.Asami, J.Electr.Spectr.9, 469 (1976).

[33] F.J.Himpsel,G.Hollinger, and R.A.Pollak,Phys.Rev.B, 28,7014(1983).

[34] S.Hasegawa, and S.Ino, Surf.Sci.283, 438 (1993).

[35] H.Ishida, N.Shima, and M.Tsukada, Surf.Sci.158, 438 (1985).

[36] Z.H.Lu, T.K.Sham, and R.P.Norton, Solid State Commun.85, 957 (1993).

[37] J.J.Yeh, J.Hwang, R.Cao, K.A.Bertness and I.Lindau, J.Vac.Sci.Technol.,A6, 1557 (1988).

[38] N.V.Dobrodey, L.I.Ziegelman, V.G.Zavodinsky and I.A.Kuzanov, Surf.Rev.Lett.1, 273 (1994).

[39] R.Plass and M.D.Marks, Surf.Sci.342, 233 (1995).

[40] J.Falta, A.Hille, D.Novikov, G.Materlik, L.Seehofer, G.Falkenberg, and R.L.Johnson, Surf.Sci. **330**, L673 (1995).

[41] M.Chester and T.Gustafsson, Surf.Sci.**256**, 135 (1991).

[42] G.S.Herman, J.C.Woicik, A.B.Andrews, and J.L.Erskine, Surf.Sci. **290**, L643 (1993).

[43] K.C.Pandey,Phys.Rev.B **14**,1557(1976).

[44] For
example, K.A.Mills, R.F.Davis, S.D.Kevan, G.Thornton, D.A.Shirley, Phys.Rev.B**22** (1980) 581 and references therein.

# Chapter 7

# 2D-ARPES of the Transition Metal Dichalcogenides ($1T$-TaS$_2$, $2H$-TaSe$_2$ and $2H$-NbSe$_2$)

## 7.1 Introduction

### 7.1.1 Preface

In this chapter I describe our 2D-ARPES measurements of the layered transition metal dichalcogenides(TX$_2$; T:Transition metal, X;Chalcogen) compounds. I first review, the properties of layered transition metal dichalcogenides compounds related to the interpretation of our 2D ARPES results. Firstly I describe the crystal structures of the $1T$- and $2H$- polytypes. Then the electronic structures of these polytypes of TX$_2$ are reviewed. After that a brief explanation about the charge density wave(CDW) phenomena in TX$_2$ sample will be reviewed. After describing the experimental details, I discuss the results of the photoelectron angular distribution(PEAD) patterns in regard to the band structures and the symmetry of the electron wave function of the initial state. The difference of the electronic structure between $1T$- and $2H$- polytypes is also discussed. Then I give results of the photon energy dependence of the PEAD patterns. Finally I briefly discuss about the shape of Fermi surface of these TX$_2$ with referring to the CDW.

### 7.1.2 Crystal structure of TX$_2$

Basically, crystal structure of TX$_2$ consists of X-T-X sandwiches and each X-T-X sandwich is weakly connected with each other along their hexagonal $c$-axis by the van-der-Waals force. Thus these layered compounds, TX$_2$ can be easily cleaved. An interesting property of these layered compounds TX$_2$ is that the same compound can often be prepared with different crystal structures. There are many different types of polytypes such as $1T$-, $2H$-, $3R$-, $4H$a-,$4H$b-,$4H$c-, and $6H$- phases. These crystal structures of this layered compounds, TX$_2$, share in common the X-T-X sandwich sequence of the atomic layers, however, they differ in the coordination of T atoms, and also in the stacking and registry of successive sandwiches with respect to each other. In these abbreviated notations, the integer indicates the number of the X-T-X sandwiches per unit cell along the hexagonal $c$-axis and $T$, $H$, and $R$ denote the symmetry of trigonal, hexagonal, and rhombohedral, respectively. In my work I have investigated only the two simplest crystals, namely $1T$- and $2H$- polytypes (*ie.* $1T$-TaS$_2$,

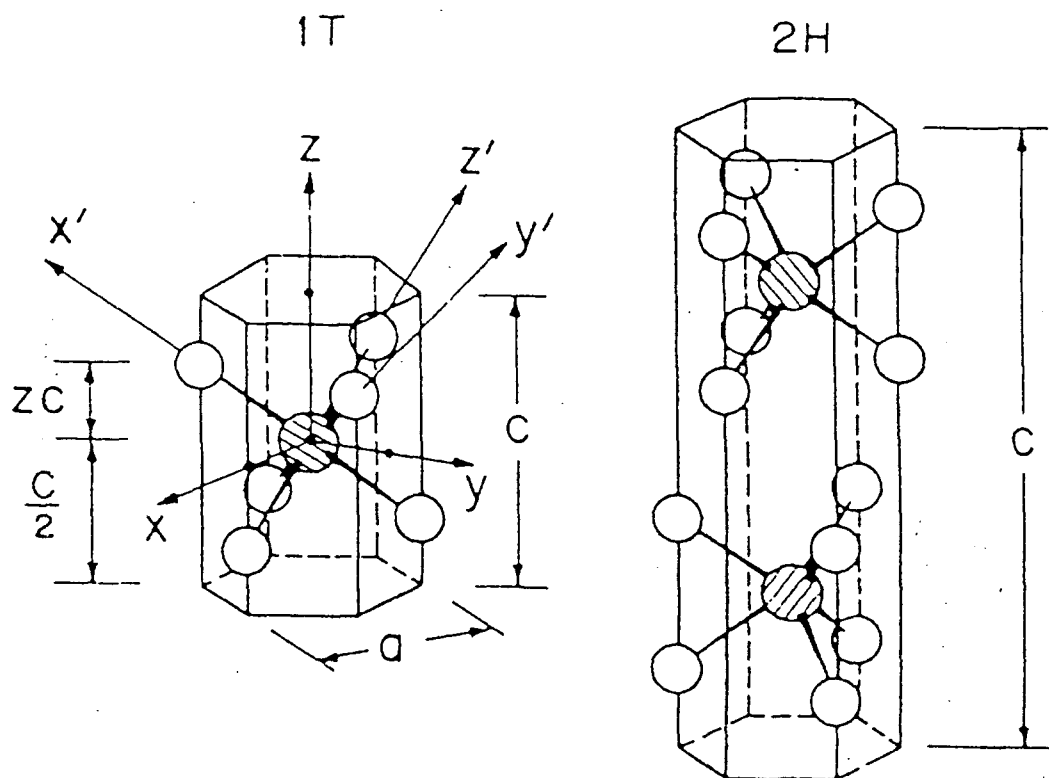$2H$-TaSe$_2$, $2H$-NbSe$_2$). Their unit cells are illustrated in Fig. 7.1. In the $1T$- structure which



Fig. 7.1: Unit cells of the crystal structures of the $1T$ and $2H$ polytypes of the layered transition metal dichalcogenides. Cross hatched circles and open circles represent metal atoms(T) and chalcogen atoms(X), respectively.

has $D^3_{3d}$ space group, each T atoms is octahedrally coordinated with X atoms. Only one sandwich is required to define the unit cell in the $c$ direction, and the structure has trigonal symmetry about the $c$-axis. To be more precise, the coordination is not quite octahedral, but due to distortion along the $c$-axis, is actually trigonal antiprismatic. Another refinement concerns the positional parameter $z$ defined in Fig. 7.1. The value of $z$ was estimated as $0.25\pm0.01$ namely $1/4$ for $1T$-TaSe$_2$, by Bjerkelund and Kjekshus[1]. In the $1T$- unit cell of Fig. 7.1 I also indicate the directions of the x,y,z axes and alternative set of axes x', y', z' which will prove convenient when we discuss about the crystal field splitting in an octahedral ligand field.

On the other hand $2H$- polytype has space group of $D^4_{6h}$ and the coordination of the T atoms is trigonal prismatic as shown in Fig. 7.1. The unit cell in the $c$ direction spans two sandwiches, and the crystal point group is hexagonal. As can be seen in Fig. 7.1 each individual X-T-X sandwich has three fold rotational symmetry about the $c$-axis. The orientations of alternate sandwiches are separated by a 180° rotation about the $c$-axis. Namely, by nonprimitive translation parallel to the $c$-axis and the 60° rotation, six fold symmetry is realized. The values of $z$ are estimated as 0.118 and 0.1163 for $2H$-TaS$_2$ and $2H$-NbSe$_2$[2], respectively. These values are near $1/8$ but little bit smaller and it means that the separation between neighboring unit cells are little bit larger than that of the $1T$- type crystal.

## 7.1.3 Electronic structure

Because of the weak interaction along $c$-axis, these $TX_2$'s have quasi-two dimensional properties. Thus, the electronic structures of these materials are expected to be quasi-two dimensional system.

Band structures for these $TX_2$ have been presented by a number of authors[3, 4]. First principles band structures for $1T$-TaS$_2$, $2H$-TaS$_2$ and $2H$-NbSe$_2$ calculated by Mattheiss[4] using the augmented plane wave(APW) method are shown in Fig. 7.2, Fig. 7.3, and Fig. 7.4.
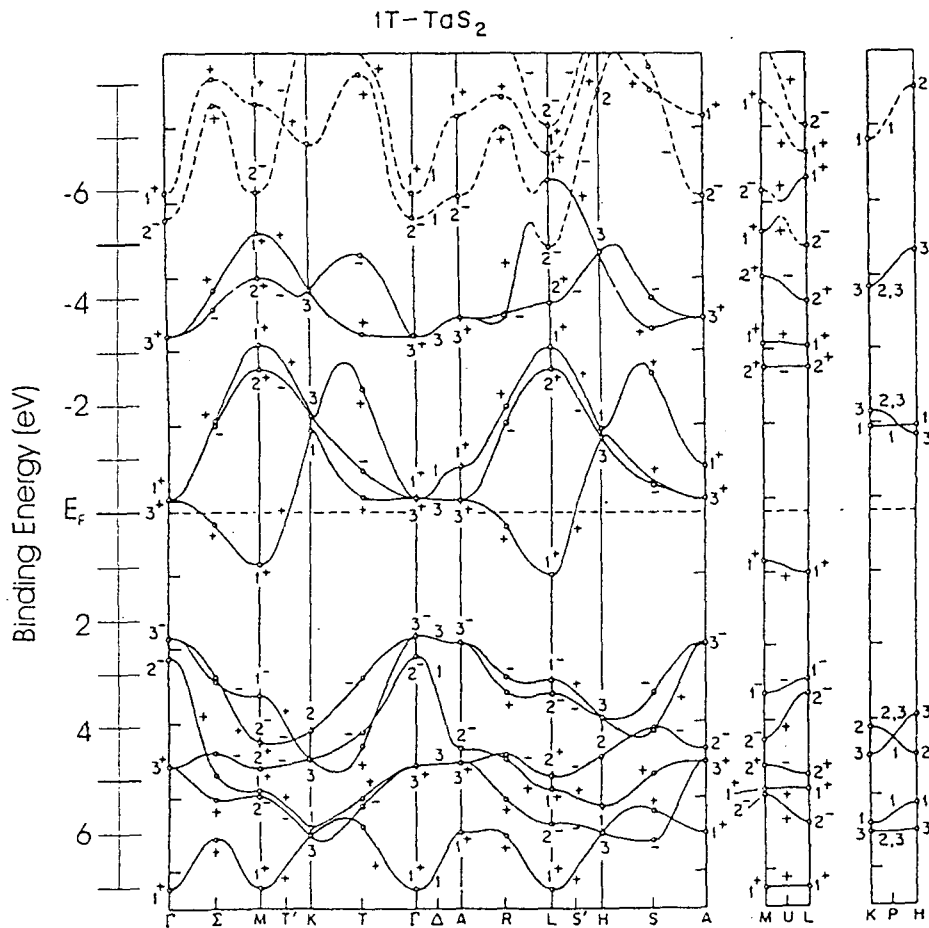


Fig. 7.2: Energy band structure of $1T$-TaS$_2$ from ref.[4]

In these $TX_2$ two $s$ and two $d$ electrons of the most outer shell of the T atoms are transferred to the two X atoms and filled the $p$ state of X atoms that the only one $d$ electron of T atoms and twelve electrons of X atoms make the valence band of the $1T$-$TX_2$. For example in TaS$_2$ the occupation of Ta is Ta $5p^6 5d^1$ and that of S is S $4s^2 4p^6$. In the results of the band calculation, at the energy range about 2 to 7eV there exists a group of bands which are derived primarily from the S $3p$ orbitals in both polytypes of TaS$_2$. On the other hand the Se $4p$ bands are around 1 to 7eV in the $2H$-NbSe$_2$ Ta- or Nb- derived $5d$ or $4d$ bands which are occupied by only one electron lie at slightly higher energies. The dashed bands in the upper portions correspond to the unoccupied Ta(Nb) $6s(5s)$ and $6p(5p)$ band. According to the Mattheiss the five fold Ta $5d$ band is split into two nonoverlapping subbands. The three fold lower subband is associated with the $d_{3z^2-r^2}$, $d_{xy}$, and $d_{x^2-y^2}$ and the two fold upper subband is associated with the $d_{yz}$ and $d_{zx}$. These lower and higher subbands are

114

Fig. 7.3: Energy band structure of $2H$-TaS$_2$ from ref.[4]

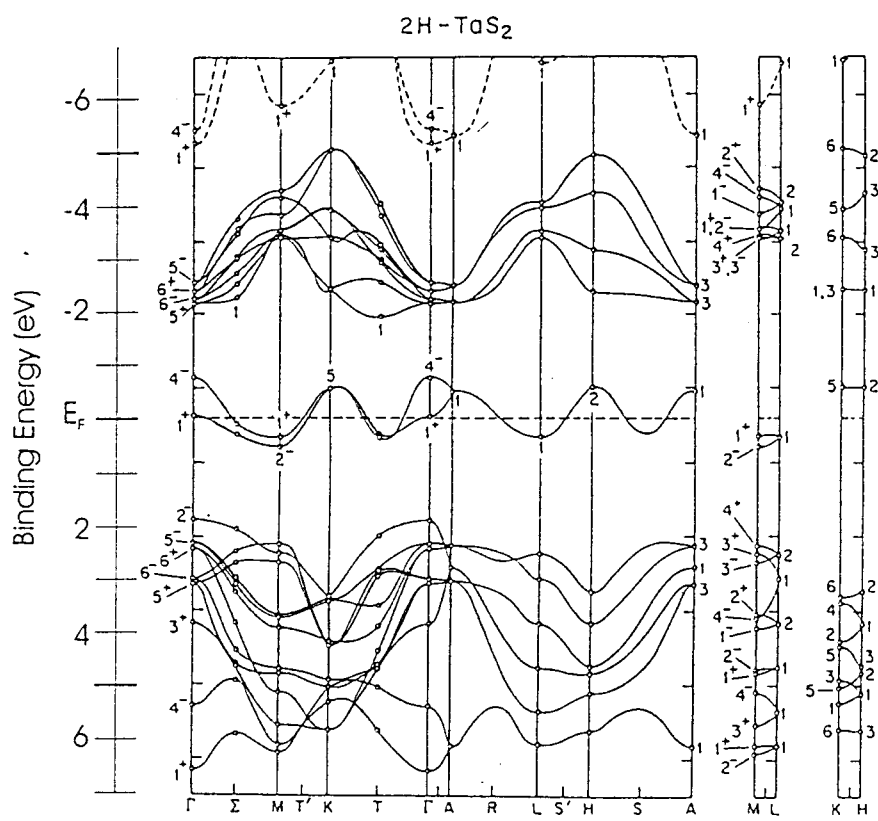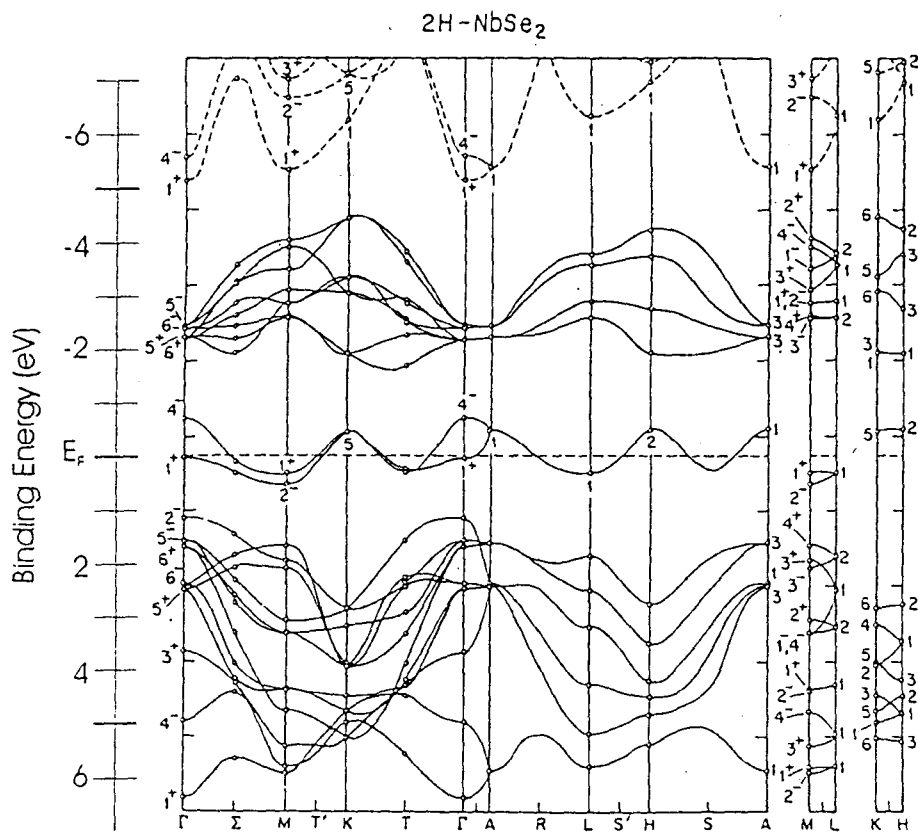Fig. 7.4: Energy band structure of $2H$-NbSe$_2$ from ref.[4]

loosely refereed to as the "$t_{2g}$" and "$e_g$" orbitals, respectively considering the octahedral coordination in the $x',y'$ and $z'$ axes. However, these orbitals are not the exactly true "$t_{2g}$" orbitals. The occupied $d$ state consists of the "$t_{2g}$" like state and is considered to be mainly the $d_{3z^2-r^2}$ orbital. Mattheiss suggested, however, other $d_{xy}$, and $d_{x^2-y^2}$ orbitals are also strongly represented in the occupied region.

In $2H$- polytypes there are twice as many bands as in $1T$- type crystals and Ta(or Nb) $d$ bands are split into an eight-fold upper subband and a narrow two fold lower subband. The latter corresponds roughly to the $d_{3z^2-r^2}$ band but other "$t_{2g}$" like $d_{xy}$, and $d_{x^2-y^2}$ orbitals are admixed strongly as the same as $1T$- polytype.

Brillouin zone of the $1T$ structure is shown in Fig. 7.5 (a). The irreducible wedge of the



Fig. 7.5: Brillouin zones of the (a)$1T$- and (b)$2H$- polytypes. In side of shaded and unshaded area of (a) are different from each other because of the three fold symmetry of the $1T$-polytype.

Brillouin zone is indicated by bold lines in Fig. 7.5 and the symmetry points $\Gamma$, $A$, $L(L')$, $M(M')$, $H$, and $K$ are labeled. The perimeters of the rectangles $\Gamma ALM$ and $\Gamma AL'M'$ are

fully equivalent to each other by symmetry, but the interiors of these rectangles are not. Therefore the energy bands are expected to retai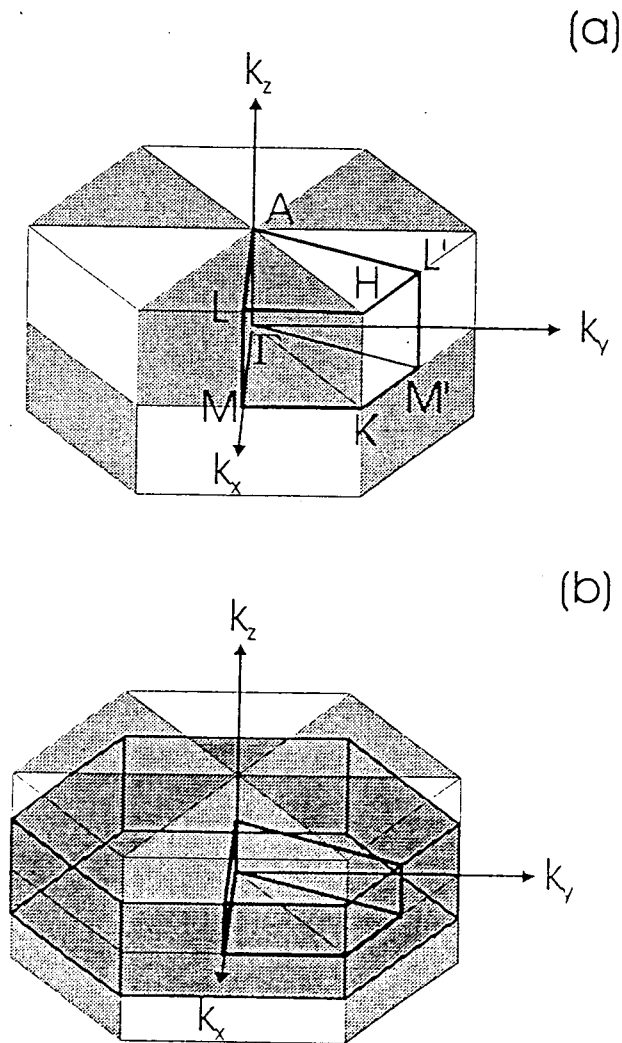n the three fold rotational symmetry of the real-space crystal structure. The $k_x,k_y,k_z$ axes of Fig. 7.5 are parallel to the $x$, $y$, $z$ axes of Fig. 7.1, respectively, so that the unshaded wedges of Fig. 7.5 are the ones which would correspond to the locations of the nearest-neighbor chalcogen atoms if one were to imagine a metal atom placed at the origin of $k$ space. However, band dispersion are constrained to be identical over the BZ surfaces of the two kinds of wedge, one expects some tendency for them to be similar in the interiors. This tendency is greatly reinforced if one invokes the approximation of two dimensionality. If the bands were perfectly flat in the $k_z$ direction, the energy bands along $\Gamma$-$M$ would then be identical with those along $A$-$L$, and any other direction parallel to $\Gamma$-$M$ or $\Gamma$-$M'$. Inspection of the band calculation of Fig. 7.2 for the $\Gamma$-$A$, $M$-$L$ and $K$-$H$ directions reveals that there is some justification for the assumption of flatness of the bands along $k_z$ in the occupied region. Thus one expect the occupied energy bands in $1T$- polytypes to have six-fold symmetry or something close thereto.

The BZ for the $2H$- structure is very similar to that for the $1T$- structure as shown in Fig. 7.5(b) by the darker shaded area with thick lines. Because of the almost the twice longer unit cell along $c$-axis the length of the Brillouin zone along $k_z$ direction is about half of that of $1T$- structure and the dispersions along $k_z$ must be small in $2H$- polytypes. Some calculated bands of $1T$- and $2H$- structure in the Fig. 7.2 and Fig. 7.3 seem to show some proof of that. In addition, since the crystal has six-fold rotational symmetry there is no longer any distinction between the shaded and unshaded wedges of Fig. 7.5 (a) in the BZ of $2H$ polytype.

As mentioned already in section3.3 by the display type analyzer we can measure the cross section of the band structure of the materials. The two dimensional materials such as TX$_2$ is the most suitable materials to measure the band cross section because the small dispersion along the surface normal direction is expected as mentioned above. Thus we measured the cross section of the band structures of the TX$_2$($1T$-TaS$_2$ , $2H$-TaSe$_2$ , $2H$-NbSe$_2$ ) precisely and discuss about their band structures as well as the symmetry of the electron wave function.

In our previous 2D-ARPES measurement of the $1T$-TaS$_2$ , the observed PEAD patterns at h$\nu$=21.2eV and 40.8eV are little bit different from each other[5] and to measure the photon energy dependence of the PEAD patterns more precisely we have performed the 2D-ARPES of $1T$-TaS$_2$ in different photon energies(h$\nu$=33, 40, 42.5, 49 and 60eV). These photon energies include the Ta $5p5d$ resonance photoemission region and we discuss the resonance photoemission effect to the PEAD patterns.

### 7.1.4  Charge density wave(CDW)

One of the characteristic physical properties of the low-dimensionality of these TX$_2$ is occurrence of charge density wave(CDW). $1T$-TaS$_2$, $2H$-TaSe$_2$, and $2H$-NbSe$_2$ show complex behaviors of CDW[6] as shown in the Fig. 7.6. For example in $1T$-TaS$_2$ the various CDW phases exist. The normal $1T$- phase without CDW, appears in a narrow temperature range between 543K and 570K and above 570K the $1T$- structure irreversibly changes into the $2H$- polytype. Below 543K the crystal structure is slightly distorted by electron phonon interaction and incommensurate CDW phase($1T_1$ phase) is appeared. Upon further cooling, another CDW phase($1T_2$ phase) which is called nearly commensurate CDW(NCCDW) takes place below 350K. The final phase transition to a commensurate CDW phase($1T_3$ phase) occurs at 180K. This phase transition have hysteresis and when we warm up the sample the
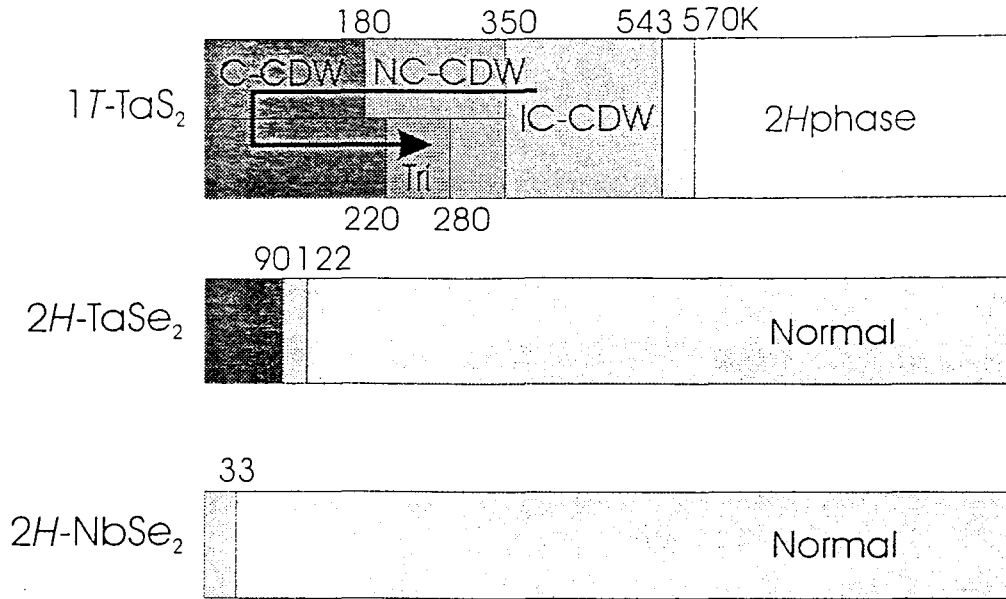
Fig. 7.6: Phase diagram of the charge density waves of $TX_2$

phase transition from CCDW to a new triclinic phase at 220K and NCCDW occurs again at 280K. Figure 7.7 is the resistivity change of the $1T$-$TaS_2$ which were used in ARPES measurement. The resistivity change indicate clearly the hysteresis of the phase transition and even the small resistivity change due to the transition from triclinic phase to NCCDW phase.

Most of the measurements described in this thesis were performed at room temperature, namely NCCDW phase for $1T$-$TaS_2$, ICCDW phase for $2H$-$TaSe_2$ and normal phase for $2H$-NbSe2. In addition we also measured the $1T$-$TaS_2$ at below 180K(CCDW phase).

The LEED pattern of the low-temperature phase(CCDW phase) of $1T$-$TaS_2$ can be described by a commensurate $\sqrt{13} \times \sqrt{13}$ super lattice, made up of 13 atom clusters which is called "star of David" which is rotated 13.9° about $c$-axis with respect to the underlying atomic lattice as shown in Fig. 7.8[7]. The nearly commensurate CDW phase is now considered to consists of domains of the commensurate CDW separated by discommensurations in which the CDW phase changes rapidly[8]. Recently measured STM image in which commensurate domains are ordered in a hexagonal arrays strongly supported this picture of the NCDW phase[9].

An obvious effect of the low-temperature CDW phase on the electronic structure would be the back folding of the bands of the undistorted $1T$- phase into the smaller CDW Brillouin zone because of the large unit cell of the $\sqrt{13} \times \sqrt{13}$ super lattice. Smith and Traum[10] observed the considerable density of state(DOS) at $E_F$ even the small angle of their ARPES measurement and discuss about the possibility of the CDW effect. In an empirical tight-binding calculation with taking the CDW atomic displacements into account, Ta $5d_{z^2}$ derived bands decomposed into three submanifolds separated by energy gaps have been found[11]

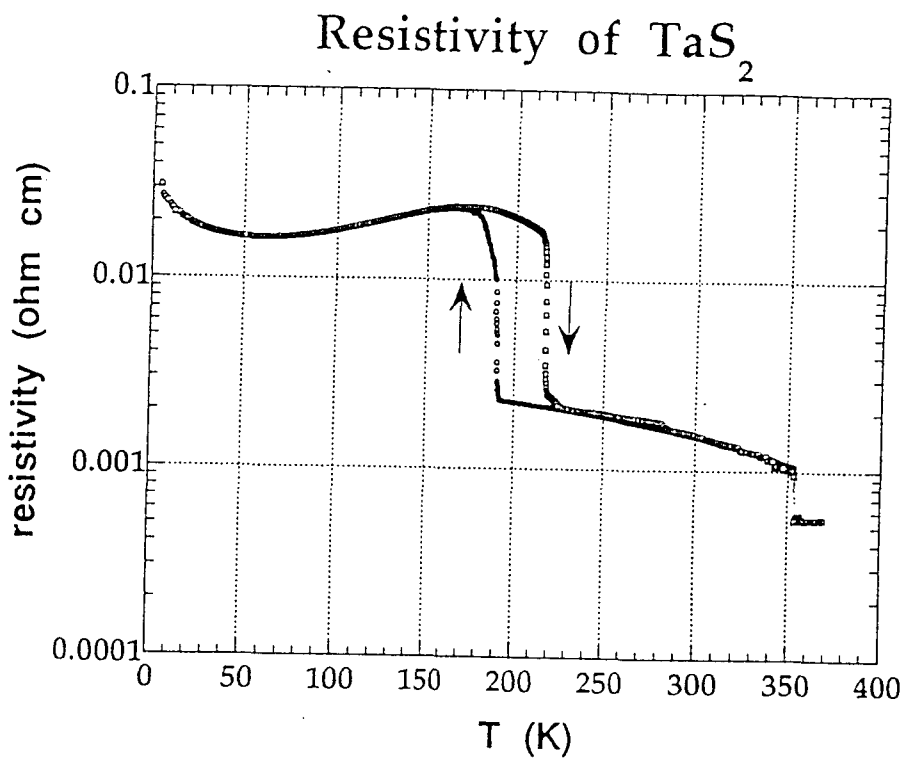Fig. 7.7: Temperature dependence of the resistivity of the $1T$-$TaS_2$ (courtesy of T. Hasegawa). The hysteresis of the resistivity change is clearly seen.
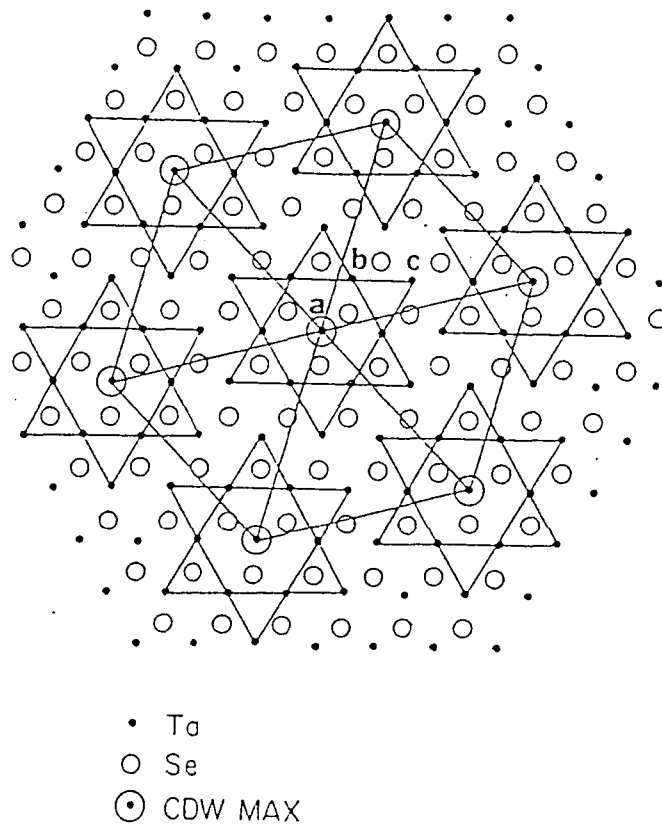
Fig. 7.8: $\sqrt{13} \times \sqrt{13}$ super lattice and "Star of David" clusters of CCDW phase

and confirmed by several ARPES studies at low temperature[11, 12, 13]

It is well known that the phase transition from NCCDW to CCDW phase accompany the metal-insulator transition. The increasing of the resistivity in Fig. 7.7 is one of the proof of this metal-insulator transition. This metal-insulator transition have also been observed by several photoemission experiments[12, 13, 14] and the energy gaps have been estimated as 125meV by Pollakg et al.[12] and 150~200meV by Dadel et al.. This energy gap has been also expected by the band calculation considering the CDW effect and the largest gap has been obtained to be 0.2eV[15]. By the inverse photoemission measurement[16], however, only the linear shift of the electronic structure but no CDW gap was observed within their experimental accuracy.

The origin of this metal-insulator transition is explained by famous Peierls transition[17] which is caused by the lattice periodic distortion. Aforementioned electron diffraction studies[7, 8] suggested the existence of the lattice distortion on the $1T$-$TaS_2$ . In the one dimensional metal, the wave length of the periodic lattice distortion is $2k_F$ where $k_F$ is the Fermi wave number. By this lattice distortion a band gap appeared at the $k_F$ as shown in Fig. 7.9 and the metal-insulator transition occurs. In the assumption of the free electron,
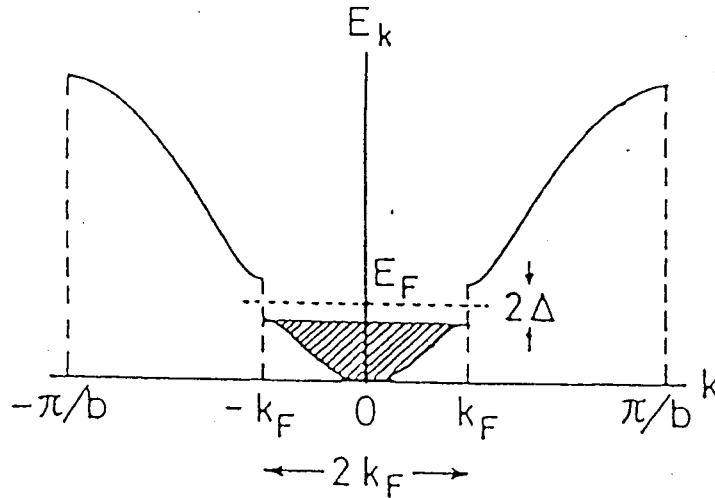


Fig. 7.9: Schematic view of the energy gap of the 1D metal caused by lattice distortion of $2k_F$

by the lattice distortion having $2k_F$ periodicity the CDW occurs completely in one dimensional(1D) system but in the two dimensional system(2D) the completeness of the CDW is worth compared to the one dimensional system. The probability of the occurrence of CDW is well described by the concept called Fermi surface nesting. Figure 7.10 is the schematic of the concept of Fermi surface nesting. In the one and two dimensional systems the Fermi surface is the Fermi point and Fermi circle, respectively, however, we expand these Fermi point or Fermi circle into three dimensional Fermi surface. In this expansion of the concept of the Fermi surface, the Fermi point of the 1D metal becomes Fermi surface like a flat plate and the Fermi circle of the 2D metal becomes Fermi surface like a cylinder. When we move these "Fermi surfaces" by $2k_F$, the Fermi surface of 1D metal overlaps completely with the next Fermi surface. On the other hand in the 2D metal by $2k_F$ moving the Fermi surface overlaps with the next Fermi surface only as a line. In the 3D metal the overlapping is only

Fig. 7.10: Schematic view of the concept of Fermi surface nesting for 1D, 2D and 3D metals

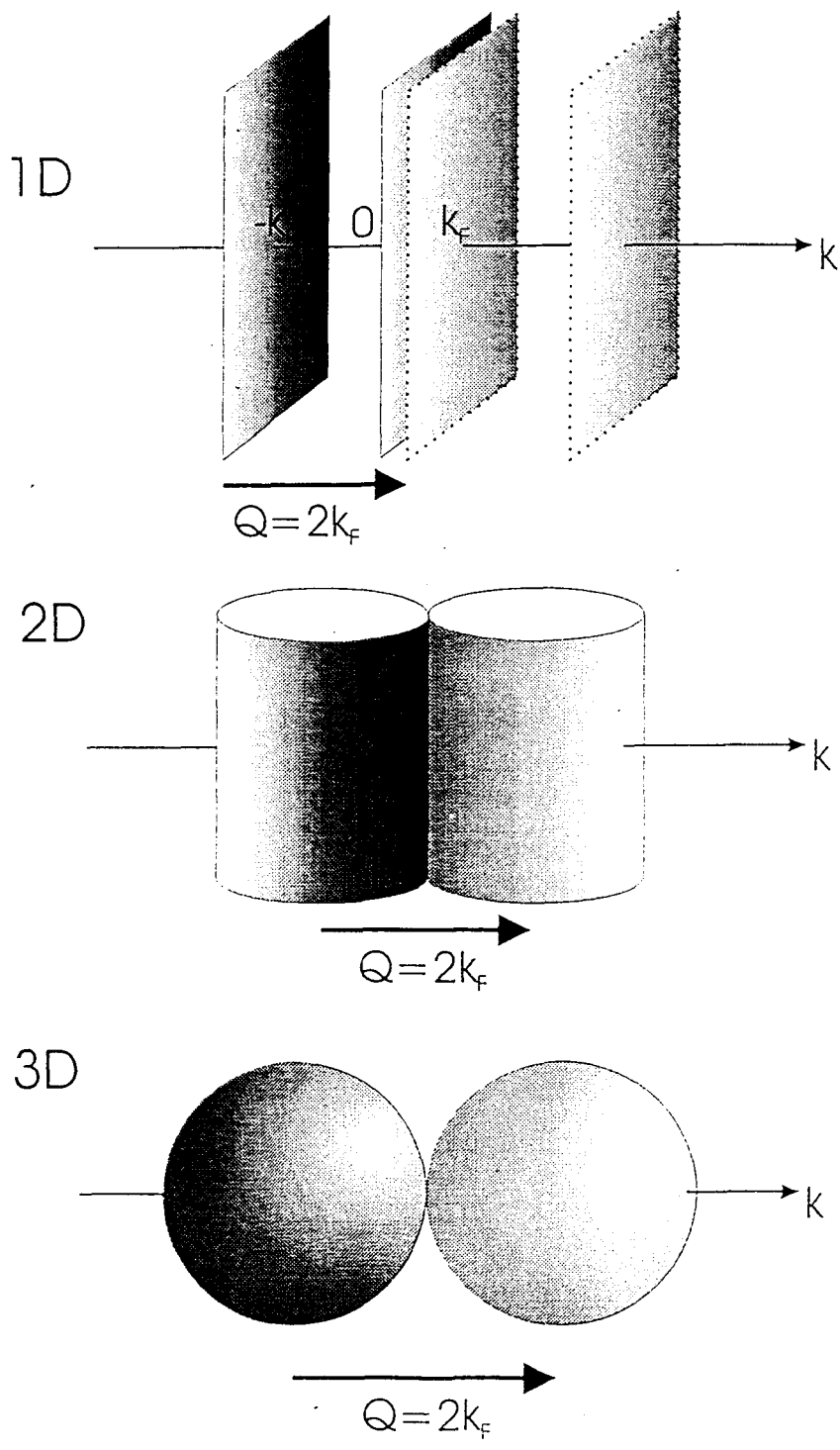the point. Therefore the Fermi surface overlapping which is called "nesting" is larg 1D metal and smallest in 3D metal and the size of the nesting determine the completeness or probability of the occurrence of the CDW. The energy gap of the band appears at the momentum space where the Fermi surface nesting is large.

From Fig. 7.10 one may think that the two dimensional free electron metal hardly cause the CDW. However, the electron of the real metal is not the free electron and the shape of the Fermi surface is not always cylindrical. Figure 7.11 is the illustration of the top view of the 2D metal's Fermi surfaces with different shapes. If the shape of the Fermi surface is distorted from the cylinder like shape to the shape like the upper picture of the figure, the Fermi surface nesting becomes larger and the CDW occurs more strongly.
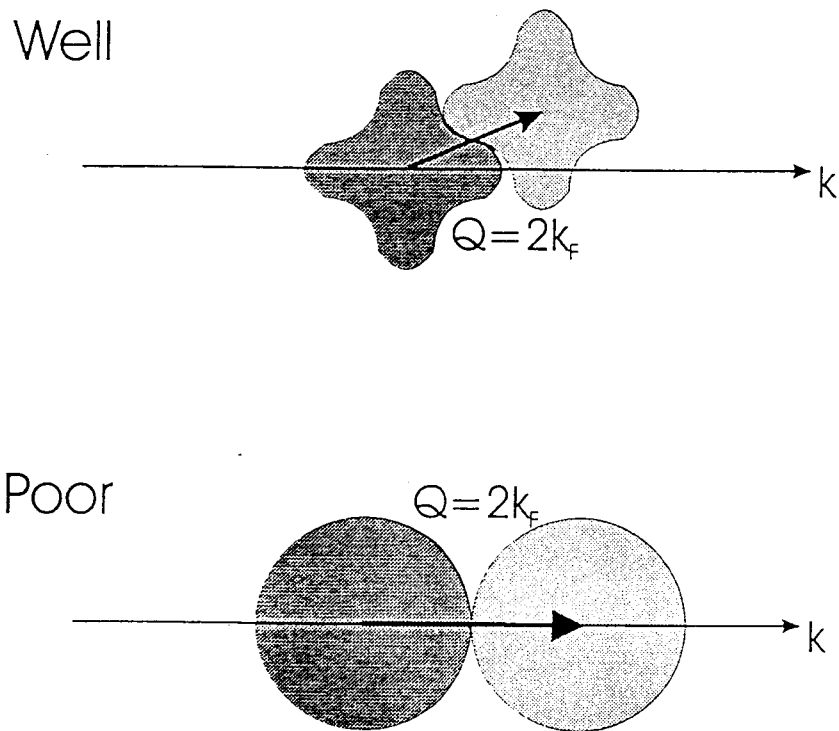
Fig. 7.11: Schematic view of the Fermi surface nesting in different shapes of Fermi surfaces

Therefore we can know the completeness or probability of the occurrence of CDW by knowing the shape of the Fermi surface. As mentioned in the section3.3 by the display type analyzer we can observe the Fermi surface directly and we can obtain this kind of information.

At the end of this thesis, I discuss about the Fermi surface of the $1T$-$TaS_2$, $2H$-$TaSe_2$ and $2H$-$NbSe_2$, and consider the Fermi surface nesting of these $TX_2$'s referring to the CDW. The temperature dependence of the PEAD patterns of $1T$-$TaS_2$ is also discussed.

# 7.2 Experimental details

The experiments are performed at the beamline BL-4 of the SOR-RING constructed by the staff of SRL-ISSP, the university of Tokyo, in Tanashi, Tokyo. As mentioned in section3.3 the measurements of two dimensional angle resolved photoelectron spectroscopy(2D-ARPES) were performed with using the two dimensional display type hemispherical mirror analyzer[18] The samples were cleaved by aforementioned scotch tape method in the preparation chamber with a base pressure of $1.0 \times 10^{-9}$ Torr and immediately transferred into the main chamber. The base pressure of the main chamber was $1.5 \times 10^{-10}$ Torr. These transition metal dichalcogenides are very inactive against oxidation because of their weak bonding character of the surface and the clean surfaces remain more than one week in the ultra high vacuum(UHV) chamber. The quality of the cleaved surfaces was checked by LEED patterns which was also observable by the display type analyzer using small electron gun inside the analyzer. The incident angle of the linearly polarized light is surface normal direction thus the light was $s$ polarized. The range of the used photon energies in this experiment was the 33~60eV which covers the Ta $5p$-$5d$ resonant photo-excitation region and we observed the photon energy dependence of the PEAD patterns. Since the acceptance cone of the analyzer is $\pm$ 60° we can observe the PEAD patterns up to the reciprocal space of 2nd Brillouin zones. The overall energy resolution of the measurement was about 250~400meV estimated from the Fermi level cut off of the Au. The Fermi level positions are estimated from the Fermi edge of the metallic $d$ bands of the transition metals of the sample in their angle integrated PES spectra measured by the display type analyzer by means of scanning the detected photoelectron energies. The PEAD patterns at certain $E_B$ were measured by commercial CCD camera with fixing the pass energy of the analyzer. It took about 10 minutes to get each image when we set the shutter speed of CCD camera as 4sec. Only for taking the images of the Fermi surface in which the photoelectron intensity was rather weak we set the image-sampling time as long as 20 minutes. All of the presented PEAD patterns in this study are not subjected to any symmetry operation. We only performed the normalization by dividing the raw image by the image of the analyzer transmittance. There are several ways to obtain the analyzer transmittance pattern which is attributed to the asymmetry of the analyzer transmitting power. One of the ways is summing up the images of signal in different azimuthal angles by rotating the sample(sample rotating method)[5]. Another way is proposed by Himpsel et al.[19] that by using the photon energy about 10~20eV higher energies than the true measurement and detect the structureless secondary electrons' pattern at the same analyzer energies to the true measurement. When we measure the very many patterns in relatively large range of $E_B$, and the photoemission distribution having very much varieties, more handy way is also available. The way is only the summing up the obtained PEAD patterns in different $E_B$(simple summing up method) though the normalization of the intensities of the patterns may be needed. This way is easy since we do not need any extra measurement. This method is, however, available only when the transmittance of the analyzer is not so much affected in different pass energies. In this study we use the sample rotating method as well as the simple summing up method. The signal noise ratio(S/N) of our raw data of the patterns, however, was large enough and the patterns were so clear without the dividing by the transmittance pattern that the dividing procedure was not so effective and the patterns hardly changed before and after the dividing process.

For most of the measurements including that of the photon energy dependence of the PEAD pattern, we took the data at room temperature. In the attempt to observe the Fermi surface difference between the commensurate and nearly commensurate CDW phases, we

cooled the $1T$-$TaS_2$ down to about 150K by using liquid nitrogen cooling system.

# 7.3 Results and Discussion

## 7.3.1 2D band structure of the transition metal dichalcogenides

*1T-TaS₂*

Figure 7.12 shows the angle integrated photoelectron spectrum of the $1T$-TaS$_2$ measured at h$\nu$=33.0eV. As seen in the figure, there are two main features, a large broad peak with some shoulders around 2eV$<E_B<$8eV corresponding to the S $3p$ band and a small sharp peak in the region of the $E_F < E_B <$2eV corresponding to the Ta $5d$ band. According
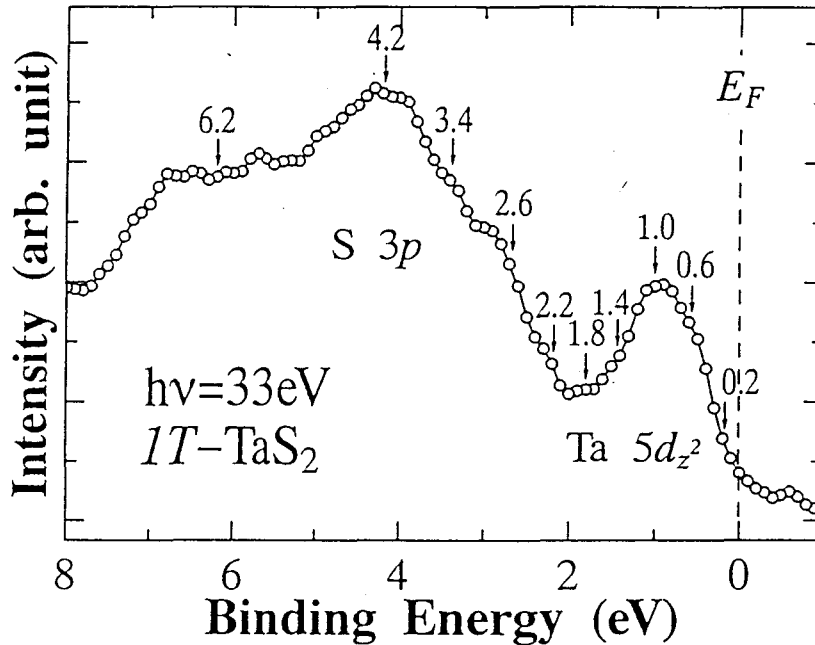


Fig. 7.12: Angle integrated spectrum of the $1T$-TaS$_2$ measured at h$\nu$=33.0eV for off-resonance photoemission condition.

to the band calculation of Mattheiss[4], this $d$ band consists of mainly $d_{z^2}$ band which is half filled. The metallic character of the Ta $5d$ peak is consistent with the expectation. We measured at first the PEAD patterns of $1T$-TaS$_2$ at h$\nu$=33eV which corresponds to the off-resonance photoemission condition. The typical PEAD patterns corresponding to the binding energies between $E_F$ to 6.2eV as indicated in Fig. 7.12 are presented in Fig. 7.13. The configuration between the electric field of the incident photon(indicated by an arrow) and the crystal orientation is presented by illustration in the upper right panel. That is to say, the experimental configuration between the electric field and the crystal structure of right-handed patterns is rotated 30° from that of left-handed ones. I determined these configurations of left- and right-handed patterns as the series of _0 and _30 in this thesis. In the illustration of the crystal structure, the triangles with thick lines and thin lines indicate the upper and lower chalcogen layers. Although we did not determine the crystal orientations of the measurements, from the comparison between observed PEAD patterns and the simulated PEAD patterns(which are mentioned later), we determined the crystal orientation of the illustration. The Brillouin zones corresponding to these configurations

are also illustrated in the upper left panel. In the figures of PEAD, the white region of the PEAD patterns indicates the region of strong photoelectron intensities. Since the raw image is recorded on a flat screen as shown in Fig. 7.14, we use the relation of $k_{\parallel}=A\cos\theta$ to the PEAD patterns of Fig. 7.13 to get the electron distribution patterns in the uniform momentum space. Therefore the center of the patterns indicates the $\bar{\Gamma}$ point of the Brillouin zone(see Fig. 7.5) and the distance from the center of the figure is proportional to the wave numbers in the momentum space. On the observed PEAD patterns we added the lines of the BZ of $TX_2$ by white hexagon afterward.

In these figures, the binding energy dependence of the PEAD pattern is clearly seen. These PEAD patterns are mainly attributed to the band structure of the $1T\text{-}TaS_2$. Comparing gross features of the PEAD patterns of 33_0 with 33_30, the rotation of the PEAD patterns in accord with the sample rotation by 30° is directly observed for example at $E_B=1.0$ and 1.4eV. (Contrary to the observed PEAD rotation the intensity by the electric discharge of the MCP which are seen at the bottom of the images does not rotate.) When we further rotate the sample by 30° (ie. the configuration of _60), the PEAD patterns rotated further and changed to the flipped patterns of the 33_0 pattern about the plane which is perpendicular to the electric field vector as shown clearly in Fig. 7.15. This is because the reversed configuration of 33_60 between the crystal structure and the electric field of light to that of 33_0.

The Ta $5d$ band which disperses from the Fermi level near the region with 1/3 of the wave vector of the $\bar{M}$ point to the $\bar{M}$ point for larger wave vector on the $\Sigma$ line in the band calculation of Mattheiss(Fig. 7.2) is clearly observed in the PEAD patterns of $E_B=0.2$ to 1.8eV in both series of 33_0 and 33_30. In addition, the $5d$ band dispersion along the T' line is also represented in the PEAD pattern of $E_B=0.2eV$ to 1.8eV. That is to say the oval corresponds to the $d$ band around the $\bar{M}$ point becomes smaller and smaller from $E_B=0.2$ to 1.8eV. Thus the band calculation seems to well explain the Ta $5d$ band except that the dispersion width of the band derived from the experiments is about 1.8eV, which is a little bit larger than that of the calculation of about 1eV.

As for the S $3p$ bands the observed PEAD patterns are also in qualitative agreement with the band calculation. The intensity near the $\bar{\Gamma}$ point for $E_B=1.4eV$ in the PEAD patterns spreads to the $\bar{M}$ points with increasing $E_B$ is considered to represent the uppermost S $3p$ bands which disperse rapidly from the $\bar{\Gamma}$ at about 2.3eV to the $\bar{M}$ point for larger $E_B$ in the calculation. The long two(one) bright and two faint slips of the PEAD patterns of $E_B=2.6eV$ in 33_0(33_30) are considered to correspond to the flat dispersion at about $E_B\sim3.4eV$ around the $\bar{M}$ point in the calculation. The drastic changes of the PEAD patterns in higher $E_B$'s may represent the intricate band structure of the six fold S $3p$ bands. It seems that the $E_B$'s of the calculated dispersions for S $3p$ bands, however, are generally higher than those of experiments by about 0.8eV$\sim$0.9eV as far as we compare the PEAD patterns with the calculated band dispersion of Mattheiss. This rigid shift of the S $3p$ bands is consistent with the ARPES results by Smith and Traum[10].

The observed cross sectional view of the band structure seems to have a three fold symmetry as far as the shapes of the PEAD patterns are concerned, as typically observed for the patterns of the Ta $5d$ band for $E_B=1.0$ and 1.4eV or for the S $3p$ band at $E_B=2.6$ and 3.4eV. The threefold symmetry is considered to reflect the crystal structure of $1T$- type $TX_2$. This three fold symmetry of the photoemission intensity of the $1T$- type crystal was also discussed by Smith and Traum[10]. In a rigorous sense, however, when we consider the observed PEAD patterns have only a mirror symmetry. The mirror plane is parallel and vertical to the electric field vector for the patterns of 33_0 and 33_30, respectively. This symmetry breaking is
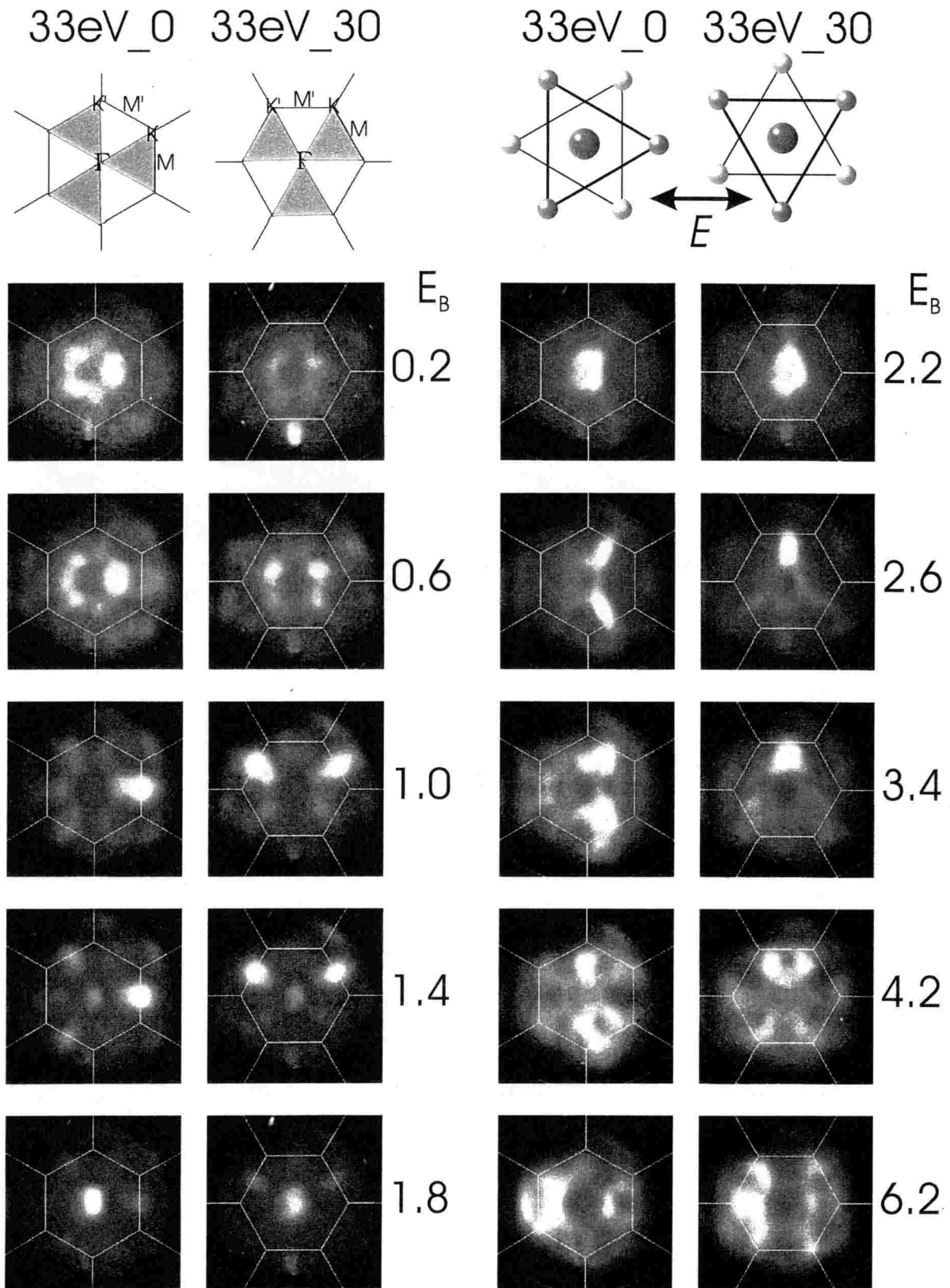
Fig. 7.13: PEAD patterns of the $1T$-$TaS_2$ measured at h$\nu$=33.0eV for off-resonance photoemission condition. The configuration between electric field of the incident photon(indicated by an arrow) and the direction of the crystal are presented by illustration. That is the configuration between electric field and the sample of right-hand is rotated 30° from that of left-hand. The Brillouin zone corresponding to each configuration is also presented.
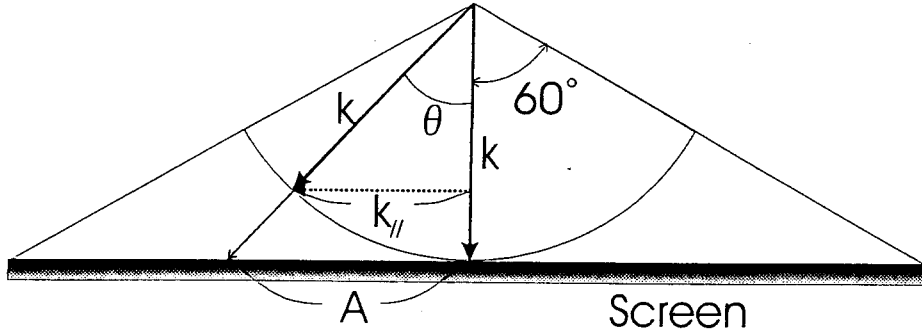
$$k_{//} = k \sin \theta$$
$$A = k \tan \theta$$
$$k_{//} = A \cos \theta$$

Fig. 7.14: Schematic view of the relation between observed pattern on screen and the momentum space. $A$ is the length which is observed on the screen and $k_{\parallel}$ is the wave number on the $k$ space corresponding to the length of $A$.

due to the selection rule of the dipole transition which is requested by the linear polarity of the incident light and the symmetry of the wave function of the initial state. Figure 7.16 is the simulated PEAD patterns of $1T$-$TaS_2$ at various $E_B$ for the linear polarity of the light. In this simulation the wave functions of the initial state and final state are assumed to be the Bloch state in the tight binding approximation and plane waves, respectively. The parameters of the base functions of the initial states used in the calculations are obtained by fitting the band dispersions presently derived from the tight-binding calculation with those calculated by Mattheiss[4]. The details of the calculation have been described in our previous papers[5, 20, 21]. The calculated patterns are presented by negative images to give clear features of the patterns. To compare the calculated patterns with the experimental ones an energy resolution of $\Delta E = 0.3$eV is also considered. The calculated results are in fair agreement with those of experiments especially at the lower binding energies corresponding to Ta $5d$ band. The mirror symmetry of the experimental patterns is successfully reproduced by the calculation[5, 20, 21]. According to the calculation[5, 20, 21] the PEAD patterns can be understood as the products of the three terms that "one-dimensional density of state; the band structure", "photoemission structural factor", and "angular distribution from atomic orbital". And the intensity distributions of the PEAD patterns depend on the photoelectron transition probability between the final state and the atomic orbitals of the initial states. Therefore, both experimental and calculated images of the Ta $5d$ band have very small intensity in the central zone perpendicular to the electric field of the incident light because of the dominant $d_{z^2}$ component in the Ta $5d$ occupied band. Namely the matrix element of $\langle \epsilon p | p \cdot A | d_{z^2} \rangle$ or $\langle \epsilon f | p \cdot A | d_{z^2} \rangle$ has no intensity in the plane perpendicular to the electric field of the excitation light[5]. Thus the photoelectron intensity distribution from the atomic $d_{z^2}$ orbital should be like the illustration of Fig. 7.17. We named this plane which is perpendicular to the electric field of the excitation light as the forbidden plane in this thesis here after.

130

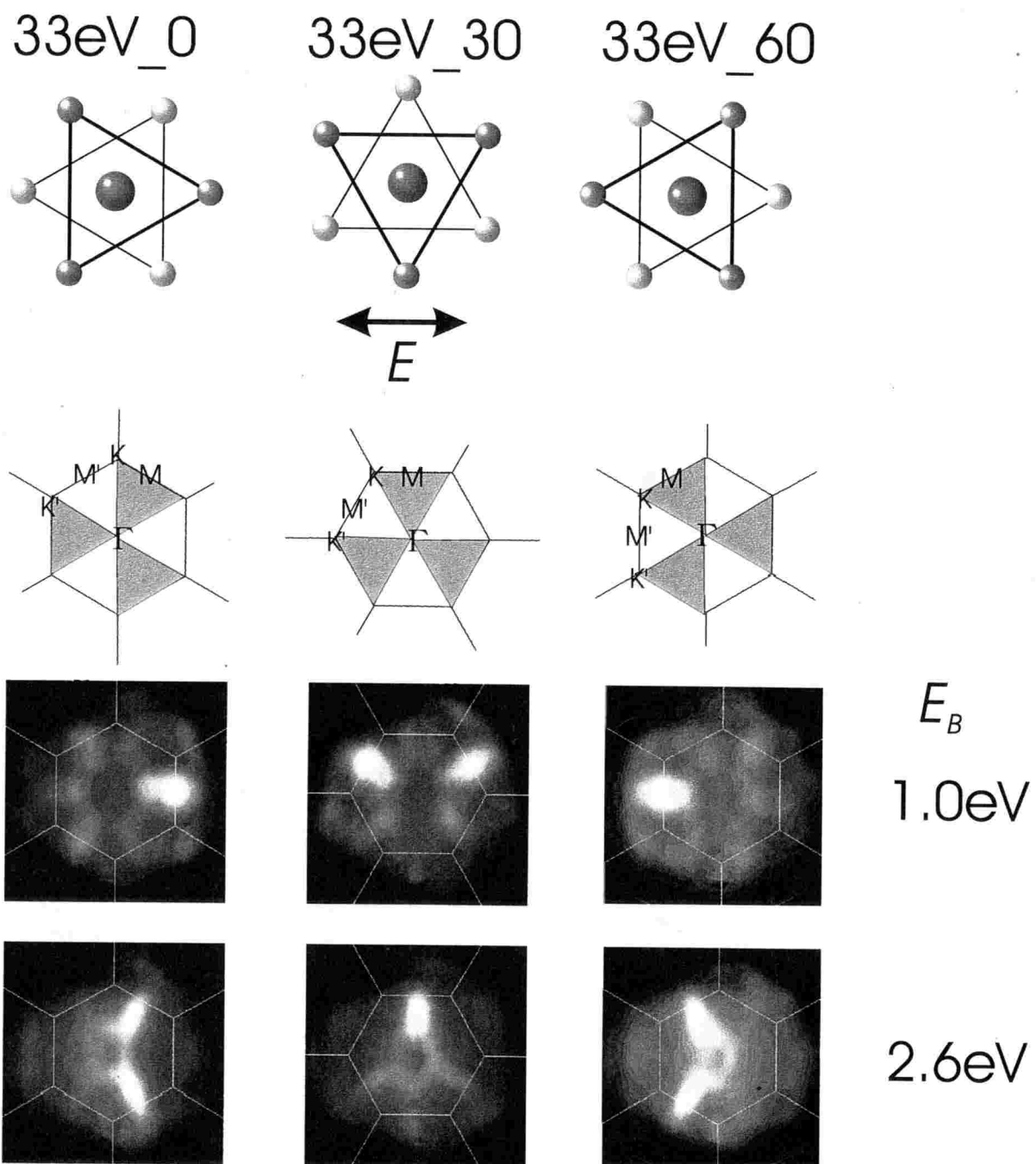33eV_0    33eV_30    33eV_60

$E$

$E_B$

1.0eV

2.6eV

Fig. 7.15: Observation of the rotation of the PEAD pattern. The meaning of the illustrations of the figure are the same as to that of the previous figures.
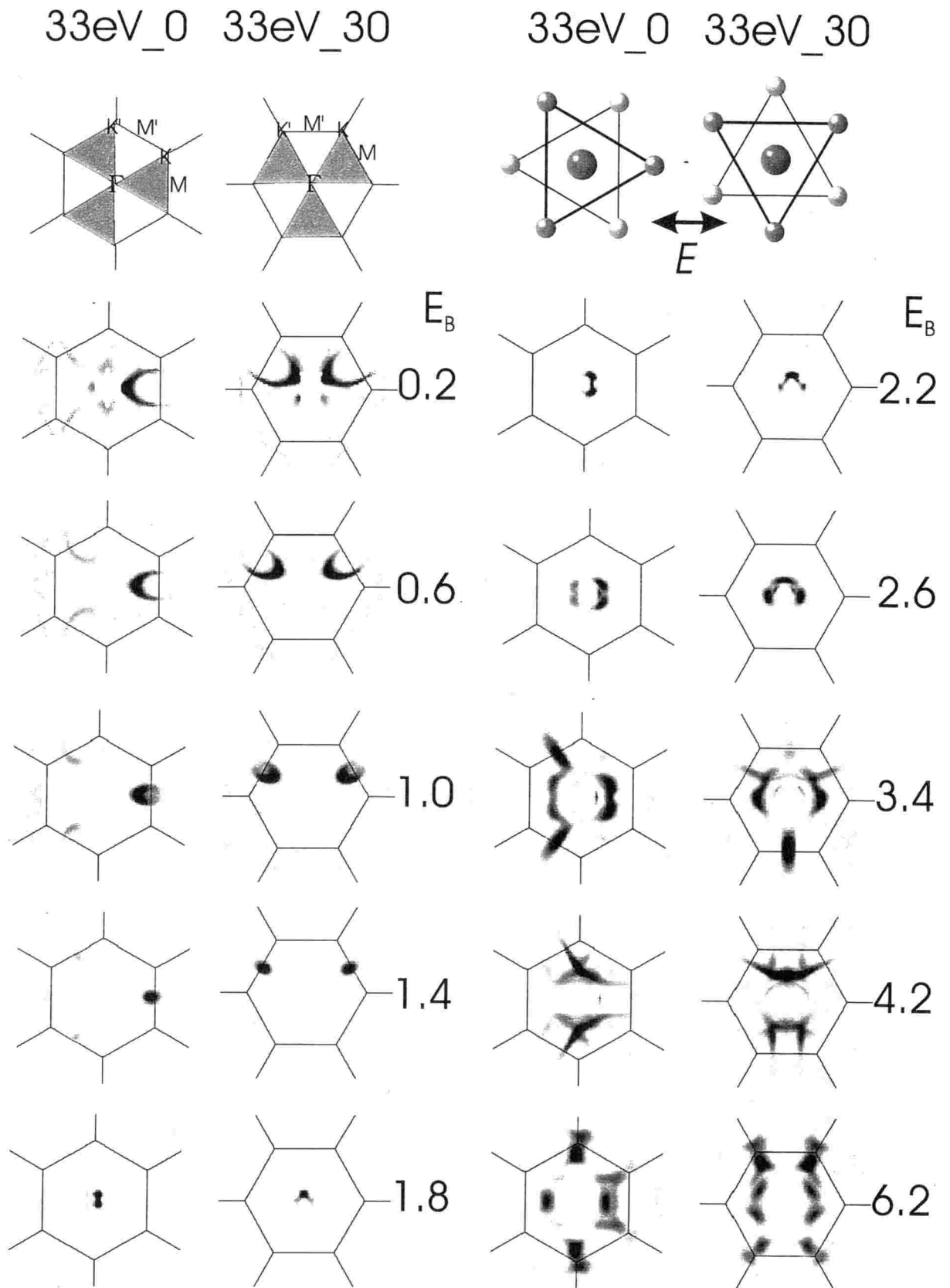
Fig. 7.16: Simulated PEAD patterns of the $1T$-$TaS_2$ at h$\nu$=33eV. The calculation had performed at the same $E_B$ to the experimental PEAD patterns of Fig. 7.13.

For the same reason the atomic $p_z$ orbital can not be observed in the same forbidden plane to that of the $d_{z^2}$ orbital and the PEAD pattern of $E_B$=6.2eV which has no intensity on the forbidden plane is considered to be the band structure of the S $3p_z$ orbital. According to the band calculation of Mattheiss, the S $3p$ band with the highest $E_B$($1^+$ band in his notation) has the symmetry of the $p_z$ orbital which is consistent with our PEAD patterns.



Intensity distribution from $d_{z^2}$ orbital($E_B$=0eV)
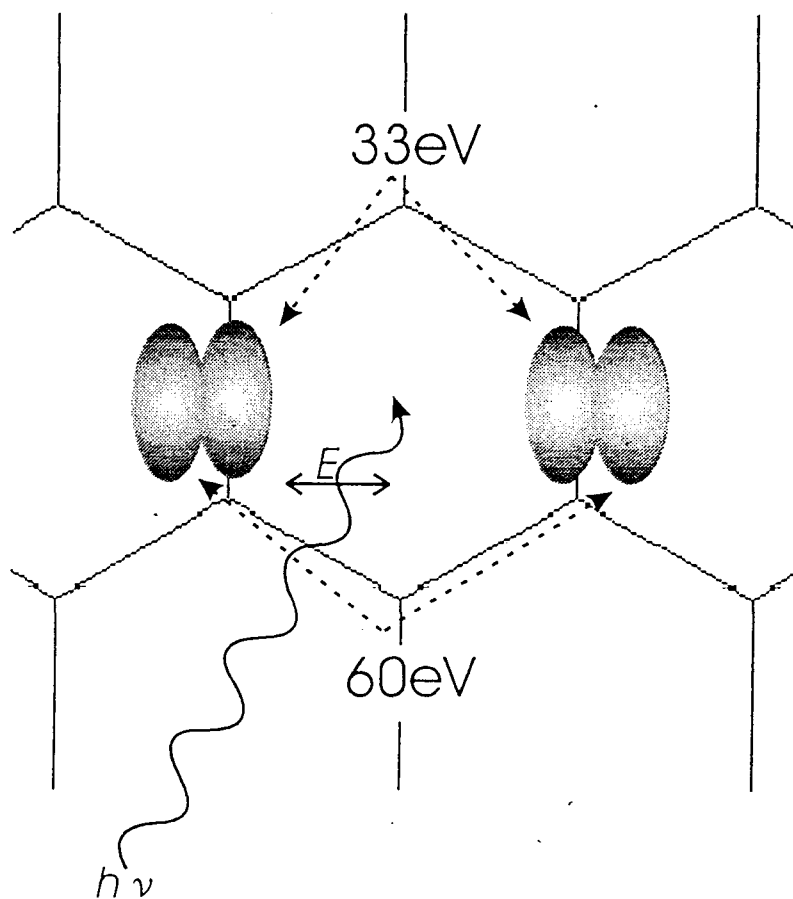
Fig. 7.17: Photoelectron angular distribution from the atomic $d_{z^2}$ orbital excited by linearly polarized light

Faint intensities are seen in the region even for binding energies of 0.2 or 0.6eV which correspond to the Ta $5d$ band, especially in the series of 33_0. These faint intensities are considered to be due to the other $d$ components such as $d_{xy}$ or $d_{x^2-y^2}$ which are contained slightly in the occupied Ta $5d$ band as expected by calculation of Mattheiss. These faint intensities are also expected by our PEAD calculation. Thus these faint intensities are understandable only considering the mixing of the other $d$ components with $d_{z^2}$ orbital and we need not consider the CDW effect as discussed by Smith and Traum[10]. In higher $E_B$ region of Ta $5d$ band, the intensity reduction on the forbidden plane is remarkable as seen for

$E_B$=1.0eV. Especially for the patterns of $E_B$=1.0 or 1.4 eV in the 33_30 series, no intensities are observed on the plane.

Regarding to the S $3p$ band the consistency between the experiment and the simulation calculation is not so good. The PEAD pattern at $E_B$=1.4eV of Fig. 7.13 has shown that the S $3p$ band has already appeared at the $\bar{\Gamma}$ point in contrast to Fig. 7.16. The characteristic shapes at $E_B$=2.6eV are also not reproduced by the calculation. The calculated patterns for the $E_B$=3.4eV are similar to that of the experimental patterns of $E_B$=2.6eV, although the intensity distribution of calculated patterns are reversed comparing to experiments. Thus it seems to be necessary to shift the $E_B$ of the calculation by about 0.6~ 0.8eV toward the $E_F$. The reason of the reversal of the intensity distribution of the calculated patterns for the S $3p$ state is not evident at present. First the value of the phase shift which strongly affects the intensities of the PEAD patterns may be deviated from the adequate values of the S $3p$ band in 1$T$-TaS$_2$ , because in our calculation we used the value of phase shift for "atomic" S $3p$ electrons. Another possibility is that the employed parameters of the base functions for the S $3p$ states may not be correct. Then more precise calculations considering second nearest neighbor atoms or(and) final state effects $etc.$ are required.

The faint intensities of the Ta $5d$ band at $E_B$=1.8eV in Fig. 7.13 are neither reproduced by the simulation though we consider the energy resolution effect in the calculation. Thus the band width of the Ta $5d$ band should be larger than that of the calculation.

According to Smith and Traum[10] the azimuthal angle dependence of the Ta $5d$ photoemission intensity of 1$T$-TaSe$_2$ shows the dip structure in the direction of the $\bar{M}$ point. They concluded that the reason of this dip structure is due to the shadowing effect by the nearest Se atoms. However, as shown in the simulation patterns of $E_B$=0.2, 0.6 and 1.0eV, the cross sections of the Ta $5d$ band have oval edges around the $\bar{M}$ point that the whole intensity of the Ta $5d$ photoemission will have dip at the direction of $\bar{M}$ point without considering shadowing effect. In the experimental patterns of the $E_B$=1.0eV we cannot see the oval edges because of the finite angular and energy resolutions(about $\pm2°$ , 0.25eV), but the patterns at $E_B$=0.6eV seem to have oval edges around $\bar{M}$ point.


*2H-TaSe$_2$ and 2H-NbSe$_2$*

To compare the PEAD patterns between 1$T$- and 2$H$- polytypes we have also performed 2D-ARPES for 2$H$-TaSe$_2$ and 2$H$-NbSe$_2$. Figures 7.18 and 7.19 are the angular integrated photoemission spectra of 2$H$-TaSe$_2$ at h$\nu$=28.4 and 40.6eV and 2$H$-NbSe$_2$ at h$\nu$=34.7 and 45.2eV, respectively. Sharp peaks at $E_F$<$E_B$<1.0eV in both samples are Ta $5d$ and Nb $4d$ bands, respectively. The band widths of these Ta$5d$ and Nb$4p$ bands seems to be relatively smaller than that of 1$T$-TaS$_2$ . The following broad peaks of $E_B$>1.0eV are Se $4p$ bands and we can see the five sub peaks and shoulders in these Se $4p$ bands in both 2$H$-TaSe$_2$ and 2$H$-NbSe$_2$ at h$\nu$=28.4 and 34.7eV. These peaks' or shoulders' positions are very similar both in 2$H$-TaSe$_2$ and 2$H$-NbSe$_2$ . The lower binding energies of the Se $4p$ than S $3p$ bands are consistent with the previous results of Smith and Traum[10] or the band calculation of Mattheiss[4].

Figures 7.20 and 7.21 are typical PEAD patterns of 2$H$-TaSe$_2$ and 2$H$-NbSe$_2$ which are obtained at h$\nu$=28.4eV and h$\nu$=34.7eV, respectively. The configurations between linear polarized light and the samples, and each BZ's are also indicated. The changes of the band structure cross section are clearly seen in both samples. In spite of the difference of the transition metals (Ta and Nb), the observed patterns of their $d$ bands are generally similar to each other. According to the band calculation of Mattheiss one of the largest differences

134
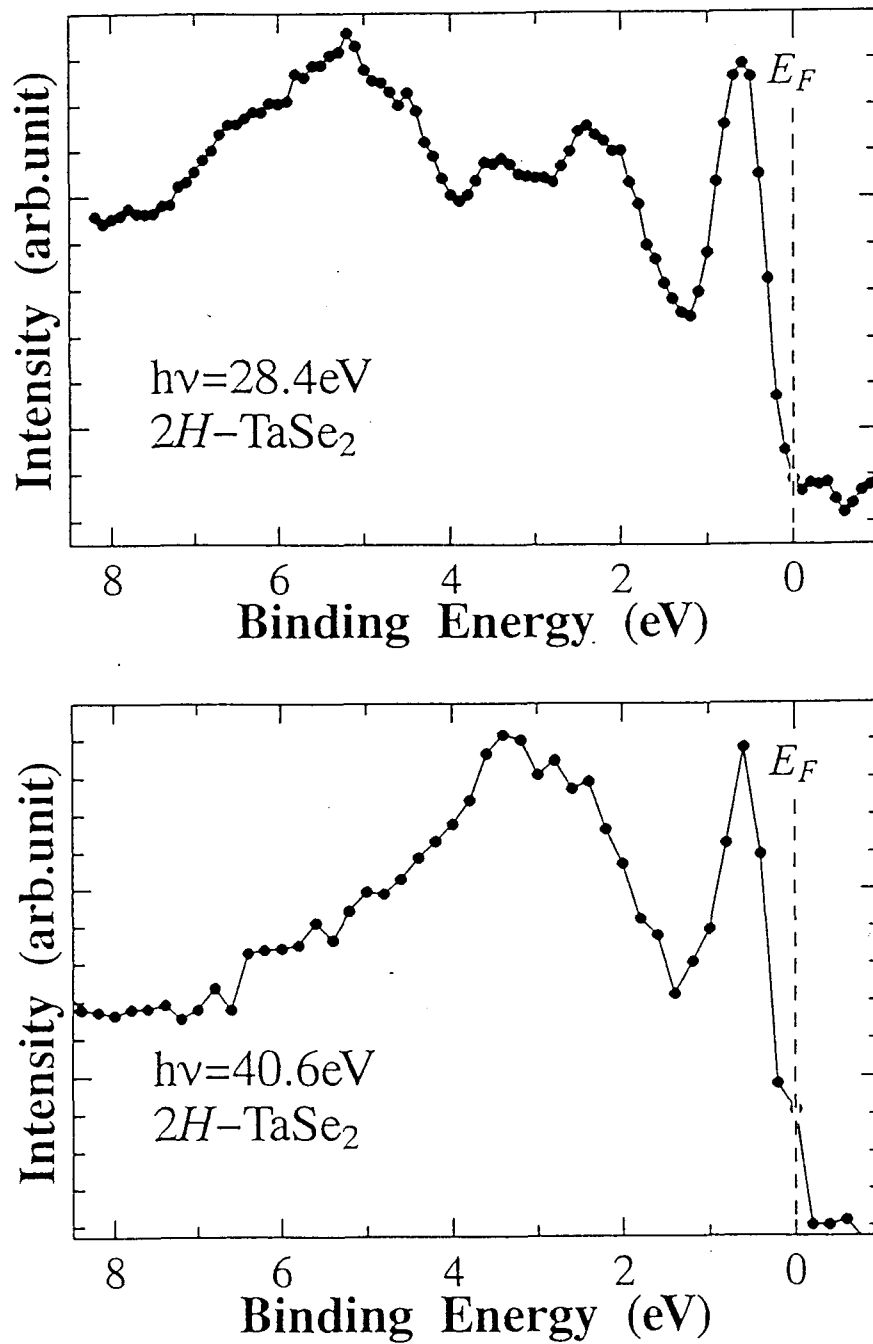
Fig. 7.18: Angular integrated photoemission spectra of $2H$-TaSe$_2$ at h$\nu$=28.4 and 40.6eV
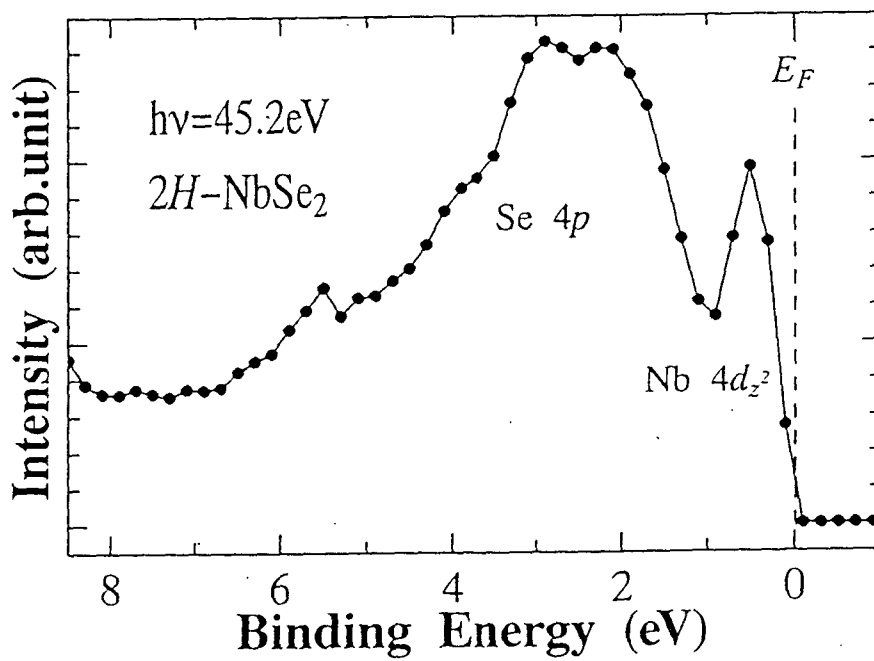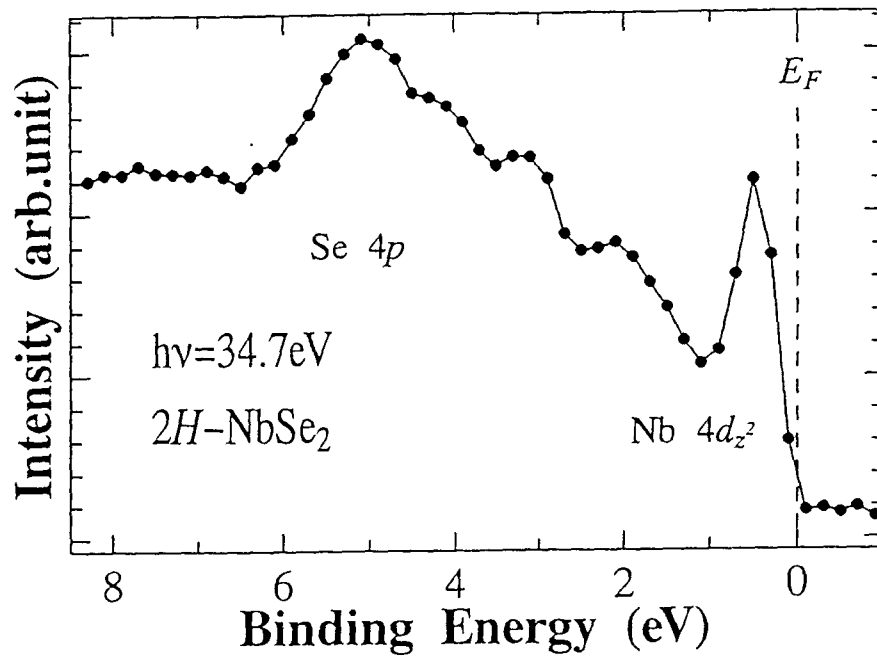
Fig. 7.19: Angular integrated photoemission spectra of $2H$-NbSe$_2$ at h$\nu$=34.7 and 45.2eV

## 28.4eV_0      _30          28.4eV_0      _30

$E_B$

0.1
(0,0)

0.3

0.6

0.8

1.1

1.5

$E_B$

1.9

2.4

3.0

3.5

4.7

5.3

Fig. 7.20: PEAD patterns of $2H$-TaSe$_2$ observed at h$\nu$=28.4eV

137

Fig. 7.21: PEAD patterns of 2H-NbSe$_2$ observed at h$\nu$=34.7eV. The dark dot near the $\bar{\Gamma}$ point in the each pattern is the traces of the electric discharge of the screen and not significant.

of the $d$ bands between $1T$- and $2H$- polytypes is the extra Fermi level crossing of the $d$ bands for the $2H$- type materials along $\Gamma$ to K (and A to H) direction in addition to along $\Gamma$ to M direction (See Fig. 7.3 and Fig. 7.4). In the PEAD patterns of these $2H$- type samples the both $d$ bands of $2H$-TaSe$_2$ and $2H$-NbSe$_2$ have intensities along the $\bar{\Gamma}$ to $\bar{\text{K}}$ lines and the results are consistent with the calculation. Another difference between $1T$- and $2H$- structures is that only one $d$ band in half filled exists in the former structure but there are two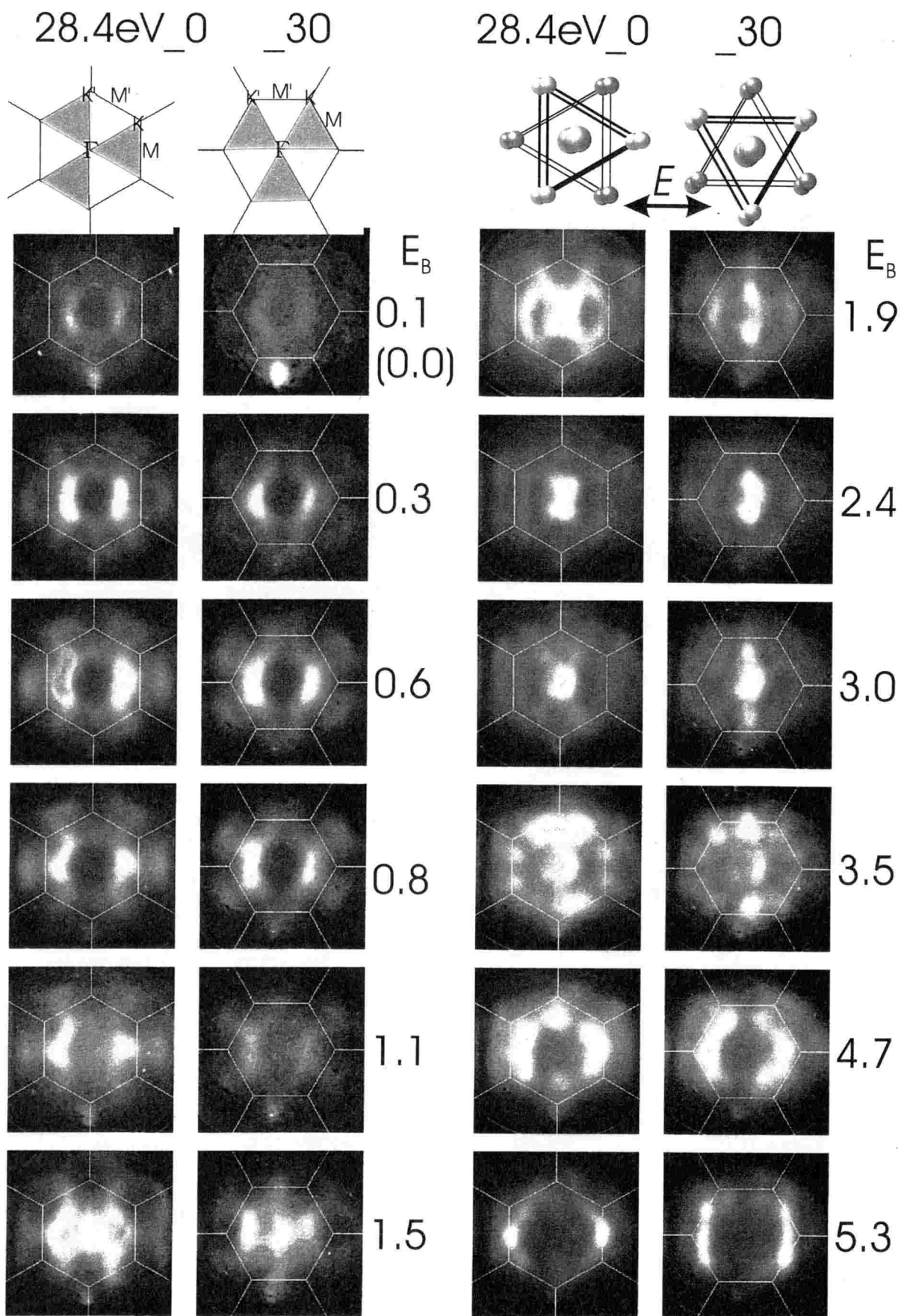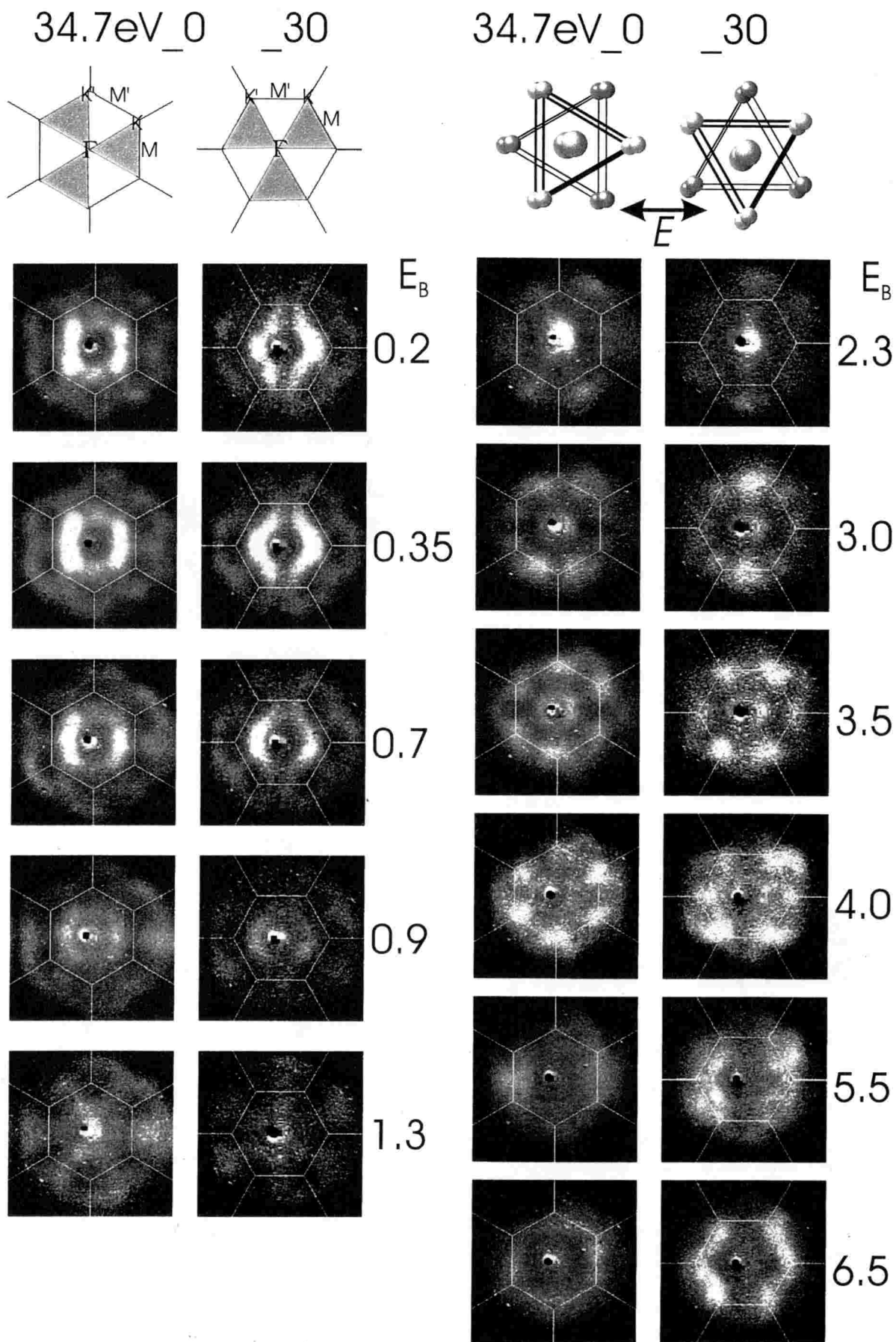 $d$ bands in the latter one. In the case of $2H$-NbSe$_2$ , one of these two $d$ bands of the calculation does not cross the Fermi level along the $\Gamma$ to M or K points and occupied even at the $\Gamma$ point. In the case of $2H$-TaS$_2$ of the Mattheiss' calculation which is considered to have similar band structure with $2H$-TaSe$_2$ , the Fermi level crossing points of the $d$ band are very close to $\Gamma$ point. Our PEAD patterns of the $d$ band, however, seem to have only one $d$ band and there is no intensity at $\bar{\Gamma}$ point. One of the possible reason of the absence of the intensity at $\bar{\Gamma}$ point is that the $d$ band is considered to consist of mainly $d_{z^2}$ orbital and the intensity is restrained by the aforementioned selection rule. Reflecting the character of $d_{z^2}$ orbital, the $d$ band patterns have no intensities along the lines perpendicular to the electric field especially 34.7_30 or 28.4eV_30. However, the existence of only one $d$ band at $E_F$ in our experiment may be due to the finite energy resolution of our experiments, and in the PEAD patterns of $E_B$=0.6eV of 28.4_0 of $2H$-TaSe$_2$ , the valley of the intensity distribution is observed in the Ta $5d$ pattern and it may be the evidence of the two separated $d$ bands.

Differences between $2H$-TaSe$_2$ and $2H$-NbSe$_2$ are observed in the patterns of $E_B$=1.5 or 1.9eV of $2H$-TaSe$_2$ and $E_B$=1.5eV of $2H$-NbSe$_2$ . In the PEAD pattern of $2H$-TaSe$_2$ at $E_B$=1.5eV there are still signal of $d$ band which has similar cross section to those of lower binding energies which have no intensity on the forbidden plane. In this PEAD pattern in addition to this residual Ta $5d$ signal, at $\bar{\Gamma}$ and $\bar{\text{M}}$ points Se $4p$ derived bands are also observable. This $p$ bands have intensity on the forbidden plane indicating the different symmetry from the $d$ band. This Se $4p$ bands are also seen in the PEAD pattern at $E_B$=1.5eV of $2H$-NbSe$_2$ , but do not coexist with $d$ band as the case of $2H$-TaSe$_2$ . Thus the band width of Ta $5d$ band of $2H$-TaSe$_2$ is larger than that of Nb $4d$ band of $2H$-NbSe$_2$ . This result is consistent with the relatively large dispersion width($\sim$ 1.8eV) of the Ta $5d$ band of $1T$-TaS$_2$ which is estimated from our measurement of $1T$-TaS$_2$ . In more larger $E_B$ region the PEAD patterns change very drastically and seem to be different between $2H$-TaSe$_2$ and $2H$-NbSe$_2$ especially at $E_B$=3.0 or 3.5eV. As seen in Fig. 7.4 the Se $4p$ bands are entangled each other and the large differences may be observed by small differences of $E_B$ or small differences of band widths of Se $4p$ bands between $2H$-TaSe$_2$ and $2H$-NbSe$_2$ . The Se $4p$ bands at $E_B$=5.3eV of $2H$-TaSe$_2$ or $E_B$=6.5eV of $2H$-NbSe$_2$ there is no intensity on the forbidden plane indicating that the Se $4p$ bands have $p_z$ symmetry and this result is roughly consistent with the band calculation which suggests that the highest three Se $4p$ bands have $p_z$ like character.

The PEAD patterns of these $2H$- type sample seem to have two mirror symmetries rather than one mirror symmetry. This result indicates the higher symmetry of $2H$- type samples than $1T$- type ones. However, this result is inconsistent with the result of Smith and Traum in which three fold symmetry of the $d$ bands of $2H$-TaS$_2$ excited by unpolarized light(h$\nu$=10.2eV) is observed and they concluded that the three fold symmetry of the $2H$-TaS$_2$ is due to the small mean free path of their photoemission measurements[10]. The difference of mean free path between the measurements of h$\nu$=10.2 and about 30eV, however, is not so large and the mean free path of the 30eV is rather smaller than that of the 10.2eV considering the universal curve. Thus the reason of the inconsistency is not clear. Even if the mean free path of our measurement is small, if our observed sample has two domains;

X-T-X-X'-T'-X' and X'-T'-X'-X-T-X, however, the three fold symmetry of the surface region may be compensated. To investigate the PEAD patterns of 2H- type crystals more precisely including this problem, the simulation of the PEAD patterns of 2H- polytypes is desired in the future.

## 7.3.2 Photon energy dependence of the photoelectron angular distribution patterns of TX$_2$

*1T-TaS$_2$*

We investigated the photon energy dependence of the PEAD patterns. Figure 7.22 is the total yield spectrum of the 1T-TaS$_2$ . In the figure two prominent peaks are observed at
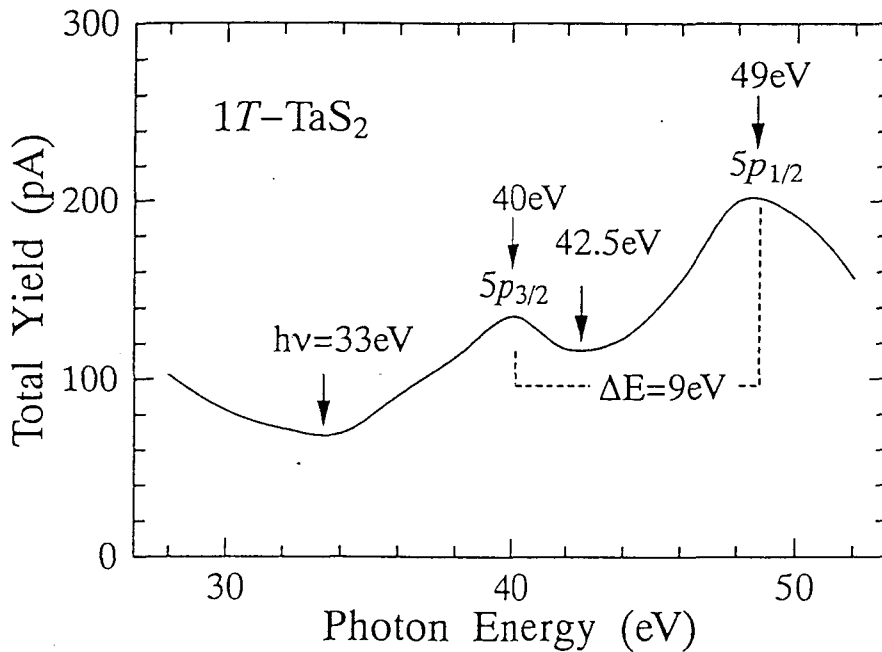


Fig. 7.22: Total yield spectrum of 1T-TaS$_2$ .

h$\nu$=40 and 49eV. This energy difference of 9eV is corresponding to the spin orbit splitting of Ta 5$p$ state and the intensity enhancement of the total yield spectrum at 40 and 49eV corresponds to the Ta 5$p$-5$d$ resonance photoemission. Namely the resonance between the process of Auger decay, Ta $5p^6 5d^1$+h$\nu$ $\rightarrow$ Ta $5p^5 5d^2$ $\rightarrow$ Ta $5p^6 5d^0$+$\epsilon l$ and that of the direct photoemission, Ta $5p^6 5d^1$+h$\nu$ $\rightarrow$Ta $5p^6 5d^0$+$\epsilon l$ occurs at the h$\nu$=40 and 49eV. The photon energies of resonant condition are comparable with those of resonance photoemission study of 1T-TaSe$_2$(h$\nu$=39 and 49eV) reported by Sakamoto *et al.*[22]. The PES spectra of the valence band of 1T-TaS$_2$ recorded by different photon energies which are normalized at about $E_B$=8eV are shown in Fig. 7.23. The photoelectron intensity enhancements are observed for both Ta 5$d$ and S3$p$ bands(indicated by arrows). The behaviors of the intensity changes are also shown in Fig. 7.24. The maxima of the intensity enhancements of both Ta 5$d$ and S 3$p$ are at about 40eV and 49eV which correspond to the resonance photoemission conditions. We have measured the PEAD patterns of 1T-TaS$_2$ at these on resonant conditions(40 and
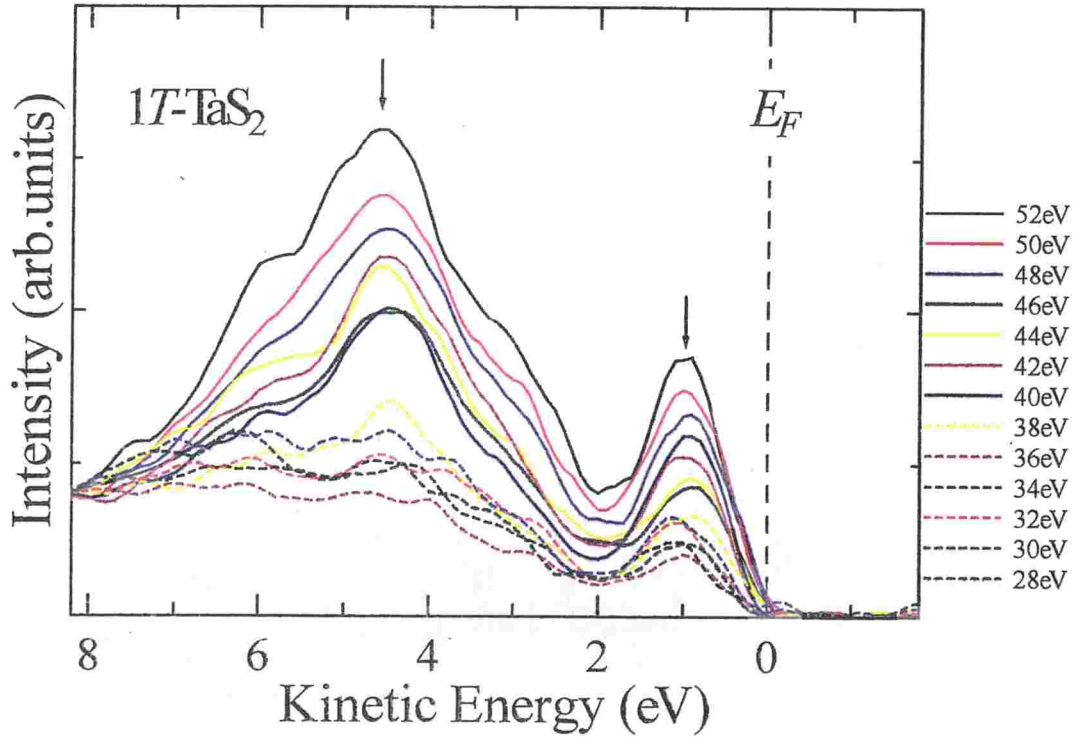
Fig. 7.23: PES spectra of $1T$-TaS$_2$ at different excitation photon energies

49eV) as well as at the mid of the resonance(42.5eV), and over-resonance condition(60eV) and compared with those of the off-resonance condition(33eV).

Figure 7.25 is the PEAD patterns of $1T$-TaS$_2$ which are recorded by h$\nu$=40.0eV(=on-resonance condition). The illustrations of the BZ's and configurations between electric field and crystal structure are in the same manner to those of the Fig. 7.13. We can see the changes of the PEAD patterns in accordance with the band structure of the $1T$-TaS$_2$ as the same way in the measurement of h$\nu$=33eV. Because of the higher photon energy than the previous measurement of h$\nu$=33eV the patterns are extended to the 2nd BZ's.

The most striking result of these PEAD patterns at h$\nu$=40.0eV is the relaxation of the photoemission selection rule. Namely, the photoemission intensities of the Ta $5d$ band which were observed only at M points but not observed at M' points of the illustrated BZ in Fig. 7.13 in the measurement of h$\nu$=33eV, are observed in the PEAD patterns in the measurement of h$\nu$=40.0eV. Especially, in the PEAD patterns of $E_B$=1.0 or 1.4eV the relaxation of the photoemission selection rule are remarkable. In these binding energies the intensities of Ta $5d$ bands are observed at every M and M' points in contrast with the PEAD patterns of h$\nu$=33eV.

In order to see the photon energy dependence of the PEAD patterns more clearly, I presented the PEAD patterns at different photon energies(h$\nu$=33, 40, 49, and 60eV) in the same binding energies in Fig. 7.26 and Fig. 7.27. Figure 7.26 and Fig. 7.27 are different from each other only in the measurement configuration($\phi$=0° and 30° ). As with increasing the photon energy we can obtain the information of larger wave length in momentum space. Namely, for higher h$\nu$ measurement, we can see the PEAD patterns of 2nd BZ's more clearly. In Fig. 7.26 and Fig. 7.27 the changes of the PEAD patterns in different photon energies
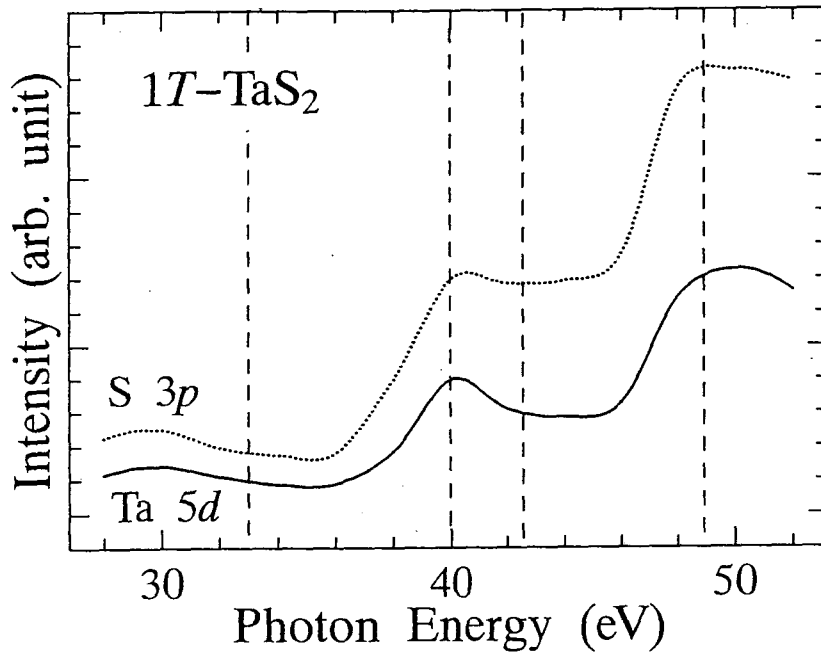
Fig. 7.24: Photon energy dependence of Ta $5d$ and S $3p$ photoemission intensities of $1T$-TaS$_2$

are more clearly seen. In the PEAD patterns of $h\nu$=49eV in the resonance condition, the patterns of Ta $5d$ band, especially of $E_B$=1.0 or 1.4eV, have intensities at M' points as well as M points indicating the breaking of photoemission selection rule. In the results of photon energy of 60eV which is over the resonance photoemission condition, however, the patterns have no intensities at some M' points and are different from the those of the on-resonance conditions of $h\nu$=40 or 49eV. The PEAD patterns of $h\nu$=42.5eV(not shown here), which is mid of the on-resonance conditions, indicated almost the same PEAD patterns to those of $h\nu$=40eV. This result indicates that the influence of the resonance photoemission must remain at $h\nu$=42.5eV.

In the PEAD patterns of another measurement configuration($\phi$=30° ,Fig. 7.27) we can also see the additional intensities at M' points at the on-resonance condition. On the contrary, in the over-resonance condition(60eV) we cannot see the $d$ emission intensities at M' points. Therefore we can conclude that on the resonance condition the intensities of $d$ bands are observable even on the forbidden plane.

Figure 7.28 and 7.29 are the simulated PEAD patterns corresponding to the experiments(Fig. 7.26 and Fig. 7.27) of $1T$-TaS$_2$ calculated by the same way as mentioned above.

In the calculation, the different phase shifts for different excited photon energies were considered but resonance photoemission effects were neglected. As seen in the figures, the calculated PEAD patterns are almost the same in different photon energies and the difference between them are only the intensity of each pattern and Ta $5d_{z^2}$ band has no intensities along the forbidden plane. The intensity difference between different photon energies is relatively large in S $3p$ band. The intensity differences are due to the different kinetic energies of the photoelectron in final states and different phase shifts and the experimentally observed unusual PEAD patterns cannot be explained by this effect.

The reason why the Ta $5d$ PEAD patterns have intensities on forbidden plane in the

142

40eV_0 40eV_30 40eV_0 40eV_30
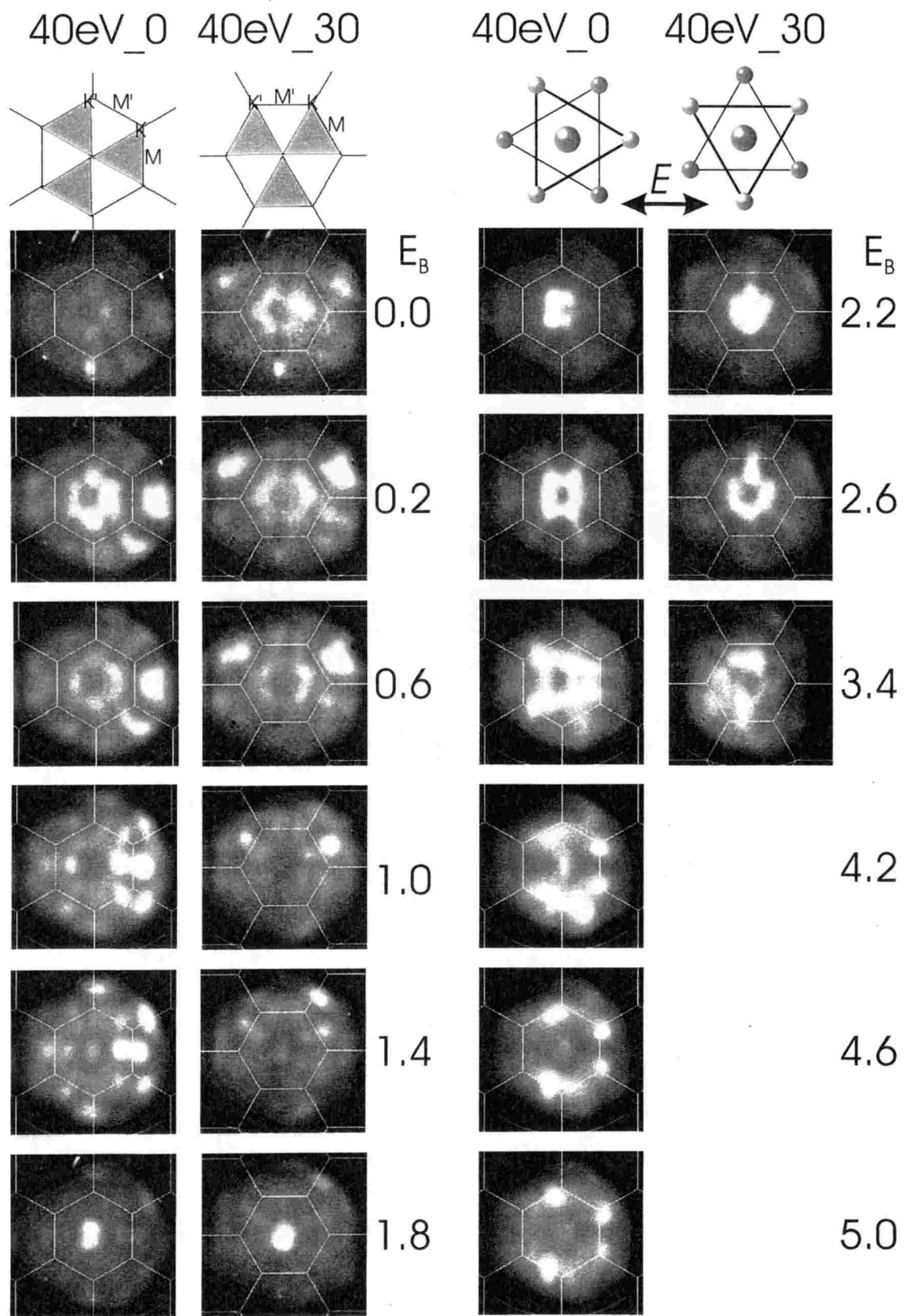


Fig. 7.25: PEAD patterns of 1$T$-TaS$_2$ at h$\nu$=40.0eV.
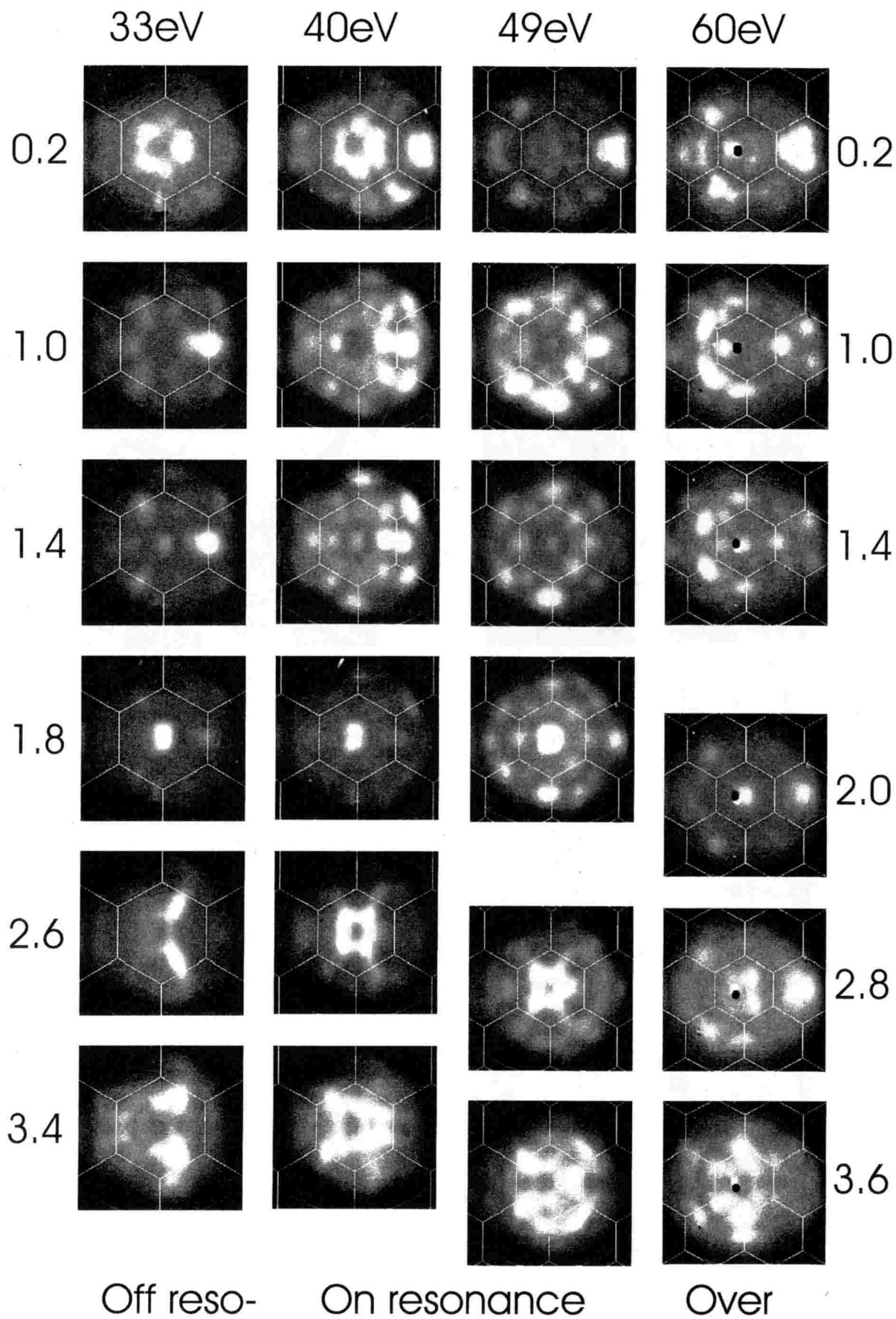
Fig. 7.26: Photon energy dependence of PEAD patterns of $1T$-$TaS_2$ ($\phi=0°$ ). The dark dot near the $\bar{\Gamma}$ point in the patterns of h$\nu$=60eV is the traces of the electric discharge of the screen and not significant.
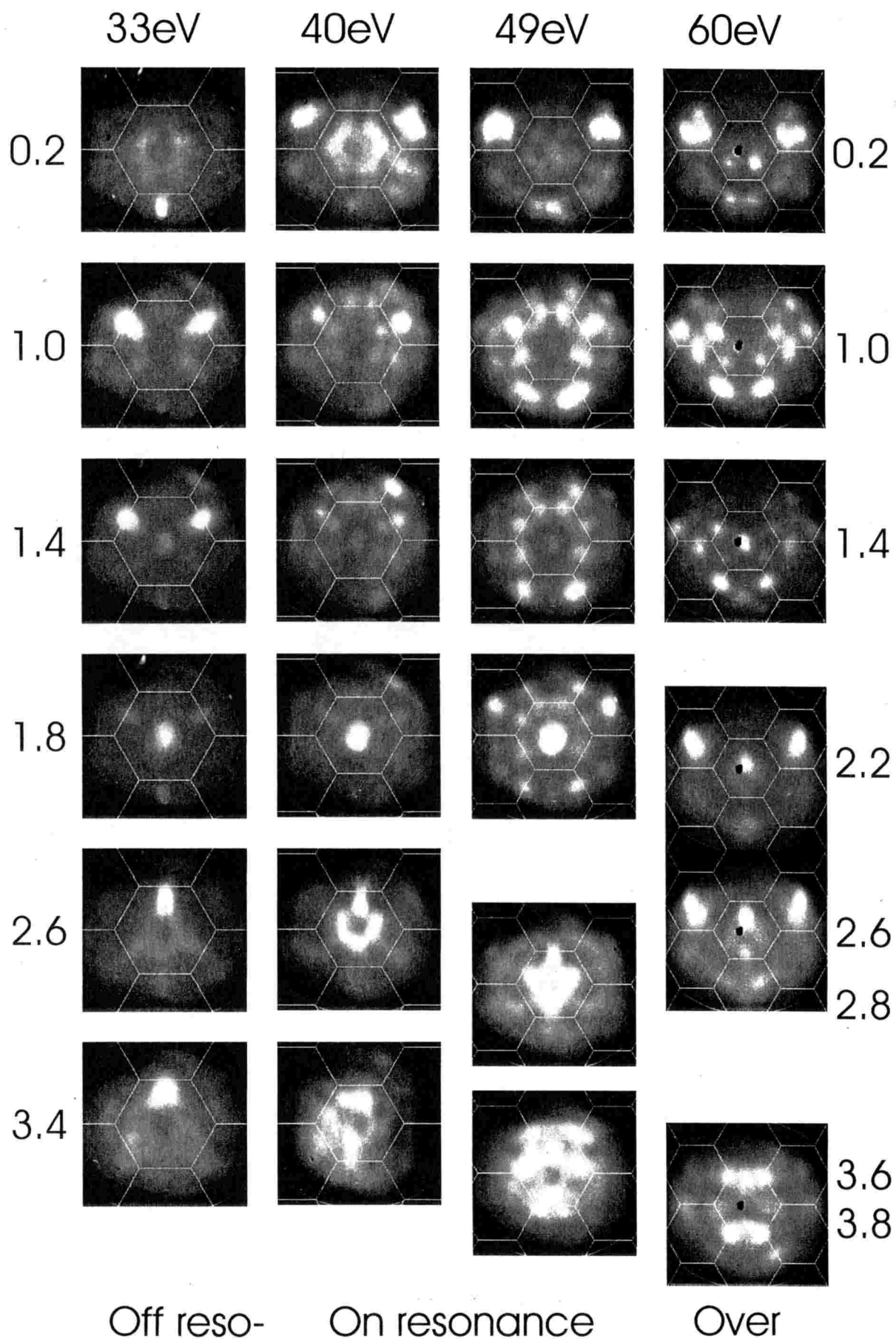
Fig. 7.27: Photon energy dependence of PEAD patterns of $1T$-$TaS_2$ ($\phi=30°$).The dark dot near the $\bar{\Gamma}$ point in the patterns is the traces of the electric discharge of the screen and not significant.

## 33eV     40eV     49eV     60eV
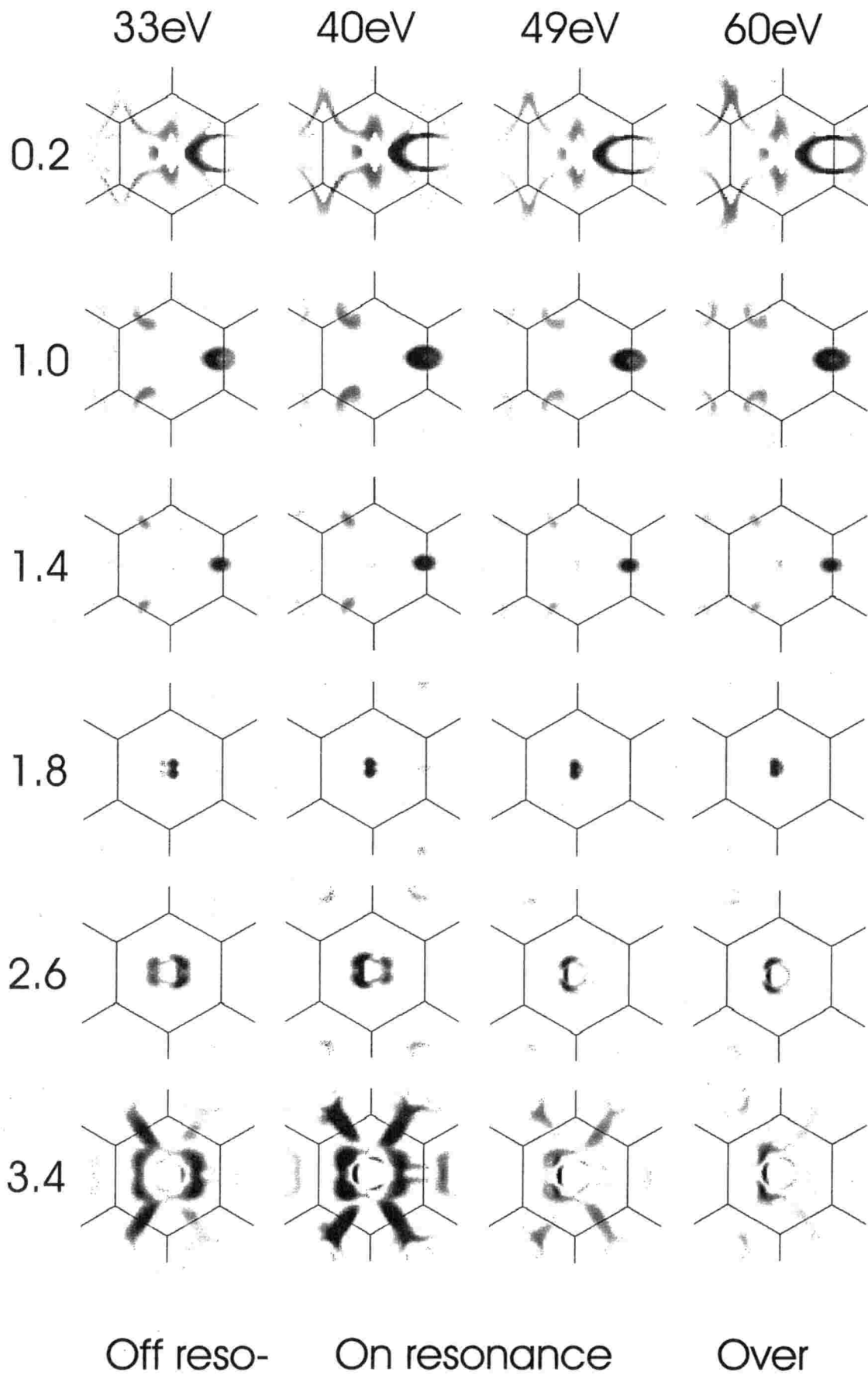
Fig. 7.28: Simulated PEAD patterns of the $1T$-$TaS_2$ by different $h\nu$'s at $\phi=0°$ . In this calculation the resonance photoemission effect is neglected.
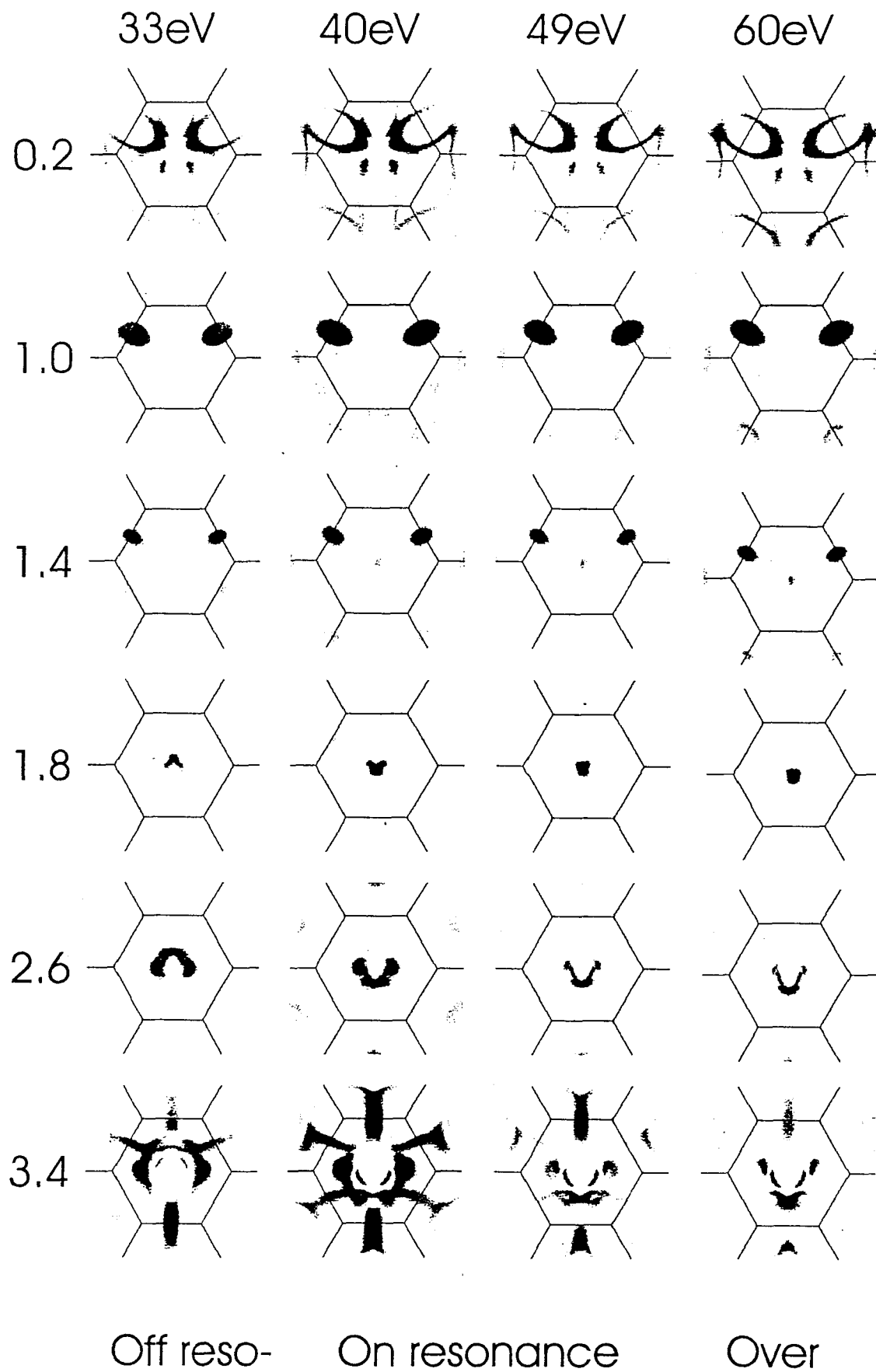
Fig. 7.29: Simulated PEAD patterns of the 1$T$-TaS$_2$ by different h$\nu$'s at $\phi$=30° . In this calculation the resonance photoemission effect is neglected.

on-resonance condition, has not been evident yet. In the resonance photoemission process, the direct recombination process of $5p^5 5d^2 \rightarrow 5p^6 5d^0 + \epsilon l$ takes place after the $5p$ excitation due to the Coulomb interaction $\langle 5d5d|1/r|5p\ \epsilon l \rangle$ and the $Y_{l'm'}$ of the photoelectron which is emitted by the direct recombination process can have the $l'm'$ vales which are not accessible by the dipole excitation. Dipole-forbidden $m'$ may allowed due to the spin-orbit interaction of the Ta $5p$ core hole in the intermediate state. In this interpretation, if the photo-excited electron of Ta $5d$ state directly recombines with the core hole of Ta $5p$ state, the electrons of Ta $5d$ state with the $k$ values which are not accessible by dipole excitation can also be excited as far as the energy conservation rule is satisfied. As mentioned already, in the PEAD patterns of h$\nu$=60eV of $E_B$=1.0 or 1.4eV, the intensity vanishing at forbidden plane is observed in 1st BZ, however, in the 2nd BZ there is faint intensity on the M points on the forbidden plane. This result may be due to the small amount of the contribution of this direct recombination process, ie. Auger decay in the h$\nu$=60eV measurement.

Recently the result of the angular distribution of the photoelectron of atomic Ca in resonance photoemission condition has been reported that the angular distribution of this Ca atom did not change from that of the off-resonance photoemission condition and the symmetry breaking of the photoemission in resonance photoemission was not observed in this atomic Ca[23]. Thus in order to understand the symmetry breaking of the PEAD patterns of the 1$T$-TaS$_2$ at resonance photoemission condition in our data, the effect of the solid may be important.

The proof of the three fold symmetry of the band structure of 1$T$-TaS$_2$ reflecting the three fold symmetry of the crystal structure is more clearly observed in the PEAD patterns of h$\nu$=40 or 49eV than those of h$\nu$=33eV. In the PEAD patterns of h$\nu$=40 or 49eV, the shape of Ta $5d$ band cross sections at M' point of $E_B$=0.2eV to 1.4eV are separated into two strips contrast to the almost one oval shapes at M point. These results seem to show the three fold symmetry of the 1$T$-TaS$_2$ clearly.

### 2H-TaSe$_2$ and 2H-NbSe$_2$

To investigate the photon energy dependence of PEAD patterns of 2$H$- type crystals, we have also performed 2D-ARPES measurement of 2$H$-TaSe$_2$ and 2$H$-NbSe$_2$ using different photon energies. Figure 7.30 shows the total yield spectrum of 2$H$-TaSe$_2$ . As shown in the figure, the spectrum have two prominent peaks at about h$\nu$=40 and 49eV as the same as that of 1$T$-TaS$_2$ . This two peaks also correspond to the photoemission enhancement due to the Ta $5p$-$5d$ resonance photoemission and consistent with the previous results[22]. We measured the PEAD patterns at this h$\nu$=40eV(on-resonance condition) in addition to the aforementioned 28.4eV(off-resonance condition). Figure 7.31 shows the observed patterns. As seen in the figure the observed patterns have a full of variety and change drastically as the change of the binding energies. The shapes of these PEAD patterns in 2nd BZ's are almost the same to those of the 1st BZ's. Contrary to the 1$T$-TaS$_2$ case, the PEAD patterns of 2$H$-TaSe$_2$ at h$\nu$=40.0eV seems to have forbidden plane which is perpendicular to the electric field. Namely the $d$ band PEAD patterns have a dark canal along the forbidden plane. To compare the PEAD patterns of h$\nu$=28.4 and 40eV directly we displayed the typical PEAD patterns of them in Fig. 7.32. The intensity distributions of observed patterns in the 1st BZ are almost the same in both h$\nu$=28.4 and 40eV in contrast to the case of 1$T$-TaS$_2$ . At first glance, it seems that the main difference between these two measurements is only the range of the observable wave length and the photoemission selection rule is conserved even in the h$\nu$=40 eV measurement. However, comparing the width of the dark canal of
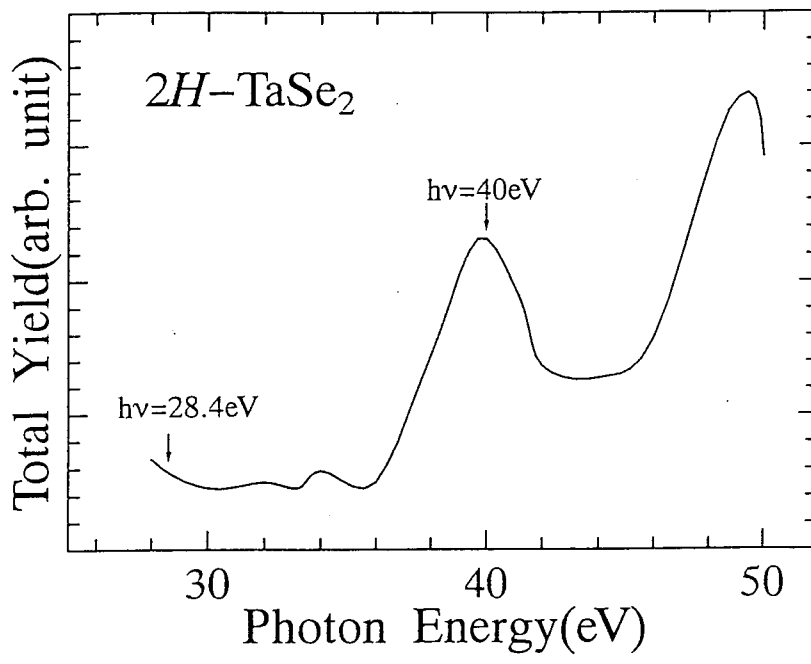
Fig. 7.30: Total yield spectrum of $2H$-TaSe$_2$
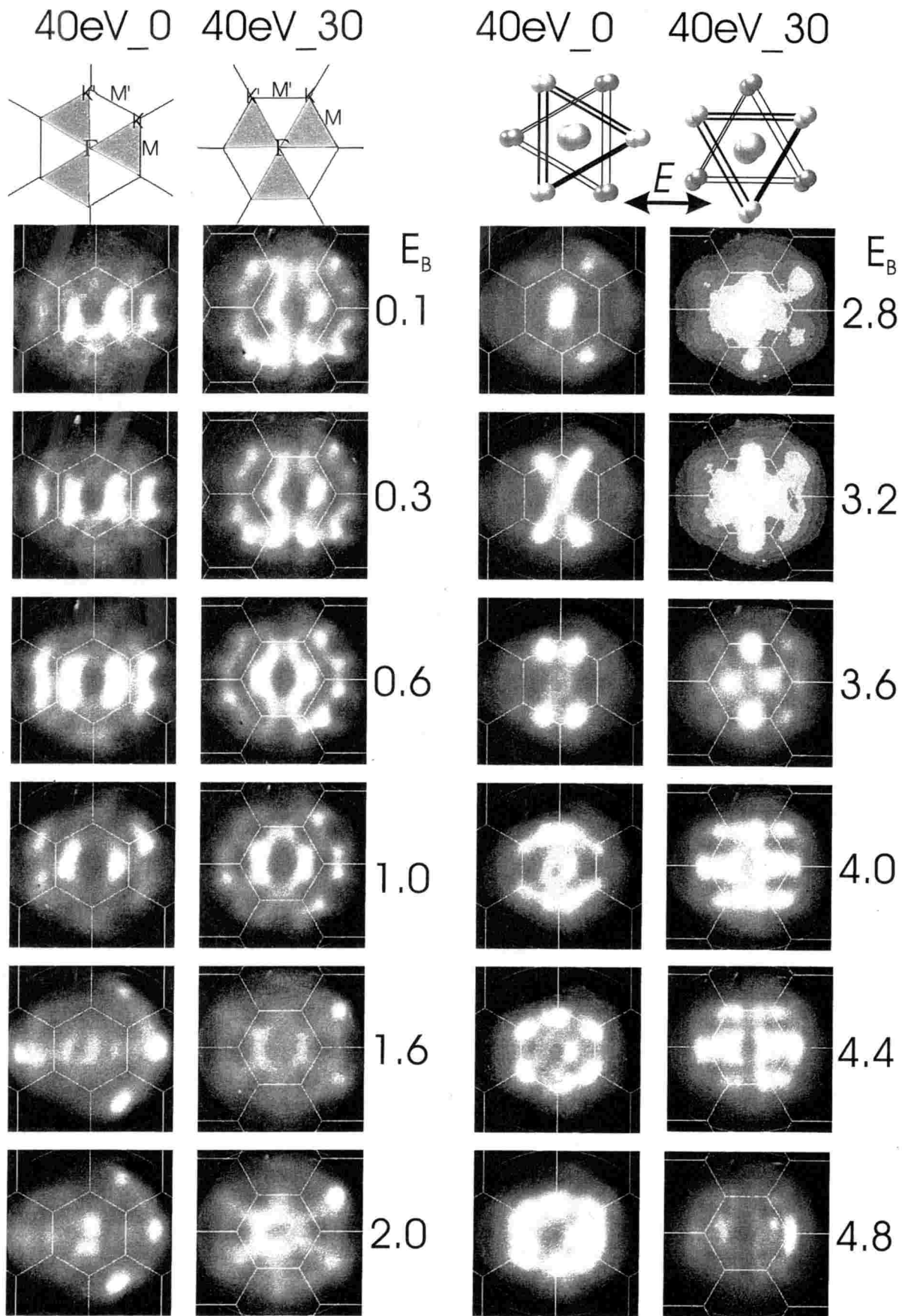
Fig. 7.31: PEAD patterns of the $2H$-TaSe$_2$ measured at h$\nu$=40eV. The meanings of the illustration are the same as to Fig. 7.13.
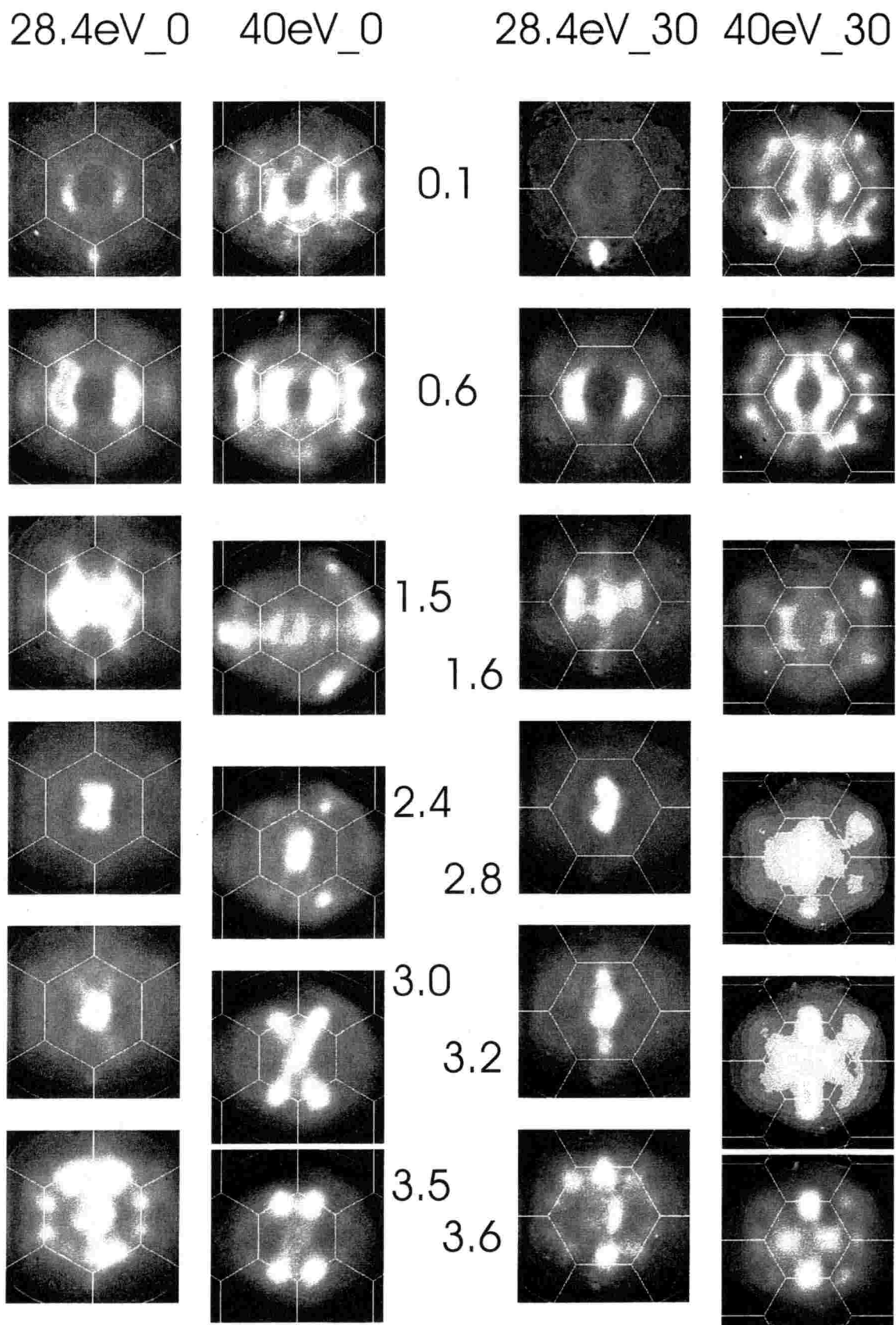
28.4eV_0    40eV_0        28.4eV_30  40eV_30



0.1

0.6

1.5
1.6

2.4
2.8

3.0
3.2

3.5
3.6

Fig. 7.32: PEAD patterns of the $2H$-TaSe$_2$ measured at h$\nu$=28.4 and 40eV.

151

the PEAD patterns of Ta $5d$ band between h$\nu$=40eV and 28.4eV measurements the width of former measurement is narrower than that of latter one. Considering the wider k-space range of h$\nu$=40eV measurement than that of 28.4eV, the width of the forbidden region in BZ of h$\nu$=40eV measurement, however, should be larger than that of 28.4eV one. Therefore we think that the narrowing of the forbidden region at the h$\nu$=40eV measurement comparing to the 28.4eV measurement is due to the effect of the resonance photoemission process.

For the 2$H$-NbSe$_2$ we did not perform the measurements at the photon energy of resonance photoemission condition but the measurement of higher photon energy at 45.4eV has done. Figure 7.33 shows the PEAD patterns of the 2$H$-NbSe$_2$ excited by the h$\nu$=45.4eV photon. At first glance the PEAD of Nb $4d$ band of series of 45.4_30 shows very interesting shape and seems to be different from those observed in the measurement of h$\nu$=34.7eV. These complex patterns ,however, consist of the repeated patterns of $d$ band structure in 1st BZ. In these patterns of Nb $4d$ the clear intensity reduction along forbidden plane can be seen. On the other hand the PEAD patterns of series 45.4_0 is very similar to those of 37.2_0. This similarity between the measurement of 45.4 and 34.7eV are more clearly seen in Fig. 7.34. Not only the PEAD patterns of Nb $4d$ band but also those of the Se $4p$ band are quite similar in each other.

One thing which we are concerned is the existence of the Nb $4d$ intensity along the forbidden plane in the PEAD pattern of the 45.4_0 measurement at $E_B$=0.5eV. These $d$ band intensity is also observable in the PEAD patterns of 34.7_0 though its intensity is very weak. Though we did not ensure the photon energy of the Nb $4p$-$4d$ resonance photoemission condition, from the $E_B$ of the atomic Nb $4p$ state($\sim$30eV) the h$\nu$'s which we used in this measurements are considered to be lower than the that of the resonance photoemission condition. However, as the measurement of the h$\nu$=60eV of 1$T$-TaS$_2$ in which some extra photoemission intensities on forbidden plane were observed, the remanent effects of the Auger decay may contribute the PEAD patterns in these 2$H$-NbSe$_2$ measurements. These extra intensities are not observed in _30 measurements of both 34.7 and 45.4eV measurements and the intensity may not be the evidence of the breaking of the dipole transition selection rule, and the extra intensity may be due to the existence of the other symmetry $d$ orbitals such as $d_{xy}$ or $d_{x^2-y^2}$ which are expected by the calculation of Mattheiss. In addition, in contrast to the case of the measurements of 2$H$-TaSe$_2$ , the width of the canal of the forbidden area in BZ for the h$\nu$=45.4eV measurement is larger than that of the 34.7eV measurement and the resonance photoemission effect which is observed in the 2$H$-TaSe$_2$ measurement may have not been observed in these 2$H$-NbSe$_2$ measurements.

## 7.3.3 Fermi surfaces of 1$T$-TaS$_2$, 2$H$-TaSe$_2$ , and 2$H$-NbSe$_2$

I would like to discuss about the Fermi surface of the 1$T$-TaS$_2$ , 2$H$-TaSe$_2$ , and 2$H$-NbSe$_2$ in this section. From the observed PEAD patterns of these TX$_2$ at near $E_F$ we can, in principle, know the shape of their Fermi surface directly. As already shown in Fig. 7.6 all these samples which we measured have CDW phase transitions and as mentioned in the section7.1.4 the occurrence of the CDW closely relates with the Fermi surface nesting. Thus the measurement of the shape of Fermi surface is very important.

Figure 7.35 is the comparison between the PEAD pattern of 1$T$-TaS$_2$ at $E_B$=0.2eV recorded by h$\nu$=33eV and that of simulated by aforementioned calculation. The S/N of the PEAD patterns at $E_F$ was too bad that we compared the PEAD patterns of $E_B$=0.2eV as the patterns of Fermi surface. As seen in the figure the experimental PEAD pattern has no(or very faint) intensities around the M point in contrast to the clear oval edge around
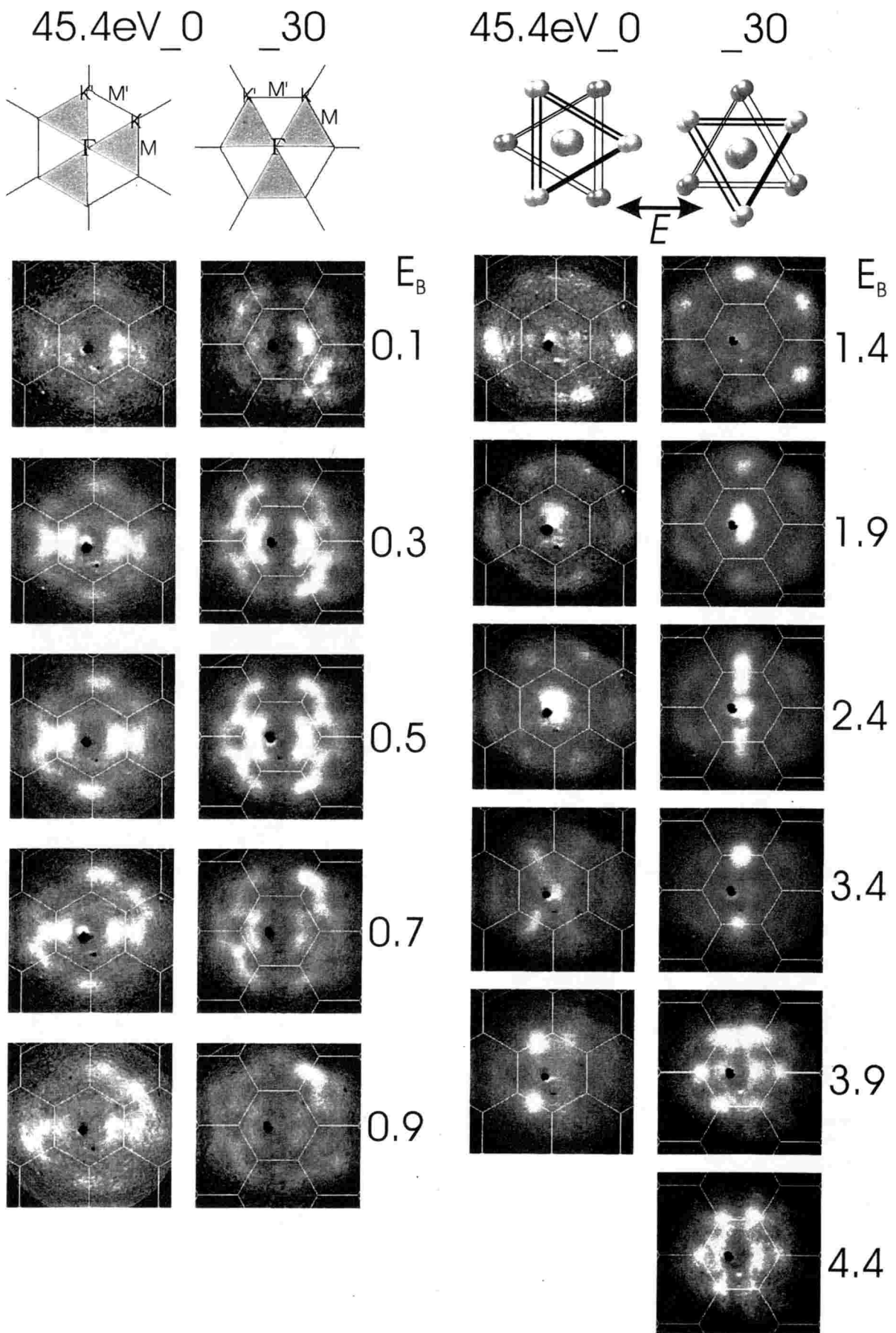
Fig. 7.33: PEAD patterns of the $2H$-NbSe$_2$ measured at h$\nu$=45.4eV. The meanings of the illustrations are the same as to those of Fig. 7.13. The dark dot near the $\bar{\Gamma}$ point in the each pattern is the traces of the electric discharge of the screen and not significant.

153
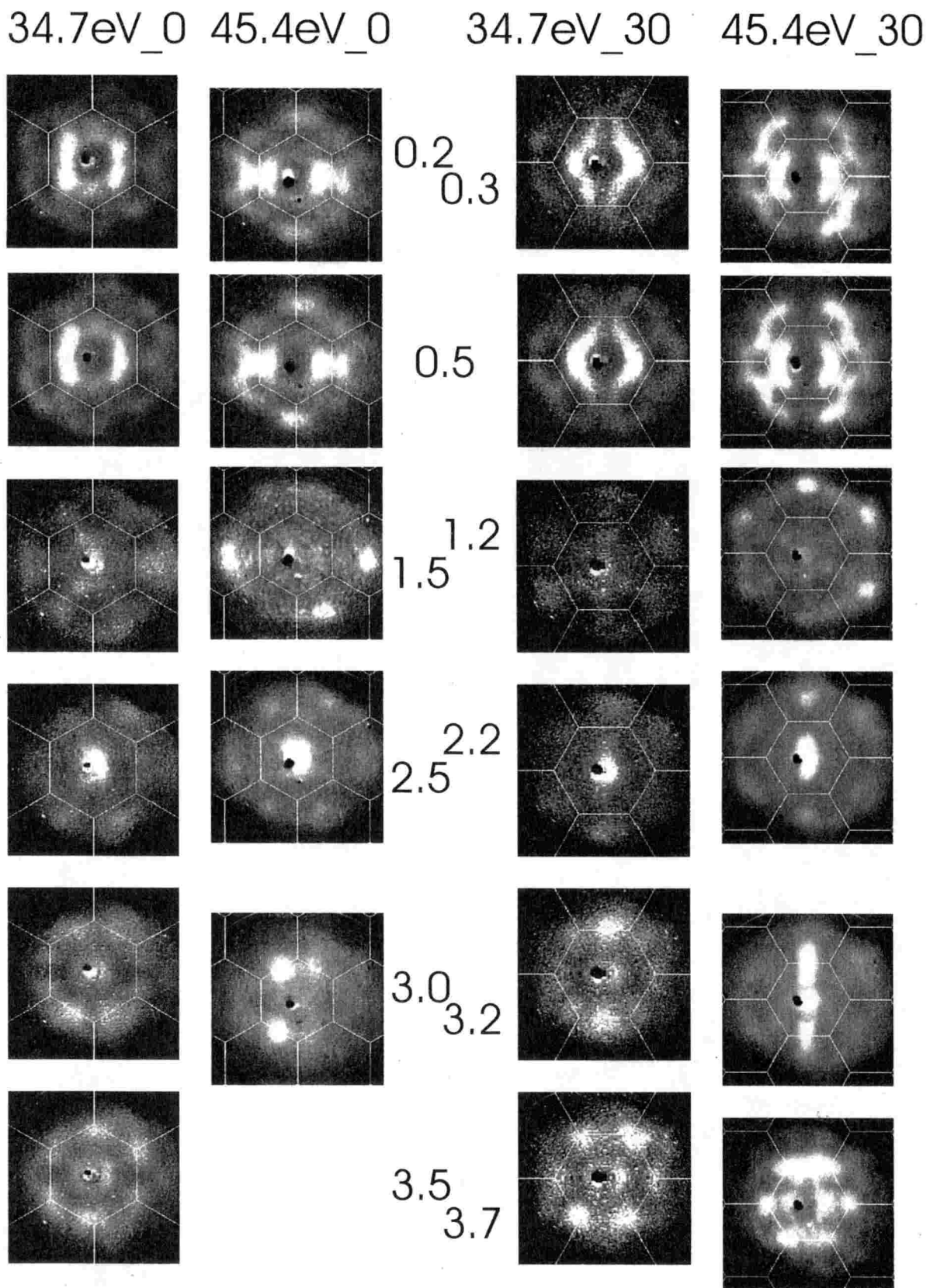
Fig. 7.34: Comparison of the PEAD patterns of the $2H$-NbSe$_2$ between h$\nu$=34.7 and 45.4eV. The dark dot near the $\bar{\Gamma}$ point in the each pattern is the traces of the electric discharge of the screen and not significant.

the M point of the calculated PEAD patterns. As mentioned in section7.1.4 the LEED patterns of the $1T$-$TaS_2$ indicates the $\sqrt{13} \times \sqrt{13}$ super lattice peaks rotated 13.9° due to the CDW distortion. From this results, the absolute value of nesting vector is that of the $1/\sqrt{13}$ reciprocal lattice vector and the direction of the vector should be rotated 13.9° from the $\Gamma$-M direction. We indicated the nesting vector by arrows in the figure. According to the calculated pattern the nesting vector almost connects the edges of the Fermi surface around M point, and the shape of these parts of the Fermi surface is so flat that the large nesting will occur. Interestingly, these parts of the Fermi surface in the experimental pattern vanishes as mentioned above and we consider the vanishing of the Fermi surface at these parts is due to the CDW gap opened at the large nesting parts. Therefore the CDW of the $1T$-$TaS_2$ is considered to be explained by the concept of the Fermi surface nesting.

As discussed above, in $1T$-$TaS_2$ the CDW exists even at R.T. as the NCCDW phase and the CDW gap has seemed to appear in the PEAD pattern. This NCCDW phase has been considered to consist of the domains of the commensurate CDW separated by discommensurations in which the CDW phase changes rapidly[8]. When we cool down the sample, the phase transition from the NCCDW to the CCDW occurs and this phase transition is accompanied with the metal-insulator transition and the PEAD pattern of the Fermi surface under the critical temperature($T_C$=180K) may change from that at R.T. This change of the Fermi surface has been tried to observe by Pollak $et$ $al.$ by the Eastman type display analyzer[12]. The change of their observed PEAD pattern was, however, distorted because of the characteristic of the analyzer and not clear. In the Fig. 7.36 we presented the results of the Fermi surface($E_B$=0.2eV) measurements of $1T$-$TaS_2$ at different sample temperature(R.T. and $T_S$=178K). As seen in the figure, the observed Fermi surface around M point at 178K is little bit smaller than that at R.T. and the intensity distributions also changed. Because of the finite energy and angular resolutions the change of the Fermi surface shape is not clear but the size reduction of the Fermi surface would be the evidence of the opening of the CDW gap.

In Fig. 7.37 we presented the PEAD patterns of (a)the $2H$-$TaSe_2$ and (b)the $2H$-$NbSe_2$ at $E_B$=0.3eV measured at h$\nu$=40eV and 45.4eV, respectively and calculated Fermi surfaces((c)~(e)) of $2H$-$NbSe_2$ by Nishino$et$ $al.$[27] with using tight binding approximation. The (c) and (d) are the Fermi surfaces of the $2H$-$NbSe_2$ at $\Gamma$-M-K plane of two different Nb $4d$ bands. These two bands are degenerated at the A-L-H plane and the Fermi surface at the plane is (e). Though we cannot determine the exact Fermi surfaces of $2H$-$TaSe_2$ and $2H$-$NbSe_2$ from our PEAD patterns because of their finite resolutions and the lack of the data along the forbidden plane, the observed patterns show the dark holes around K points which are considered to be the hole pockets at the K points from the comparison with higher $E_B$ patterns. In addition the round pattern like a circle around $\Gamma$ point has been also observed and the pattern is also the hole pocket at the $\Gamma$ point. These results is consistent with the calculated Fermi surface and band structures of $2H$-polytypes.

# 7.4 Summary

We have performed the 2D-ARPES measurements of the transition metal dichalcogenides, $1T$-$TaS_2$ , $2H$-$TaSe_2$ , and $2H$-$NbSe_2$ and observed photoelectron angular distribution(PEAD) patterns of these layered compounds. Because of the structural two dimensionality of these layered compounds the electronic structures of them are expected to indicate the two dimensionality. As the results the PEAD patterns of these $1T$-$TaS_2$ , $2H$-$TaSe_2$ , and $2H$-

$NbSe_2$ clearly shows their binding energy dependence which is due to mainly the band structure of each materials. As well as these patterns of the band cross section, the strong intensity asymmetries are also observed in these PEAD patterns. These asymmetry of the patterns can be understood by the dipole transition selection rule considering the electric field of the linearly polarized light and the symmetry of the wave function of the electrons in initial states. The simulated PEAD patterns which are calculated considering these effects of the linear polarization of the light and the wave function symmetry of the electronic bands which are described by tight binding approximation well reproduced the experimental PEAD patterns of $1T\text{-}TaS_2$ . Contrast to the three fold symmetry of the band structure of $1T\text{-}TaS_2$ , the PEAD patterns of the $2H\text{-}$ polytypes shows the six fold symmetry reflecting the higher symmetry of their crystal structure than that of the $1T\text{-}$ polytypes.

To investigate the photon energy dependence of the PEAD patterns, we have also observed the PEAD patterns of $1T\text{-}TaS_2$ using several photon energies. In consequence, the breaking of the above mentioned selection rule of the dipole transition is observed in the PEAD patterns of h$\nu$=40,(42.5) and 49eV, which correspond to the Ta $5p5d$ resonance photoemission conditions. That is to say in the resonance photoemission conditions, some additional intensities appear on the forbidden plane where the PEAD patterns of the h$\nu$=33eV, the off-resonance condition, have no intensities. This difference between on- and off-resonance photoemission conditions were also shown in the measurement of $2H\text{-}TaSe_2$ .

Finally, we discussed about the Fermi surface nesting of the $1T\text{-}TaS_2$ . As the results the vanishing of the Fermi surface intensities at the parts where large nesting will occur deducing from the shape of the Fermi surface which is derived from the theoretical calculation. We have also tried to observe the change of the Fermi surface due to the CDW phase transition from NCCDW to CCDW which accompany the metal-insulator transition and the intensity reduction of the Fermi surface at $T_{Si}T_C$ was observed. The observed PEAD patterns of the $2H\text{-}TaSe_2$ and $2H\text{-}NbSe_2$ near $E_F$ is also in fair agreement with the recently calculated Fermi surface of $2H\text{-}NbSe_2$ .

$1T\text{-}TaS_2$ (R.T.)

Exp.                    Calc.
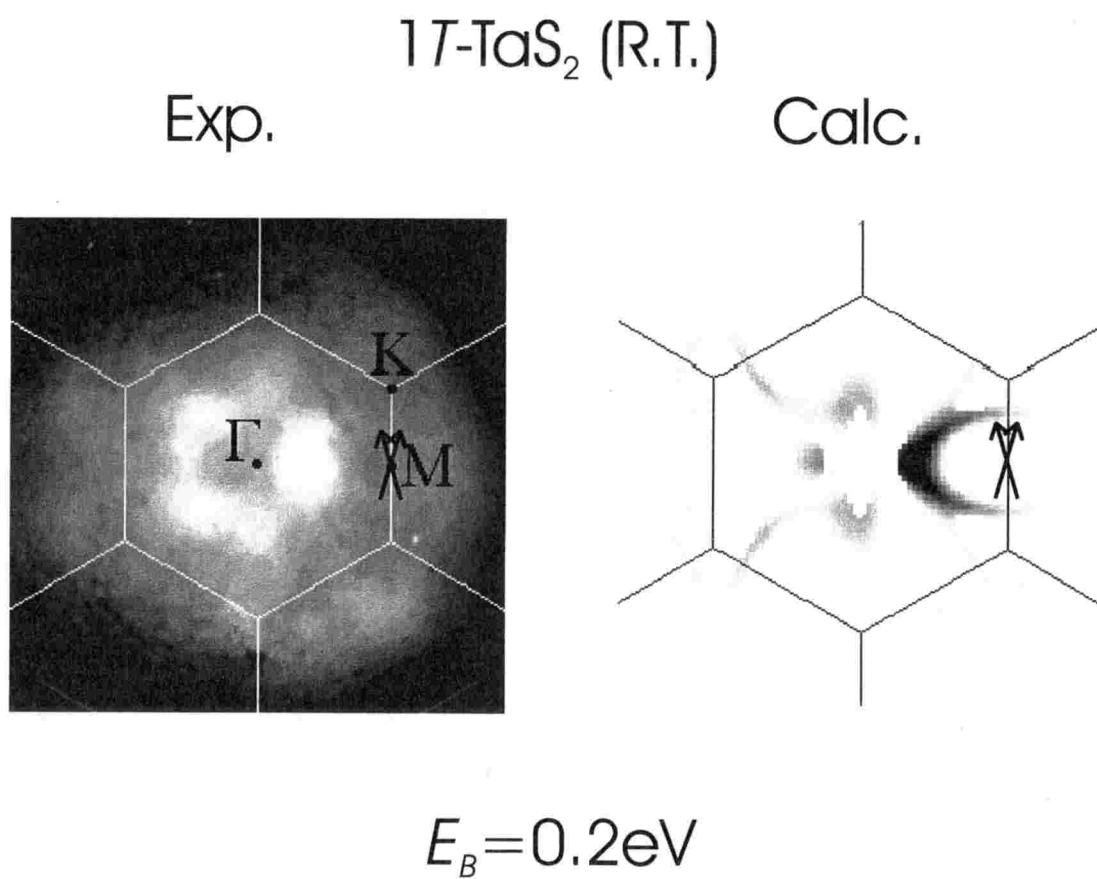
$E_B = 0.2eV$

Fig. 7.35: Comparison of the Fermi surface patterns of $1T\text{-}TaS_2$ between experiment and calculation. The nesting vector which is derived from the LEED pattern is indicated by arrow.
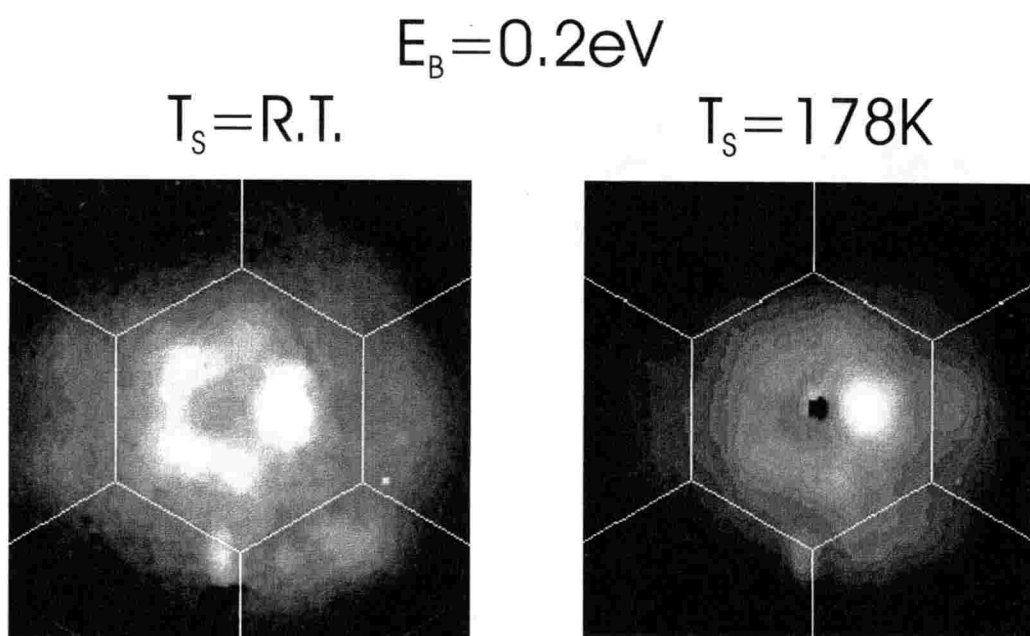
Fig. 7.36: Comparison of the Fermi surface patterns of $1T$-TaS$_2$ between the measurements of $T_S$=300K and 178K.
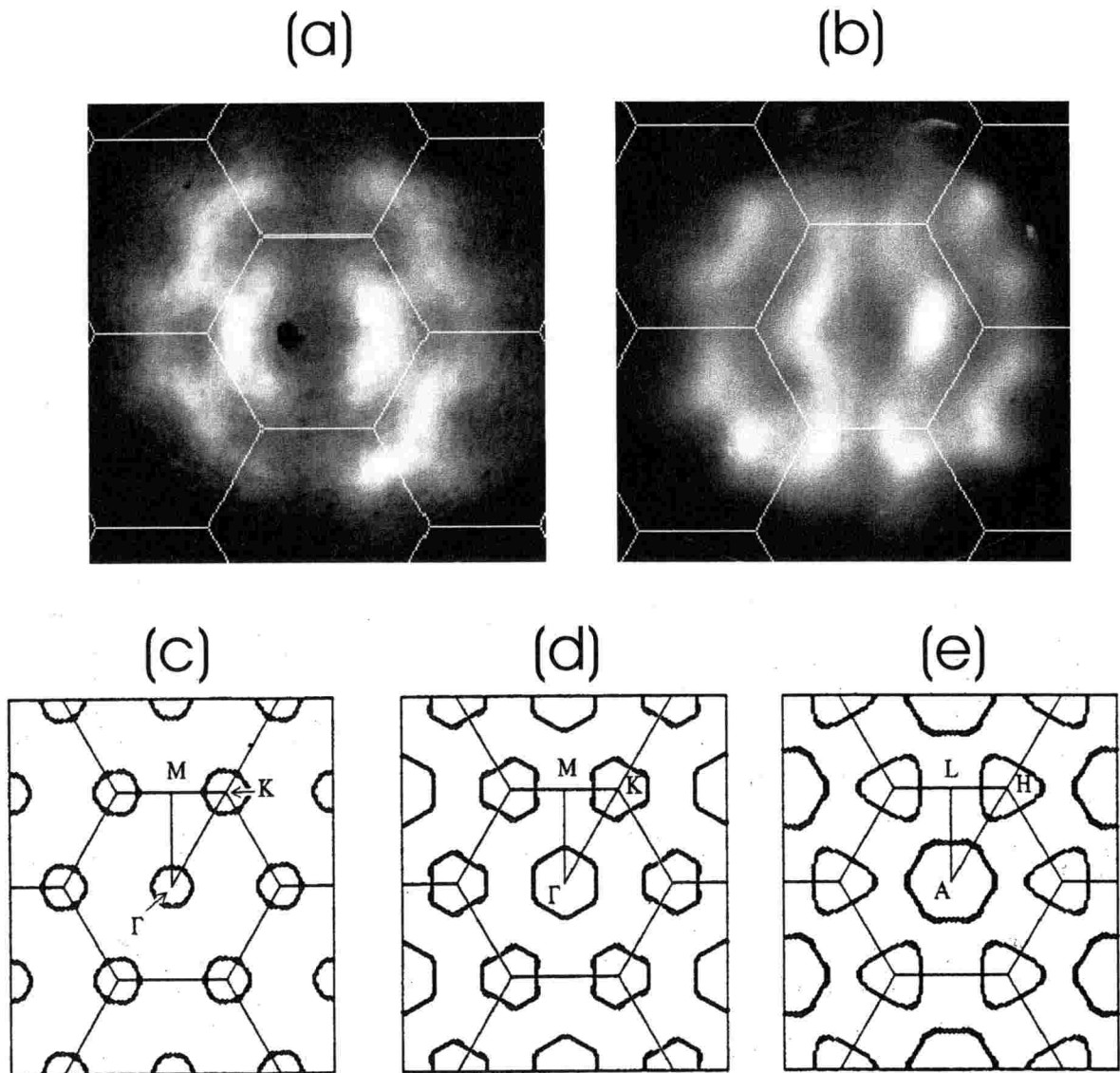
Fig. 7.37: Fermi surface patterns of $2H$-polytypes. (a) and (b) are the experimental PEAD patterns at $E_B$=0.3eV of the $2H$-TaSe$_2$ and $2H$-NbSe$_2$ measured at h$\nu$=40eV and 45.4eV.(c),(d) and (e) is the calculated Fermi surfaces of the $2H$-NbSe$_2$ by Nishino *et al.*. The (c) and (d) are the Fermi surfaces of the $2H$-NbSe$_2$ at $\Gamma$-M-K plane of two different Nb $4d$ bands. These two bands are degenerated at the A-L-H plane and the Fermi surface at the plane is (e).

159

# References

[1] E.Bjerklund and A.Kjekshus, Acta Chem. Scand., **21**, 513 (1967).

[2] M.Mstrxio, P.D.Dernier, A.Menth, and G.W.Hull, Jr., J.Solid State Chem. **4**, 425 (1972).

[3] For example, H.W.Myron and A.J.Freeman, Phys.Rev.B **11**,2087 (1975).

[4] L.F.Mattheiss, Phys.Rev.B, bf 8, 3719 (1973).

[5] H.Nishimoto, T.Okuda, T.Nakatani, H.Daimon, T.Matsushita, S.Imada,S.Suga, H.Namba, T.Ohta, y.Kagoshima and T.Miyahara, Solid State Commun. **98**, 671 (1996).

[6] R.Claessen, B.Burandt, H.Carstensen and M.Skibowski,Phys.Rev.B41,8270(1990).

[7] C.B.Scruby, P.M.Silliams and G.S.Parry, Phylos. Mag. **31**, 255(1975).

[8] W.L.McMillan, Phys.Rev.B **14**, 1496 (1976), K.Nakanishi, and H.Shiba, J.Phys.Soc.Jpn.**53**, 1103 (1984).

[9] X.L.Wu and C.M.Lieber, Science **243**, 1703 (1989).

[10] N.V.Smith and M.M.Traum, Phys.Rev.B **11**, 2087 (1975).

[11] N.V.Smith, S.D.Kevan, and F.J.DiSalvo, J.Phys.C18,3175(1985).

[12] R.A.Pollak, D.E.Eastman, F.J.Himpsel, P.Heimann and B.Reihl, Phys.Rev.B, **24**, 7435 (1981).

[13] R.Manzke, O.Anderson and M.Skibowski, J.Phys. C21, 2399 (1988).

[14] B.Dardel, M.Grioni, D.Malterre, P.Weibel, Y.Baer and F.Levy. Phys.Rev.B **46**, 7407 (1992).

[15] N.Suzuki, A.Yamamoto, and K.Motizuki, Solid State Commun. **49**, 1039 (1984).

[16] R.Claessen, B.Burandt, H.Carstensen, and M.Skibowski, Phys. Rev. B **41**, 8270 (1990).

[17] R.E.Peierls, *Quantum Theory of Solids, Clarendon Press, Oxford,* (1955).

[18] H.Daimon, Rev.Sci.Instrum.59,545(1988).

[19] A.Santoni, L.J.Terminello, F.J.Himpsel, and T.Takahashi, Appl.Phys. A52, 299 (1991).

[20] H.Nishimoto, T.Nakatani, T.Matsushita, S.Imada, H.Daimon, and S.Suga, J.Phys.:Condens. Matter **8**, 2715 (1996).
T.Matsushita, H.Nishimoto, T.Okuda, T.Nakatani, H.Daimon, S.Suga, H.Namba, T.Ohta, Y.Kagoshima, and T.Miyahara, J.Electron Spectrosc.Relat.Pheonom. **78**, 489 (1996).

[21] H.Daimon, S.Imada, H.Nishimoto, and S.Suga, J.Electron Spectrosc.Relat.Phenom., **76**, 487 (1995).

[22] H.Sakamoto, S.Suga, M.Taniguchi, H.Kanzaki, M.Yamamoto and M.Seki, Solid State Commun. **52**, 721 (1984).

[23] S.Al Mousalami, J.M.Bizau, B.Rouvellou, D.Cubaynes, L.Journel, F.J.Wuilleumier, J.Obert, J.C.Putaux, T.J.Morgan and M.Richter, Phys.Rev.Lett**76**,4496 (1996).

[24] J.A.Wilson, F.J.Disalvo, and S.Mahajan, Phys.Rev.Lett.**32**, 882 (1974).

[25] P.M.Williams, G.S.Parry and C.B.Scruby, Phil.Mag.**29**, 695(1974).

[26] Y.Yamada, J.C.Tsang, and G.V.Subba-Rao, Phys.Rev.Lett.**34**, 1389 (1975).

[27] Y.Nishino, M.Shirai, N.Suzuki, and K.Motizuki, J.of Phys.Soc.Jpn. **63**, 156 (1994).

# Chapter 8

# Concluding remarks

To investigate the surface geometric and electronic structures of the alkali metal(AM) and Ag induced Si(111)3×1 reconstructions, I have performed surface sensitive Si $2p$ core level photoelectron spectroscopy and angle resolved photoelectron spectroscopy(ARPES) for the Si(111)3×1-Na, -Rb, and -Ag surfaces and determined the surface core level shifts(SCLS) of these surfaces and surface state band dispersions of the Si(111)3×1-Na surface.

As a result I have found the saturation coverage of the 3×1-Na as 1/3ML. The SCLS results show the existence of at least two kinds of surface Si atoms charged positively and negatively on these surfaces. The ARPES results indicate that there are at least four occupied surface states on the Si(111)3×1-Na surface, and the surface is semiconducting. One of the surface states, $S_1$ has the characteristic dispersion being similar to that of the $\pi$-bonded chain structure of the Si(111)2×1 surface. From these results I have proposed three types of surface structural models. By comparing the experimental dispersions with the theoretical ones I concluded that the 5-6-7 model is most plausible for the 3×1-AM surface among the so far proposed models.

Some discrepancies between AM induced 3×1 surfaces and Ag induced one are observed in the SCLS measurement suggesting the different surface structure or some modified structure on the 3×1-Ag surface compared with that on the 3×1-AM.

Next, I have performed Si $2p$ core level spectroscopy and ARPES measurement for the Si(111)5×2, $\alpha$-$\sqrt{3}$, $\beta$-$\sqrt{3}$ and 6×6-Au surfaces and determined their SCLS's and surface band structure. The strong band bending was observed on every surface. From the SCLS result, the difference between the $\alpha$-$\sqrt{3}$ and $\beta$-$\sqrt{3}$-Au and the similarity between the $\beta$-$\sqrt{3}$ and 6×6 structures are suggested. This structural similarity of the $\beta$-$\sqrt{3}$ and 6×6 structures is also supported by ARPES measurement.

So far proposed models for the 5×2-Au and the $\sqrt{3} \times \sqrt{3}$-Au surfaces could not successfully explain their SCLS results when we consider uniform surfaces without domain walls. Assuming that one of the surface component of the $\sqrt{3} \times \sqrt{3}$ surface is the contribution of the Si atoms at the domain walls, our SCLS results are consistent with the picture that the ordering domain wall causes the phase transition from the $\alpha$-$\sqrt{3} \times \sqrt{3}$ to 6×6 surface via $\beta$-$\sqrt{3} \times \sqrt{3}$ surface.

The evidence of the existence of non-bonding and bonding Au $5d$ electrons were observed in every Au/Si(111) reconstructed surfaces in ARPES, and the bonding of Au $5d$ electrons was also confirmed in the SCLS measurement. In addition metallic character of the $\beta$-$\sqrt{3}$ and 6×6 was observed. The main difference between the $\alpha$-$\sqrt{3}$ and $\beta$-$\sqrt{3}$ surfaces is the clear metallic surface states of the $\beta$-$\sqrt{3}$ surface compared to the defect-like very faint metallic

states of $\alpha$-$\sqrt{3}$ surface. Among these reconstructions the 5×2 surface has relatively different and complex surface dispersions from those of the other surfaces indicating the different bonding characters between the Si and Au atoms on this surface.

Finally, I have performed the 2D-ARPES measurements on the transition metal dichalcogenides, 1$T$-TaS$_2$ , 2$H$-TaSe$_2$ , and 2$H$-NbSe$_2$ and observed photoelectron angular distribution(PEAD) patterns of these layered compounds. The PEAD patterns of these 1$T$-TaS$_2$ , 2$H$-TaSe$_2$ , and 2$H$-NbSe$_2$ clearly show their binding energy dependence reflecting mainly the band structure of each material. In addition, the strong intensity asymmetries are also observed in these PEAD patterns, which are due to the dipole transition selection rule including the electric field of the linearly polarized light and the symmetry of the wave function of the electrons in the initial states. Contrast to the three fold symmetry of the PEAD patterns of 1$T$-TaS$_2$ , those of the 2$H$- polytypes show the six fold symmetry reflecting the higher symmetry of their crystal structure than that of the 1$T$- polytypes.

I have also investigated the photon energy dependence of the PEAD patterns of 1$T$-TaS$_2$ . In consequence, the breaking of the above mentioned selection rule of the dipole transition was observed in the PEAD patterns in the resonance photoemission conditions.

From the obtained PEAD patterns of these 1$T$-TaS$_2$ , 2$H$-TaSe$_2$ , and 2$H$-NbSe$_2$ we also determined the Fermi surfaces of these layered compounds. The presently observed Fermi surface of the 1$T$-TaS$_2$ is in good agreement with some previously deduced ones and suggests the existence of strong nesting in this material. We have also tried to observe the change of the Fermi surface by the CDW phase transition from NCCDW to CCDW, and some changes of the Fermi surface were observed. The determined Fermi surfaces for the 2$H$-TaSe$_2$ and 2$H$-NbSe$_2$ are also in fair agreement with the calculated Fermi surfaces of recently performed band calculations.

# Acknowledgement

In completion of this doctoral thesis I am much obliged to so many people.

In particular I am grateful to Prof. S.Suga, for his stimulating discussion and careful reading of manuscripts, and his insight and great knowledge of the field of photoemission was an inspiration to me.

I would also like to heartfelt thank to Prof.Daimon for his appropriate discussion and giving me the experience to use the peerless interesting analyzer. I was very much stimulated by his vigorous imagination.

I would also like to thank:

to all the members of Suga research group including Dr. S.Imada, Ms. T.Ukawa, Mr. K.Nakatsuji, and Mr. H.Oki for their help with my study, daily life of laboratory, and data acquisition in the experiments.

to all the graduate students of Suga laboratory including Dr. T.Matsushita for his computer programs of PEAD simulation, Dr. T.Nakatani for his computer programs for analysis of the 2D data and for the measurement, Dr. K.Sakamoto, Dr. H.Nishimoto, Mr. H.Shigeoka, and Mr. J.Shinoda for their help with the experiments.

to Prof. T.Ishii, Prof. S.Shin, Dr. Y.Tezuka, and Mr. M.Fujisawa, the staff of solid state spectroscopy and instrumentation group of Synchrotron Radiation Laboratory of Institute for Solid State Physics(SRL-ISSP) for their supports to my experiments at SOR-RING.

to Prof. Y.Kamiya, Dr. T.Koseki, Mr. H.Takaki, Mr. K.Shinoe, Mr.H.Kudoh, and Ms.Y.Hara, the staff of accelerator physics group of SRL-ISSP for their operation of SOR-RING and to Ms. Y.Kobayashi for her help with my daily life in Tanashi.

to Prof. A.Kakizaki, Dr. T.Kinoshita, Dr. A.Kimura, and Ms. A.Harasawa, the staff of solid state spectroscopy and instrumentation group of SRL-ISSP of Tsukuba branch, for their kind supports to my experiments in Tsukuba and many discussions.

to Dr. Y.Tezuka and Prof. S.Ino of ISSP for their cooperation of the experiments of ARPES on Si(111)-Au surfaces.

to Prof. Y.Kitazawa, Prof. T.Hasegawa of Univ. of Tokyo and Prof. T.Kanomata of Tohoku Gakuin Univ. for their providing good quality samples of transition-metal dichalcogenides.

and finally I would like to thank to my family for their unchanged supports to my life.

# List of Publication

1. "Surface and Bulk Core Level Shifts of the Si(111)3×1-Na and Si(111)$\delta7$×7-Na Surfaces."
<u>T.Okuda</u>, H.Shigeoka, H.Daimon, S.Suga, T.Kinoshita, and A.Kakizaki, Surf.Sci.**321**, 105 (1994).

2. "Photoemission Study of the Si(111)3×1-K Surface."
K.Sakamoto, <u>T.Okuda</u>, H.Nishimoto, H.Daimon, S.Suga, T.Kinoshita, and A.Kakizaki, Phys.Rev.B **50**, 1725 (1994).

3. "Surface Core Level Shifts of the Au Adsorbed Si(111) Reconstructed Surfaces."
<u>T.Okuda</u>, H.Daimon, H.Shigeoka, S.Suga, T.Kinoshita, and A.Kakizaki, J. Electron Spectrosc. Relat. Pheonm. **80**, 229 (1996).

4. "Unusual Two-Dimensional Angular Distribution of Photoelectrons of Kish Graphite and 1$T$-Ta$_2$."
H.Nishimoto, <u>T.Okuda</u>, T.Nakatani, H.Daimon, T.Matsushita, S.Imada,S.Suga, H.Namba, T.Ohta, Y.Kagoshima and T.Miyahara, Solid State Commun. **98**, 671 (1996).

5. "Angle-resolved Photoemission Study of $M_x$TiS$_2$($M$=Mn, Fe, Co, Ni; x=1/3, 1/4)."
T.Matsushita, S.Suga, Y.Tanaka, H.Shigeoka, T.Nakatani, <u>T.Okuda</u>, T.Terauchi, T.Shishidou, A.Kimura, H.Daimon, S.-J.Oh, A.Kakizaki, T.Kinoshita, H.Negishi and M.Inoue, J. Electron Spectrosc. Relat. Phenom. **78**, 477 (1996).

6. "Two-dimensional angular distribution of photoemission spectra from the valence band of 1$T$-TaS$_2$ ."
T.Matsushita, H.Nishimoto, <u>T.Okuda</u>, T.Nakatani, H.Daimon, S.Suga, H.Namba, T.Ohta, Y.Kagoshima and T.Miyahara, J. Electron Spectrosc. Relat. Phenom. **78**, 489 (1996).

7. "Angle Resolved Photoelectron Spectroscopy of the Si(111)3×1-Na Surface."
<u>T.Okuda</u>, K.Sakamoto, H.Nishimoto, H.Daimon, S.Suga, T.Kinoshita, and A.Kakizaki, Phys.Rev.B **55**(1997) to be appeared.

8. "Surface Electronic Sturcture of Alkali and Noble Metal Overlayers on Si(111) Surfaces."
<u>T.Okuda</u>, H.Daimon, S.Suga, Y.Tezuka, and S.Ino, Appl.Surf.Sci. to be appeared in 1997.

9. "Systematic Study of the Surface Core Level Shifts of Si(111)5×2, $\alpha$- and $\beta$- $\sqrt{3}$ × $\sqrt{3}$ and 6×6-Au surfaces."
<u>T.Okuda</u>, H.Daimon, H.Shigeoka, S.Suga, T.Kinoshita, and A.Kakizaki, Surf. Sci. in submission.

10. "Angle-Resolved Photoemission Study of the Si(111)5×2, $\alpha$- and $\beta$- $\sqrt{3}$ × $\sqrt{3}$ and 6×6-Au surfaces."
<u>T.Okuda</u>, H.Daimon, S.Suga, Y.Tezuka, and S.Ino, in preparation.

11. "Two dimensional angle resolved photoelectron spectroscopy of transition metal dichalcogenides."
<u>T.Okuda</u>, K.Nakatsuji, S.Suga, H.Daimon, Y.Tezuka, and S.Shin, Activity report of synchrotron radiation laboratory 1995 (1996).